Curing Simulations of a Fibre-Reinforced Thermoset on a Micro- and Nano-Scale

Zur Erlangung des akademischen Grades eines
**DOKTORS DER INGENIEURWISSENSCHAFTEN
(Dr.-Ing.)**
von der KIT-Fakultät für Maschinenbau des
Karlsruher Institut für Technologie (KIT)

angenommene

Dissertation

von

Felix Konrad Schwab, M.Sc.

Kurzfassung

Die Eigenschaftskombination hoher Steifigkeit und Festigkeit bei gleichzeitig niedriger Massendichte rückt die Materialklasse der faserverstärkten Polymere generell stärker in den Fokus von Mobilitätsanwendungen und bewegten Massen. Nachteilig an der Kombination von steifen Fasern und einer zähen, leichten Polymermatrix erweist sich oft die Verwendung unterschiedlicher Materialtypen. Die in dieser Arbeit verwendete Paarung des *glasfaserverstärkten Duromers* zeichnet sich speziell durch unterschiedliche thermische Ausdehnungskoeffizienten und die chemische Aushärtereaktion des Duromerharzes aus. Da der Produktionsprozess eines Bauteils aus glasfaserverstärktem Duromer oft bei erhöhter Temperatur stattfinden muss, um entweder die chemische Vernetzungsreaktion zu aktivieren oder zu beschleunigen, erfährt jedes Bauteil thermische Dehnungen und chemischen Schwund. Diese Dehnungen ändern sich nochmals, sobald sich das Bauteil auf Raumtemperatur abkühlt, bleiben aber grundsätzlich aufgrund der Bindung zwischen Fasern und Matrix erhalten. Durch diesen Eigendehnungszustand werden Verzug und lokale Eigenspannungen induziert, wobei sich insbesondere lokale Spannungsspitzen an der Faser-Matrix-Grenzfläche und an den Faserenden ausbilden können. Diese innere Vorbelastung kann eine Vorschädigung des Bauteils in Form von Mikrorissen verursachen, wodurch insgesamt die Bauteileigenschaften und -belastbarkeit herabgesetzt werden.

Ein besseres Verständnis der Aushärteprozesse und des Einflusses unterschiedlicher Prozessparameter auf das induzierte Eigendehnungsfeld ist daher unerlässlich, um die effektive und verlässliche Einsetzbarkeit von faserverstärkten Duromeren zu erhöhen. Diese Arbeit beschäftigt sich deshalb mit der Modellierung und Simulation des Aushärteprozesses und der Aushärtereaktion von faserverstärkten Duromeren. Hierbei wird der Fokus skalenübergreifend auf die Mikrostruktur und auf die Molekularebene gelegt, und die Auswirkungen der Aushärtung auf der jeweiligen Skala untersucht. Auf Mikrostrukturebene wird die rechnergestützte Phasenfeldmethode zur Darstel-

lung von Faser-Matrix-Strukturen verwendet, und darauf aufbauend ein Modell zur Beschreibung der mechanischen, thermischen und chemischen Effekte während eines Aushärteprozesses abgeleitet. Weiterhin wird die Rissausbreitung innerhalb faserverstärkter Mikrostrukturen modelliert und ebenfalls mithilfe der Phasenfeldmethode umgesetzt. Hiermit wird ein Beispielprozess simuliert und dessen Verlauf ausgewertet und diskutiert. Die Entwicklung von lokalen Eigendehnungs- und Eigenspannungszuständen bildet hierbei einen Fokus dieser Arbeit. In einem weiteren Schritt wird überprüft, ob diese lokalen Spannungen in eine Mikroriss-Ausbreitung münden. Diese mikroskaligen Betrachtungen werden durch rechnergestützte Molekulardynamiksimulationen auf der Nanoebene begleitet. Die chemische Aushärtereaktion eines Duromers wird hierbei durch Algorithmen zur Herstellung und Auflösung chemischer Bindungen nachgestellt, und so die Aushärtereaktion anhand von Materialkenngrößen wie Volumenschwund nachvollzogen und diskutiert. Die hierdurch erzeugten Polymernetzwerke dienen dann der Berechnung von temperatur- und aushärtegradabhängigen Materialeigenschaften, welche zur Durchführung der Prozesssimulation auf der Mikroebene benötigt werden.

Abstract

The combination of high stiffness and toughness, available at low mass density, makes the material class of fibre-reinforced polymers interesting for applications in the mobility sector and for all kinds of moving masses in general. The advantageous mechanical material properties, arising from the stiff fibres supported by a tough and light polymer matrix, often go along with disadvantages emerging from combining two different material types. This work makes use of the combination of glass fibres and thermoset matrix, which exhibit differences in the thermal expansion coefficient, and the thermoset has to be cured, resulting in chemical shrinkage. When producing a fibre-reinforced thermoset structure, the process is often run at an elevated temperature to either trigger the chemical curing reaction or to accelerate selfsame. Through these temperature changes and the progressing curing reaction, each structure is subject to thermal and curing strains. The induced strains may change when the structure is cooled down to room temperature, but they are preserved due to the bonding between fibres and matrix. These eigenstrains result in warpage and local eigenstresses, which mainly concentrate at fibre-matrix interfaces and fibre tips. As a consequence these internal loads may yield the formation and propagation of micro-cracks, which in total reduce the structure's performance and reliability.

Therefore, a more profound understanding of the curing process and the influence of process parameters is essential to provide for a safe and effective application of fibre-reinforced thermosets. This work thus deals with modelling and simulating the curing process and reaction of fibre-reinforced thermosets. The emphasis is the examination of the consequences of curing within the fibre-matrix microstructure and on a molecular scale. On a micro-scale, the phase-field method is used as a computational tool to describe the fibre-matrix domains, and based thereon a curing process model is derived, taking into account mechanical, thermal and chemical effects. Furthermore a phase-field crack model is implemented capable of simulating crack propagation within

fibre-reinforced microstructures. The former model is used to simulate a virtual process, whose progress and outcome is evaluated and discussed focussing on the development of local eigenstrains and eigenstresses. The latter model then is used to examine whether these local stresses lead to micro-crack propagation. These micro-scale simulations are accompanied by molecular dynamics simulations. On a nano-scale the chemical reactions are described by algorithms forming and dissociating chemical bonds. These are used to simulate the curing reaction of a thermoset, which is discussed on the basis of quantities such as volume shrinkage. The hereby artificially cured polymer networks are further analysed for micro-scale material properties at different temperatures and degrees of cure, which are necessary for the aforementioned micro-scale curing process simulations.

Acknowledgements

Contents

Contents

1

Introduction and Motivation

Fibre-reinforced polymers (FRP), a sub-class of composite materials, is a rather modern class of materials [8]. Two of its key characteristics are the ability to tailor behaviour and properties with regard to the field of application and the low density of the composite, compared to steel or aluminium, for example [80, 151]. This comes from the vast variety of fibres (e.g. glass, carbon, aramid or natural fibres) [26] and matrix types (thermoplasts or thermosets) [11] available, which may be combined based on the application area or the restrictions of production processes. A second dimension of tailoring arises due to the possibility of directly influencing the composite properties and behaviour when fibre length, orientation and volume content are varied [8]. In the context of mechanics, the fibres are responsible for bearing externally

applied loads, while the matrix fixes and supports the fibres. Apart from load transfer, many other behaviours, such as corrosion-resistance, thermal and electric conductance or crashworthiness, are excellent and may be further adjusted [162]. A disadvantage from the viewpoint of design and production technique is that composite properties and performance strongly correlate with fibre placement and orientation, which demands both a thorough design process and production processes capable of implementing design specifications at a reproducible quality, often against the background of restrictions arising from mass production. This is especially important as the combination of two different materials, fibres and matrix, bears the risk of introducing significant residual stresses and warpage or micro-cracks through the production process, which lowers the effective material properties of the overall composite structure [8, 139].

An early field of application was and still is the aerospace industry [162], where weight reduction and lightweight construction always were and are an important aspect. Due to relatively small quantities in this industry, production processes and quality control are partially manual work and hence not critical in terms of time [170]. Nowadays the possibilities of lightweight construction, emerging from the use of FRPs, also reaches other industries and the mass market, e.g. the automotive industry or the energy sector in the form of windmill rotors [8, 162].

Especially in industries where large quantities and low cycle times are established, it becomes desirable to be able to predict the aforementioned residual stresses and micro-cracks and to thereby deduce process parameters which minimise these effects. Due to the complexity of such production processes, often involving mechanical, thermal and chemical effects, trial-and-error process design is still common and widespread [2, 70]. A more extensive approach, also targeted on a comprehension of the basic processes, is opened by the field of process simulation, which also allows a more direct examination and evaluation of material behaviour and process influences.

The scope of this work is to derive and implement models describing parts of an

industrial production process of FRPs. The application is generally restricted to a fibre-reinforced thermoset (FRTS), and in particular, isotropic glass fibres (GF) and an unsaturated polyester-polyurethane hybrid (UPPH) matrix are used as a prototypical background. The FRTS is simulated in the moulding process, which is mainly governed by the exothermic TS curing reaction. The curing process of the thermoset (TS) matrix has an extensive influence on the final behaviour, properties and shape of a FRTS. The curing process itself is a chemical process, in which exothermic chemical reactions lead to the formation of polymer chains and networks that change the internal structure and hence the properties and volume of the thermoset. This takes place at an elevated temperature to trigger the exothermic reaction, and is followed by a cooling process to reach room temperature [101]. Within the thermoset, the globally applied temperature is distributed heterogeneously, due to both the fibres and the varying reaction speeds. This opens out into a heterogeneous development of thermoset material properties and, in combination, temperature and cure-driven strain gradients are induced [139]. Ultimately, this yields local eigenstresses, especially with fibres staying approximately constant in their properties and behaviour under the induced temperature changes. Cooling down the FRTS after curing induces additional thermal eigenstresses due to variations in thermal expansion coefficients. The overall residual stresses may lead to warpage or sink marks in thermoset regions. This relaxation of stress peaks is constrained close to fibres, where thermoset and fibres are bonded. Hence stress peaks prevail close to fibres which may result in pre-stressed and pre-damaged FRTS structures [60, 61]. The extent of localised stresses highly depends on the material properties of fibres and matrix material, where the latter depends on the curing process itself [203]. In general, the cure shrinkage and the resulting stresses result in compression in fibres and tension in the surrounding matrix regions, which may cause fibre-matrix interface debonding and further micro-cracking, already early in the production process. Together with residual stresses, this may significantly reduce the theoretically possible material performance and properties. In contrast, a positive example of cure

shrinkage are hoop stresses around reinforcing fibres [134]. Elevated fibre pull-out energy dissipation may be the consequence leading to an increased toughness.

The processes and effects mentioned define the physical and chemical framework to be modelled. Chemical, thermal and mechanical processes and influences and their interplay have to be considered. To connect these processes correctly, a common thermodynamic framework is formulated. Extensive derivation and discussion of models describing the curing process on the basis of finite deformation is found in the work of Lion and Höfer [108], Adolf and Chambers [1], Klinge *et al.* [92] and Mahnken [110]. In the small-strain context, Hossain and Steinmann [81] follow similar reasoning. Generally, material properties used within the derived models have to be fitted to data determined through experiments [149]. The number of material properties, which often show a temperature and degree of cure dependence, greatly influences the applicability of a model and an effective determination through experiments. Lastly, the simulatively predicted eigenstresses have to be checked for the ability to cause micro-cracking [10].

1.1 Scale-bridging the curing process

Consistent with the cited models, the FRTS curing process will be mainly examined and simulated on a *micro-scale*, resolving fibres and matrix regions explicitly. The curing process of the TS is also considered on a *nano-scale* simulation to learn about the internal structure and hence the material property development throughout the curing reaction. Local eigenstresses predicted on the basis of the material properties found are examined in micro-scale fracture simulations.

Micro-scale: Phase-field Method   As a simulation technique, the phase-field method (PFM) is used on a micro-scale to cover the FRTS curing process and crack propagation. The strength of this computational method lies in its

ability to easily track the movement of free boundaries [128] and to represent complex geometries without the need to re-mesh [107] the simulation domain during a simulation, both on the basis of domain parametrisation via smooth order parameter fields. Hence, a key task is to handle free boundaries of neighbouring physically separable regions, e.g. grains, under the influence of different thermodynamic fields. Within a thermodynamic framework, this ansatz allows the simulation of microstructures and their evolution in a computationally efficient way, which opens up the method to a variety of fields in material science and physics [124].

The origins of the PFM may be traced back to the works of van der Waals [194], Ginzburg and Landau [187] and Cahn and Hilliard [28], among others. Nowadays the range of application comprises microstructural processes such as solidification [20], coarse graining [173], solid-solid phase transition [34, 124], martensitic transformation [111, 161] and crack propagation [6, 155]. Another field of application is shape and topology optimisation of structures [180]. The potential of representing complex geometries without special effort was shown in [107].

Despite the numerical advantage and the versatile applicability, spreading the sharp interface to a diffuse interface has a major drawback: Inside the volumetric interface, different physical regions may overlap. If quantities such as mechanical stress or temperature influence or drive the movement of the interface, the calculation of those quantities has to follow a homogenisation procedure in the diffuse interface to harmonise the behaviour of the neighbouring regions. As all of the above microstructural processes follow thermodynamics, the challenge arises in choosing a homogenisation procedure and interface dynamics, which satisfies the thermodynamic necessities. In the following, the research on mechanical models in this field is outlined.

Over the last few years, several researchers put effort into enhancing the mechanical models which are used within the phase-field method. Until recently, the typical choices were simple homogenisation schemes such as those by Voigt/Taylor [192] (VT) or Reuss/Sachs [146] (RS). As they represent only

the upper (VT) and lower (RS) bound of homogenisation, respectively, they lead to the true mechanically admissible behaviour only in special (quasi-1D) cases. Yet their use is widespread, mainly due to their simplicity and the argument that in the limit case, they lead to a sharp interface behaviour. A combination of both homogenisation schemes is Khachaturyan's approach [90]. While this approach falls back to the VT scheme in purely elastic media, it incorporates inelastic parts of the RS scheme. Chen and Shu [33] apply a homogenisation based on the well-known Hashin-Strikhman bounds to solve martensitic phase transformations. Durga *et al.* [46] had a closer look at the VT and RS homogenisation schemes and their respective excess stress, strain and elastic energy. Their findings lead to the conclusion that a straight interface bears no excess energy if either it is loaded uniaxially in the normal direction and RS homogenised, or loaded uniaxially in the tangential direction and VT homogenised. The latest advances in this topic aim at fulfilling consistent mechanical jump conditions; hence kinematic compatibility and continuous traction across the interface. Mosler *et al.* [125] introduced a model for finite deformation and two phases consistent with these jump conditions. For infinitesimal deformations and two phases, Schneider *et al.* [159] suggested a homogenisation scheme which intrinsically uses the jump conditions to construct a locally compatible stiffness matrix. In the same work, they derived phase-field-based configurational forces for their homogenisation scheme, cf. [68], and demonstrated the accuracy of this mechanical driving force for Eshelby's inclusion problem. In [12, 91], the work of Mosler *et al.* is continued and extended by configurational and micro-forces, on a two-phase basis. Simultaneously, Schneider *et al.* [158] introduced an ansatz for finite deformations and multiphase systems, based on a locally implicit scheme, to solve both mechanical jump conditions. In the same work, configurational and micro-forces are derived as a thermodynamically consistent driving force for multiphase-field models. The same group generalised their approach for infinitesimal deformations to multiphase systems, by introducing a generalised normal vector for regions with more than two phases [157].

The implementation of fracture behaviour within a phase-field framework often happens in the spirit of Griffith's theory [65], which balances surface energy and energy release. On this basis, Francfort and Margio [56] suggested an evolution law for crack propagation closely linked to the driving principle of global energy minimisation. Due to their ability to implicitly track a free boundary, phase-field models for crack evolution have become an early favourite in applying this energy minimising approach for brittle fracture [22, 23, 88, 96, 120, 171]. Further or advanced applications tackle, amongst others, ductile materials [6, 97], anisotropy [104, 133] or multi-physics [24, 119, 121]. These models are mainly formulated for homogeneous materials and structures. In contrast, many fracture and failure mechanisms often occur on a micro-scale, where many materials have a heterogeneous appearance. Recently, cohesive zone models were introduced to the phase-field crack method (e.g. [31, 43, 132, 140]) to account for interfacial effects. Another approach is to lower the crack resistance G^c in the interface region to realise an interfacial crack resistance, accounting for weaknesses at phase boundaries. An example is Hansen-Dörr *et al.* [73] who model a locally varying G^c value upon a virtual phase boundary. Hence, different phases only exist in the sense of a pre-calculated G^c field.

The main objective of this work is to derive and implement a curing model on the basis of the PFM for the micro-scale. As the curing process is not linked to a phase transition, there is no explicit preliminary work in the literature where such a model was implemented within a phase-field approach. Hence, the theoretical background lies mostly in general work in the field of curing process models, which were mentioned above. As a consequence, when deriving a model for the curing process, a main focus is put on a thermodynamically meaningful implementation, in the phase-field context. The basis for this is the work of Mosler *et al.* [125] and Schneider *et al.* [157–159], who showed a consistent approach for purely mechanical problems. This procedure is analogously and coherently applied to heat conduction. The complete model is applied to simulate the curing process of FRTS, with the objective to observe

the formation of eigenstresses.

To consider fracture and crack propagation on the basis of predicted eigen-
stresses in an FRTS environment, the phase-field model for crack propagation
by Schneider *et al.* [155] and Nestler *et al.* [130] is modified and extended for
the use in FRPs. The main focus is the implementation of a separate interfacial
crack resistance (interface strength) to be able to mimic debonding processes
in fibre-matrix interfaces. The modified crack propagation model is used to
simulate micro-cracks on the basis of local eigenstresses, induced by the curing
process.

Nano-scale: Molecular Dynamics Examinations on a nano-scale are con-
ducted with the computational method of molecular dynamics (MD). As gen-
erally intrinsic to simulative methods, and in particular for the calculation of
material properties, this enables the observation of material behaviour, without
being restricted to experimental constraints. In the scope of a curing ther-
moset, observations at, e.g. a constant temperature and a degree of cure would
pose severe difficulties in experiments, whereas they are straightforward in a
simulation.

On the basis of Newton's laws of motion, MD simulates atom or particle
movement on a molecular scale. Emerging from the work of Alder and Wain-
wright [3–5], where mainly particle collisions were simulated, the method
finds a broad application in the fields of physics, chemistry and biology [145]:
The possibilities range from simulating effects in solids such as defect for-
mation, fracture, grain boundaries and mechanical properties, over to fluid
dynamics questions, including laminar and unstable flow, to polymer chem-
istry, biomolecules and proteins, to mention just a few. Lately, with increasing
computational resources and hence larger possible simulation domains, some
topics have opened up to questions of material science, which allows the de-
velopment of a more profound understanding of material behaviour [143].
Among the first applications of MD to thermosetting polymers are the works

of Barton *et al.* [13, 14] and Hamerton *et al.* [72], who calculated material behaviour of cross-linked polymers. The predictions comprised mechanical and thermal behaviour and happened on the basis of pre-generated artificial network structures. Doherty *et al.* [44] used MD simulations to form cross-links in a thermoset. The basic approach, which is still common to use nowadays, is to allow the formation of a bond when the functional groups of two monomers move into the vicinity of each other. An analysis of material properties was not conducted. In the following years, however, research combined the simulation of bond formation with the material characterisation of the cross-linked thermosets. Examples are the work of Yarovsky and Evans [202], Heine *et al.* [76] and Wu and Xu [200]. On the basis of different states of chemical conversion, Li *et al.* [105, 106] analysed an amorphous thermoset for thermal and mechanical properties. A different approach to cross-link thermosets was introduced by Okabe *et al.* [136, 137], who used an Arrhenius-type equation to incorporate activation energies as a probabilistic feature into the bond formation process, while the aforementioned distance criterion was still used as a first step in determining reaction partners. Recently, Sharp *et al.* [165] examined the effect of varying water content on the curing rate and the glass transition temperature of thermosets.

In this work, the previously mentioned algorithms for bond formation are applied, extended and adjusted for the use with a UPPH resin. Besides the distance criterion, a probabilistic model, based on an Arrhenius-type equation, is used to determine if bond formation does occur. The overall bond formation algorithm is implemented in a way such that the process may take place during a regular MD simulation, without the need for intermediate minimisation runs. The main objective is to use simulation results of partial and full thermoset cures to calculate macroscopic material properties, which are used by the phase-field simulations.

1.2 Structure of this work

This work is divided into five chapters. The introduction, Chapter 1, gives a general background to the overall topic of this work and defines its scope. A theoretical background to different aspects of this work is introduced in Chapter 2. The topics range from an introduction to continuum mechanics with singular surfaces and material theory to linear elastic fracture mechanics, which are relevant for derivations and implementations on a micro-scale phase-field theory. Furthermore, thermoset chemistry and modelling is outlined: A description of the UPPH thermoset used within this work is supplied, the modelling of such polymer structures in molecular dynamics is addressed and a phenomenological point of view on the curing reaction is given for the continuum scale. This chapter is closed by different techniques for the determination of material properties, on the basis of MD simulations. In Chapter 3, models for the curing process and crack propagation on a micro-scale are derived on the basis of the theoretically introduced background, in the context of the PFM. Emphases are the derivation and motivation of the micro-scale models, on the basis of thermodynamic reasoning, and a thorough regularisation from sharp interface limits. Especially for the curing process, each model aspect is discussed. For MD, an approach for simulating thermoset curing and its algorithmic implementation is presented. All derived models are briefly evaluated on the basis of prototypical simulations. Broader application of the models occurs in Chapter 4. Here the different simulation techniques are combined: With MD, the curing process of the TS is conducted on the nano-scale and the results are used to determine material properties. With these material properties, the curing process of FRTS volume elements is simulated and evaluated for eigenstresses. In a last step, on the basis of these local eigenstresses, phase-field fracture simulations are performed to examine whether micro-cracking occurs under the given conditions. Summarising the derived models and the simulation results, Chapter 5 concludes this work and outlines fields of further research, regarding the scope of this work.

The implementation of models and parts of the post-processing builds on existing software packages. In the phase-field context, the multiphase and multiphysics in-house code PACE3D [82] (Parallel Algorithms for Crystal Evolution in 3D) is used, whose basis is the work of Nestler *et al.* [129]. Molecular dynamics implementations and simulations are conducted with the open source software LAMMPS [150] (Large-scale Atomic/Molecular Massively Parallel Simulator), which originates in the work of Plimpton [142]. Besides tools of the PACE3D framework, the software packages OVITO [174, 175] and VISIT [35, 103] are used for post-processing and visualisation. To build molecules for the use in LAMMPS, the open-source molecular builder AVOGADRO [9, 74] is used.

1.3 Notation

In this work, notation follows Einstein's summation convention [49]. Furthermore, a fixed Cartesian coordinate system exists in general, and therefore only subscripts are used. Tensors of all orders are not highlighted, and the number of unique indices indicates the order of the tensor. *Scalars*, or 0th-order tensors, are small letters without indices, e.g. a or β. *Vectors* (1st-order tensors) also commonly use small letters (u_i, χ_j or b_k). *Tensors of 2nd order* are often represented by capital letters (A_{ij}, Q_{kl}), but traditionally, some small Greek letters are used as well (σ_{ij}, ε_{kl}). A special operator is the *Kronecker delta*,

$$\delta_{ij} = \begin{cases} 1, & i = j \\ 0, & i \neq j \end{cases}, \tag{1.1}$$

which represents the identity in index notation. The *Levi-Civita operator* - or permutation symbol - is a special operator in the form of a 3rd-order tensor. It is defined as

$$\epsilon_{ijk} = \begin{cases} +1, & \text{forward permutation of } ijk \\ -1, & \text{backward permutation of } ijk \\ 0, & \text{if } i, j \text{ or } k \text{ are equal} \end{cases} . \tag{1.2}$$

Calculations within this notation are governed by the following rules:

Rule 1: A subscript index occurring **once** is free to vary from $1, \dots, N$.

Rule 2: Subscript indices occurring **twice** are implicitly summed over.

Rule 3: A term must not contain **three or more** instances of the same index, and each term must contain identically unique indices.

Rule 4: A comma indicates that a partial derivative has to be taken.

With these rules, basic algebraic tensor operations are introduced. The *inner product*, or *scalar product*, is written as $c = a_i b_i$. Thus, the norm of a vector d_i is described by $\sqrt{d_i d_i}$. The *outer product*, or *dyadic product*, defines a 2nd-order tensor in the following way:

$$T_{ij} = a_i b_j. \tag{1.3}$$

Another operation is the *cross product* of vectors a_j and b_k, which is noted

$$c_i = \epsilon_{ijk} a_j b_k. \tag{1.4}$$

Further, the transpose of a tensor A_{ij} is defined by switching the indices, A_{ji}, whereas its trace is the sum of the diagonal entries, A_{ii}. The inverse of a tensor A_{ij} is written as A_{ij}^{-1}, and the determinant as

$$J_A = \frac{1}{6}\epsilon_{ijk}\epsilon_{lmn}A_{il}A_{jm}A_{kn}. \tag{1.5}$$

The multiplication of a 2nd-order tensor with a vector is given by $c_i = A_{ij}b_j$. For a 4th-order tensor and a 2nd-order tensor, $\sigma_{ij} = C_{ijkl}\varepsilon_{kl}$ is equally noted. With the help of an arbitrary quantity ψ and the position vector x_i, the gradient, the divergence and the curl operator are introduced:

$$g_{ij} = \frac{\partial \psi_i}{\partial x_j} = \psi_{i,j}, \tag{1.6}$$

$$d = \frac{\partial \psi_i}{\partial x_i} = \psi_{i,i}, \tag{1.7}$$

$$c_i = \epsilon_{ijk}\frac{\partial \psi_k}{\partial x_j} = \epsilon_{ijk}\psi_{k,j}. \tag{1.8}$$

Here, the vector x_i depicts the position in the material (Euler) configuration (cf. Section 2.1.1.1), and therefore all three operators are defined in with respect to this configuration. The definitions of the reference (Lagrange) configuration can be achieved by using reference positions defined by a capital letter X_i, e.g. for the gradient

$$G_{ij} = \frac{\partial \psi_i}{\partial X_j} = \psi_{i,j}. \tag{1.9}$$

Generally, it can be said that if a notation or an operator is affine to the current or the reference configuration, the former often uses small letters, whereas the latter is marked by capital letters. In cases where no capitalisation happens in the reference configuration, this placement is indicated by the use of a superscripted zero, e.g. ρ^0. The placement of the derivate, via the comma

notation, is defined by context. An important identity, regarding the curl operator, is formulated as

$$\epsilon_{ijk}\frac{\partial \epsilon_{klm}a_l b_m}{\partial x_j} = a_i\frac{\partial b_j}{\partial x_j} + b_j\frac{\partial a_i}{\partial x_j} - b_i\frac{\partial a_j}{\partial x_j} - a_j\frac{\partial b_i}{\partial x_j}. \tag{1.10}$$

2

Selected Topics from Continuum Mechanics, Chemistry and Statistical Mechanics

The intent of this chapter is to give the necessary theoretical background on topics which are used in the derivation and the description of models. The range of topics spans from continuum mechanics to chemistry and statistical mechanics. Firstly, an introduction to continuum mechanics is given in Section 2.1, where kinematics, deformation, balance laws and material theory are considered. Further emphases are singular surfaces and transport. The separate but related Section 2.2 presents the basics of linear elastic fracture mechanics, focussing on Griffith's theory [65] and on the failure behaviour

of fibre-reinforced polymers (FRP). In Section 2.3, some chemical aspects of thermosets and chemical reactions are recapitulated. This is done by introducing the thermoset class used within this work and describing its composition and chemical curing reactions. Further, it is illustrated how such polymeric molecules can be described on a nano-scale by an atomistic force field, and how curing reactions can be characterised on a continuum scale by differential scanning calorimetry (DSC) measurements. The chapter closes with a brief discourse on equilibrium and non-equilibrium molecular dynamics, in Section 2.4, pointing out how material properties are determined on the basis of atomistic simulations. No background on numerical methods and frameworks used in this work is given in this chapter. For general information on the phase-field framework PACE3D introduced by Nestler *et al.* [129], the work of Hötzer *et al.* [82] is referred to. Especially for schemes used for solving mechanical quantities, Schneider *et al.* [158, 159] is mentioned, regarding the local numerical treatment of jump conditions, while the global scheme is addressed in Schoof *et al.* [161] and Herrmann *et al.* [78]. For thermal quantities, the schemes are used analogously. For a numerical background on the molecular dynamics package LAMMPS the work of Plimpton [142] is mentioned. Further details are listed in the documentation found on the LAMMPS web page [150].

2.1 Continuum mechanics and material behaviour

When zoomed in on scales below the macroscopic level, each body is found to consist of discrete material quanta, which may show as atoms, molecules, particles, grains, polymer chains or others [32, 169]. In continuum mechanics, it is postulated that this discrete character of the material is irrelevant if the length scale of interest is large, compared to characteristic lengths of the material quanta. If these intrinsic gaps become negligible at the considered length scale, the material distribution may be imagined as smooth; hence

the body is a *continuum* [42]. Likewise, physical quantities acting on such continua are represented by continuous fields [169]. Exceptions to this general continuous theory are given by the possible existence of a finite number of surfaces, lines or points, which may locally subdivide the body and/or introduce physical discontinuities.

2.1.1 Body, kinematics and deformation

In continuum mechanics, a body is composed of an infinite number of *material points* [115, 169]. This material body may move smoothly through an Euclidean space, occupying a certain spatial domain at each time [19]. On this basis, the kinematics of such bodies describes their movement in space and time. Throughout this work, material points are considered to have three translational degrees of freedom[1].

2.1.1.1 Body placement: Lagrange and Euler description

The position of a single material point P, within a body $\mathbb{B}$, at a reference time $t = t^0$, is described by the reference position vector $X_i(P)$, see Figure 2.1. This placement is called the *reference* or *Lagrangian configuration*. The body $\mathbb{B}$ has the volume V and has a surface ∂V, oriented by an outer unit normal vector N_i. If the body $\mathbb{B}$ is exposed to external physical influences, the material points start to move, and at current time $t > t^0$, the body $\mathbb{B}$ transforms to the current body $\mathbb{b}$ with volume v and the surface ∂v oriented by the unit normal n_i. The position of the material point P is now given by the current position vector $x_i(P, t)$. Analogously, this placement is called the *current* or *Eulerian configuration*. The movement of material points never results in two material points occupying the same position at the same time, and the coordinates of a material point within the set of material points never changes. Following the reasoning that material points do not superpose in space at any time, it is

---

[1] A so-called *Boltzmann continuum*, implying the symmetry of stress. If this axiom [21, 152] is dropped, rotational degrees of freedom and couple stresses are possible as postulated in [191]. A first mathematical model was introduced in [38] giving such bodies the name *Cosserat continua*.
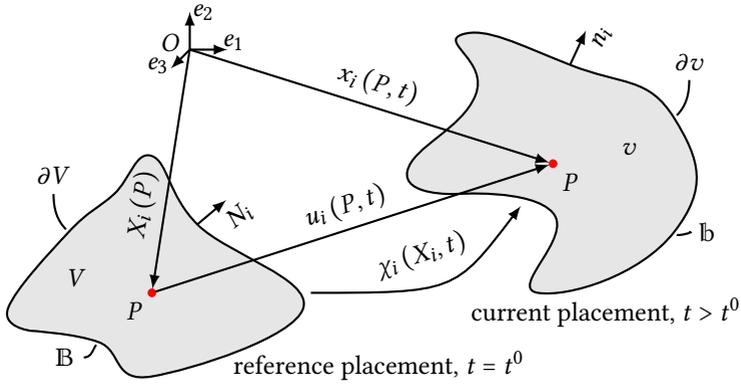
Figure 2.1: Material body: reference and current placement

possible to map the reference position vector X_j of each material point uniquely to its current position counterpart x_i, using the *motion*

$$x_i = \chi_i\left(X_j, t\right),\tag{2.1}$$

which implies that the inverse operation $X_i = \chi_i^{-1}\left(x_j, t\right)$ is valid as well. If the motion keeps the distances between material points constant, a rigid-body motion is in effect. Otherwise, if the distances change, the body experiences *deformation* [169]. The displacement from P at $t = t^0$ to P at $t > t^0$ is given by the *displacement vector*,

$$u_i = x_i - X_i = \chi_i\left(X_j, t\right) - X_i = u_i\left(X_j, t\right).\tag{2.2}$$

2.1.1.2 Deformation gradient

The line element $\mathrm{d}x_i$ in the Eulerian configuration directly connects two material points in an infinitesimal neighbourhood. This line element is uniquely determined by the Lagrangian line element $\mathrm{d}X_j$, using the chain rule

$$\mathrm{d}x_i = \frac{\mathrm{d}x_i}{\mathrm{d}X_j}\mathrm{d}X_j = \frac{\mathrm{d}\chi_i\,(X_k, t)}{\mathrm{d}X_j}\mathrm{d}X_j = F_{ij}\mathrm{d}X_j, \tag{2.3}$$

where the non-singular tensor F_{ij} is called *deformation gradient* [15, 169]. Despite the name, this tensor does not solely contain deformation, but also describes rigid rotations [19]. A deformation gradient is compatible if and only if the *compatibility condition*

$$\epsilon_{ijk}\frac{\partial F_{lk}}{\partial X_j} = 0 \tag{2.4}$$

holds in the simply connected body. The non-singularity ensures the existence of an inverse deformation gradient, given by

$$F_{ij}^{-1} = \frac{\mathrm{d}\chi_i^{-1}\,(x_k, t)}{\mathrm{d}x_j}\mathrm{d}x_j = \frac{\mathrm{d}X_i}{\mathrm{d}x_j}. \tag{2.5}$$

The transformation of the *line element* can be further specified towards

$$\mathrm{d}x_i = t_i\mathrm{d}x = F_{ij}T_j\mathrm{d}X = F_{ij}\mathrm{d}X_j, \tag{2.6}$$

where t_i and T_j are tangential unit vectors in their respective configuration, defining the orientation of the line element. An infinitesimal *volume element*, in Lagrangian configuration, is constructed by three independent line elements, forming a triple product. Formulating the change in volume from the Lagrangian to the Eulerian configuration gives

$$\frac{\mathrm{d}v}{\mathrm{d}V} = \frac{1}{6}\epsilon_{ijk}\epsilon_{lmn}F_{il}F_{jm}F_{kn} = J_F, \tag{2.7}$$

with J_F being the *Jacobian determinant*. Due to the invertibility of the motion, $J_F > 0$ follows for all material points. In this work, for the sake of brevity, $J_F = J$. Infinitesimal *surface elements* are composed of the cross product of two linearly independent line elements. In the current and reference configuration, they may be written as $da_i = \epsilon_{ijk} dx_j dy_k$ and $dA_i = \epsilon_{ijk} dX_j dY_k$, where the surface elements are oriented by their outward pointing unit normal vectors n_i and N_i. Using an arbitrary vector c_i to scalarly multiply the current surface element, and evaluating the triple product with respect to the reference configuration, the surface element is transformed by

$$
\begin{aligned}
da_i c_i &= \epsilon_{ijk} dx_j dy_k c_i \\
&= J F_{ji}^{-1} dA_j c_i \\
&\quad \Big\downarrow \text{ by arbitrariness of } c_i \\
n_i da &= J F_{ji}^{-1} N_j dA,
\end{aligned}
\tag{2.8}
$$

which is also called *Nanson's formula* [19]. It is possible to multiplicatively decompose the deformation gradient into its rotation and stretch parts,

$$
F_{ik} = R_{ij} U_{jk} = V_{ij} R_{jk},
\tag{2.9}
$$

where R_{ij} is the orthogonal *rotation tensor* and U_{ij}, V_{ij} are the *right* and *left stretch tensor*, respectively.

The *displacement gradient* H_{ij} is connected to the deformation gradient, by applying a similar reasoning as in (2.3),

$$
\frac{\partial u_i}{\partial X_j} = \frac{\partial x_i}{\partial X_j} - \frac{\partial X_i}{\partial X_j} = F_{ij} - \delta_{ij} = H_{ij}.
\tag{2.10}
$$

2.1.1.3 Strain measures

For the description of local material behaviour, it is desirable to introduce a measure for the change of shape [109, 169], which is free from a change in orientation, and hence resembles the actual local deformation within a body. This is possible using the previously introduced polar decomposition of the deformation gradient (2.9), which allows the introduction of the *right Cauchy-Green tensor*,

$$C_{ij} = U_{ik}U_{kj} = F_{ki}F_{kj},$$ (2.11)

which only depends on the right stretch tensor, and hence is free from rotation. As an example of a strain measure, the *Green-St. Venant strain tensor* E_{ij}^{G} is introduced [15, 19]. The change in angle between two line elements and the their change in length when going from the reference configuration to the current configuration is expressed by their scalar product, thus with inserting Equation (2.6)

$$\mathrm{d}x_i \mathrm{d}y_i = \left(F_{ij}\mathrm{d}X_j\right)\left(F_{ik}\mathrm{d}Y_k\right) = \mathrm{d}X_j F_{ij}F_{ik}\mathrm{d}Y_k = \mathrm{d}X_j C_{jk}\mathrm{d}Y_k,$$ (2.12)

and the change in shape is noted as

$$\mathrm{d}x_i \mathrm{d}y_i - \mathrm{d}X_k \mathrm{d}Y_k = \mathrm{d}X_i \left(C_{ik} - \delta_{ik}\right)\mathrm{d}Y_k = \mathrm{d}X_i \left(2E_{ik}^{\mathrm{G}}\right)\mathrm{d}Y_k.$$ (2.13)

This finally gives the Green-St.-Venant strain tensor,

$$E_{ij}^{\mathrm{G}} = \frac{1}{2}\left(C_{ij} - \delta_{ij}\right),$$ (2.14)

the finite strain tensor in the referential configuration. There exist further strain measures with respect to both configurations. An overview is given by [19], for example. Generally, all strain tensors may be used to obtain any stress-strain response (the construction of the material model is decisive), but

dependent on the application, one strain tensor may be more advantageous than another.

2.1.1.4 Singular surfaces

In Figure 2.1, the tacit assumption was made that the material body behaves homogeneously, due to identical material characteristics and properties at every point. If the body consists of sets of points which show different characteristics [168], e.g. different thermal conductivities, stiffness, orientation and so forth, points of identical characteristics may be collected in sub-bodies or *phases* if they form a coherent and homogeneous volume themselves, as depicted in Figure 2.2 for two phases α and β. These two material volumes
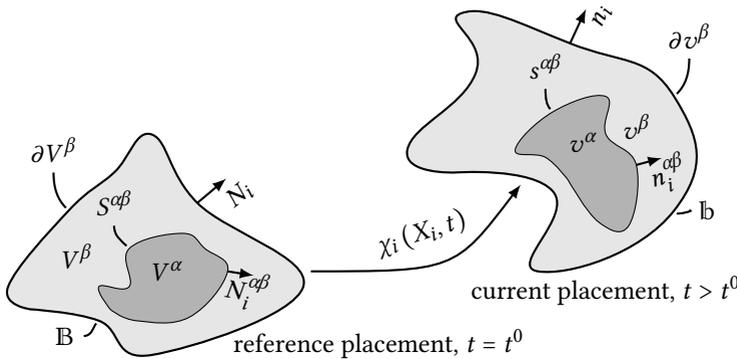
Figure 2.2: Material body subdivided in two regions, denoted by α and β, separated by a singular surface: reference and current placement.

are separated by an internal singular surface, or *interface*. Analogously to the above-mentioned phase-specific characteristics, each phase may have physical quantities of its own, e.g. there exist deformation gradients F_{ij}^{α} and F_{ij}^{β}. If the body $\mathbb{B}$ is exposed to external physical influences, each phase undergoes a motion, which is restricted by the type of connection given at the interface (the *compatibility condition*). Hence, the motion of the interface in the reference

configuration, $S^{\alpha\beta}$, follows those of the neighbouring phases, imposing a deformation and a rigid rotation on it. Dependent on the nature of the involved phases, such quantities, acting on the phase boundary, may induce a motion of the interface itself, converting one of the neighbouring phases into the energetically more favourable one (a *phase transition*). Therefore the interfaces themselves are generally dependent on time, $S^{\alpha\beta}(t)$ and $s^{\alpha\beta}(t)$. If physically meaningful, interfaces may have characteristics of their own. In the simplest case, this consists of a constant interface surface energy, which influences the motion and phase transitions [15].

To describe quantities at singular surfaces separating two regions α and β, the notation

$$\llbracket \psi \rrbracket^{\alpha\beta} = \psi^{\alpha}\Big|_{s_{+}^{\alpha\beta}} - \psi^{\beta}\Big|_{s_{-}^{\alpha\beta}} \quad \text{Eulerian configuration,} \tag{2.15}$$

$$\llbracket \psi \rrbracket^{\alpha\beta} = \psi^{\alpha}\Big|_{S_{+}^{\alpha\beta}} - \psi^{\beta}\Big|_{S_{-}^{\alpha\beta}} \quad \text{Lagrangian configuration,} \tag{2.16}$$

is used for a jump of an arbitrary quantity ψ [109]. For jumps, the identity

$$\llbracket fg \rrbracket^{\alpha\beta} = \llbracket f \rrbracket^{\alpha\beta} \langle g \rangle^{\alpha\beta} + \langle f \rangle^{\alpha\beta} \llbracket g \rrbracket^{\alpha\beta} \tag{2.17}$$

applies for scalars or scalar products, whereas $\langle f \rangle^{\alpha\beta} = (f^{\alpha}+f^{\beta})/2$ is the mean value of the quantity f [84].

For simplicity, the existence of lines and points, where singular surfaces meet outer surfaces or different singular surfaces meet each other, are not discussed. Such *triple lines* or multi lines and points require a separate treatment, which is not the focus of this work.

2.1.1.5 Time derivatives

Following [19], the time derivative of the motion χ_i, of body B, is the velocity in the reference configuration,

$$V_i\left(X_j, t\right) = \frac{\partial \chi_i\left(X_j, t\right)}{\partial t}, \tag{2.18}$$

and analogously, the acceleration is

$$A_i\left(X_j, t\right) = \frac{\partial^2 \chi_i\left(X_j, t\right)}{\partial t^2}. \tag{2.19}$$

The velocity in the current configuration is retrieved by a change of variables,

$$v_i\left(x_j, t\right) = V_i\left(\chi_j\left(X_k, t\right), t\right) = V_i\left(X_k, t\right). \tag{2.20}$$

This kind of transformation may be applied to any other arbitrary quantity $\psi\left(\chi_i\left(X_j, t\right), t\right) = \Psi\left(X_j, t\right)$, which may be a tensor of any order. The total time derivative is given by

$$\begin{aligned}
\dot{\Psi} &= \frac{\partial \Psi}{\partial t} \\
&= \frac{\partial \psi}{\partial t} + \frac{\partial \psi}{\partial x_i} v_i = \dot{\psi},
\end{aligned} \tag{2.21}$$

where a *convective* term $\psi_{,i} v_i$ arises in the Eulerian description. Applied to the velocity in the current configuration, the acceleration [169] is found to be

$$a_i\left(x_j, t\right) = \dot{v}_i\left(x_j, t\right) = \frac{\partial v_i}{\partial t} + \frac{\partial v_i}{\partial x_j} v_j. \tag{2.22}$$

Another often needed quantity is the *velocity gradient*, which is introduced via the time derivation of the deformation gradient (see Section 2.1.1.2),

$$\dot{F}_{ij} = \frac{\partial V_i}{\partial X_j} = \frac{\partial v_i}{\partial x_k} \frac{\partial x_k}{\partial X_j} = \frac{\partial v_i}{\partial x_k} F_{kj}, \tag{2.23}$$

and the spatial velocity gradient is noted as $l_{ij} = \partial v_i / \partial x_j = \dot{F}_{ik} F_{kj}^{-1}$ [15].

2.1.1.6 Transport and Stokes' theorems

The rather mathematically motivated, generalised Stokes' theorem (cf. [58]) links a differential quantity, integrated over M, to the same quantity, integrated over the boundary ∂M. Two particular and often used cases in vector calculus are Gauss' theorem and the Kelvin-Stokes theorem, which are introduced in the Eulerian configuration.

For a volume with two subdomains α and β, divided by a singular surface, *Gauss' theorem* [19, 168] states

$$\int_{v(t)} \frac{\partial \psi_j}{\partial x_j} \mathrm{d}v = \int_{\partial v(t)} \psi_j n_j \mathrm{d}a - \int_{s^{\alpha\beta}(t)} [\![\psi_j]\!]^{\alpha\beta} n_j^s \mathrm{d}a, \tag{2.24}$$

which relates the volume integral of the divergence of an arbitrary vector field $\psi_j(x_i, t)$ with its flux over the outer volume surface, characterised by the normal vector n_j, and with its jump at the singular surface. Furthermore, n_j^s is the unit normal vector of the singular surface $s^{\alpha\beta}(t)$ in between the two subdomains. The *Kelvin-Stokes theorem* [32] connects the surface integral of the curl of an arbitrary vector field $\epsilon_{ijk} \partial \psi_k / \partial x_j$ to its tangential component along the surface boundary, defined by the tangential vector t_k:

$$\int_{s(t)} \epsilon_{ijk} \frac{\partial \psi_k}{\partial x_j} n_i \mathrm{d}a = \oint_{\partial s(t)} \psi_k t_k \mathrm{d}x. \tag{2.25}$$

Further theorems relevant for this work involve the change of a volume or surface over time, which are again introduced in an Eulerian description. The transport equation for a scalar quantity $\psi(x_i, t)$ in a volume [19, 168], which, as before, comprises a singular surface, reads as

$$\frac{\mathrm{d}}{\mathrm{d}t} \int_{v(t)} \psi \mathrm{d}v = \int_{v(t)} \frac{\partial \psi}{\partial t} \mathrm{d}v + \int_{\partial v(t)} \psi v_j n_j \mathrm{d}a$$
$$- \int_{s^{\alpha\beta}(t)} [\![\psi]\!]^{\alpha\beta} v_j^s n_j^s \mathrm{d}a, \tag{2.26}$$

where v_j^s is the velocity of the singular surface. This equation is also known as *Reynolds transport theorem*. With Gauss' theorem (2.24), the surface term may be transformed to a volume integral. A moving surface or interface [15, 85, 122, 126], relating to a vector field, is characterised by

$$
\frac{d}{dt} \int_{s(t)} \psi_j n_j \mathrm{d}a = \int_{s(t)} \left\{ \frac{\partial \psi_j}{\partial t} + v_j^s \frac{\partial \psi_k}{\partial x_k} \right\} n_j \mathrm{d}a \\
+ \int_{\partial s(t)} \epsilon_{ijk} \psi_j v_k^s t_i \mathrm{d}x.
$$

(2.27)

Analogously to the volume transport equation, the line integral is re-written to a surface integral, by using the Kelvin-Stokes theorem (2.25).

With the Kelvin-Stokes theorem (2.25), but used in the Lagrangian notation, it is possible to evaluate the compatibility condition of the deformation gradient, Equation (2.4), in the presence of a singular surface [67]. For a contour, integrating the deformation gradient, this generally gives

$$
B_k = \oint_C F_{kl} \mathrm{d}X_l = \int_{A^C} \epsilon_{ijk} \frac{\partial F_{lk}}{\partial X_j} \mathrm{d}A_i,
$$

(2.28)

where B_i is identified as the Burger's vector, which has to be zero for all admissible deformations, which again gives the bulk compatibility condition for the deformation gradient:

$$
\epsilon_{ijk} \frac{\partial F_{lk}}{\partial X_j} = \epsilon_{ijk} \frac{\partial^2 x_l}{\partial X_k \partial X_j} = 0.
$$

(2.29)

With these preliminaries, the surface A^C, enclosed by the contour C, is placed in such a way that it intersects with a singular surface, separating two phases α, β, see Figure 2.3. The intersection is named as curve $\Gamma^{\alpha\beta}$, and the deformation gradient is assumed smooth everywhere but on $\Gamma^{\alpha\beta}$. Splitting the surface area A^C in its α and β parts, the integration path of the encircling curve may also be split. Thereby, the inner integration path form the left and right limit to
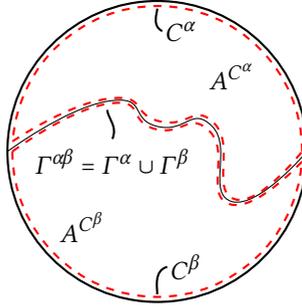
Figure 2.3: Kelvin-Stokes theorem at an singular surface: A different surface consisting of the parts α, β and contoured by C^α, C^β is imagined, which crosses the singular surface such that $\Gamma^{\alpha\beta}$ is the intersection of both.

the actual interface. With this subdivision, the Kelvin-Stokes theorem for both sub-bodies reads as follows:

$$
\begin{aligned}
\alpha - \text{body:} \quad & \int_{A^{C^\alpha}} \epsilon_{ijk} \frac{\partial F_{lk}}{\partial X_j} \mathrm{d}A_i = \int_{C^\alpha = \partial A^{C^\alpha} \smallsetminus \Gamma^{\alpha\beta}} F_{kl} \mathrm{d}X_l + \int_{\Gamma^{\alpha\beta}} F_{kl}^\alpha \mathrm{d}X_l, \\
\beta - \text{body:} \quad & \int_{A^{C^\beta}} \epsilon_{ijk} \frac{\partial F_{lk}}{\partial X_j} \mathrm{d}A_i = \int_{C^\beta = \partial A^{C^\beta} \smallsetminus \Gamma^{\alpha\beta}} F_{kl} \mathrm{d}X_l - \int_{\Gamma^{\alpha\beta}} F_{kl}^\beta \mathrm{d}X_l,
\end{aligned}
\tag{2.30}
$$

where $C^\alpha = \partial A^{C^\alpha} \smallsetminus \Gamma^{\alpha\beta}$ describes the line integration along the boundary of A^{C^α}, leaving out the segment $\Gamma^{\alpha\beta}$. Analogously, the same applies to C^β. Adding up both sub-bodies and the application of all pre-assumptions yields

$$
\underbrace{B_k}_{\overset{!}{=}0} = \oint_C F_{kl}\mathrm{d}X_l = \int_{A^C} \underbrace{\epsilon_{ijk} \frac{\partial F_{lk}}{\partial X_j} \mathrm{d}A_i}_{\overset{!}{=}0} - \int_{\Gamma^{\alpha\beta}} [\![F_{kl}]\!]^{\alpha\beta} \mathrm{d}X_l
$$

$$
0 = \int_{\Gamma^{\alpha\beta}} [\![F_{kl}]\!]^{\alpha\beta} \mathrm{d}X_l,
\tag{2.31}
$$

for an arbitrary area A^C. With line elements being oriented in the tangential direction, a deformation gradient compatibility condition is retrieved for singular surfaces:

$$
\begin{aligned}
0 &= \int_{\Gamma^{\alpha\beta}} [\![F_{kl}]\!]^{\alpha\beta} T_l \mathrm{d}X \\
0 &= [\![F_{kl}]\!]^{\alpha\beta} T_l,
\end{aligned}
\tag{2.32}
$$

which states that the jump of the tangential components of F_{kl} has to be zero to satisfy the equation. Re-writing this equation with N_i as the unit normal vector of the singular surface results in another form of the same statement:

$$
\begin{aligned}
0 &= [\![F_{kl}]\!]^{\alpha\beta} T_l T_m \\
0 &= [\![F_{kl}]\!]^{\alpha\beta} (\delta_{lm} - N_l N_m) \\
0 &= [\![F_{km}]\!]^{\alpha\beta} - [\![F_{kl}]\!]^{\alpha\beta} N_l N_m \\
[\![F_{km}]\!]^{\alpha\beta} &= \underbrace{[\![F_{kl}]\!]^{\alpha\beta} N_l}_{=K_k} N_m,
\end{aligned}
\tag{2.33}
$$

predicting K_k as the jump of the normal components of F_{km}. This condition is called *Hadamard's compatibility condition* and has the underlying assumption that the motion χ_i is continuous across singular surfaces. Hence, no slip is allowed along the singular surface (a constant misalignment, at the utmost). By softening the basic assumptions, more general compatibility conditions may be derived.

2.1.2 Balance laws

The following sections introduce the fundamental principles of continuum mechanics and thermodynamics, which govern the behaviour of the body under external influences, mainly following standard literature [15, 19, 32, 109, 166, 169, 183], among others. Generally, they are given in their integral form, including a singular surface, and in an Eulerian description, but also their local forms are briefly noted. Furthermore, selected consequences and restrictions of the balances are discussed.

2.1.2.1 Mass balance

In continuum mechanics, every body has a (total) *mass* $\mathcal{M}$, and if a body consists of sub-bodies the sum of their masses is the total mass. It is now assumed that the total mass remains constant under all deformations [19] and is independent of time. With the above requirements, it follows that every material point has a *mass density* ρ, and the *conservation of mass* yields

$$\mathcal{M}(\mathbb{B}) = \mathcal{M}(\mathbb{b})$$
$$\int_V \rho^0 \mathrm{d}V = \int_v \rho \mathrm{d}v \tag{2.34}$$
$$0 = \int_V \left\{ \rho^0 - J\rho \right\} \mathrm{d}V,$$

where the relation $\rho^0 = J\rho$ is the *continuity condition* for mass at each material point [169]. Evaluating the time derivative of the total mass with the Reynolds transport (2.26) and Gauss' theorem (2.24) gives the mass balance

$$\dot{\mathcal{M}}(\mathbb{b}) = 0 = \frac{\mathrm{d}}{\mathrm{d}t} \int_v \rho \mathrm{d}v$$
$$0 = \int_v \frac{\partial \rho}{\partial t} + (\rho v_i)_{,i} \, \mathrm{d}v - \int_{s^{\alpha\beta}(t)} \llbracket \rho (v_i - v_i^s) \rrbracket^{\alpha\beta} n_i^{\alpha\beta} \mathrm{d}a. \tag{2.35}$$

From this follows a different local form of the continuity condition in bulk regions and a local form at singular surfaces,

$$0 = \frac{\partial \rho}{\partial t} + (\rho v_i)_{,i} \quad \text{and} \quad \llbracket \rho (v_i - v_i^s) \rrbracket^{\alpha\beta} n_i^{\alpha\beta} = 0. \tag{2.36}$$

If the mass density is constant in time, this yields the incompressibility condition $v_{i,i} = 0$.

2.1.2.2 Momentum balances and stresses

The (linear) *momentum vector* $\mathcal{I}_i$ of a body $\mathbb{b}$ is defined by

$$\mathcal{I}_i(\mathbb{b}) = \int_v \rho v_i \mathrm{d}v, \qquad (2.37)$$

and its *force vector* f_i is composed of a mass-specific body force density b_i and a force density t_i, acting normal on the body's surface [15]. With the time derivative of linear momentum being the force and by using the Reynolds transport (2.26) and Gauss' theorem (2.24), the *balance of linear momentum* is

$$
\begin{aligned}
\dot{\mathcal{I}}_i(\mathbb{b}) = \frac{\mathrm{d}}{\mathrm{d}t} \int_v \rho v_i \mathrm{d}v &= \int_v \rho b_i \mathrm{d}v + \int_{\partial v} t_i \mathrm{d}a \\
0 &= \int_v \rho \dot{v}_i - \rho b_i - \sigma_{ij,j} \mathrm{d}v \\
&\quad + \int_{s^{\alpha\beta}(t)} \left\{ [\![\rho v_i \left(v_j - v_j^s \right)]\!]^{\alpha\beta} \right. \\
&\qquad\qquad \left. - [\![\sigma_{ij}]\!]^{\alpha\beta} \right\} n_j^{\alpha\beta} \mathrm{d}a,
\end{aligned}
\qquad (2.38)
$$

where the *traction-stress relation* $t_i = \sigma_{ij} n_j$ is used to describe the internal forces at each material point, with the *Cauchy stress tensor* σ_{ij} [169]. Additionally, the balance of mass (2.35) is used during the calculation. In cases when the body is in equilibrium, the local forms are given by

$$0 = \rho b_i + \sigma_{ij,j} \quad \text{and} \quad [\![\sigma_{ij}]\!]^{\alpha\beta} n_j^{\alpha\beta} = 0, \qquad (2.39)$$

where the second condition implies continuous traction across interfaces. Before continuing with the *balance of angular momentum*, the stress tensor is discussed in more detail. The Cauchy stress tensor is completely defined in the current configuration. It is the current force per current area, $\mathrm{d}f_i = \sigma_{ij} \mathrm{d}a_j$.

If the current force is evaluated with respect to the reference configuration, the area element has to be pulled back,

$$\mathrm{d}f_i = \underbrace{J\sigma_{ik}F_{jk}^{-1}}_{=P_{ij}}\,\mathrm{d}A_j,$$

(2.40)

which introduces P_{ij}, the *1st Piola-Kirchhoff stress tensor* [32]. It may be convenient to pull back the force vector f_i as well to have both quantities in the reference configuration, which gives the *2nd Piola-Kirchhoff stress tensor S_{ij}*,

$$\mathrm{d}f_i^0 = \underbrace{F_{ik}^{-1}P_{kj}}_{=S_{ij}}\,\mathrm{d}A_j.$$

(2.41)

At this point, a connection to the deformation gradient 2.1.1.2 and the strain tensors 2.1.1.3 is made. The mass-specific stress power is defined as $\mathcal{P} = \frac{1}{\rho}\sigma_{ij}l_{ij}$. A specific stress tensor is called work conjugate to some strain tensor, if they fulfil the specific stress power formula in the reference position [19]. For the introduced stress tensors, these are

$$\mathcal{P} = \frac{1}{\rho^0}P_{ij}\dot{F}_{ij} \quad \text{and} \quad \mathcal{P} = \frac{1}{\rho^0}S_{ij}\dot{E}_{ij}^{\mathrm{G}}.$$

(2.42)

A work conjugate may be used to construct a constitutive relation between stress and strain (see Section 2.1.3).

As mentioned in the beginning of this subchapter, the theory used here is that of non-polar continua. Hence, the balance of angular momentum is not explicitly introduced, but its statement, the symmetry of the Cauchy stress tensor, is briefly given:

$$\sigma_{ij} = \sigma_{ji}, \quad S_{ij} = S_{ji} \quad \text{and} \quad P_{ik}F_{jk} = F_{ik}P_{jk}.$$

(2.43)

2.1.2.3 First law of thermodynamics: Energy balance

To formulate the *first law of thermodynamics*, the *total energy* of body $\mathbb{b}$, $\mathcal{E} = K + E$, is introduced [32, 109], with K and E being the kinetic and internal energy, defined as

$$K\,(\mathbb{b}) = \frac{1}{2} \int_v \rho v_i v_i \mathrm{d}v \quad \text{and} \quad E\,(\mathbb{b}) = \int_v \rho e \mathrm{d}v, \tag{2.44}$$

where e is the mass-specific *internal energy*. The change in these is balanced by the *heat* supplied Q and the *work W* done to the body $\mathbb{b}$, which are given as

$$
\begin{aligned}
Q\,(\mathbb{b}) &= \int_v \rho r \mathrm{d}v - \int_{\partial v} q_i n_i \mathrm{d}a, \\
W\,(\mathbb{b}) &= \int_v \rho v_i b_i \mathrm{d}v + \int_{\partial v} v_i t_i \mathrm{d}a,
\end{aligned}
\tag{2.45}
$$

identifying r as a mass-specific *heat source* and q_i as the *heat flux vector*. The mass-specific body force vector b_i and the traction vector t_i were introduced in the previous section. With the Reynolds transport (2.26) and Gauss' theorem (2.24), the balances of mass (2.35) and linear momentum (2.38), and the above definitions, the energy balance is

$$
\begin{aligned}
\dot{\mathcal{E}}\,(\mathbb{b}) &= Q\,(\mathbb{b}) + W\,(\mathbb{b}) \\
\frac{\mathrm{d}}{\mathrm{d}t} \int_v \frac{1}{2} \rho v_i v_i + \rho e \mathrm{d}v &= \int_v \rho \left\{ r + b_i v_i \right\} \mathrm{d}v + \int_{\partial v} \left\{ v_i \sigma_{ij} - q_j \right\} n_j \mathrm{d}a \\
0 &= \int_v \rho \left\{ \dot{e} - r \right\} + q_{i,i} - \sigma_{ij} v_{i,j} \mathrm{d}v \\
&\quad + \int_{s^{\alpha\beta}(t)} \left\{ \left[\!\left[\left(\frac{1}{2} \rho v_i v_i + \rho e \right) \left(v_j - v_j^s \right) \right]\!\right]^{\alpha\beta} \right. \\
&\quad \left. + \left[\!\left[q_j - v_i \sigma_{ij} \right]\!\right]^{\alpha\beta} \right\} n_j^{\alpha\beta} \mathrm{d}a,
\end{aligned}
\tag{2.46}
$$

where $\sigma_{ij} v_{i,j}$ is identified as the *stress power*. For bulk regions, the local version of the energy balance is

$$\rho \dot{e} = \rho r - q_{i,i} + \sigma_{ij} v_{i,j}, \tag{2.47}$$

and for singular surfaces the expression

$$0 = \left\{ \llbracket \left(\frac{1}{2}\rho v_i v_i + \rho e \right) \left(v_j - v_j^s \right) \rrbracket^{\alpha\beta} + \llbracket q_i - v_i \sigma_{ij} \rrbracket^{\alpha\beta} \right\} n_j^{\alpha\beta} \qquad (2.48)$$

holds. If the body is in equilibrium, it can be concluded that the heat flux across the singular surface has to be continuous in the normal direction.

2.1.2.4 Second law of thermodynamics: Entropy balance

The *second law of thermodynamics* states that the *entropy production* of a body $\mathbb{b}$, Π^η, consists of the change of its *entropy* H^η, subtracted by its *entropy supply* $\mathcal{S}^\eta$ [109],

$$\Pi^\eta \left(\mathbb{b} \right) = \dot{H}^\eta \left(\mathbb{b} \right) - \mathcal{S}^\eta \left(\mathbb{b} \right) \geq 0, \qquad (2.49)$$

and has to be non-negative; hence it is not a conservative quantity. The entropy H^η is defined as

$$H^\eta \left(\mathbb{b} \right) = \int_v \rho \eta \mathrm{d}v, \qquad (2.50)$$

with η denoting the mass-specific entropy, and the entropy supply $\mathcal{S}^\eta$ as

$$\mathcal{S}^\eta \left(\mathbb{b} \right) = \int_v \rho s \mathrm{d}v - \int_{\partial v} \varsigma_i n_i \mathrm{d}a, \qquad (2.51)$$

where s is the source of local entropy and ς_i is the entropy flux. These rather general quantities are often assumed to be related to the heat supply and heat flux by the *absolute temperature* Θ [32, 109],

$$s = \frac{r}{\Theta} \quad \text{and} \quad \varsigma_i = \frac{q_i}{\Theta}. \qquad (2.52)$$

This form of the entropy inequality,

$$
\begin{aligned}
\Pi^\eta\left(\mathbb{b}\right) &= \frac{\mathrm{d}}{\mathrm{d}t}\int_v \rho\eta\mathrm{d}v + \int_{\partial v}\frac{q_i}{\Theta}n_i\mathrm{d}a - \int_v \rho\frac{r}{\Theta}\mathrm{d}v \ge 0 \\
&= \int_v \rho\dot\eta + \left(\frac{q_i}{\Theta}\right)_{,i} - \rho\frac{r}{\Theta}\mathrm{d}v \\
&\quad + \int_{s^{\alpha\beta}(t)}\left\{\llbracket \rho\eta\left(v_i - v_i^s\right)\rrbracket^{\alpha\beta} + \llbracket \frac{q_i}{\Theta}\rrbracket^{\alpha\beta}\right\}n_i^{\alpha\beta}\mathrm{d}a \ge 0,
\end{aligned}
\tag{2.53}
$$

is called the *Clausius-Duhem inequality*. Localised, the inequalities are

$$
\rho\dot\eta + \left(\frac{q_i}{\Theta}\right)_{,i} - \rho\frac{r}{\Theta} \ge 0 \quad \text{and} \quad \left\{\llbracket \rho\eta\left(v_i - v_i^s\right)\rrbracket^{\alpha\beta} + \llbracket \frac{q_i}{\Theta}\rrbracket^{\alpha\beta}\right\}n_i^{\alpha\beta} \ge 0 \tag{2.54}
$$

analogously. Using the localised form of the first law of thermodynamics (2.47), the heat supply may be replaced, and the internal energy enters the inequality. Following Coleman and Noll [36], the entropy inequality imposes restrictions on constitutive relations, which are necessary conditions for stable equilibrium states [15]. Hence, constitutive relations have to be of a form which satisfies the second law of thermodynamics for any thermodynamic process.

2.1.3 Material theory

Before discussing the material behaviour of the two relevant materials used in this work, elastic glass fibres and a visco-elastic thermoset, the connection of stress and strain is made. Generally, the relation for rate-independent materials reads as

$$
\sigma_{ij} = f_{ij}\left(x_k, F_{lm}\right). \tag{2.55}
$$

Hence, the Cauchy stress tensor depends on the deformation gradient, and the mapping f_{ij} itself depends on the position x_k [169]. This dependence accounts for material inhomogeneity of the body, either due to the material itself or due to other influences, e.g. temperature. For simplicity of the notation, this dependence is not noted in the upcoming sections, but is always valid. The processes to be simulated in this work are assumed to only induce small

deformations. Therefore the following theory only focusses on linear models, and the geometric linearisation is briefly discussed.

2.1.3.1 Kinematic linearisation

If a body is expected to only exhibit small deformations within the process of interest, the equations of continuum mechanics simplify considerably [75]. For the application of this theory, three requirements, based on the displacement gradient (2.10), have to be met throughout the motion:

$$\|H_{ij}\| \ll 1, \quad |u_i| \ll L^0 \quad \text{and} \quad \dot{H}_{ij} \ll 1. \tag{2.56}$$

Thus, with the displacement gradient being small, displacements themselves being small compared to the characteristic length L^0 of the body, and small deformation rates $\dot{H}_{ij}$, a *geometric linearisation* is possible. The Green-St.-Venant strain tensor (2.14) is re-written as

$$
\begin{aligned}
E_{ij}^{\mathrm{G}} &= \frac{1}{2}\left\{F_{ki}F_{kj} - \delta_{ij}\right\} \\
&= \frac{1}{2}\left\{\left(\delta_{ki} + H_{ki}\right)\left(\delta_{kj} + H_{kj}\right) - \delta_{ij}\right\} \\
&= \frac{1}{2}\left\{\delta_{ij} + H_{ij} + H_{ji} + \underbrace{H_{ki}H_{kj}}_{\approx 0} - \delta_{ij}\right\} \\
&= \frac{1}{2}\left\{H_{ij} + H_{ji}\right\} = \varepsilon_{ij},
\end{aligned}
\tag{2.57}
$$

where ε_{ij} is called the *infinitesimal strain tensor*, to which every other strain tensor reduces as well. Similarly, all stress tensors may be approximated by the Cauchy stress tensor σ_{ij}. Furthermore, derivatives with respect to the current and to the reference configuration are approximately the same $\partial/\partial x_i \approx \partial/\partial X_i$, and hence it becomes obsolete to distinguish between them.

2.1.3.2 Linear elasticity

Elasticity describes rate-independent material behaviour without any hysteresis [75]. This means that a body reverts to its initial configuration once it is unloaded, and during unloading, it is expected to release the same amount of strain energy as it absorbed during loading. The latter requirement has to be ensured by *hyperelasticity*, which demands that the time derivative of the strain energy is equal to the stress power (2.42).

On the basis of these formalities, linear elasticity, or *Hooke's law*, for infinitesimal deformations is introduced as

$$\sigma_{ij} = C_{ijkl}\varepsilon_{kl}, \tag{2.58}$$

with C_{ijkl} as the *stiffness tensor*, characterising a specific material. Rheologically, this behaviour may be characterised by a spring, as depicted in Figure 2.4. Due to the symmetry of the stress and strain tensors and the hyperelasticity,
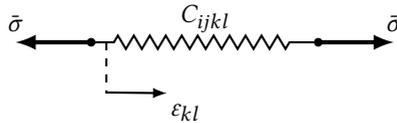
Figure 2.4: Rheological model: Under an external loading the spring is strained inducing an internal stress response. If unloaded, the spring returns to its initial state.

the fourth-order stiffness tensor has at most twenty-one independent components [19, 169]. Most materials show further symmetries which reduce the number of independent components significantly, and for an infinite number of symmetries, isotropy, only two are required. Isotropic behaviour may be characterised by a variety of material parameters, which are all related, and hence may be converted into each other [116]. Popular combinations are *elastic modulus* and *Poisson's ratio* E, ν and the *Lamé parameters* λ, μ. In the following, the combination *bulk modulus* and *shear modulus* K, G is used, as they are related to types of completely separated deformation.

2.1.3.3 Linear visco-elasticity

The theory of *visco-elasticity*, as pure elasticity, shows no equilibrium hysteresis, but is rate-dependent [75]. Hence, the rate-independent Equation (2.55) is extended and written for infinitesimal deformations as

$$\sigma_{ij} = f_{ij}\left(\varepsilon_{kl}\right) + h_{ij}\left(\varepsilon_{kl}, \dot{\varepsilon}_{mn}\right), \tag{2.59}$$

and if $\dot{\varepsilon}_{mn} = 0$, the equilibrium elastic behaviour is yielded. Under a constant stress load, a visco-elastic material creeps towards its equilibrium by slowly increasing strain. If the material is under a constant strain load, the material relaxes its stress state towards its equilibrium. The *Generalised Maxwell Model* (see Figure 2.5) implements the behaviour outlined in Equation (2.59) by splitting the function h_{ij} into N differently behaving functions, each realising different creep and relaxation processes within a material, often connected to different time scales. The implementation of an indefinite number of such *Maxwell elements* allows for a model adjustment to a general visco-elastic material, hence the name. Rheologically the Generalised Maxwell Model con-
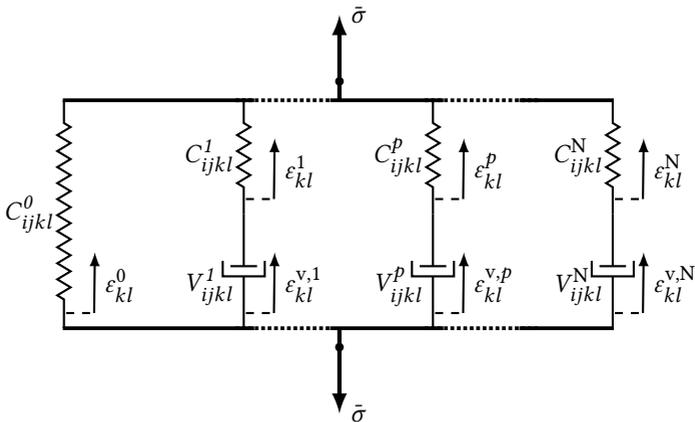
Figure 2.5: Rheological model of the Generalised Maxwell Model: A zeroth spring in parallel with N Maxwell elements.

sists of springs, characterised by a stiffness C_{ijkl}, representing the elastic, time-independent behaviour and dampers, characterised by a viscosity V_{ijkl}, representing a viscous, time-dependent behaviour. The connection in parallel allows the total strain and stress to be written as

$$\varepsilon_{ij}^{\text{GM}} = \varepsilon_{ij}^{0} = \varepsilon_{ij}^{\text{M},p} \quad \text{and} \quad \sigma_{ij}^{\text{GM}} = \sigma_{ij}^{0} + \sum_{p=1}^{N} \sigma_{ij}^{\text{M},p}, \tag{2.60}$$

where the quantities superscripted by GM and M represent resulting quantities of the Generalised Maxwell Model and a single Maxwell element, respectively. Inside a Maxwell element, spring and damper are connected in series, leading to

$$\varepsilon_{ij}^{\text{M},p} = \varepsilon_{ij}^{p} + \varepsilon_{ij}^{\text{v},p} \quad \text{and} \quad \sigma_{ij}^{\text{M},p} = \sigma_{ij}^{p} = \sigma_{ij}^{\text{v},p}. \tag{2.61}$$

By applying the behaviour of springs and dampers,

$$\sigma_{ij}^{p} = C_{ijkl}^{p} \varepsilon_{kl}^{p} \quad \text{and} \quad \sigma_{ij}^{\text{v},p} = V_{ijkl}^{p} \dot{\varepsilon}_{kl}^{\text{v},p}, \tag{2.62}$$

the total behaviour may be retrieved,

$$\sigma_{ij}^{\text{GM}} = C_{ijkl}^{0} \varepsilon_{kl}^{\text{GM}} + \sum_{p=1}^{N} C_{ijkl}^{p} \left\{ \varepsilon_{kl}^{\text{GM}} - \varepsilon_{kl}^{\text{v},p} \right\}. \tag{2.63}$$

The rheological representation also yields the evolution equation for each Maxwell element,

$$\dot{\varepsilon}_{ij}^{\text{v},p} = V_{ijkl}^{p}{}^{-1} C_{ijkl}^{p} \left\{ \varepsilon_{kl}^{\text{GM}} - \varepsilon_{kl}^{\text{v},p} \right\}. \tag{2.64}$$

A common assumption is that viscous effects only occur under shear deformation, hence only the deviatoric part of the viscous strain is applied, $\varepsilon_{ij}^{\text{v},p,\text{dev}} = \varepsilon_{ij}^{\text{v},p} - \varepsilon_{kk}^{\text{v},p}/3\delta_{ij}$.

2.2 Linear elastic fracture mechanics

Within this section, the concept of *linear elastic fracture mechanics* (LEFM) is briefly summed up to give a basic background for crack propagation modelling in Section 3.3. This section mainly follows Gross and Seelig [66], which is also referred to for a more detailed discussion of this topic. Close to the crack tip
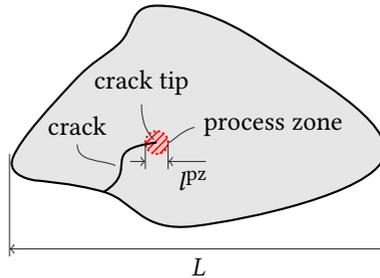
Figure 2.6: Body with crack: Crack tip singularity surrounded by a process zone.

singularity in Figure 2.6, stresses tend to approach infinity, which is limited due to non-linearities arising in the process zone around the crack tip. In a brittle material, this region is much smaller than the size of the body, $l^{pz} \lll L$, which allows for the description of the body by linear elasticity and LEFM. As crack initiation happens below the continuum mechanics scale, fracture mechanics assumes each body to be imperfect in the sense of not being defect-free. Under load, these defects then may cause stress localisations resulting in growth to cracks relevant for the investigated length scale. In the following, the focus is the theory by Griffith [65], which gives an energetic view of crack propagation.

2.2.1 Basic concepts

At places where bulk areas are separated, a crack introduces *crack surfaces* into a body. The crack surfaces are generally traction-free and meet at the *crack tip* or *crack front* [66], see Figure 2.7. Opposing crack surfaces may only
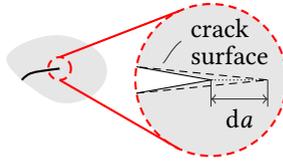
Figure 2.7: Enlarged crack tip: Creation of new crack surfaces by crack propagation da

transfer forces under compression or when under a frictional connection. If a body with an initial crack of length a is loaded sufficiently, a crack propagates by the distance da, resulting in the creation of new crack surface by further separating the body. Otherwise, if the loading is not sufficient, the crack is at rest. Any crack propagation is a superposition of the three basic crack extension modes [59], shown in Figure 2.8. The most common form of crack

(a) Crack mode I   (b) Crack mode II   (c) Crack mode III
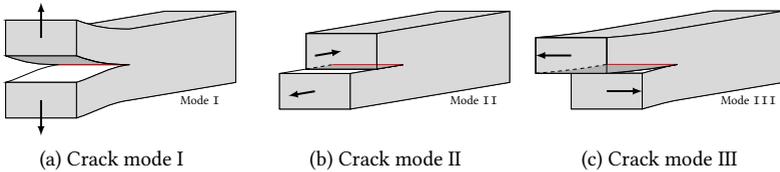
Figure 2.8: Crack opening modes

propagation happens under mode I, the *opening mode*, where the two opposite crack surfaces are pulled apart symmetrically, hence they move in the crack surface normal direction and normal to the crack front. In mode II, the *sliding mode*, the crack surfaces move along planes parallel to the crack surfaces, but in opposite directions normal to the crack front. As a last possibility, the crack surfaces may also move in their tangent planes, but strictly in the tangential direction of the crack front, which introduces the crack mode III, the *tearing mode*. Within one material, each mode may impose a different resistance against crack propagation.

2.2.2 Griffith theory

An energetic way of examining a fracture process is Griffith's criterion [65],

$$G - G^{\mathrm{c}} = 0. \tag{2.65}$$

It states that during quasi-static crack propagation, the *released energy G* must be equal to the critical energy G^{c}, which is needed to separate a volume [66]. Specifying these quantities gives

$$G = -\frac{\mathrm{d}\Pi}{\mathrm{d}a} \quad \text{and} \quad G^{\mathrm{c}} = \frac{\mathrm{d}\Gamma}{\mathrm{d}a} = 2\gamma, \tag{2.66}$$

hence the energy release is the change in potential energy Π due to an advance of the crack front by the area $\mathrm{d}a$. The critical energy is identified as the energy γ opposing the creation of two new material surfaces, hence breaking atomic bonds. In the following, this quantity is called *energetic crack resistance*. The consequences for an assumed quadratic potential function Π are demonstrated in Figure 2.9. As long as the crack has a size $a < a^{\mathrm{c}}$ a propagation is only
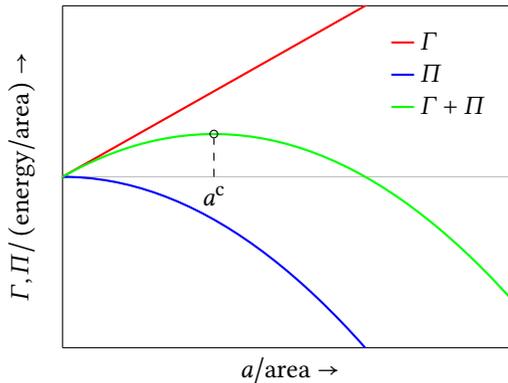
Figure 2.9: Griffith's fracture criterion

possible if the load increases. It is considered to be *stable*. If a critical size a^{c}

is surpassed, the crack becomes *unstable* as crack growth happens without a further increase of load [59, 66]. This scenario often results in complete *failure of a body*, meaning the body loses its ability to transfer loads.

2.2.3 *J*-Integral

In LEFM, the *J*-integral by Rice [147] is equivalent to the energy release G, introduced in the previous section. The advantage of the *J*-integral is its applicability to non-elastic materials [66]. Nevertheless, in the following, the scope is restricted to a homogeneous and hyperelastic body. Body forces are neglected, and for simplicity, infinitesimal strains are assumed. With W being a strain energy density the *J*-integral is denoted in a two dimensional case as a contour integral

$$J_k = \int_C \left\{ W\delta_{jk} - \sigma_{ij}u_{i,k} \right\} n_j^C \mathrm{d}l, \tag{2.67}$$

where n_j^C is the outward unit normal vector of the contour path. In a defect-free body the integral yields $J_k = 0$ for an arbitrary closed contour C. In three dimensions, when J_k corresponds to a surface integral, this may be shown by applying Gauss' theorem (2.24). If the body contains singularities or cracks as depicted in Figure 2.10, the *J*-integral is, in general, non-zero. This
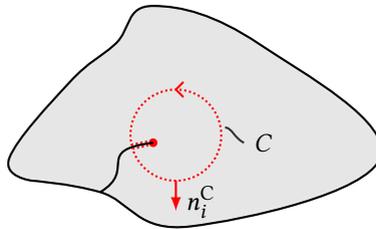
Figure 2.10: *J*-Integral: Contour path around crack tip

may be used to quantify the change in energy when a crack grows within the integration limits of the *J*-integral. As indicated earlier, the change in energy equals the energy release necessary to propagate the crack tip, $J = G$.

The *J*-integral is path-independent as long as the crack surfaces enclosed are traction-free and straight [59]. Thus, the *J*-integral allows for the calculation of the energy release and hence observation of crack propagation without the need to consider the crack tip singularity explicitly.

2.2.4 Cracks in interfaces

Composite materials such as FRPs consist of at least two different materials. Within each material, which is a homogenous sub-volume, the LEFM theory introduced above may be applied. Hence, characteristic failure mechanisms, such as matrix rupture or fibre breakage, are covered. A third failure mechanism is the *debonding* of the fibre-matrix interface [62], which may happen through a fibre pull-out. Fibre-matrix interfaces are of special interest when working with FRPs, because they define and influence effective material properties as they link fibres and matrix. However, when linking two different materials, interfaces may become a weak-spot due to stress peaks and weak bonding between the material types. This makes it essential to include fibre-matrix interfaces into fracture mechanics examinations of FRPs. Further details on the fracture behaviour of FRPs are found in the literature, e.g. [62, 89, 181]. Commonly, it is assumed that the *interfacial crack resistance* is influenced by the neighbouring materials, but also might be higher or lower in magnitude. In [66], the energetic crack resistance strongly depends on the proportion of the crack resistances of different crack modes; hence also the location and orientation of the crack tip within a interfacial region may play a role.

2.3 Resin chemistry and its description

There is a variety of thermosets which are used within FRTS [162]. Each of them is characterised by its own composition and curing reaction, resulting in individual development of material behaviour. Although the models presented in this work are developed from a general point of view, nevertheless, later on, they are applied to a specific matrix material. Therefore the resin type

used within this work and its chemical reactions are introduced and presented on the following pages, and its representation on a micro- and nano-scale is discussed. Especially Sections 2.3.1 and 2.3.2 are largely based on the work of Schwab and Denniston [164].

2.3.1 Resin type and reactions

Within this work, an *unsaturated polyester-polyurethane hybrid* resin (UPPH) is used for simulations. This resin class combines two resin types: A *polyurethane* resin (PU), providing flexibility and toughness, and a cross-linking *unsaturated polyester* resin (UP), giving stiffness and thermal resistance. More details on this class of hybrid resins may be found in [190].

A representative of the UPPH resin class is the commercially available resin Daron® AQR 1009, available from Aliancys AG. This compound consists of three components, which are schematically described in Figure 2.11:

- Lupranate® M 20 R, available from BASF SE, a non-uniform collection of (poly-) methylene diphenyl diisocyanates ((P-)MDI),

- Daron® AQR 1009, available from Aliancys AG, a UP dissolved in styrene, which also gives the name to the resin system, and

- Trigonox® C, available from AkzoNobel N.V., an organic peroxide.

When the resin is cured, the three components of the UPPH resin perform two separate main reactions; thus, the resin is referred to as a two-stage resin. Firstly, the isocyanate groups of the (P-)MDI (Figure 2.11a), together with hydroxyl groups of the UP (Figure 2.11b) component, allows for the formation of long polyurethane chains through *urethane polyaddition*. Secondly, the unsaturated carbon bonds in the UP are cross-linked in a *radical polymerisation* process by the provided styrene, a reaction which is initiated by the peroxide molecules (Figure 2.11c).

To initiate the first reaction step, the urethane polyaddition, all components are mixed together as shown in Figure 2.12. Upon mixture the reaction starts

(a) Collection of (P-)MDI   (b) UP dissolved in styrene   (c) Organic peroxide molecule
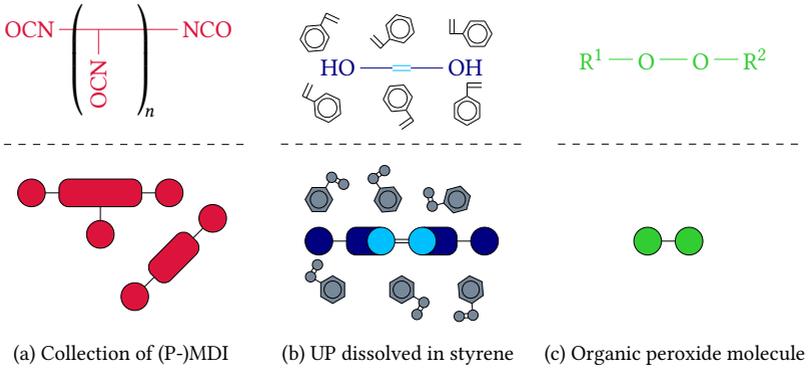
Figure 2.11: Components of the resin: schematic representations
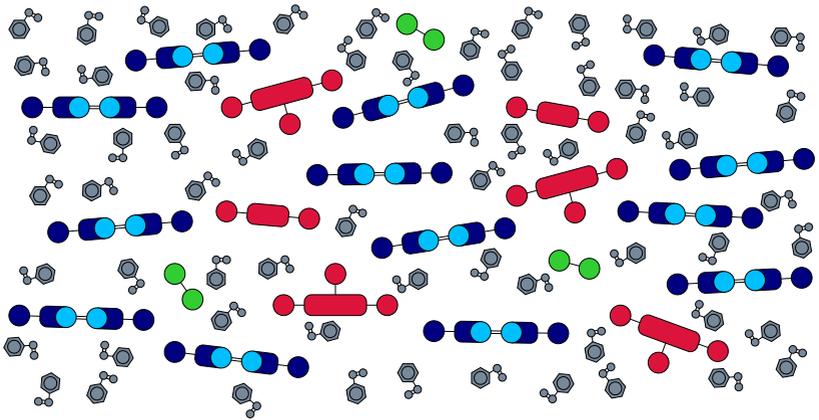
Figure 2.12: Resin components mixed

at room temperature and may be accelerated by elevated temperatures. On a molecular scale this leads to chemical reactions between the isocyanate groups of the (P-)MDI and the hydroxyl groups of the UP, forming urethane connections (see Figure 2.13). As a result long polyurethane chains stretch through wide areas of the resin, which thickens the compound. Macroscopically this
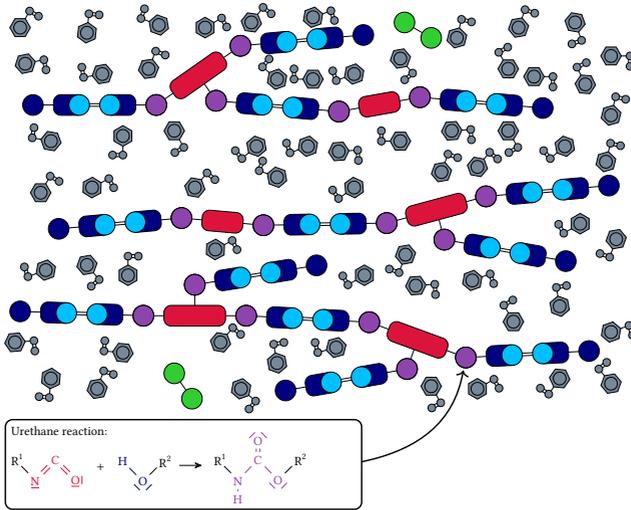
Figure 2.13: First reaction step: Isocyanate and hydroxyl groups react to urethane connections (violet circles).

shows in a gum-like consistency and an initial toughness and stiffness. In an industrial application, this first solid-like behaviour allows for intermediate production steps, such as cutting or pre-forming. Furthermore, if a FRP is realised, the fibres have to be placed in the resin during this reaction step. If the second reaction step is not subsequently initiated, the semi-finished product may be stored for several weeks.

For the second reaction step the thickened resin has to be heated above 60 °C, which dissociates the O-O bonds of the organic peroxide molecules. When O-O bonds break, both oxygen atoms become radical. These electrophile centres move to the nucleophile regions of the unsaturated carbon bonds found in the polyurethane chains and the styrene. This first step initiates the radical polymerisation and is called *chain initiation*. If the radical oxygen finds an unsaturated bond, the carbon double bond reduces its order and donates an electron to form a bond between the oxygen and one of the carbon atoms. With only one of the electrons bonded in the newly formed bond, the leftover
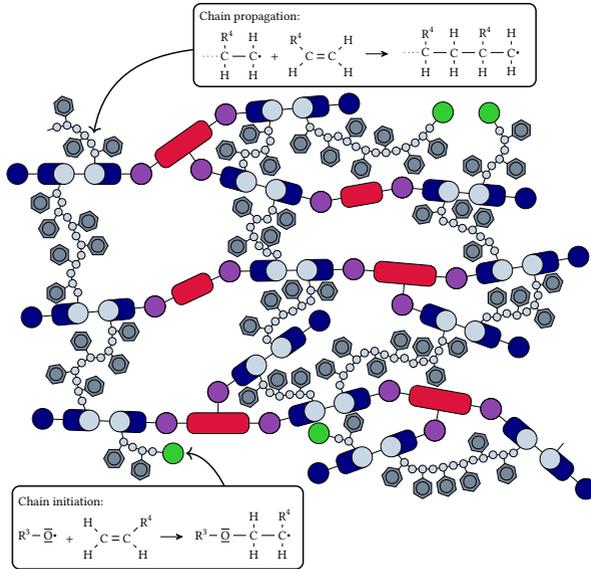
Figure 2.14: Second reaction step: Peroxide bonds dissociate and initiate the radical polymerisation (in light grey), which cross-links the previously formed polyurethane chains with styrene molecules. The radical propagation depends on breaking unsaturated carbon bonds.

carbon atom is now electrophile itself, and the radical reaction continues by connecting to the next unsaturated bond (Figure 2.14). This *chain propagation* three-dimensionally cross-links the long polyurethane molecules by styrene chains forming a stiff polymer network. The reaction process stops through *chain termination*, when two radical atoms meet and form a bond, or when no further reaction partners move in proximity. From a macroscopic viewpoint this step gives the product its final shape and moreover its final material properties and defines its behaviour. Thus, this reaction step goes along with e.g. moulding: The thickened resin is placed in a pre-heated mould to initiate the final cure step, which happens under external pressure.

The molecular structure of the resin components is not publicly available. Hence, the molecules and the resin used in this work are not exact representa-

tions of the resin Daron® AQR 1009, but provide a prototypical example of the UPPH resin class to derive basic behaviour from. A one-to-one replica is not the aim or scope of this work. The idea is to yield a thermoset used for FRTS with close to realistic material behaviour, regardless of the molecular sub-structure. Therefore details of molecular backbones are not discussed here in detail, but are based on typical thermoset backbones of PU and UP resins to have a defined structure for simulation setups. A few characteristics, provided by Aliancys AG [189], are given in the form of the schematics in Figure 2.11 and by the information listed in Table 2.1. Following this information each

Daron® AQR 1009			Lupranate® M 20 R		
OH value	mg KOH/g	100.0	NCO eq. weight	g/eq. NCO	135.0
functionality	—	2.0	functionality	—	2.7

Table 2.1: Information on Daron® AQR 1009 and Lupranate® M 20 R.

UP molecule has always two hydroxyl groups. In contrast the (P-)MDI has a functionality of 2.7, which indicates that there have to be molecules with a different amount of isocyanate groups to yield this mean. The second bit of information in the form of NCO equivalent weight relates each isocyanate group to a part of the molecule's backbone with the atomic weight of 135.0. For the organic peroxide, the structure is basically of low relevance, as according to its role, it only makes up for a small percentage of the compound and is of negligible importance for the later polymer structure. With this information, a compound composition is derived as presented in Table 2.2 as a basis for simulation setups with this resin type. From this, the composition of a basic unit compound is calculated, which is given in Table 2.3. At this point it should be stressed, that the choice regarding the composition are made on the basis of the available information and through educated guesses. This means that the presented choice is not unique and is only of exemplary nature, as previously stated.

Commercial Variant	phr	Component	wt.%
Lupranate® M 20 R	25	MDI P-MDI	45 55
Daron® AQR 1009	100	Unsaturated polyester polyol Styrene	65 35
Trigonox® C	1	Organic peroxide	100

Table 2.2: Hybrid resin composition: Components are given in parts per hundred resin (phr, weight-based composition), while involved molecule types are given in weight percentage.

Resin component	parts
Isocyanate	57
UP Styrene	40 262
Peroxide	4

Table 2.3: Hybrid resin: Composition proportions based on weight.

2.3.2 Description of molecular bonds with interaction potentials

In MD, *force fields* model a potential energy which describes the interactions between particles or atoms and the resulting arrangement. If atoms are bonded and form molecules, force fields have to describe the energy of different molecule conformations and the interplay between different molecules. Therein a position of a single atom is defined by forces imposed due to distance to and different angles with its bonded neighbour atoms. Moreover, it is influenced by *van der Waals* and *Coulomb forces* arising from its non-bonded neighbours, which implicitly implies a long-range effect. In this framework, the energy of a bond between two atoms may be characterised by the energy of a spring connecting both. A common approach is to model this spring through a Taylor series expansion around the equilibrium bond distance and calculat-

ing the spring constants from the experimentally or simulatively determined vibrational modes of this bond type [154].

Within this work, the Compass force field [176–178] is used to describe the potential energy. The intra- and intermolecular forces depend on relative *atom positions* r^{ij} and their combinations as *bond length* b^{ij}, *angle* φ^{ijk}, *dihedral* or *torsion angle* ϑ^{ijkl} and *out-of-plane angle* χ^{ijkl}, where the superscripts indicate the involved atoms and their position, e.g. $r^{ij} = r\,(x_i, x_j)$. Besides the basic potential terms, governed by the introduced distance and angles, there are also cross-terms incorporated to describe molecule behaviour more accurately, which gives the total potential energy as

$$
\begin{aligned}
e^{\text{tot}} = \ & \left\{ e^{\text{bonds}} \right\} + \left\{ e^{\text{angles}} + e^{\text{bond-bond}} + e^{\text{bond-angle}} \right\} \\
& + \left\{ e^{\text{dihedrals}} + e^{\text{middle-bond-torsion}} + e^{\text{end-bond-torsion}} \right. \\
& \quad \left. + e^{\text{angle-torsion}} + e^{\text{angle-angle-torsion}} + e^{\text{bond-bond-13-torsion}} \right\} \\
& + \left\{ e^{\text{impropers}} + e^{\text{angle-anlge}} \right\} + \left\{ e^{\text{vdW}} + e^{\text{Coulomb}} \right\}.
\end{aligned}
\tag{2.68}
$$

Inter-molecular or non-bonded interaction terms are modelled by e^{vdW} and e^{Coulomb}, which act on atoms of different molecules but also on atoms of the same molecule if they do not directly influence each other through one of the listed intra-molecular potentials. The Coulomb potential introduces electrostatic behaviour, while the van der Waals forces are modelled by a

Lennard-Jones potential of type 9-6. When giving each potential explicitly, the total potential energy expands to

$$
\begin{aligned}
e^{\text{tot}} = \ & \sum_{i,j} \left\{ K^{\text{b2}} \left(b^{ij} - b^{0,ij} \right)^2 + K^{\text{b3}} \left(b^{ij} - b^{0,ij} \right)^3 + K^{\text{b4}} \left(b^{ij} - b^{0,ij} \right)^4 \right\} \\
& + \sum_{i,j,k} \left\{ A^{\text{a2}} \left(\varphi^{ijk} - \varphi^{0,ijk} \right)^2 + A^{\text{a3}} \left(\varphi^{ijk} - \varphi^{0,ijk} \right)^3 + A^{\text{a4}} \left(\varphi^{ijk} - \varphi^{0,ijk} \right)^4 \right. \\
& \qquad + A^{\text{bb}} \left(b^{ij} - b^{0,ij} \right) \left(b^{jk} - b^{0,jk} \right) \\
& \qquad \left. + A^{\text{ba1}} \left(b^{ij} - b^{0,ij} \right) \left(\varphi^{ijk} - \varphi^{0,ijk} \right) + A^{\text{ba2}} \left(b^{jk} - b^{0,jk} \right) \left(\varphi^{ijk} - \varphi^{0,ijk} \right) \right\} \\
& + \sum_{i,j,k,l} \left\{ D^{\text{d1}} \left[1 - \cos(\vartheta^{ijkl}) \right] + D^{\text{d2}} \left[1 - \cos(2\vartheta^{ijkl}) \right] + D^{\text{d3}} \left[1 - \cos(3\vartheta^{ijkl}) \right] \right. \\
& \qquad + \left(b^{jk} - b^{0,jk} \right) \left[D^{\text{mbt1}} \cos(\vartheta^{ijkl}) + D^{\text{mbt2}} \cos(2\vartheta^{ijkl}) + D^{\text{mbt3}} \cos(3\vartheta^{ijkl}) \right] \\
& \qquad + \left(b^{ij} - b^{0,ij} \right) \left[D^{\text{ebt1}} \cos(\vartheta^{ijkl}) + D^{\text{ebt2}} \cos(2\vartheta^{ijkl}) + D^{\text{ebt3}} \cos(3\vartheta^{ijkl}) \right] \\
& \qquad + \left(b^{kl} - b^{0,kl} \right) \left[D^{\text{ebt4}} \cos(\vartheta^{ijkl}) + D^{\text{ebt5}} \cos(2\vartheta^{ijkl}) + D^{\text{ebt6}} \cos(3\vartheta^{ijkl}) \right] \\
& \qquad + \left(\varphi^{ijk} - \varphi^{0,ijk} \right) \left[D^{\text{at1}} \cos(\vartheta^{ijkl}) + D^{\text{at2}} \cos(2\vartheta^{ijkl}) + D^{\text{at3}} \cos(3\vartheta^{ijkl}) \right] \\
& \qquad + \left(\varphi^{jkl} - \varphi^{0,jkl} \right) \left[D^{\text{at4}} \cos(\vartheta^{ijkl}) + D^{\text{at5}} \cos(2\vartheta^{ijkl}) + D^{\text{at6}} \cos(3\vartheta^{ijkl}) \right] \\
& \qquad + D^{\text{aat}} \left(\varphi^{ijk} - \varphi^{0,ijk} \right) \left(\varphi^{jkl} - \varphi^{0,jkl} \right) \cos(\vartheta^{ijkl}) \\
& \qquad \left. + D^{\text{bb13}} \left(b^{ij} - b^{0,ij} \right) \left(b^{kl} - b^{0,kl} \right) \right\} \\
& + \sum_{i,j,k,l} \left\{ I \chi^{ijkl^2} + I^{\text{aa1}} \left(\varphi^{ijk} - \varphi^{0,ijk} \right) \left(\varphi^{kjl} - \varphi^{0,kjl} \right) \right. \\
& \qquad + I^{\text{aa2}} \left(\varphi^{ijk} - \varphi^{0,ijk} \right) \left(\varphi^{ijl} - \varphi^{0,ijl} \right) \\
& \qquad \left. + I^{\text{aa3}} \left(\varphi^{ijl} - \varphi^{0,ijl} \right) \left(\varphi^{kjl} - \varphi^{0,kjl} \right) \right\} \\
& + \sum_{i,j} \left\{ \epsilon^{ij} \left[2 \left(\frac{r^{0,ij}}{r^{ij}} \right)^9 - 3 \left(\frac{r^{0,ij}}{r^{ij}} \right)^6 \right] + \frac{q^i q^j}{r^{ij}} \right\}.
\end{aligned}
\tag{2.69}
$$

The parameters describing stiffnesses against the respective movements are given in [176–178]. In these references, the force field used is validated for different molecules in terms of energetic behaviour.

2.3.3 Kamal-Sourour-Model for exothermic reactions

The previous sections mainly dealt with the chemical curing processes within a resin on a molecular level. To be able to describe developments in material behaviour caused by these chemical reactions it is desirable to have a description of the curing process on a continuum level. On this level, a *degree of cure* $\zeta \in [0, 1]$ is introduced, which describes the chemical conversion per volume. A value of $\zeta = 0$ denotes the uncured state. Accordingly, $\zeta = 1$ is the fully cured state. Commonly, there are two approaches to describe and quantify the degree of cure ζ [70, 118]: mechanistic models, which are based on the involved chemical reactions and hence need detailed information on the internal processes, and empirical models, which often map the overall reaction behaviour with a single equation and thus have to be fitted to experimental data. In this work the wide-spread *Kamal-Sourour kinetic model* [87] is used, which is able to describe exothermic reactions such has the radical polymerisation described in Section 2.3.1. The advantage of this model is its simplicity, which also shows in a small number of parameters. This comes at the cost of a loss in accuracy at lower temperatures, where vitrification plays a role, a process which is not separately captured by this model [18]. The model formulates an equation of state,

$$\dot\zeta \left(\zeta, \Theta \right) = \left\{ k^1 + k^2 \zeta^m \right\} \left\{ 1 - \zeta^n \right\}, \tag{2.70}$$

which solely depends on ζ itself and the absolute temperature Θ. The reaction kinetics k^1, k^2 follow an Arrhenius-type law of the form

$$k^i = k^{0,i} \exp \left(-\frac{\Delta E^i}{R\Theta} \right), \tag{2.71}$$

where $k^{0,i}$ are kinetic constants, ΔE^i are activation energies and R is the gas constant. Furthermore, from Equation (2.70) there are the exponents m and n. Hence, in total, the model has six fitting parameters. As previously noted, the model is unable to capture the point of vitrification, which occurs when the

glass transition temperature reaches the cure temperature, $\Theta^g = \Theta^{cure}$. Due to its exothermic nature, the main part of the curing reaction automatically takes place at temperatures $\Theta^{cure} > \Theta^g$. Depending on the process parameters it may occur that the local curing temperature drops below Θ^g, especially at later stages when the conversion rate has slowed down. At this point, the reaction slows down tremendously and becomes diffusion-controlled. To be able to predict this point a second model describing the development of the glass transition temperature Θ^g may be used. Then the further development of ζ may be stopped on the basis of such an equation of state. A common model for this is DiBenedetto's approach [41],

$$\frac{\Theta^g(\zeta) - \Theta^{g,0}}{\Theta^{g,\infty} - \Theta^{g,0}} = \lambda\zeta\left\{1 - (1-\lambda)\zeta\right\}^{-1}, \tag{2.72}$$

which depends on the glass transition temperature Θ^g itself and the degree of cure ζ. The parameters are the initial and maximum glass transition temperature $\Theta^{g,0}$ and $\Theta^{g,\infty}$, respectively, and the fitting parameter is λ. If the product $\Delta c_p \cdot \Theta^g$, with Δc_p being the change in the specific heat capacity at constant pressure, keeps constant throughout an experiment, the fitting parameter may be chosen $\lambda \approx \Theta^{g,0}/\Theta^{g,\infty}$ [141].

Experiments to characterise the curing reaction often involve differential scanning calorimetry (DSC) measurements [193, 197]. The basic approach is to measure the heat flux generated by the exothermic reaction and assume it to be proportional to the released reaction enthalpy, as depicted in Figure 2.15. In a series of measurements the total reaction enthalpy, h^{tot}, is found and via the relation,

$$\zeta(t) = \frac{h(t)}{h^{tot}}, \tag{2.73}$$

the chemical conversion is characterised by the degree of cure ζ, which may be used to fit the Kamal-Sourour model. An overview on the phenomenological modelling of curing processes and a discussion on fitting of these models is found in [18].
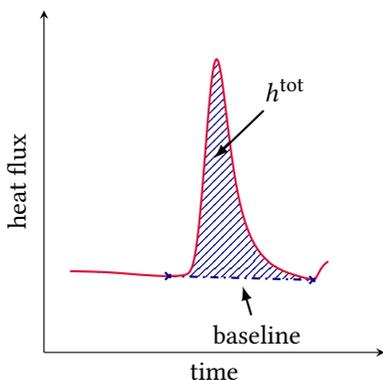
Figure 2.15: Prototypical development of the recorded heat flux during a DSC measurement: The integrated heat flux is associated with the reaction enthalpy $h(t)$.

2.4 Evaluation techniques for molecular dynamics

In this section, the theoretical background for the evaluation of MD simulations is outlined in terms of material properties. There are two basic approaches to follow: The first uses equilibrium molecular dynamics (EMD), where thermodynamic properties are evaluated when the observed system is in equilibrium. Then the fluctuations of, e.g. total energy e^{tot}, absolute temperature Θ, or volume V are connected to thermodynamic relations to obtain certain material constants [57]. A second approach is non-equilibrium molecular dynamics (NEMD), which basically is conducting an experiment known from a macroscopic viewpoint and simulative application of selfsame on the nano-scale simulation domain. Then a property of the observed system is externally forced to change, e.g. the volume, and the system response, e.g. pressure, is recorded. The relation of both stands for a material property. In the example given, the bulk modulus K is retrieved. In addition, NEMD opens the door to non-linear system response, which commonly occurs the farther a system is from equilibrium [145]. Close to equilibrium it is a matter of choice which

method is applied, often following practical necessities of the observed system or material property to calculate.

A topic relevant in this context, but not discussed here, are *finite size effects*. For small simulation domains, MD calculations may exhibit an influence from their relatively small physical size. For the calculation of material properties, this may show in deviations from macroscopically determined material properties in magnitude or degree of anisotropy. These may occur independently from the idealised conditions a MD simulation is exposed to. Common remedies are to either enlarge the system size or to simulate different realisations of a small domain. The former effectively moves the domain to a behaviour closer to its macroscopic counterpart, hence opening the system to a behaviour only to be observed in a larger volume, but also increases computational cost. The latter implies that different realisations cover different patterns of behaviour, and when averaging over all realisations, hence behaviours, the average and more macroscopic behaviour is observed.

2.4.1 Measuring properties using equilibrium molecular dynamics

In the following, the specific heat capacity at constant volume, c_V, and the thermal conductivity at constant volume, κ_{ij}, are given from statistical mechanics on the basis of the *fluctuation-dissipation theorem*. A more thorough view and derivations may be found in [144, 185]. Both material properties are defined in an NVT ensemble, meaning constant particle number n, volume V and absolute temperature Θ.

Specific heat capacity   In thermodynamics the heat capacity at constant volume, C_V, is given as

$$C_V = \left. \frac{\partial e^{\mathrm{tot}}}{\partial \Theta} \right|_{V,n},\qquad(2.74)$$

with the total energy e^{tot}. For the mass-specific quantity C_V is divided by the system mass $m = \rho V$. On the basis of the ensemble average of the total energy, this expression is re-written to

$$c_V = \frac{1}{m} \frac{\langle e^{\text{tot}\,2} \rangle - \langle e^{\text{tot}} \rangle^2}{k_B \Theta^2}, \tag{2.75}$$

where k_B is the *Boltzmann constant*. Hence, the heat capacity is determined by the energy fluctuations at equilibrium conditions [144].

Thermal conductivity   Fourier's law describes the thermal conductivity as the proportionality tensor between heat flux q_i and temperature gradient $\Theta_{,j}$,

$$q_i = -\kappa_{ij} \Theta_{,j}. \tag{2.76}$$

On the basis of the Green-Kubo formalism [64, 94, 95], the auto-correlation of the heat flux is used to retrieve the thermal conductivity tensor,

$$\kappa_{ij} = \frac{1}{k_B \Theta^2 V} \int\limits_0^{+\infty} \langle q_i(0)\, q_j(t) \rangle \, \mathrm{d}t. \tag{2.77}$$

With this expression it is possible to calculate each component of the thermal conductivity by combining the respective heat fluxes q_i, q_j. In Cartesian coordinates, $\{x, y, z\}$, and under the assumption of isotropy, the thermal conductivity tensor is expressed by the scalar $\kappa = (\kappa_{xx} + \kappa_{yy} + \kappa_{zz})/3$.

2.4.2 Measuring properties using non-equilibrium molecular dynamics

Within this work the mechanical behaviour is assumed to be isotropic and possible viscous behaviour is only associated to shear deformation. Hence, the mechanical properties are clearly separated. For volume-changing but

shape-preserving deformations, the bulk modulus K is calculated, whereas the shear modulus G and the viscosity η are relevant for shape-changing but volume-preserving deformations. Additionally, volume expansion and shrinkage with varying absolute temperature is used to determine the isotropic thermal expansion coefficient α.

Thermal expansion coefficient and glass transition temperature   The (isotropic and) volumetric thermal expansion coefficient (see e.g. [99]) is defined via the thermodynamic relation

$$\alpha^{\mathrm{vol}} = \frac{1}{V} \left.\frac{\partial V}{\partial \Theta}\right|_p,$$ (2.78)

which is valid at constant pressure. The volumetric expansion with temperature is expected to be small, $\alpha^{\mathrm{vol}} \ll 1$, which allows calculation of the linear thermal expansion coefficient via the relation $\alpha^{\mathrm{lin}} = \alpha^{\mathrm{vol}}/3$.

The glass transition temperature Θ^{g} is determined by the change in slope of the volume expansion [98]. As the volume changes are expected to be small and to be in the range of underlying volume fluctuations, simulative measurements are not conducted via a steadily increase in temperature. Instead, average volumes may be found at a sufficiently large number of distinct constant temperature values and then be used to fit the volume change.

Bulk modulus   The thermodynamic relation for the bulk modulus K is defined by (see e.g. [100])

$$\frac{1}{K} = -\frac{1}{V} \left.\frac{\partial V}{\partial p}\right|_\Theta,$$ (2.79)

where p is the hydrostatic pressure. The relation is defined at constant absolute temperature Θ. To calculate the bulk modulus the simulation domain is gradually expanded and compressed while volume and pressure are recorded.

An externally applied change in volume can directly be related to the system response in form of a pressure change, and with this, the bulk modulus is calculated.

Dynamic-mechanical analysis   To calculate shear modulus G and viscosity η a dynamic-mechanical analysis (DMA) is performed. In the macroscopic experiment a sinusoidal shear deformation is imposed on a body and the stress response is measured [138]. To gain knowledge about the stress response at different strain rates, experiments with different deformation frequencies are conducted. Similar to the macroscopic experiment a sinusoidal shear deformation is applied to the simulation domain, while the volume is kept constant. To save computational cost, several angular deformation frequencies ω^i are superposed:

$$u\left(t\right) = \sum_i a^i \sin\left(\omega^i t\right), \tag{2.80}$$

with a^i as the amplitude associated with a specific angular frequency. To circumvent resonance frequencies and to be able to distinguish the induced system responses, the angular frequencies have to be based on multiples of prime numbers. In the simulation the shear deformation $\gamma\left(t\right)$ is applied to the simulation domain and the shear stress response $\tau\left(t\right)$ is measured. Via *Fourier transformation* it is possible to find the shear strain and matching shear stress for each angular frequency ω^i. The definition of the loss factor δ is

$$\tan\left(\delta\left(\omega\right)\right) = \frac{G'\left(\omega\right)}{G''\left(\omega\right)}, \tag{2.81}$$

which describes the phase shift between the applied shear strain and the material response. On this basis, the complex shear modulus is calculated,

$$G^* \left(\omega \right) = \frac{\tau \left(\omega \right)}{\gamma \left(\omega \right)} = G' \left(\omega \right) + \mathrm{i} G'' \left(\omega \right), \tag{2.82}$$

with the storage modulus defined as $G' \left(\omega \right) = \left| G^* \left(\omega \right) \right| \cos \left(\delta \left(\omega \right) \right)$ and the loss modulus given as $G'' \left(\omega \right) = \left| G^* \left(\omega \right) \right| \sin \left(\delta \left(\omega \right) \right)$.

Similarly, the solid-state complex viscosity is noted as

$$\eta^* \left(\omega \right) = \frac{\tau \left(\omega \right)}{\dot{\gamma} \left(\omega \right)} = \eta' \left(\omega \right) - \mathrm{i} \eta'' \left(\omega \right) = \frac{G'' \left(\omega \right)}{\omega} - \mathrm{i} \frac{G' \left(\omega \right)}{\omega}, \tag{2.83}$$

where the viscous component is identified as $\eta' \left(\omega \right)$, whereas $\eta'' \left(\omega \right)$ is the elastic component.

By applying several angular frequencies the material response is estimated over a range of angular frequencies showing the response to different deformation rates. For use in simulations, these values may be used as a fitting basis for material parameters of a visco-elastic model.

3

Models used in Phase-field and Molecular Dynamics Simulations

Within this chapter models are derived enabling the simulation of fibre-reinforced thermoset (FRTS) on a micrometre scale and a thermoset (TS) material on a nanometre scale. The simulations on a micro-scale concern for the most part the curing process of FRTS volume elements under industrial boundary conditions. The model has to be able to predict the formation of eigenstresses in structures resolving matrix and fibre regions on the basis of temperature and curing influences. To check if this intrinsic pre-load causes local damage and micro-cracks, a phase-field model for crack propagation has to be derived with extension to map specific fibre-reinforced polymer (FRP) failure behaviour. The range of models to describe these processes requires a

broad set of material properties, especially for the curing process in a range of temperature and degree of cure. This experimentally challenging task is circumnavigated by measuring parts of the material properties on the basis of molecular dynamics simulations. Therefore models are extended to simulate the polymeric chemical reactions on a molecular scale resolving single atoms. Being able to control and stop the chemical reactions in this simulative approach enables the calculation of material properties for specific temperatures and degrees of cure.

The chapter starts by deriving and evaluating a basic phase-field model from continuum mechanic arguments in Section 3.1. On the basis of the geometric representation, given by the phase-field method, further physical quantities are introduced in Section 3.2, which are necessary to describe the curing process, involving temperature and degree of cure changes, which themselves trigger a mechanic response and vice-versa. The behaviour of the different individual models involved in the curing process are evaluated at the end of the section. For the phase-field fracture model in Section 3.3 similar reasoning is applied as done for the standard phase-field model. Necessities caused by the different nature of a crack surface are carved out and introduced as modifications into the model for crack propagation. A characterisation follows pointing out the effects of these modifications. Lastly, the reaction models used within the molecular dynamics framework are presented and explained in Section 3.4. The models are broken down to basic reaction steps, and are tested on general behaviour.

3.1 Phase-field model from Clausius-Duhem-Inequality

The classical phase-field approach uses a free energy functional to describe domains with different properties and behaviour and a variational formulation to determine the equilibrium conditions for the phases involved and other physical quantities. Emerging from works of van der Waals [194], Ginzburg

and Landau [187], Hillert [79] and Cahn and Hilliard [27–29] the phase-field method found wide-spread application in materials science [37, 93, 198]. Since then, the range of application has been extended to several phenomena such as elasticity, often following the work of Khachaturyan [90]. All extensions have in common that the basis still remains the a priori assumption of a volumetric description of interfaces with a free energy functional, despite the range of scales addressed and model types incorporated, which may set the stage for inaccuracies and deviations in behaviour and quantitativeness. Hence, before developing a phase-field based model for the curing process, a thorough derivation of the phase-field equations on a continuum mechanics scale is given. The idea is to introduce the basic model background in a monolithic integral description of the physical behaviour on the basis of thermodynamics and with the assumption of a sharp interface common on this length scale. The transition from a sharp interface to an interfacial transition region is done by including all quantities considered to keep information on the behaviour at interfaces and to not suppress effects due to variational assumptions and simplifications.

3.1.1 Entropy inequality with a sharp interface

For the following derivation, a system only exposed to mechanical effects is considered. The influence of temperature and heat is neglected. Following these assumptions and Gurtin [69], the integral form of the Clausius-Duhem inequality in the current configuration simplifies to the free energy imbalance and is written as

$$
\underbrace{\int_{\partial v(t)} v_i \sigma_{ij} n_j \mathrm{d}a + \int_{v(t)} v_i \rho b_i \mathrm{d}v}_{A}
$$
$$
- \underbrace{\frac{\mathrm{d}}{\mathrm{d}t}\left(\Psi^{\mathrm{tot}} + \int_{v(t)} \frac{1}{2}\rho v_i v_i \mathrm{d}v \right)}_{B} \geq 0.
$$
(3.1)

Here v_i is identified as the velocity, σ_{ij} as the Cauchy stress tensor, n_j as the surface normal vector, ρ as mass density, b_i as the body force vector and Ψ^{tot} as the (total) Helmholtz free energy functional. The term $1/2\rho v_i v_i$ may be identified as the macroscopic kinetic energy density.

Re-writing term A of Equation (3.1) using Gauss' theorem (2.24), Reynolds transport theorem (2.26), the jump relation (2.17), the pull-back operations defined in Section 2.1.1.2 and the *Piola Identity* $\partial\left(JF_{jk}^{-1}\right)/\partial X_k = \partial\left(JF_{kj}^{-1}\right)/\partial X_k = 0$ yields

$$
\int_{\partial v(t)} v_i \sigma_{ij} n_j \mathrm{d}a + \int_{v(t)} v_i \rho b_i \mathrm{d}v
$$

$$
= \int_{v(t)} \frac{\partial\left(v_i\sigma_{ij}\right)}{\partial x_j}\mathrm{d}v + \int_{v(t)} v_i\rho b_i \mathrm{d}v + \int_{s^{\alpha\beta}(t)} [\![v_i\sigma_{ij}]\!]^{\alpha\beta} n_j^s \mathrm{d}a
$$

$$
= \int_V \left\{ \frac{\partial\left(v_i\sigma_{ij}\right)}{\partial x_j} + v_i\rho b_i \right\} J\mathrm{d}V + \int_{S^{\alpha\beta}(t)} [\![v_i\sigma_{ik}]\!]^{\alpha\beta} JF_{jk}^{-1} N_j^S \mathrm{d}A
$$

$$
= \int_V \left\{ \frac{\partial v_i}{\partial x_j}\sigma_{ij} + v_i\frac{\partial \sigma_{ij}}{\partial x_j} + v_i\rho b_i \right\} J\mathrm{d}V + \int_{S^{\alpha\beta}(t)} [\![v_i P_{ij}]\!]^{\alpha\beta} N_j^S \mathrm{d}A
$$

$$
= \int_V \left\{ \dot{F}_{ik} J\sigma_{ij} F_{kj}^{-1} + v_i\frac{\partial\left(J\sigma_{ij}F_{kj}^{-1}\right)}{\partial X_k} + v_i J\rho b_i \right\} \mathrm{d}V + \int_{S^{\alpha\beta}(t)} [\![v_i P_{ij}]\!]^{\alpha\beta} N_j^S \mathrm{d}A
$$

$$
= \int_V \left\{ P_{ij}\dot{F}_{ij} + v_i\left(\frac{\partial P_{ij}}{\partial X_j} + \rho^0 b_i^0 \right) \right\} \mathrm{d}V
$$

$$
+ \int_{S^{\alpha\beta}(t)} \left([\![v_i]\!]^{\alpha\beta}\langle P_{ij}\rangle^{\alpha\beta} + \langle v_i\rangle^{\alpha\beta}[\![P_{ij}]\!]^{\alpha\beta} \right) N_j^S \mathrm{d}A,
$$

$$(3.2)$$

where $P_{ij} = J\sigma_{ik}F_{jk}^{-1}$ is the 1$^{\text{st}}$ Piola-Kirchhoff stress tensor, $\rho^0 = J\rho$ is the mass density and $b_i^0\left(X_j, t\right) = b_i\left(\chi_j\left(X_j, t\right), t\right)$ is the body force in the reference

configuration. Assuming Hadamard's compatibility condition (no slip) at interfaces $S^{\alpha\beta}$ and following the reasoning in [109] gives

$$
\left([\![v_i]\!]^{\alpha\beta} N_j^S \right) N_j^S = -[\![F_{ij}]\!]^{\alpha\beta} v_k^S N_k^S N_j^S
$$

$$
[\![v_i]\!]^{\alpha\beta} = -[\![F_{ij} N_j^S]\!]^{\alpha\beta} v_\perp^S
$$

$$
[\![v_i]\!]^{\alpha\beta} \langle P_{ik} N_k^S \rangle^{\alpha\beta} = -[\![F_{ij} N_j^S]\!]^{\alpha\beta} \langle P_{ik} N_k^S \rangle^{\alpha\beta} v_\perp^S
$$

$$
[\![v_i]\!]^{\alpha\beta} \langle P_{ik} \rangle^{\alpha\beta} N_k^S = -[\![F_{ij}]\!]^{\alpha\beta} N_j^S \langle P_{ik} \rangle^{\alpha\beta} N_k^S v_\perp^S
$$

$$
\text{(3.3)}
$$

or

$$
= \left(-[\![F_{ij} N_j^S P_{ik} N_k^S]\!]^{\alpha\beta} + \langle F_{ij} N_j^S \rangle^{\alpha\beta} [\![P_{ik} N_k^S]\!]^{\alpha\beta} \right) v_\perp^S,
$$

which finally leads to

$$
\int_{\partial v(t)} v_i \sigma_{ij} n_j \mathrm{d}a + \int_{v(t)} v_i \rho b_i \mathrm{d}v
$$

$$
= \int_V \left\{ P_{ij} \dot{F}_{ij} + v_i \left(\frac{\partial P_{ij}}{\partial X_j} + \rho^0 b_i^0 \right) \right\} \mathrm{d}V \qquad \text{(3.4)}
$$

$$
+ \int_{S^{\alpha\beta}(t)} \left(-[\![F_{ij}]\!]^{\alpha\beta} N_j^S \langle P_{ik} \rangle^{\alpha\beta} N_k^S v_\perp^S + \langle v_i \rangle^{\alpha\beta} [\![P_{ij}]\!]^{\alpha\beta} N_j^S \right) \mathrm{d}A.
$$

For term B of Equation (3.1), the total time derivative $\mathrm{d}/\mathrm{d}t$ has to be evaluated. In addition, the total Helmholtz free energy functional Ψ^{tot} may be decomposed into interface and bulk parts. In the presence of two subdomains this is

$$
\int_{s^{\alpha\beta}(t)} \gamma^{\alpha\beta}(n_i^s) \, \mathrm{d}a = \Psi^{\mathrm{tot}} - \int_{v^\alpha(t)} \rho^\alpha \psi^\alpha \mathrm{d}v - \int_{v^\beta(t)} \rho^\beta \psi^\beta \mathrm{d}v
$$

$$
= \Psi^{\mathrm{tot}} - \sum_\alpha^2 \int_{v^\alpha(t)} \rho^\alpha \psi^\alpha \mathrm{d}v, \qquad \text{(3.5)}
$$

where $\gamma^{\alpha\beta}(n_i^s)$ is the surface energy density dependent on the surface's orientation and $v = v^\alpha \cup v^\beta$. Using again Reynolds transport theorem (2.26) the bulk term can be re-written to

$$\frac{\mathrm{d}}{\mathrm{d}t} \sum_{\alpha}^{2} \int_{v^\alpha(t)} \rho^\alpha \psi^\alpha \mathrm{d}v$$

$$= \sum_{\alpha}^{2} \int_{V^\alpha} \frac{\mathrm{d}}{\mathrm{d}t} \left(\rho^\alpha \psi^\alpha J \right) \mathrm{d}V - \int_{S^{\alpha\beta}(t)} [\![\rho\psi]\!]^{\alpha\beta} v_j^s J F_{ij}^{-1} N_i^S \mathrm{d}A$$

$$= \sum_{\alpha}^{2} \int_{V^\alpha} \left\{ \frac{\mathrm{d}\rho^\alpha}{\mathrm{d}t} \psi^\alpha J + \rho^\alpha \frac{\mathrm{d}\psi^\alpha}{\mathrm{d}t} J + \rho^\alpha \psi^\alpha \frac{\mathrm{d}J}{\mathrm{d}t} \right\} \mathrm{d}V$$

$$\qquad - \int_{S^{\alpha\beta}(t)} [\![\rho^0 \Psi]\!]^{\alpha\beta} v_i^S N_i^S \mathrm{d}A \qquad\qquad (3.6)$$

$$= \sum_{\alpha}^{2} \int_{V^\alpha} \left\{ \psi^\alpha J \underbrace{\left(\frac{\partial \rho^\alpha}{\partial t} + \frac{\partial (\rho^\alpha v_i)}{\partial x_i} \right)}_{=0} + \rho^{0,\alpha} \frac{\partial \Psi^\alpha}{\partial t} \right\} \mathrm{d}V$$

$$\qquad - \int_{S^{\alpha\beta}(t)} [\![\rho^0 \Psi]\!]^{\alpha\beta} v_i^S N_i^S \mathrm{d}A$$

$$= \sum_{\alpha}^{2} \int_{V^\alpha} \rho^{0,\alpha} \frac{\partial \Psi^\alpha}{\partial t} \mathrm{d}V - \int_{S^{\alpha\beta}(t)} [\![\rho^0 \Psi]\!]^{\alpha\beta} v_i^S N_i^S \mathrm{d}A,$$

with $\Psi^\alpha (X_j, t) = \psi^\alpha (\chi_j (X_j, t), t)$. Before continuing with the interface term, the time derivative is applied to the kinetic energy term:

$$\frac{\mathrm{d}}{\mathrm{d}t} \int_{v(t)} \frac{1}{2} \rho v_i v_i \mathrm{d}v$$

$$= \int_V \frac{\mathrm{d}}{\mathrm{d}t} \left(\frac{1}{2} J \rho v_i v_i \right) \mathrm{d}V - \int_{S^{\alpha\beta}(t)} [\![\frac{1}{2} \rho v_i v_i]\!]^{\alpha\beta} v_j^s J F_{kj}^{-1} N_k^S \mathrm{d}A \qquad (3.7)$$

$$= \int_V \rho^0 v_i \frac{\partial v_i}{\partial t} \mathrm{d}V - \int_{S^{\alpha\beta}(t)} [\![\frac{1}{2} \rho^0 v_i v_i]\!]^{\alpha\beta} v_k^S N_k^S \mathrm{d}A.$$

The interface term is derived by using the surface transport theorem (2.27) with indicating additional reformulation steps. This is accomplished through inserting $n_k^s n_k^s = 1$ into the interface term. Furthermore the covariant pull-back

operation $n_k^s = F_{jk}^{-1} N_j^S$ is used, and it is stressed that the interface normal vector N_j^S is generally not normed. Together with formulas from Section 2.1.1.2 and the vector identity (1.10) the integral interface energy is re-written to

$$
\frac{\mathrm{d}}{\mathrm{d}t} \int_{s^{\alpha\beta}(t)} \gamma^{\alpha\beta}(n_i^s) \, \mathrm{d}a
$$

$$
= \frac{\mathrm{d}}{\mathrm{d}t} \int_{s^{\alpha\beta}(t)} \gamma^{\alpha\beta}(n_i^s) \, n_j^s n_j^s \mathrm{d}a
$$

$$
= \int_{S^{\alpha\beta}(t)} \frac{\mathrm{d}}{\mathrm{d}t} \left\{ \gamma^{\alpha\beta}(n_i^s) \, n_j^s J F_{jk}^{-1} \right\} N_j^S \mathrm{d}A
$$

$$
= \int_{S^{\alpha\beta}(t)} \left\{ \frac{\mathrm{d}}{\mathrm{d}t} \left(\gamma^{\alpha\beta}(n_i^s) \, n_j^s \right) J F_{jk}^{-1} + \gamma^{\alpha\beta}(n_i^s) \, n_j^s \frac{\mathrm{d}}{\mathrm{d}t} \left(J F_{jk}^{-1} \right) \right\} N_j^S \mathrm{d}A
$$

$$
= \int_{s^{\alpha\beta}(t)} \left\{ \frac{\partial \left(\gamma^{\alpha\beta}(n_i^s) \, n_j^s \right)}{\partial t} + \frac{\partial \left(\gamma^{\alpha\beta}(n_i^s) \, n_j^s \right)}{\partial x_k} v_k^s \right. \tag{3.8}
$$

$$
\left. + \gamma^{\alpha\beta}(n_i^s) \, n_j^s \frac{\partial v_k^s}{\partial x_k} - \gamma^{\alpha\beta}(n_i^s) \, n_k^s \frac{\partial v_k^s}{\partial x_j} \right\} n_j^s \mathrm{d}a
$$

$$
= \int_{s^{\alpha\beta}(t)} \left\{ \frac{\partial \left(\gamma^{\alpha\beta}(n_i^s) \, n_j^s \right)}{\partial t} + v_j^s \frac{\partial \left(\gamma^{\alpha\beta}(n_i^s) \, n_k^s \right)}{\partial x_k} \right\} n_j^s \mathrm{d}a
$$

$$
+ \int_{\partial s^{\alpha\beta}(t)} \epsilon_{jkl} \gamma^{\alpha\beta}(n_i^s) \, n_k^s v_l^s t_j^{\partial s} \mathrm{d}x,
$$

where the last transformation also involves the Kelvin-Stokes theorem (2.25). Pulling back the terms found to the Lagrangian configuration yields

$$
\begin{aligned}
&\int_{S^{\alpha\beta}(t)} \left\{ \frac{\partial \left(\gamma^{\alpha\beta} F_{kj}^{-1} N_k^S \right)}{\partial t} \right. \\
&\left. + v_j^S \left(\frac{\partial \left(\gamma^{\alpha\beta} F_{lk}^{-1} N_l^S \right)}{\partial X_n} F_{kn}^{-1} \right) \right\} J F_{mj}^{-1} N_m^S \mathrm{d}A \\
&+ \int_{\partial S^{\alpha\beta}(t)} \epsilon_{jkl} \left(\gamma^{\alpha\beta} F_{mk}^{-1} N_m^S \right) \left(v_\perp F_{nl}^{-1} N_n^S \right) F_{jo} T_o^{\partial S} \mathrm{d}X \\
&= \int_{S^{\alpha\beta}(t)} \left\{ J \frac{\partial \gamma^{\alpha\beta}}{\partial t} \underbrace{F_{kj}^{-1} N_k^S F_{mj}^{-1} N_m^S}_{= n_j^s n_j^s = 1} + J \gamma^{\alpha\beta} \underbrace{\frac{\partial \left(F_{kj}^{-1} N_k^S \right)}{\partial t} F_{mj}^{-1} N_m^S}_{= \partial \left(n_j^s n_j^s \right) / \partial t = \partial n_j^s / \partial t \, n_j^s = 0} \right. \\
&\left. + v_j^S F_{mj}^{-1} N_m^S \left(\frac{\partial \left(\gamma^{\alpha\beta} F_{lk}^{-1} N_l^S \right)}{\partial X_n} J F_{nk}^{-1} + \gamma^{\alpha\beta} F_{lk}^{-1} N_l^S \underbrace{\frac{\partial \left(J F_{nk}^{-1} \right)}{\partial X_n}}_{=0} \right) \right\} \mathrm{d}A \\
&+ \int_{\partial S^{\alpha\beta}(t)} \underbrace{\epsilon_{jpr} \left(\gamma^{\alpha\beta} F_{pq} F_{qk}^{-1} F_{mk}^{-1} N_m^S \right) \left(v_\perp F_{rs} F_{sl}^{-1} F_{nl}^{-1} N_n^S \right) F_{jo} T_o^{\partial S}}_{\Rightarrow \epsilon_{jpr} \left(F_{pq} a_q \right) \left(F_{rs} b_s \right) F_{jo} c_o = J \epsilon_{oqs} a_q b_s c_o} \mathrm{d}X \\
&= \int_{S^{\alpha\beta}(t)} \left\{ J \frac{\partial \gamma^{\alpha\beta}}{\partial t} + v_\perp \frac{\partial \left(J \gamma^{\alpha\beta} F_{nk}^{-1} F_{lk}^{-1} N_l^S \right)}{\partial X_n} \right\} \mathrm{d}A \\
&+ \int_{\partial S^{\alpha\beta}(t)} \epsilon_{oqs} \left(J \gamma^{\alpha\beta} F_{qk}^{-1} F_{mk}^{-1} N_m^S \right) \left(v_\perp F_{sl}^{-1} F_{nl}^{-1} N_n^S \right) T_o^{\partial S} \mathrm{d}X,
\end{aligned}
\tag{3.9}
$$

under the assumption that $v_j^s = v_\perp n_j^s$ and with $\gamma^{\alpha\beta} = \gamma^{\alpha\beta} \left(n_i^s \right)$ for the sake of brevity. On the above equation, the following is noted:

- The line integral clearly does not have any influence if there is only one singular surface in the system, which arises due to $\epsilon_{jkl} \left(\bullet \right)_k \left(\bullet \right)_l$.

- When the singular surface connects with two or more singular surfaces along a triple or multi line, parts of the line integral form a common line

and the velocity is the velocity of the common line to keep compatibility. In this case a force balance of the form $\left\{ \sum_{\alpha \neq \beta} \gamma^{\alpha\beta} n_i^{\alpha\beta} \right\} v_i^{cl}$ arises, where $v_i^{cl} = \sum_{\alpha \neq \beta} v_i^{\alpha\beta}$, cf. [77].

- The time derivative $\partial \gamma^{\alpha\beta} / \partial t$ plays a role as soon as the free interface energy density has a time dependence, e.g. a surface deformation gradient or anisotropy based on current normal vector is present.

- If an isotropic $\gamma^{\alpha\beta}$ = const. is the case, the time derivative vanishes and the gradient term simplifies.

- The interface energy density is transformed to the Lagrangian configuration via $\gamma^{0,\alpha\beta} = J \gamma^{\alpha\beta}$.

- In the reference configuration the remaining deformation gradients correct the balance due to deformation influencing vector orientation.

Hence, in the simplest case of isotropic interface energy density and only one singular surface present Equation (3.9) reduces to

$$\int_{S^{\alpha\beta}(t)} v_\perp \gamma^{0,\alpha\beta} \left(n_i^s \right) \frac{\partial \left(F_{nk}^{-1} F_{lk}^{-1} N_l^S \right)}{\partial X_n} \, \mathrm{d}A. \tag{3.10}$$

If there is no or infinitesimal deformation, $F_{nk}^{-1} F_{lk}^{-1} \approx \delta_{nl}$, the integrand simplifies to $\partial N_n^S / \partial X_n$, which is the definition of the double mean curvature (cf. Gurtin [68]).

Before assembling all terms, the purely mechanical Helmholtz free energy is assumed to be $\Psi^\alpha = \Psi^\alpha \left(F_{ij}, Y \right)$, where - besides F_{ij} - the collection $Y = \left\{ v^a, v_i^b, v_{ij}^c, \ldots \right\}$ is introduced as a general representation of all internal vari-

ables, no matter if scalar- or vector- or tensor-valued. This specifies the entropy inequality and the collected terms are

$$
\int_V \left\{ \left(P_{ij} - \rho^{0,\alpha} \frac{\partial \Psi^\alpha}{\partial F_{ij}} \right) \dot{F}_{ij} - \rho^{0,\alpha} \frac{\partial \Psi^\alpha}{\partial Y} \dot{Y} \right.
$$
$$
\left. + v_i \left(\frac{\partial P_{ij}}{\partial X_j} + \rho^0 b_i^0 - \rho^0 \dot{v}_i \right) \right\} dV
$$
$$
+ \int_{S^{\alpha\beta}(t)} \left\{ v_\perp^S \left([\![\rho^0 \Psi]\!]^{\alpha\beta} + [\![\tfrac{1}{2}\rho v_i v_i]\!]^{\alpha\beta} - \gamma^{0,\alpha\beta} \frac{\partial \left(F_{ki}^{-1} F_{ji}^{-1} N_j^S \right)}{\partial X_k} \right. \right.
$$
$$
\left. \left. - [\![F_{ij}]\!]^{\alpha\beta} N_j^S \langle P_{ik} \rangle^{\alpha\beta} N_k^S \right) + \langle v_i \rangle^{\alpha\beta} [\![P_{ij}]\!]^{\alpha\beta} N_j^S \right\} dA \geq 0.
$$

(3.11)

Examination of this result under the premises of the non-negativity as well as for arbitrary $\dot{F}_{ij}$, $\dot{Y}$, v_i and $v_\perp^S$, the entropy inequality delivers a set of equations describing a mechanical body close to equilibrium (see Table 3.1). If a static

in bulk regions	
thermodyn. relation for stress	$P_{ij} = \rho^{0,\alpha} \frac{\partial \Psi^\alpha}{\partial F_{ij}}$
linear momentum balance	$\frac{\partial P_{ij}}{\partial X_j} + \rho^0 b_i^0 = \rho^0 \dot{v}_i$
dissipation inequality	$-\rho^{0,\alpha} \frac{\partial \Psi^\alpha}{\partial Y} \dot{Y} \geq 0$
at the interface	
interface energy balance	$[\![\rho^0 \Psi + \tfrac{1}{2}\rho v_i v_i]\!]^{\alpha\beta} - \gamma^{0,\alpha\beta} \frac{\partial \left(F_{ki}^{-1} F_{ji}^{-1} N_j^S \right)}{\partial X_k}$ $- [\![F_{ij}]\!]^{\alpha\beta} N_j^S \langle P_{ik} \rangle^{\alpha\beta} N_k^S = 0$
the force balance holds	$[\![P_{ij}]\!]^{\alpha\beta} N_j^S = 0$

Table 3.1: Thermodynamical findings from the second law with a sharp interface under the assumption of Hadamard's compatibility condition.

system is assumed, the interface energy balance and the linear momentum

balance reduce to $[\![\rho^0\Psi]\!]^{\alpha\beta} - [\![F_{ij}]\!]^{\alpha\beta}N_j^S\langle P_{ik}\rangle^{\alpha\beta}N_k^S - \gamma^{0,\alpha\beta}\left(F_{ki}^{-1}F_{ji}^{-1}N_j^S\right)_{,k} = 0$ and $P_{ij,j} + \rho^0 b_i^0 = 0$, respectively. The former is known as the configurational force balance, which is e.g. described by Gurtin [68].

3.1.2 Preliminary consideration regarding the introduction of order parameters

In this section a mathematical framework is given, which allows a consistent change of description from a sharp interface area to a diffuse interface region within an Eulerian configuration. As a physical background and motivation the approach of a continuously changing volume fraction within a small transition region in between two subdomains is used. The following considerations follow the work of Umantsev and Roĭtburd [186], Mémoli and Spiro [117] and Duduchava *et al.* [45].

The basis for the introduction of an order parameter is given by the mathematical possibility of extending the unit normal vector field of a hypersurface $s^{\alpha\beta}$ to its neighbourhood v^s, where $s^{\alpha\beta}$ is an arbitrary interface area between two subdomains α and β and v^s is the transition region of the order parameter. Following [45] (see Def. 1.1.) such an extension is possible by the existence and uniqueness result for the following boundary value problem of the *eikonal equation*. Find a function ϕ^s such that

$$\begin{cases} \sqrt{\dfrac{\partial \phi^s(x_i)}{\partial x_j}\dfrac{\partial \phi^s(x_i)}{\partial x_j}} = c\left(x_i\right), & \forall x_i \in v^s \\ \phi^s\left(x_i\right) = \frac{1}{2}, & \forall x_i \in s^{\alpha\beta} \\ \dfrac{\partial \phi^s(x_i)}{\partial x_j} = v_j^s\left(x_i\right), & \forall x_i \in s^{\alpha\beta} \end{cases} \qquad (3.12)$$

where $c\left(x_i\right)$ is a slowness function (inverted velocity function) and v_j^s is the unit normal vector field on $s^{\alpha\beta}$. In addition the second line is modified compared

to [45], as a function value of 0.5 is desired at the hypersurface. The function ϕ^s is a solution to problem (3.12), and therefore the gradient

$$n_j^s(x_i) = \frac{1}{c(x_i)} \frac{\partial \phi^s(x_i)}{\partial x_j}, \quad \forall x_i \in v^s \tag{3.13}$$

is a proper extension of the unit normal vector field v_j^s.

As the extension is thought to be always orthogonal to $s^{\alpha\beta}$, which means that the values of the scalar field ϕ^s, on a surface parallel to $s^{\alpha\beta}$ (level set), are constant, the coordinate system may be changed to a curvilinear coordinate system $\{u, v, w\}$, such that only the coordinate orthogonal to the the surface $s^{\alpha\beta}$ is important for a change of ϕ^s.

$$\begin{cases} \sqrt{\dfrac{\partial \phi^s(w)}{\partial w} \dfrac{\partial \phi^s(w)}{\partial w}} = c(w), & \forall w \in v^s \\ \phi^s(w) = \frac{1}{2}, & \forall w \in s^{\alpha\beta} \\ \dfrac{\partial \phi^s(w)}{\partial w} = v_j^s(w), & \forall w \in s^{\alpha\beta} \end{cases} \tag{3.14}$$

Following Lavrentiev *et al.* [102] and Fomel [54], the eikonal equation can be re-written to:

$$n_j^s n_j^s = 1, \tag{3.15}$$

$$n_j^s \frac{\partial \phi^s}{\partial x_j} = c, \tag{3.16}$$

which has the integral solution

$$\phi^s = \int_{\Gamma\left(n_j^s\right)} c \, \mathrm{d}L. \tag{3.17}$$

The solution expresses that the value ϕ^s is computable by integrating the slowness c along the ray $\Gamma\left(n_j^s\right)$, which is in every point tangent to the local normal vector n_j^s. This means that the change of a scalar value ϕ^s from 0 to 1
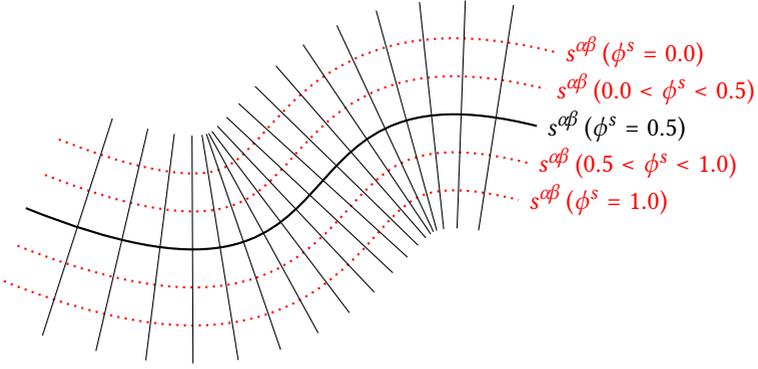
Figure 3.1: Level sets and perpendicular rays $\Gamma\left(n_j^s\right)$ of the sharp interface $s^{\alpha\beta}$

is describable by a slow or smooth transition of the value itself. Having shown this, the function ϕ^s is now modelled in a way, such that

- $\phi^s\big|_{s^{\alpha\beta}} = \frac{1}{2}$,

- ϕ^s is symmetric with respect to the hypersurface $s^{\alpha\beta}$ and

- $\phi^s(w) = \{\forall w \in v;\ \phi^s(w) = [0..1]\}$.

In addition, the volumetric interface should strictly only be present in a small volume around the sharp interface $s^{\alpha\beta}$. Therefore $\phi^s(w)$ is modelled by a sin-function, which is typical for so-called phase-field models with obstacle potential:

$$\phi^s(w) = \frac{1}{2}\left(1 + \sin\left(\frac{4}{\epsilon\pi}w\right)\right), \tag{3.18}$$

which meets the above requirements. The scalar parameter ϵ controls the volume of the extension or the thickness of the interface. To be complete it should be mentioned, that in general the order parameters follow, in the sense of their volume fractions, a local volume constraint, $\sum_\alpha \phi^\alpha = 1$.

3.1.3 Reformulating the interface energy term with an order parameter

Under consideration of the definition of the normal vector via the parametrisation ϕ^s close to the interface in the previous section, the interface energy term in its reduced and simplified form (3.10) is reformulated in the Eulerian configuration (cf. Beckermann [16], Sun and Beckermann [179]) as

$$
\gamma^{\alpha\beta} \frac{\partial n_i^s}{\partial x_i} = \gamma^{\alpha\beta} \left(\frac{\phi_{,i}^s}{\sqrt{\phi_{,j}^s \phi_{,j}^s}} \right)_{,i}
\tag{3.19}
$$

$$
= \gamma^{\alpha\beta} \frac{\phi_{,ii}^s \sqrt{\phi_{,j}^s \phi_{,j}^s} - \phi_{,i}^s \left(\sqrt{\phi_{,j}^s \phi_{,j}^s} \right)_{,i}}{\left(\sqrt{\phi_{,j}^s \phi_{,j}^s} \right)^2}
\tag{3.20}
$$

$$
= \gamma^{\alpha\beta} \frac{1}{\sqrt{\phi_{,j}^s \phi_{,j}^s}} \left(\phi_{,ii}^s - \frac{\phi_{,i}^s \left(\sqrt{\phi_{,j}^s \phi_{,j}^s} \right)_{,i}}{\sqrt{\phi_{,j}^s \phi_{,j}^s}} \right),
\tag{3.21}
$$

where $\phi^s = \phi^s(x_i, t) = \phi^s(w, t)$. For further reformulations, the profile function of ϕ^s is used, which is given by Equation (3.18), and which is re-written for later purposes:

$$
w(\phi^s) = -\frac{\epsilon\pi}{4} \arcsin(1 - 2\phi^s).
\tag{3.22}
$$

With the above information the terms in equation (3.19) are identified as

$$
\sqrt{\phi_{,j}^s \phi_{,j}^s} = \frac{\partial \phi^s}{\partial w} = \left(\frac{\partial w}{\partial \phi^s} \right)^{-1} = \frac{4}{\epsilon\pi} \sqrt{\phi^s(1 - \phi^s)},
\tag{3.23}
$$

$$
\frac{\phi_{,i}^s \left(\sqrt{\phi_{,j}^s \phi_{,j}^s} \right)_{,i}}{\sqrt{\phi_{,j}^s \phi_{,j}^s}} = \frac{\partial^2 \phi^s}{\partial w^2} = -\frac{\partial^2 w}{\partial \phi^{s2}} \left(\frac{\partial \phi^s}{\partial w} \right)^3 = \frac{8}{\epsilon^2\pi^2}(1 - 2\phi^s).
\tag{3.24}
$$

Using these terms in Equation (3.18) the well-known phase-field description of diffuse interfaces is retrieved,

$$\gamma^{\alpha\beta} \frac{\partial n_i^s}{\partial x_i} = \frac{1}{\sqrt{\phi_{,j}^s \phi_{,j}^s}} \gamma^{\alpha\beta} \left(\phi_{,ii}^s - \frac{16}{\epsilon^2 \pi^2} \frac{(1 - 2\phi^s)}{2} \right), \qquad (3.25)$$

times a pre-factor $1/\sqrt{\phi_{,j}^s \phi_{,j}^s}$. For Lagrangian description the Laplace operator has to be pulled back, which gives

$$\frac{1}{\sqrt{\phi_{,l}^S \phi_{,l}^S}} \gamma^{0,\alpha\beta} \left(\phi_{,ij}^S F_{ik}^{-1} F_{jk}^{-1} - \frac{16}{\epsilon^2 \pi^2} \frac{(1 - 2\phi^S)}{2} \right). \qquad (3.26)$$

In the following this will be the starting point for rewriting the interface integral to a volume integral.

3.1.4 From surface integrals to volume integrals

To ensure the same behaviour, the interface (sharp interface) integral is defined as a limit of a volume (diffuse interface) integral with $\epsilon \to 0$, where ϵ controls the interface thickness. With the delta distribution δ and its regularised version δ^ϵ follows:

$$\delta(w) = \lim_{\epsilon \to 0^+} \delta^\epsilon(w) \quad \text{with coordinate } w \text{ normal to the interface.} \qquad (3.27)$$

To prove the same behaviour, it is shown that $\epsilon \to 0^+$ leads to $\delta^\epsilon\big|_{w=0} \to \infty$:

$$
\begin{aligned}
\delta(w = 0) &= \lim_{\epsilon \to 0^+} \left(\delta^\epsilon(w) \big|_{w=0} \right) \\
&= \lim_{\epsilon \to 0^+} \left(\frac{\partial \phi}{\partial w} \Big|_{w=0} \right) \\
&= \lim_{\epsilon \to 0^+} \left(\frac{4}{\pi \epsilon} \cos\left(\frac{4}{\pi \epsilon} w \right) \Big|_{w=0} \right) \\
&= \lim_{\epsilon \to 0^+} \frac{4}{\pi \epsilon} \to \infty.
\end{aligned}
\qquad (3.28)
$$

Furthermore $\phi^s \geq 0$ is satisfied and the identity

$$1 = \int_{-\infty}^{+\infty} \delta(w)\,\mathrm{d}w = \int_{-\frac{\pi^2\epsilon}{8}}^{+\frac{\pi^2\epsilon}{8}} \delta^\epsilon(w)\,\mathrm{d}w \tag{3.29}$$

holds, where δ^ϵ is only valid in the range of the diffuse interface. Therefore it is concluded:

$$
\begin{aligned}
\int_{S^{\alpha\beta}(t)} \mathrm{d}a &= \int_{S^{\alpha\beta}(t)} 1\,\mathrm{d}a \\
&= \int_{S^{\alpha\beta}(t)} \int_{-\frac{\pi^2\epsilon}{8}}^{+\frac{\pi^2\epsilon}{8}} \delta^\epsilon(w)\,\mathrm{d}w\mathrm{d}a \\
&= \int_{v^s(t)} \sqrt{\frac{\partial\phi^s}{\partial x_i}\frac{\partial\phi^s}{\partial x_i}}\,\mathrm{d}v \\
&\stackrel{\epsilon \to 0}{=} \int_{S^{\alpha\beta}(t)} \mathrm{d}a
\end{aligned}
\tag{3.30}
$$

In the following, the Lagrangian description of the curvature term is used, which is given in Equation (3.26). Furthermore the order parameter ϕ^S is renamed to $\phi^\alpha = 1 - \phi^\beta$ to match the arbitrary phases α and β forming the interface $S^{\alpha\beta}$ and reformulation of the interface terms of Equation (3.11) by expanding it to a volumetric region gives

$$
\begin{aligned}
&\int_{S^{\alpha\beta}} \left\{ v_\perp^{\alpha\beta} \left([\![\rho^0\Psi]\!]^{\alpha\beta} + [\![\tfrac{1}{2}\rho v_i v_i]\!]^{\alpha\beta} - \gamma^{0,\alpha\beta}\frac{\partial F_{jk}^{-1}F_{ik}^{-1}N_i^S}{\partial X_j} \right.\right. \\
&\qquad\left.\left. - [\![F_{ij}]\!]^{\alpha\beta}N_j^{\alpha\beta}\langle P_{ij}\rangle^{\alpha\beta}N_j^{\alpha\beta} \right) + \langle v_i\rangle^{\alpha\beta}[\![P_{ij}]\!]^{\alpha\beta}N_j^{\alpha\beta} \right\}\,\mathrm{d}A \\
&= \int_V \left\{ v_\perp^{\alpha\beta} \left([\![\rho^0\Psi]\!]^{\alpha\beta} + [\![\tfrac{1}{2}\rho v_i v_i]\!]^{\alpha\beta} - [\![F_{ij}]\!]^{\alpha\beta}N_j^{\alpha\beta}\langle P_{ij}\rangle^{\alpha\beta}N_j^{\alpha\beta} \right.\right. \\
&\qquad\left.\left. - \frac{1}{\sqrt{\phi_{,l}^\alpha\phi_{,l}^\alpha}}\gamma^{0,\alpha\beta}\left(\phi_{,ij}^\alpha F_{ik}^{-1}F_{jk}^{-1} - \frac{16}{\epsilon^2\pi^2}\frac{(1-2\phi^\alpha)}{2} \right) \right) \right.
\end{aligned}
\tag{3.31}
$$

$$+ \langle v_i \rangle^{\alpha\beta} [\![P_{ij}]\!]^{\alpha\beta} N_j^{\alpha\beta} \Bigg\} \sqrt{\phi_{,l}^{\alpha} \phi_{,l}^{\alpha}} \mathrm{d}V$$

$$= \int_V \Bigg\{ v_{\perp}^{\alpha\beta} \Bigg(\Bigg([\![\rho^0 \Psi]\!]^{\alpha\beta} + [\![\tfrac{1}{2} \rho v_i v_i]\!]^{\alpha\beta} - [\![F_{ij}]\!]^{\alpha\beta} N_j^{\alpha\beta} \langle P_{ij} \rangle^{\alpha\beta} N_j^{\alpha\beta} \Bigg) \sqrt{\phi_{,l}^{\alpha} \phi_{,l}^{\alpha}}$$

$$- \gamma^{0,\alpha\beta} \left(\phi_{,ij}^{\alpha} F_{ik}^{-1} F_{jk}^{-1} - \frac{16}{\epsilon^2 \pi^2} \frac{(1 - 2\phi^{\alpha})}{2} \right) \Bigg)$$

$$+ \sqrt{\phi_{,l}^{\alpha} \phi_{,l}^{\alpha}} \langle v_i \rangle^{\alpha\beta} [\![P_{ij}]\!]^{\alpha\beta} N_j^{\alpha\beta} \Bigg\} \mathrm{d}V.$$

By transforming the interface integral to a volume integral the jump brackets, which define the jump of a arbitrary quantity ψ across a surface, have to be re-thought. To conserve the meaning, the jump brackets are now used analogously to a volumetric manner: They now describe the jump of a quantity ψ across two volume fractions within a infinitesimal volume element as shown in Figure 3.2:

$$[\![\psi]\!]^{\alpha\beta} = \psi \Big|_{S_+^{\alpha\beta}} - \psi \Big|_{S_-^{\alpha\beta}} \longrightarrow [\![\psi]\!]^{\alpha\beta} = \psi^{\alpha} \Big|_{\phi^{\alpha}} - \psi^{\beta} \Big|_{\phi^{\beta}} \tag{3.32}$$

This definition guarantees that the jump of ψ in the sharp interface behaviour is distributed along the volumetric region in such a way that, by integrating in normal direction, the original jump may be recovered.

Analysing expression (3.31) shows the close relationship to the sharp interface terms of Equation (3.11):

- the linear momentum balance on singular surfaces for $\phi_{,i}^{\alpha} \neq 0$ and arbitrary v_i:

$$\sqrt{\phi_{,l}^{\alpha} \phi_{,l}^{\alpha}} \langle v_i \rangle^{\alpha\beta} [\![P_{ij}]\!]^{\alpha\beta} N_j^{\alpha\beta} = 0$$

$$[\![P_{ij}]\!]^{\alpha\beta} N_j^{\alpha\beta} = 0, \tag{3.33}$$
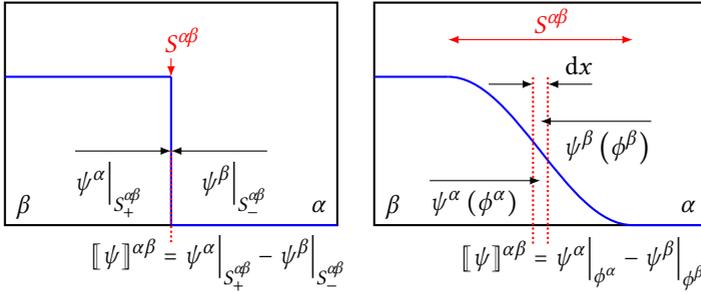
Figure 3.2: Reinterpreted jump brackets in the sense of Equation (3.32): Sharp (left) and diffuse (right) interface.

- and an energetic balance at a widened interface for arbitrary $v_\perp^{\alpha\beta}$:

$$
\left(\llbracket \rho^0 \Psi \rrbracket^{\alpha\beta} + \llbracket \frac{1}{2} \rho v_i v_i \rrbracket^{\alpha\beta} - \llbracket F_{ij} \rrbracket^{\alpha\beta} N_j^{\alpha\beta} \langle P_{ij} \rangle^{\alpha\beta} N_j^{\alpha\beta} \right) \sqrt{\phi_{,l}^\alpha \phi_{,l}^\alpha}
$$

$$
- \gamma^{0,\alpha\beta} \left(\phi_{,ij}^\alpha F_{ik}^{-1} F_{jk}^{-1} - \frac{16}{\epsilon^2 \pi^2} \frac{(1 - 2\phi^\alpha)}{2} \right) = 0. \tag{3.34}
$$

3.1.5 Revisiting volume integrals

By spreading the dividing surface to a diffuse interface volume, the volume terms of Equation (3.11) have to be adjusted with respect to the new preconditions. For a meaningful application, the following assumptions are made:

- The Helmholtz free energy may be written as $\rho^0 \Psi = \sum_\alpha \phi^\alpha \rho^{0,\alpha} \Psi^\alpha$, meaning a weighted sum of the phase-inherent Helmholtz free energies.

- A phase-inherent Helmholtz free energy is dependent on its phase-inherent variables $\Psi^\alpha = \Psi^\alpha \left(F_{ij}^\alpha, Y_{ij}^\alpha \right)$.

- For a clean interpretation, the mass density is assumed to be constant, and it is composed as $\sum_\alpha \phi^\alpha \rho^{0,\alpha}$.

- The linear momentum balance on singular surfaces (traction condition) as well as Hadamard's compatibility condition apply also in the diffuse interface region.

The volume integral is evaluated in the sense of the non-negativity of the entropy imbalance, for the whole domain and changes for two phases to

$$
\int_V \left\{ P_{ij}\dot{F}_{ij} - \frac{\partial\left(\phi^\alpha\rho^{0,\alpha}\Psi^\alpha + \phi^\beta\rho^{0,\beta}\Psi^\beta\right)}{\partial t} \right.
$$
$$
\left. + v_i \left(\frac{\partial P_{ij}}{\partial X_j} + \left(\phi^\alpha\rho^{0,\alpha} + \phi^\beta\rho^{0,\beta}\right)\left(b_i^0 - \dot{v}_i\right) \right) \right\} \mathrm{d}V, \tag{3.35}
$$

where for arbitrary velocities v_i the linear momentum balance for diffuse interface regions is found

$$
\frac{\partial P_{ij}}{\partial X_j} + \left(\phi^\alpha\rho^{0,\alpha} + \phi^\beta\rho^{0,\beta}\right)\left(b_i^0 - \dot{v}_i\right) = 0. \tag{3.36}
$$

Applying the time derivative in Equation (3.35) gives further insights:

$$
\int_V \left\{ P_{ij}\dot{F}_{ij} - \phi^\alpha\rho^{0,\alpha}\frac{\partial\Psi^\alpha}{\partial F_{ij}^\alpha}\dot{F}_{ij}^\alpha - \phi^\beta\rho^{0,\beta}\frac{\partial\Psi^\beta}{\partial F_{ij}^\beta}\dot{F}_{ij}^\beta - \phi^\alpha\rho^{0,\alpha}\frac{\partial\Psi^\alpha}{\partial Y_{ij}^\alpha}\dot{Y}_{ij}^\alpha \right.
$$
$$
\left. - \phi^\beta\rho^{0,\beta}\frac{\partial\Psi^\beta}{\partial Y_{ij}^\beta}\dot{Y}_{ij}^\beta - \dot{\phi}^\alpha\rho^{0,\alpha}\Psi^\alpha - \dot{\phi}^\beta\rho^{0,\beta}\Psi^\beta \right\} \mathrm{d}V. \tag{3.37}
$$

For the 1$^{\text{st}}$ Piola-Kirchhoff stress tensor, the thermodynamic relation to the Helmholtz free energy reads as follows, in the style of the sharp interface results:

$$
P_{ij}\dot{F}_{ij} - \phi^\alpha\rho^{0,\alpha}\frac{\partial\Psi^\alpha}{\partial F_{ij}^\alpha}\dot{F}_{ij}^\alpha - \phi^\beta\rho^{0,\beta}\frac{\partial\Psi^\beta}{\partial F_{ij}^\beta}\cdot\dot{F}_{ij}^\beta = 0, \tag{3.38}
$$

which has to be evaluated for bulk regions and for the diffuse interface region as described in Appendix A. For bulk regions, Equation (A.4) applies

$$
\begin{aligned}
\alpha\text{-region: } P_{ij} &= \rho^{0,\alpha} \frac{\partial \Psi^{\alpha}}{\partial F_{ij}^{\alpha}} = P_{ij}^{\alpha}, \\[2mm]
\beta\text{-region: } P_{ij} &= \rho^{0,\beta} \frac{\partial \Psi^{\beta}}{\partial F_{ij}^{\beta}} = P_{ij}^{\beta},
\end{aligned}
\tag{3.39}
$$

and for interfacial regions under consideration of Hadamard's compatibility condition and the linear momentum balance on singular surfaces

$$
F_{ij} = \phi^{\alpha} F_{ij}^{\alpha} + \phi^{\beta} F_{ij}^{\beta}, \tag{3.40}
$$

$$
P_{ij} = \phi^{\alpha} P_{ij}^{\alpha} + \phi^{\beta} P_{ij}^{\beta}, \tag{3.41}
$$

as stated in Equation (A.7). For arbitrary changes of phase values in bulk regions there is an additional term, which reads

$$
-\dot{\phi}^{\alpha} \rho^{0,\alpha} \Psi^{\alpha} - \dot{\phi}^{\beta} \rho^{0,\beta} \Psi^{\beta} \geq 0. \tag{3.42}
$$

Using $\dot{\phi}^{\beta} = -\dot{\phi}^{\alpha}$, this term can be rearranged to

$$
-\dot{\phi}^{\alpha} \left(\rho^{0,\alpha} \Psi^{\alpha} - \rho^{0,\beta} \Psi^{\beta} \right) = -\dot{\phi}^{\alpha} [\![\rho^{0} \Psi]\!]^{\alpha\beta} \geq 0. \tag{3.43}
$$

It may be interpreted as an energy dissipating or consuming term depending on phase transitions:

- for an increase of phase α ($\dot{\phi}^{\alpha} > 0$): $\Psi^{\alpha} - \Psi^{\beta} < 0$

- for a decrease of phase α ($\dot{\phi}^{\alpha} < 0$): $\Psi^{\alpha} - \Psi^{\beta} > 0$.

The final inequality also contains the dissipation terms due to the internal variables Y^α:

$$-\phi^\alpha \rho^{0,\alpha} \frac{\partial \Psi^\alpha}{\partial Y_{ij}^\alpha} \dot{Y}_{ij}^\alpha - \phi^\beta \rho^{0,\beta} \frac{\partial \Psi^\beta}{\partial Y_{ij}^\beta} \dot{Y}_{ij}^\beta - \dot{\phi}^\alpha [\![\rho^0 \Psi]\!]^{\alpha\beta} \geq 0. \qquad (3.44)$$

On the stress calculation in diffuse interface regions   The findings on the thermodynamic relation for the stress and deformation tensor enables an accurate stress calculation capturing the mechanical jump conditions by obeying the following points:

1. Hadamard's compatibility condition: $[\![F_{ij}]\!]^{\alpha\beta} = a_i N_j^{\alpha\beta}$

2. linear momentum balance on singular surfaces: $[\![P_{ij}]\!]^{\alpha\beta} N_j^{\alpha\beta} = 0$

3. deformation gradient: $F_{ij} = \phi^\alpha F_{ij}^\alpha + \phi^\beta F_{ij}^\beta$ or generally $F_{ij} = \sum_\alpha \phi^\alpha F_{ij}^\alpha$

4. 1st Piola-Kirchhoff stress: $P_{ij} = \phi^\alpha P_{ij}^\alpha + \phi^\beta P_{ij}^\beta$ or generally $P_{ij} = \sum_\alpha \phi^\alpha P_{ij}^\alpha$

In the infinitesimal deformation context and for two phases Schneider *et al.* showed in their work [159] that using the above conditions lead to a homogenised stiffness matrix, which accounts for the mechanical jump conditions. Condition 3 leads to a Reuss/Sachs homogenisation in the normal direction and condition 4 describes a Voigt/Taylor homogenisation in the tangential directions. A generalisation to multiple phases by the same group can be found in [156, 157]. This procedure cannot be applied to finite deformations.
For finite deformation Mosler *et al.* [125] suggested a possibility named *partial rank-one convexification* to solve the jump conditions, which is restricted to two phases. A continuative work on this topic is provided by Bartels and Mosler [12]. In a more recent paper Schneider *et al.* [158] introduce a stress calculation based on the mechanical jump conditions for finite deformation and multiple phases. Here, the ansatz is not to gain a homogenised stiffness matrix which obeys the jump conditions but to solve for them implicitly. Therefore a

system of equations, which is constructed by conditions 1-3, has to be solved by a Newton's algorithm. As a result they obtain the stress and deformation gradient tensors P_{ij}^{α} and F_{ij}^{α} for every locally existing phase. Using condition 4 they are able to assemble the homogenised stress tensor. This method can also be linearised to be used for infinitesimal deformations or for physical non-linearities as shown in Herrmann *et al.* [78].

Comparison to phase-field models from a energy functional Before closing this section, the derived phase-field model (denoted as PF-SI, phase-field from sharp interface) is compared to a well-established formulation [82, 129] (denoted as PF-EF, phase-field from energy functional), which is as commonly derived from a free energy functional. For comparison and simplicity, the formulations are only given for a binary interface $S^{\alpha\beta}$ and in their evolutional form, using an Allen-Cahn ansatz. For infinitesimal deformations and by applying the same notation, the two models are written as

$$\text{PF-SI: } \left(M^{-1}\right)^{\alpha\beta} \dot{\phi}^{\alpha} = -\gamma^{0,\alpha\beta} \left(\phi_{,ii}^{\alpha} - \frac{16}{\epsilon^2 \pi^2} \frac{\left(1 - 2\phi^{\alpha}\right)}{2} \right) + \delta^{\epsilon} \left(\phi^{\alpha} \right) \Delta^{\alpha\beta}, \quad (3.45)$$

$$\text{PF-EF: } \left(M^{-1}\right)^{\alpha\beta} \dot{\phi}^{\alpha} = -\gamma^{0,\alpha\beta} \left(\phi_{,ii}^{\alpha} - \frac{16}{\epsilon^2 \pi^2} \frac{\left(1 - 2\phi^{\alpha}\right)}{2} \right) + \frac{1}{\epsilon} \frac{\partial h^{\alpha}}{\partial \phi^{\alpha}} \Delta^{\alpha\beta} \quad (3.46)$$

where M is a proportionality constant describing the mobility of a phase boundary α-β. In $\Delta^{\alpha\beta}$ all energies acting on the interface α-β are collected, and weighted by a ϕ^{α}-dependent pre-factor. This weighting function is the only difference between both formulations, if there are no finite deformations present. The factor $1/\epsilon$ of model PF-EF is already an integral part of the distribution function δ^{ϵ}, hence the difference lays in the formulation of h^{α} in comparison to the remaining part of δ^{ϵ}. For the model of this work and for two common h^{α} functions, their mathematical formulation is listed in Table 3.2. The difference of the distribution functions is shown in Figure 3.3b. While the formulation using $\sqrt{\phi_{,i}^{\alpha}\phi_{,i}^{\alpha}}$ is directly related to the chosen sine profile, the commonly

PFM	Interpolation	Distribution
PF-SI	ϕ^α	$\sqrt{\phi_{,i}^\alpha \phi_{,i}^\alpha} = \frac{4}{\epsilon\pi}\sqrt{\phi^\alpha\left(1 - \phi^\alpha\right)}$
PF-EF, h_0	ϕ^α	1
PF-EF, h_1	$\left(\phi^\alpha\right)^2\left(3 - 2\phi^\alpha\right)$	$6\left(\left(\phi^\alpha\right)^2 - \phi^\alpha\right)$

Table 3.2: Compared PF models and their differences in interpolation and distribution functions.

used h^α functions are approximations to the derivative of the profile function. Especially when high energies are acting on the diffuse interface, the h^α functions may fail to preserve the profile and therefore physical quantities may deviate from their sharp interface counterparts. This behaviour is qualitatively shown in Section 3.3.3 for the profile used in the phase-field fracture model. Also other authors, cf. [172] and [48], already use this square-root shaped weighting function. The motivation in [172] is for example the disturbance of the travelling wave solution, if the factor is not used. A straightforward derivation, however, is given by neither of the authors.

A second difference of the two models is the occurrence of deformation gradients in the calculation of the curvature term, cf. Equation (3.26), if a Lagrangian description is used. Furthermore, in the Eulerian description deformation induced modifications arise, mainly connected to the definition of the constant interfacial energy $\gamma^{0,\alpha\beta} = J\gamma^{\alpha\beta}$. To the author's knowledge, these thermodynamic necessities are not considered in any phase-field models presently published.

It may be summarised that the phase-field model from sharp interface thermodynamics has the advantage that the approximation by an order parameter field happens in a very late stage, when all balances and relations are fully derived in the sense of a sharp interface. Therefore it is assumed that approximation errors have very little influence on the evolution equations found. When using the diffuse free energy functional, the approximation basically already appears in the very first step by expressing the interfacial surface integral by a

gradient and a potential term. The variation of this functional happens already under the premises of approximation errors, which show in the distribution or weighting function. For the phase-field model from an energy functional this function has to be assumed, for the sharp interface model the correct distribution functions drops out of the regularisation. A further facet is, that a variation always builds upon a set of assumptions which has to list explicitly all aspects to be taken care of. If these assumptions are incomplete, the picture may stay incomplete, whereas the time derivatives of the integral entropy inequality usually show a complete picture, when no (restricting) assumptions are made. Hence, the latter kind of derivation uses assumptions just to restrict the complexity of the resulting equations and balances.

3.1.6 Driving force behaviour

In this section, the described models are analysed in a set of interface driving one-dimensional simulations. The interface movement is realised by an Allen-Cahn ansatz, as described by Equation (3.45), which relaxes the phase-field order parameter ϕ^α. Throughout this section, the following two different phase-field models are used:

- *PF-SI*: The previously derived model from sharp-interface thermodynamics

- *PF-EF*: A classic phase-field model derived from an free energy functional, e.g. Nestler *et al.* [82, 129]

The first simulation is borrowed from Eiken *et al.* [48], where a constant driving force is applied to different phase-field models. The second simulation compares mechanically-driven phase-field models.

Constant driving force   Other than in [48], this example does not compare phase-field models with and without interface correction, but compares the phase-field model derived from sharp interface continuum mechanics with

the phase-field model derived from a free energy functional. The simulation parameters are taken from the cited publication and are a constant driving force $\Delta^{\alpha\beta} = 0.0001\,\text{J/mm}^3$ and a constant mobility $M^{\alpha\beta} = 10\,\text{mm}^4/\text{Js}$. The time step width is chosen to be $\Delta t = 16/9\,\text{s}$. This yields an analytical interface velocity of $v^{\text{ana}} = 0.001\,\text{mm/s}$, which remains constant, as during the simulation no phase equilibrium is reached. The simulation study investigates different spatial discretisations Δx while keeping the interface parameter at $\epsilon = 0.5\,\text{mm} = \text{const.}$ Figure 3.3 shows that all models need approximately ten interface cells to

(a) Interface velocity

(b) Shape of distribution functions
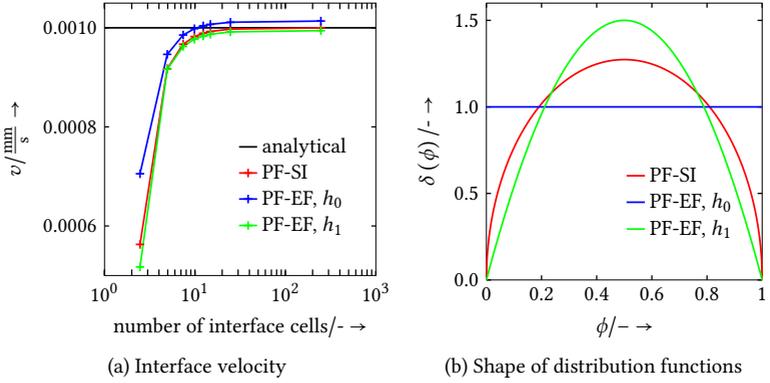
Figure 3.3: Comparison of interface velocities of different phase-field models over used interface points. The represented physical interface width remains constant.

have an error less than five percent. However, with an increasing number of interface cells only the model derived from sharp interface mechanics captures the behaviour of the analytical solution.

Constant and mechanical driving force   In this comparison, one of the phases has assigned an additional eigenstrain. Compared to the previous study this leads to a driving force moving the interface to an equilibrium. The simulation parameters are constant mobility $M^{\alpha\beta} = 10\,\text{mm}^4/\text{Js}$, constant eigenstrain $\tilde{\varepsilon} = -0.107$ and time step width $\Delta t = 0.85\,\text{s}$. The constant driving

(a) Interface position

(b) Error in interface position
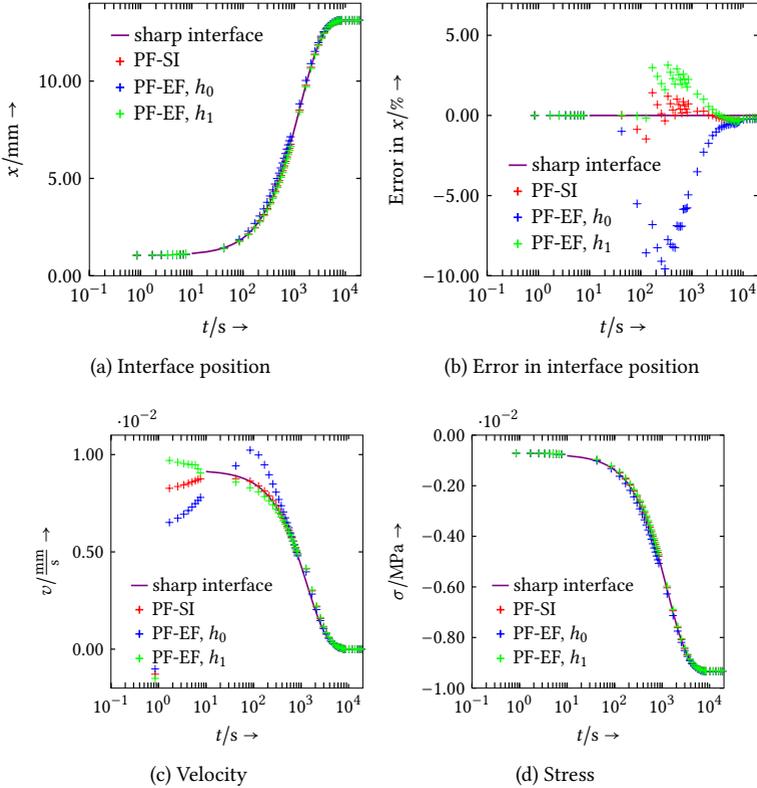
(c) Velocity

(d) Stress

Figure 3.4: Simulation with a constant and a mechanical driving force for different phase-field models. (a) showing the interface position, (b) its error, (c) the interface velocity and (d) the stress.

force $\Delta^{\alpha\beta} = 0.0001\,\text{J/mm}^3$ is balanced by an evolving mechanical driving force as shown in Equation 3.34, but without the kinetic energy and in the infinitesimal strain regime and hence of the form $[\![\rho^0\,\Psi]\!]^{\alpha\beta} - [\![u_{i,j}]\!]^{\alpha\beta}N_j^{\alpha\beta}\langle\sigma_{ij}\rangle^{\alpha\beta}N_j^{\alpha\beta}$. This yields an equilibrium stress of $\sigma \approx -9.346 \cdot 10^{-3}\,\text{MPa}$. In the following, the interface position and its error are investigated. Furthermore the evolution of the stress and the interface velocity are depicted. The results in Figure 3.4

show as well that the sharp interface based model keeps the closest to the analytical sharp interface solution. In Figures 3.4a and 3.4b this model has the least error. The same is observed for the velocity and the stress.

3.2 A curing process model based on the phase-field method

For the derivation of the thermodynamic framework for curing simulations in FRTS, the basic results of the previous section are used. The main difference is the neglect of the interface energy balance, as the curing process does not involve any phase change and hence no interface movement is present. The advantage of still using a phase-field as an underlying framework lies in its ability to describe complex structures and geometries without the need for meshing due to the order parameter description [107]. Furthermore it is assumed that the part of the curing process considered starts after the material filled the mould and therefore is at rest. With regard to moderate thermal and chemical shrinkage strains in thermosets, this implies the use of the infinitesimal deformation theory. Because the Lagrangian configuration coincides with the Eulerian configuration in this regime, the Eulerian description is used for all further modelling. In the sense of thermodynamic arguments and reasoning this section mainly follows the work of Lion and Höfer [108], Adolf and Chambers [1], Klinge *et al.* [92] and Mahnken [110].

3.2.1 Dissipation potential

In a first step the entropy balance (cf. Equation (2.54)) is developed with the help of a set of assumptions. The model shall follow

- the usage of two materials: a thermo-visco-elastic thermoset phase α, which exhibits curing, and a thermo-elastic fibre phase β, both independent of temperature gradient $\Theta_{,i}$,

- the infinitesimal deformation theory (see Section 2.1.3.1),

- the volumetric average of the Helmholtz free energy, $\rho\Psi = \sum_\alpha \phi^\alpha \rho^\alpha \Psi^\alpha$,

- the superposition of Helmholtz free energies to describe visco-elasticity within a phase α, $\Psi^\alpha\left(\ldots, \varepsilon_{ij}^{\alpha,\mathrm{v},p}\right) = \Psi^{\alpha,0}\left(\ldots\right) + \sum_p \Psi^{\alpha,p}\left(\ldots, \varepsilon_{ij}^{\alpha,\mathrm{v},p}\right)$, in the sense of a Generalised Maxwell Model (cf. Section 2.1.3.3),

- the assumption of constant mass densities ρ^α and immoveable interfaces due to no phase changes being present, hence volume fractions ϕ^α are constant,

- the curing reaction is exothermic and irreversible, hence the rate of the degree of cure is $\dot\zeta^\alpha \geq 0$ and the total reaction enthalpy $h^{\mathrm{tot}} \leq 0$.

Using the localised form of the entropy balance, re-formulation due to the non-negative entropy production and applying the Legendre transformation of the Helmholtz free energy $\Psi = e - \Theta\eta$ gives

$$\sigma_{ij}\dot\varepsilon_{ij} - \left(\phi^\alpha \rho^\alpha \dot\Psi^\alpha + \phi^\beta \rho^\beta \dot\Psi^\beta\right) - \rho\eta\dot\Theta - \frac{q_i \Theta_{,i}}{\Theta} \geq 0 \qquad (3.47)$$

as a form of the Clausius-Duhem inequality. Here σ_{ij} denotes the Cauchy stress tensor, ε_{ij} is the infinitesimal strain tensor, η is the entropy, Θ is the absolute temperature and q_i is the heat flux vector. In accordance with the previous statement on the nature of the two phases, the Helmholtz free energy of the thermoset is defined as $\Psi^\alpha = \Psi^\alpha\left(\varepsilon_{ij}^\alpha, \Theta, \varepsilon_{ij}^{\alpha,\mathrm{v},p}, \zeta^\alpha\right)$ whereas the fibre has $\Psi^\beta = \Psi^\beta\left(\varepsilon_{ij}^\beta, \Theta\right)$. The thermoset phase differs from the fibre phase by p viscous strains $\varepsilon_{ij}^{\alpha,\mathrm{v},p}$, where the superscripted p runs in the sense of a Generalised Maxwell Model from 1 to N, cf. Figure 2.5. The internal variable ζ^α is a

measure for the local degree of cure and therefore is also only valid in the thermoset phase. Expanding and collecting all terms gives

$$
\begin{aligned}
&\left\{ \sigma_{ij}\dot{\varepsilon}_{ij} - \phi^\alpha \rho^\alpha \frac{\partial \Psi^\alpha}{\partial \varepsilon_{ij}^\alpha} \dot{\varepsilon}_{ij}^\alpha - \phi^\beta \rho^\beta \frac{\partial \Psi^\beta}{\partial \varepsilon_{ij}^\beta} \dot{\varepsilon}_{ij}^\beta \right\} \\
&- \left\{ \rho\eta + \phi^\alpha \rho^\alpha \frac{\partial \Psi^\alpha}{\partial \Theta} + \phi^\beta \rho^\beta \frac{\partial \Psi^\beta}{\partial \Theta} \right\} \dot{\Theta} \\
&- \phi^\alpha \rho^\alpha \left\{ \frac{\partial \Psi^\alpha}{\partial \varepsilon_{ij}^{\alpha,\mathrm{v,p}}} \dot{\varepsilon}_{ij}^{\alpha,\mathrm{v,p}} + \frac{\partial \Psi^\alpha}{\partial \zeta^\alpha} \dot{\zeta}^\alpha \right\} \\
&- \frac{q_i \Theta_{,i}}{\Theta} \geq 0,
\end{aligned}
\tag{3.48}
$$

which allows for a reasonable interpretation of the variables involved in the following sections.

3.2.2 Heat conduction model

Before establishing a model for heat conduction and temperature evolution, the entropy and heat conduction terms of the dissipation inequality (3.48)

$$
- \left\{ \rho\eta + \phi^\alpha \rho^\alpha \frac{\partial \Psi^\alpha}{\partial \Theta} + \phi^\beta \rho^\beta \frac{\partial \Psi^\beta}{\partial \Theta} \right\} \dot{\Theta} - \frac{q_i \Theta_{,i}}{\Theta} \geq 0,
\tag{3.49}
$$

have to be evaluated. The first term, when allowing arbitrary absolute temperature rates $\dot{\Theta}$, defines the thermodynamic relation between entropy η and the Helmholtz free energy Ψ. For bulk regions they relate via

$$
\begin{aligned}
\alpha\text{-region: } \rho\eta &= -\rho^\alpha \frac{\partial \Psi^\alpha}{\partial \Theta} = \rho^\alpha \eta^\alpha, \\
\beta\text{-region: } \rho\eta &= -\rho^\beta \frac{\partial \Psi^\beta}{\partial \Theta} = \rho^\beta \eta^\beta,
\end{aligned}
\tag{3.50}
$$

and in interfacial regions the volumetric average

$$\rho\eta = \phi^\alpha \rho^\alpha \eta^\alpha + \phi^\beta \rho^\beta \eta^\beta \qquad (3.51)$$

is established. Under the strict assumption that each term separately has to fulfil non-negativity, the second term of Equation (3.49) is called the heat conduction inequality and allows for conclusions about the relation of temperature gradient $\Theta_{,i}$ and heat flux q_i. To fulfil the entropy inequality, the heat flux has to be proportional to the negative temperature gradient, which is obeyed by *Fourier's law* [55]

$$q_i = -\kappa_{ij}\Theta_{,j}, \qquad (3.52)$$

where κ_{ij} is the thermal conductivity tensor, which has to be positive semi-definite. As described in Appendix A the heat conduction inequality can be used to make statements about the heat flux and the temperature gradient in bulk regions:

$$\begin{aligned} \phi^\alpha = 1 \text{ and } \phi^\beta = 0: \quad & \Theta_{,i} = \Theta_{,i}^\alpha, \quad q_i = q_i^\alpha, \\ \phi^\alpha = 0 \text{ and } \phi^\beta = 1: \quad & \Theta_{,i} = \Theta_{,i}^\beta, \quad q_i = q_i^\beta. \end{aligned} \qquad (3.53)$$

Interfacial regions are evaluated with the help of thermal jump conditions, namely continuous heat flux in the interface normal direction, $[\![q_i]\!]^{\alpha\beta} n_i^{\alpha\beta} = 0$, and continuous temperature gradient in the interface tangential direction, $[\![\Theta_{,i}]\!]^{\alpha\beta} t_i^{\alpha\beta} = 0$. This implies the volumetric averages

$$\Theta_{,i} = \phi^\alpha \Theta_{,i}^\alpha + \phi^\beta \Theta_{,i}^\beta, \qquad (3.54)$$

$$q_i = \phi^\alpha q_i^\alpha + \phi^\beta q_i^\beta. \qquad (3.55)$$

The balance of internal energy (cf. Section 2.1.2.3) in localised form is

$$\rho\dot{e} = -q_{i,i} + \rho r + \sigma_{ij}\varepsilon_{ij}, \qquad (3.56)$$

where e is the internal energy and r is a volumetric heat source. Using the time derivative of the Legendre transformation of the Helmholtz free energy

$$\dot{\Psi} = \dot{e} - \dot{\eta}\Theta - \eta\dot{\Theta} \tag{3.57}$$

and evaluating the dependences yields

$$
\begin{aligned}
\rho\left\{\dot{\Psi} + \dot{\eta}\Theta + \eta\dot{\Theta}\right\} &= -q_{i,i} + \rho r + \sigma_{ij}\varepsilon_{ij} \\
\left\{\phi^\alpha \rho^\alpha \dot{\eta}^\alpha + \phi^\beta \rho^\beta \dot{\eta}^\beta\right\}\Theta &= \left\{\sigma_{ij}\dot{\varepsilon}_{ij} - \phi^\alpha \rho^\alpha \frac{\partial \Psi^\alpha}{\partial \varepsilon_{ij}^\alpha}\dot{\varepsilon}_{ij}^\alpha - \phi^\beta \rho^\beta \frac{\partial \Psi^\beta}{\partial \varepsilon_{ij}^\beta}\dot{\varepsilon}_{ij}^\beta\right\} \\
&\quad - \left\{\rho\eta + \phi^\alpha \rho^\alpha \frac{\partial \Psi^\alpha}{\partial \Theta} + \phi^\beta \rho^\beta \frac{\partial \Psi^\beta}{\partial \Theta}\right\}\dot{\Theta} \\
&\quad - q_{i,i} + \rho r - \phi^\alpha \rho^\alpha \left\{\frac{\partial \Psi^\alpha}{\partial \varepsilon_{ij}^{\alpha,\mathrm{v},p}}\dot{\varepsilon}_{ij}^{\alpha,\mathrm{v},p} + \frac{\partial \Psi^\alpha}{\partial \zeta^\alpha}\dot{\zeta}^\alpha\right\}.
\end{aligned}
\tag{3.58}
$$

Plugging in the thermodynamic relations, and further evaluating the left-hand-side, gives

$$
\begin{aligned}
&-\phi^\alpha \rho^\alpha \Theta\left\{\frac{\partial^2 \Psi^\alpha}{\partial \Theta \partial \varepsilon_{ij}^\alpha}\dot{\varepsilon}_{ij}^\alpha + \frac{\partial^2 \Psi^\alpha}{\partial \Theta \partial \Theta}\dot{\Theta} + \frac{\partial^2 \Psi^\alpha}{\partial \Theta \partial \varepsilon_{ij}^{\alpha,\mathrm{v},p}}\dot{\varepsilon}_{ij}^{\alpha,\mathrm{v},p} + \frac{\partial^2 \Psi^\alpha}{\partial \Theta \partial \zeta^\alpha}\dot{\zeta}^\alpha\right\} \\
&-\phi^\beta \rho^\beta \Theta\left\{\frac{\partial^2 \Psi^\beta}{\partial \Theta \partial \varepsilon_{ij}^\beta}\dot{\varepsilon}_{ij}^\beta + \frac{\partial^2 \Psi^\beta}{\partial \Theta \partial \Theta}\dot{\Theta}\right\} \\
&= \rho r - q_{i,i} - \phi^\alpha \rho^\alpha \left\{\frac{\partial \Psi^\alpha}{\partial \varepsilon_{ij}^{\alpha,\mathrm{v},p}}\dot{\varepsilon}_{ij}^{\alpha,\mathrm{v},p} + \frac{\partial \Psi^\alpha}{\partial \zeta^\alpha}\dot{\zeta}^\alpha\right\}.
\end{aligned}
\tag{3.59}
$$

Terms of the form $-\Theta(\partial^2 \Psi^\alpha)/(\partial\Theta)^2$ are identified as the specific heat capacity at constant volume (or strain), c_V^α, and a rearrangement of the terms shows the temperature evolution equation

$$
\begin{aligned}
\left\{ \phi^\alpha \rho^\alpha c_V^\alpha + \phi^\beta \rho^\beta c_V^\beta \right\} \dot{\Theta} &= \rho r - q_{i,i} - \underbrace{\phi^\alpha \rho^\alpha \left\{ \frac{\partial \Psi^\alpha}{\partial \varepsilon_{ij}^{\alpha,v,p}} \dot{\varepsilon}_{ij}^{\alpha,v,p} + \frac{\partial \Psi^\alpha}{\partial \zeta^\alpha} \dot{\zeta}^\alpha \right\}}_{A} \\
&\quad + \underbrace{\Theta \left\{ \phi^\alpha \rho^\alpha \frac{\partial^2 \Psi^\alpha}{\partial\Theta \partial \varepsilon_{ij}^\alpha} \dot{\varepsilon}_{ij}^\alpha + \phi^\beta \rho^\beta \frac{\partial^2 \Psi^\beta}{\partial\Theta \partial \varepsilon_{ij}^\beta} \dot{\varepsilon}_{ij}^\beta \right\}}_{B} \\
&\quad + \underbrace{\phi^\alpha \rho^\alpha \Theta \left\{ \frac{\partial^2 \Psi^\alpha}{\partial\Theta \partial \varepsilon_{ij}^{\alpha,v,p}} \dot{\varepsilon}_{ij}^{\alpha,v,p} + \frac{\partial^2 \Psi^\alpha}{\partial\Theta \partial \zeta^\alpha} \dot{\zeta}^\alpha \right\}}_{C},
\end{aligned}
\tag{3.60}
$$

where terms A are dissipation terms due to viscous and curing effects. Term B is the volumetric average of the thermo-mechanical coupling and terms C indicate further couplings involving viscosity and curing only present in the thermoset phase.

3.2.3 Continuum mechanics and visco-elasticity model

To specify the solid mechanics model, the relation between the Cauchy stress σ_{ij} and the Helmholtz free energy Ψ is examined with thermodynamic reasoning in the bulk and interfacial regions. For phase α, the thermoset phase, a second term representing viscous dissipation has to be brought into agreement with the entropy inequality. The terms of interest are given as

$$
\left\{ \sigma_{ij} \dot{\varepsilon}_{ij} - \phi^\alpha \rho^\alpha \frac{\partial \Psi^\alpha}{\partial \varepsilon_{ij}^\alpha} \dot{\varepsilon}_{ij}^\alpha - \phi^\beta \rho^\beta \frac{\partial \Psi^\beta}{\partial \varepsilon_{ij}^\beta} \dot{\varepsilon}_{ij}^\beta \right\} - \phi^\alpha \rho^\alpha \frac{\partial \Psi^\alpha}{\partial \varepsilon_{ij}^{\alpha,v,p}} \dot{\varepsilon}_{ij}^{\alpha,v,p} \geq 0.
\tag{3.61}
$$

The first term, giving information on stress and strain usage in the bulk and interfacial regions, is evaluated as previously done for Equations (3.38) and (3.49). Details are given in Appendix A. In bulk phases the total Cauchy stress σ_{ij} coincides with the phase-inherent stress σ_{ij}^{α}, cf. Equation (A.10),

$$
\begin{aligned}
\alpha\text{-region: } \sigma_{ij} &= \rho^{\alpha} \frac{\partial \Psi^{\alpha}}{\partial \varepsilon_{ij}^{\alpha}} = \sigma_{ij}^{\alpha}, \\
\beta\text{-region: } \sigma_{ij} &= \rho^{\beta} \frac{\partial \Psi^{\beta}}{\partial \varepsilon_{ij}^{\beta}} = \sigma_{ij}^{\beta},
\end{aligned}
\tag{3.62}
$$

and for interfacial regions, with respect to volume fractions and under application of the mechanical jump conditions, the total strain ε_{ij} consists proportionally of the phase-inherent strains $\varepsilon_{ij}^{\alpha}$ and ε_{ij}^{β},

$$
\varepsilon_{ij} = \phi^{\alpha} \varepsilon_{ij}^{\alpha} + \phi^{\beta} \varepsilon_{ij}^{\beta}, \tag{3.63}
$$

$$
\sigma_{ij} = \phi^{\alpha} \sigma_{ij}^{\alpha} + \phi^{\beta} \sigma_{ij}^{\beta}, \tag{3.64}
$$

and like-wise the total Cauchy stress is a volume average of the phase-inherent Cauchy stresses. The dissipative term involving viscous strains is reformulated by means of a thermodynamic conjugate force [71, 188] governed by a dissipation potential Ω

$$
-\rho^{\alpha} \frac{\partial \Psi^{\alpha}}{\partial \varepsilon_{ij}^{\alpha,\mathrm{v},p}} = \rho^{\alpha} \frac{\partial \Omega^{\alpha}}{\partial \dot{\varepsilon}_{ij}^{\alpha,\mathrm{v},p}} = V_{ijkl}^{\alpha,p} \dot{\varepsilon}_{kl}^{\alpha,\mathrm{v},p} = \sigma_{ij}^{\alpha,\mathrm{v},p} \tag{3.65}
$$

describing the damping effects of each Maxwell branch of the Generalised Maxwell Model, see Section 2.1.3.3. Here $V_{ijkl}^{\alpha,\mathrm{v},p}$ describes a general viscosity tensor and relates the viscous stress $\sigma_{ij}^{\alpha,\mathrm{v},p}$ to the viscous strain rate $\dot{\varepsilon}_{ij}^{\alpha,\mathrm{v},p}$. This yields for the remaining mechanical dissipation terms

$$
\mathcal{D}^{\mathrm{v},p} = -\phi^{\alpha} \rho^{\alpha} \frac{\partial \Psi^{\alpha}}{\partial \varepsilon_{ij}^{\alpha,\mathrm{v},p}} \dot{\varepsilon}_{ij}^{\alpha,\mathrm{v},p} = \phi^{\alpha} \dot{\varepsilon}_{ij}^{\alpha,\mathrm{v},p} V_{ijkl}^{\alpha,p} \dot{\varepsilon}_{kl}^{\alpha,\mathrm{v},p} \geq 0, \tag{3.66}
$$

which is fulfilled with $V_{ijkl}^{\alpha,\mathrm{v},p}$ being positive semi-definite. By using Equation (3.65) it is possible to retrieve the evolution equation for the viscous strains of each phase and Maxwell branch, $\varepsilon_{ij}^{\alpha,\mathrm{v},p}$,

$$\dot{\varepsilon}_{ij}^{\alpha,\mathrm{v},p} = -\rho^{\alpha} \left(V_{ijkl}^{\alpha,p} \right)^{-1} \frac{\partial \Psi^{\alpha}}{\partial \varepsilon_{kl}^{\alpha,\mathrm{v},p}}, \tag{3.67}$$

which was previously derived in Section 2.1.3.3 from the rheological model of the Generalised Maxwell Model.

3.2.4 Admissibility of phenomenological curing

The last term of Equation (3.48), which has to be interpreted, describes the curing reaction of thermoset phase α, characterised by the degree of cure ζ^{α},

$$\mathcal{D}^{\mathrm{cu}} = -\phi^{\alpha} \rho^{\alpha} \frac{\partial \Psi^{\alpha}}{\partial \zeta^{\alpha}} \dot{\zeta}^{\alpha} \geq 0. \tag{3.68}$$

As specified in Section 3.2.1, the rate of cure is non-negative due to the exothermic character of the curing reaction, and hence the remaining term

$$-\rho^{\alpha} \frac{\partial \Psi^{\alpha}}{\partial \zeta^{\alpha}} \geq 0 \tag{3.69}$$

has to be analysed. A possible ansatz for modelling the curing reaction is to use the change in enthalpy h, e.g. via the simple relation $h(t) = h^{\mathrm{tot}} \zeta(\zeta)$ introduced in Section 2.3.3 with h^{tot} being the total releasable reaction enthalpy. To make a connection between Helmholtz free energy and enthalpy their respective Legendre transformations are used, $\Psi = e - \Theta\eta$ and $h = e - 1/\rho \sigma_{ij}\varepsilon_{ij}$.

Re-writing Equation (3.69), by using the transformations and by inserting the thermodynamic relations for entropy and stress, leads to

$$-\rho^\alpha \frac{\partial\left(h^\alpha - \Theta\eta^\alpha + \sigma_{ij}^\alpha\varepsilon_{ij}^\alpha\right)}{\partial\zeta^\alpha} \geq 0$$

$$-\rho^\alpha \frac{\partial h^\alpha}{\partial\zeta^\alpha} - \rho^\alpha \frac{\partial^2\Psi^\alpha}{\partial\Theta\partial\zeta^\alpha}\Theta - \rho^\alpha \frac{\partial^2\Psi^\alpha}{\partial\varepsilon_{ij}^\alpha\partial\zeta^\alpha}\varepsilon_{ij}^\alpha \geq 0 \qquad (3.70)$$

$$-\rho^\alpha h^{\mathrm{tot},\alpha} - \rho^\alpha \frac{\partial^2\Psi^\alpha}{\partial\Theta\partial\zeta^\alpha}\Theta - \rho^\alpha \frac{\partial^2\Psi^\alpha}{\partial\varepsilon_{ij}^\alpha\partial\zeta^\alpha}\varepsilon_{ij}^\alpha \geq 0.$$

Due to the exothermic nature of the reaction, the first term is positive and constant. Hence, the two remaining terms have to be non-negative at least in combination. The second derivatives of the Helmholtz free energy will yield material parameters constant in their signedness. With the absolute temperature $\Theta \geq 0$ and the total strain ε_{ij}^α flexible in its sign, the inequality is capable of securing the admissibility of the thermodynamic process in at least a specific range of values. A further examination is possible when the material model is further specified by detailing the Helmholtz free energy.

3.2.5 Specification of the Helmholtz free energy and summary of relevant equations and balances

Both materials, thermoset and fibre, are modelled as a purely mechanical and quadratic Helmholtz energy

$$\Psi^{\alpha,p}\left(\varepsilon_{ij}^\alpha, \Theta, \varepsilon_{ij}^{\alpha,\mathrm{v},p}, \zeta^\alpha\right) \qquad (3.71)$$

expanded via a Taylor series around $\Psi^{0,\alpha,p}\left(\varepsilon_{ij}^{\mathrm{Ref},\alpha}, \Theta^{\mathrm{Ref}}, \varepsilon_{ij}^{\mathrm{Ref},\alpha,\mathrm{v},p}, \zeta^{\mathrm{Ref},\alpha}\right) = 0$. At the reference point $\varepsilon_{ij}^\alpha = \varepsilon_{ij}^{\mathrm{Ref},\alpha} = 0$, $\Theta = \Theta^{\mathrm{Ref}} \neq 0$, $\varepsilon_{ij}^{\alpha,\mathrm{v},p} = \varepsilon_{ij}^{\mathrm{Ref},\alpha,\mathrm{v},p} = 0$ and $\zeta^\alpha = \zeta^{\mathrm{Ref},\alpha} = 0$. Additionally, the reference configuration is stress-free, entropy-free, free from viscous stresses and no curing activity has occurred

yet. These specifications cancel all non-quadratic terms of the Taylor series expansion, and the remaining terms may be collected as

$$
\begin{aligned}
&\rho^\alpha \, \Psi^{\alpha,p} \left(\varepsilon_{ij}^\alpha, \Theta, \varepsilon_{ij}^{\alpha,\mathrm{v},p}, \zeta^\alpha \right) \\
&= \frac{1}{2} \left\{ \varepsilon_{ij}^\alpha - \frac{\partial \varepsilon_{ij}^{\mathrm{th},\alpha}}{\partial \Theta} \left(\Theta - \Theta^{\mathrm{Ref}} \right) - \varepsilon_{ij}^{\alpha,\mathrm{v},p} - \frac{\partial \varepsilon_{ij}^{\mathrm{cu},\alpha}}{\partial \zeta^\alpha} \zeta^\alpha \right\} \\
&\quad \rho^\alpha \frac{\partial^2 \Psi^{\alpha,p}}{\partial \varepsilon_{ij}^\alpha \partial \varepsilon_{kl}^\alpha} \left\{ \varepsilon_{kl}^\alpha - \frac{\partial \varepsilon_{kl}^{\mathrm{th},\alpha}}{\partial \Theta} \left(\Theta - \Theta^{\mathrm{Ref}} \right) - \varepsilon_{kl}^{\alpha,\mathrm{v},p} - \frac{\partial \varepsilon_{kl}^{\mathrm{cu},\alpha}}{\partial \zeta^\alpha} \zeta^\alpha \right\},
\end{aligned}
\tag{3.72}
$$

where also the additivity of strains $\varepsilon_{ij} = \varepsilon_{ij}^{\mathrm{el}} + \varepsilon_{ij}^{\mathrm{th}} + \varepsilon_{ij}^{\mathrm{v},p} + \varepsilon_{ij}^{\mathrm{cu}}$ is used. The following material parameters for a phase α are identified:

- $\rho^\alpha \frac{\partial^2 \Psi^{\alpha,p}}{\partial \varepsilon_{ij}^\alpha \partial \varepsilon_{kl}^\alpha} = C_{ijkl}^{\alpha,p}$, the positive semi-definite p-th stiffness tensor connecting stress and strain within one Maxwell branch,

- $\frac{\partial \varepsilon_{ij}^{\mathrm{th},\alpha}}{\partial \Theta} = \alpha_{ij}^\alpha$, the positive semi-definite thermal expansion tensor inducing thermal strains due to temperature changes and

- $\frac{\partial \varepsilon_{ij}^{\mathrm{cu},\alpha}}{\partial \zeta^\alpha} = \chi_{ij}^\alpha$, the negative semi-definite curing shrinkage tensor inducing curing strains due to an increasing degree of cure.

With these definitions, previously found relations and equations may be further specified. For the stress in thermoset phase α and fibre phase β

$$
\begin{aligned}
\alpha\text{-phase: } \sigma_{ij}^\alpha = \rho^\alpha \frac{\partial \Psi^\alpha}{\partial \varepsilon_{ij}^\alpha} &= C_{ijkl}^{\alpha,0} \left\{ \varepsilon_{kl}^\alpha - \alpha_{kl}^\alpha \left(\Theta - \Theta^{\mathrm{Ref}} \right) - \chi_{kl}^\alpha \zeta^\alpha \right\} \\
&\quad + \sum_i C_{ijkl}^{\alpha,p} \left\{ \varepsilon_{kl}^\alpha - \alpha_{kl}^\alpha \left(\Theta - \Theta^{\mathrm{Ref}} \right) \right. \\
&\qquad\qquad\qquad \left. - \chi_{kl}^\alpha \zeta^\alpha - \varepsilon_{kl}^{\alpha,\mathrm{v},p} \right\} \\
\beta\text{-phase: } \sigma_{ij}^\beta = \rho^\beta \frac{\partial \Psi^\beta}{\partial \varepsilon_{ij}^\beta} &= C_{ijkl}^\beta \left\{ \varepsilon_{kl}^\beta - \alpha_{kl}^\beta \left(\Theta - \Theta^{\mathrm{Ref}} \right) \right\},
\end{aligned}
\tag{3.73}
$$

where the thermoset phase has rheologically one elastic and p Maxwell branches. For each Maxwell branch an evolution equation for its viscous strain of the form

$$\dot{\varepsilon}_{ij}^{\alpha,\text{v},p} = \left(V_{ijkl}^{\alpha,p}\right)^{-1} C_{klmn}^{\alpha,p} \left\{\varepsilon_{mn}^{\alpha} - \alpha_{mn}^{\alpha}\left(\Theta - \Theta^{\text{Ref}}\right) - \chi_{mn}^{\alpha}\zeta^{\alpha} - \varepsilon_{mn}^{\alpha,\text{v},p}\right\} \quad (3.74)$$

is specified, which is deduced from Equation (3.67). Likewise only relevant for the thermoset phase is the curing reaction. Revising Equation (3.70) allows a more precise statement under which circumstances a curing reaction is admissible. Expressing the inequality in terms of material parameters and noting $C_{ijkl}^{\alpha} = C_{ijkl}^{\alpha,0} + \sum_p C_{ijkl}^{\alpha,p}$ gives

$$\left(\varepsilon_{ij}^{\alpha} - \alpha_{ij}^{\alpha}\Theta\right) C_{ijkl}^{\alpha}\chi_{kl}^{\alpha} - \rho^{\alpha}h^{\text{tot},\alpha} \geq 0. \quad (3.75)$$

With $\rho^{\alpha}h^{\text{tot},\alpha} \leq 0$ due to the exothermic character of the curing reaction and $C_{ijkl}^{\alpha}\chi_{kl}^{\alpha} \leq 0$ because of chemical shrinkage with a progressing reaction, the factor $\left(\varepsilon_{ij}^{\alpha} - \alpha_{ij}^{\alpha}\Theta\right)$ has to be negative for a strict conformance with the entropy inequality. This means that mainly compressive strains would be allowed, and stretching is only allowed up to a generally small amount of thermal effect $\alpha_{ij}^{\alpha}\Theta$. Loosening this strict interpretation, larger tensile strains are admissible as long as their effect is balanced by the constant value of $\rho^{\alpha}h^{\text{tot},\alpha}$, which allows for a moderate amount of tensile strains for material parameters being in the range of most thermosets [110]. To complete the models describing the curing process the state equations for the degree of cure ζ^{α} and for the glass transition temperature Θ^{g} are repeated from Section 2.3.3. For evolving the degree of cure the Kamal-Sourour model [87] is used,

$$\dot{\zeta}^{\alpha}\left(\zeta^{\alpha}, \Theta\right) = \left\{k_1 + k_2\zeta^{\alpha m}\right\}\left\{1 - \zeta^{\alpha n}\right\}, \quad (3.76)$$

which phenomenologically describes exothermic reactions on the basis of reaction kinetics $k_1\left(\Theta\right)$, $k_2\left(\Theta\right)$ and exponents m, n. This process gradually

stops as soon as the local temperature drops below the glass transition temperature Θ^g, which steadily increases with progressive curing. To check this stopping criterion, the development of Θ^g is phenomenologically predicted by the DiBenedetto model [41],

$$\frac{\Theta^g\left(\zeta^\alpha\right) - \Theta^{g,0}}{\Theta^{g,\infty} - \Theta^{g,0}} = \lambda \zeta^\alpha \left\{1 - \left(1 - \lambda\right)\zeta^\alpha\right\}^{-1}, \tag{3.77}$$

and as soon as $\Theta^g > \Theta$ a further evolution of the degree of cure ζ^α is prevented. For further details on these phenomenological models reference is made to the discussion of Equations (2.70) and (2.72) in Section 2.3.3. To complete the overall curing model the governing equations for temperature and mechanical equilibrium are noted. Applying the expression for the Helmholtz free energy, Equation (3.72), to the preliminary temperature equation (3.60) yields the form

$$\left\{\phi^\alpha \rho^\alpha c_V^\alpha + \phi^\beta \rho^\beta c_V^\beta\right\} \dot{\Theta} = \rho r - q_{i,i} - \phi^\alpha \left\{\mathcal{D}^{v,p} + \mathcal{D}^{cu}\right\}$$
$$- \Theta \left\{\phi^\alpha C_{ijkl}^\alpha \alpha_{kl}^\alpha \dot{\varepsilon}_{ij}^\alpha + \phi^\beta C_{ijkl}^\beta \alpha_{kl}^\beta \dot{\varepsilon}_{ij}^\beta\right\} \tag{3.78}$$
$$+ \Theta \phi^\alpha \left\{C_{ijkl}^{\alpha,p} \alpha_{kl}^\alpha \dot{\varepsilon}_{ij}^{\alpha,v,p} + C_{ijkl}^\alpha \alpha_{kl}^\alpha \chi_{ij}^\alpha \dot{\zeta}^\alpha\right\}.$$

For the mechanical equilibrium the static linear momentum balance in absence of body forces,

$$\sigma_{ij,j} = 0, \tag{3.79}$$

is used, where σ_{ij} is the volumetric average of the phase-inherent stresses as discussed in Section 3.2.3.

Notes on material properties The previous derivation of a phase-field-based curing model for FRTS introduces a set of material parameters (see Table 3.3), which are needed to describe the different parts of the model and their interplay. In general material parameters are dependent on variables such as temperature Θ or the degree of cure ζ^α and hence lead to additional

contributions to constitutive relations and balance equations (cf. [135]). For the desired temperature range of $\Theta < 473K$ (thermosets start to degenerate) the fibre properties can be assumed to be nearly constant due to a melting temperature $\Theta^{melt} > 1273K$ for glass fibres [26]. Therefore the material properties of (glass) fibres actually may be assumed to be constant in this temperature range. In contrast, thermosets and polymers in general are significantly dependent on the current temperature and degree of cure. Nevertheless these dependences are neglected for the derivation to keep the models as simple as possible, but they are considered when the models are applied to simulations to capture relevant parts of the thermoset behaviour. To further simplify and specify the material behaviour all material parameters are assumed to be isotropic.

Material Parameter	Thermoset	Fibre	Unit
mechanical			
Mass Density	ρ^{α}	ρ^{β}	kg/m³
Bulk Modulus	$K^{\alpha}(\zeta, \Theta)$	K^{β}	MPa
Shear Moduli	$G^{\alpha,p}(\zeta, \Theta)$	G^{β}	MPa
Viscosities	$\eta^{\alpha,p}(\zeta, \Theta)$	—	MPa·s
Thermal Expansion	$\alpha^{\alpha}(\zeta, \Theta)$	α^{β}	1/K
Reference Temperature	$\Theta^{\mathrm{Ref},\alpha}$	$\Theta^{\mathrm{Ref},\beta}$	K
Curing Shrinkage	χ^{α}	—	—
thermal			
Specific Heat Capacity	$c_V^{\alpha}(\zeta, \Theta)$	c_V^{β}	J/kgK
Thermal Conductivity	$\kappa^{\alpha}(\zeta, \Theta)$	κ^{β}	W/mK
exothermic reaction			
tot. Reaction Enthalpy	$h^{\mathrm{tot},\alpha}$	—	J/kg
Kamal-Sourour Paramters	$k^{i,0}, E^{i}, m, n$	—	1/s, J/mol, —
DiBenedetto Parameters	$\Theta^{g,\infty}, \Theta^{g,0}, \lambda$	—	K, —

Table 3.3: Curing model: Material properties needed to describe thermoset and fibre behaviour.

3.2.6 Behaviour of the individual models

Before applying the model for the curing process in Section 4.3, each part is tested on its general behaviour. A discussion on the quantitativeness of the jump conditions is forgone, as these kind of models already were thoroughly evaluated and validated in Mosler *et al.* [125], Bartels and Mosler [12] and Schneider *et al.* [157–159] for mechanical models. An evaluation for thermal models is presented by Ettrich *et al.* [51]. In general, all model evaluations are on the basis of infinitesimal deformations and the simulations use an equi-distant mesh.

Temperature equation: Heat flux and temperature gradient For the evaluation of the behaviour of the heat flux and the temperature gradient at an interface, a two-dimensional 200 mm × 200 mm domain with a grid spacing of $\Delta x = 1.0$ mm is set-up (see Figure 3.5a). Two phase, α and β, are filled such that their interface extends from the upper left to the lower right corner, and hence cuts the simulation domain under 45 degrees. For the boundary conditions the lower x-axis boundary has $\Theta = 300$ K and the upper x-axis boundary has $\Theta = 400$ K. The other two boundaries are isolated. The domain is solved for thermal quantities only, hence only the temperature equation (3.60) without any source, coupling or dissipation terms is solved. As the temporal evolution is not of interest, the reduced temperature equation reads

$$0 = -q_{i,i} = -\left(\phi^\alpha q_i^\alpha + \phi^\beta q_i^\beta \right)_{,i}, \tag{3.80}$$

where the heat fluxes depend on the thermal conductivities κ^α and the temperature gradient $\Theta_{,i}$. The two isotropic materials have $\kappa^\alpha = 0.19$ W/mK and $\kappa^\beta = 1.0$ W/mK, both independent of other quantities. The simulation is done two times: For the first simulation a simple Voigt homogenisation is used to average the thermal conductivities volumetrically, and hence calculate the heat flux via $q_i = -\left(\phi^\alpha \kappa_{ij}^\alpha + \phi^\beta \kappa_{ij}^\beta \right) \Theta_{,j}$. The second simulation uses the
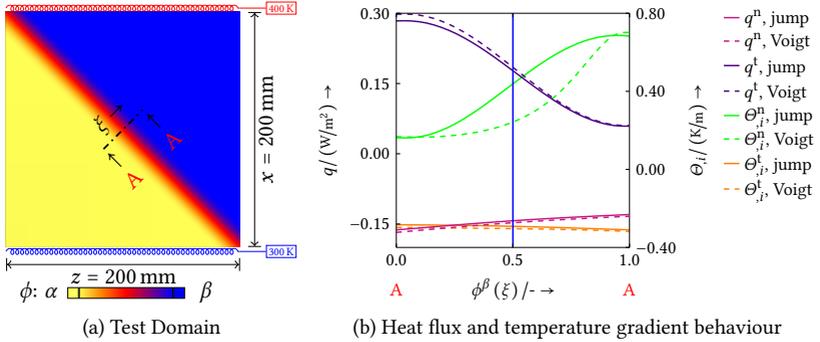
Figure 3.5: Heat flux and temperature gradient quantities across a diffuse interface: Comparison of a Voigt homogenisation and the implemented model based on jump conditions.

model incorporating thermal jump conditions at interfaces, $[\![q_i]\!]^{\alpha\beta} n_i^{\alpha\beta} = 0$ and $[\![\Theta_{,i}]\!]^{\alpha\beta} t_i^{\alpha\beta} = 0$, which is discussed in Section 3.2.2. For evaluation in Figure 3.5b the heat flux and the temperature gradient are plotted across the interfacical region in their normal and tangential components. While most components are almost identical, the temperature gradient along the interface normal direction, $\Theta_{,i}^n$, differs noticeably. For the Voigt homogenisation the discontinuity of $\Theta_{,i}^n$, which is smoothed in the diffuse interface setting, is clearly shifted towards the β phase. This contradicts the idea that the centre of the interfacial region is the position of the initial sharp interface, which implies that any (smoothed) discontinuity should have its turning point at this location. By solving the model building on the thermal jump conditions, this requirement is fulfilled.

Mechanics: Stress and strain   For the evaluation of the mechanical model the same simulation domain (see Figure 3.6a) is used as in the previous paragraph for the temperature equation evaluation. Analogously, a Voigt homogenisation ansatz for the elastic constants and the model presented in Section 3.2.3

based on mechanical jump conditions are compared. As only the linear static linear momentum balance (3.79),

$$\sigma_{ij,j} = 0, \tag{3.81}$$

and linear elasticity are evaluated, here the boundary conditions are a stress boundary condition of 10 MPa at the lower and upper x-axis and stress-free boundary conditions at the lower and upper z-axis. Again both phases are isotropic, and their independent material properties are the elastic moduli $E^\alpha = 79.0$ GPa, $E^\beta = 2.7$ GPa and the Poisson's ratios $\nu^\alpha = 0.17$, $\nu^\beta = 0.34$, respectively. Even more than for heat flux and temperature gradient, the

(a) Test Domain

(b) Stress and strain behaviour
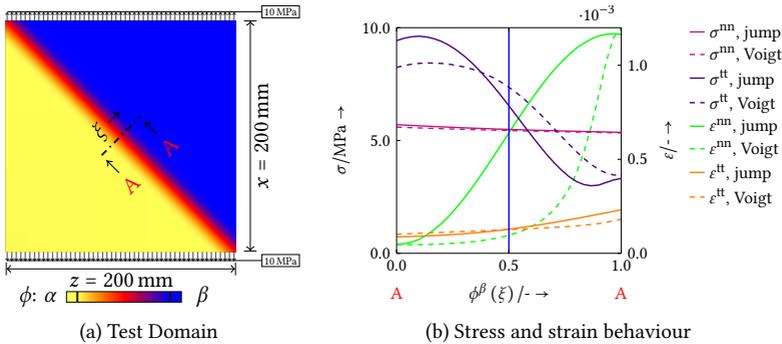
Figure 3.6: Stress and strain quantities across a diffuse interface: Comparison of a Voigt homogenisation and the implemented model based on jump conditions.

mechanical quantities plotted in Figure 3.6b differ. The stress component in the normal direction, σ^{nn}, and the strain component in the tangential direction, ε^{tt}, are nearly congruent but, as before, the discontinuous quantities, here σ^{tt} and ε^{nn}, exhibit a shift towards the β phase for the Voigt scheme. This may also be traced back to the lack of explicitly incorporating the mechanical jump condition in the diffuse interface region. Using the model building on the linear momentum balance at singular surfaces, $[\![\sigma_{ij}]\!]^{\alpha\beta} n_j^{\alpha\beta} = 0$, and

Hadamard's compatibility condition, $[\![u_{i,j}]\!]^{\alpha\beta} t_j^{\alpha\beta} = 0$, remedies this behaviour. Correspondingly, the smoothed discontinuities have their turning points at the centre of the interfacial region in accordance with the sharp interface theory.

Visco-elasticity: Bulk and interfacial regions   Due to the time dependence of the visco-elastic Generalised Maxwell Model, both bulk and interfacial, regions are tested. The simulation examples in the bulk regions are taken from Careglio *et al.* [30] and are performed for a single integration point. Again, material properties are independent of other physical quantities. For the tests a reduced Generalised Maxwell Model is used with only one Maxwell branch, a standard linear solid, as depicted in Figure 3.7a. The stiffness tensors C_{ijkl} and viscosity tensor V_{ijkl} are effectively the shear moduli μ and the viscosity η in this one-dimensional and isotropic setting, and are listed in Table 3.4. The

Test	μ^0/MPa	μ^1/MPa	η^1/MPa $\cdot$ s	Δt/s
Creep	10	10	10	0.1
Relaxation	4	10	$\{10, 50, 100\}$	0.01

Table 3.4: Material properties used in the bulk creep and relaxation tests.

creep test is done by applying a constant stress $\sigma = 100\,\text{MPa}$. For the relaxation tests the constant external load is $\varepsilon = 0.01$. For both the creep (Figure 3.7a) and the relaxation (Figure 3.7b) behaviour, the numeric results are in good agreement with the analytic solution. For the interfacial region the ansatz used is again the model based on mechanical jump conditions, which was evaluated in the previous paragraph. This formulation has the advantage of collecting and calculating quantities phase-inherently before applying volumetric averages (see Equation (3.62)). The incorporation of different mechanical behaviour is facilitated as the physical laws are freed from homogenisation schemes and the sharp interface models may be applied directly. In the case of visco-elasticity,

(a) Creep test   (b) Relaxation tests
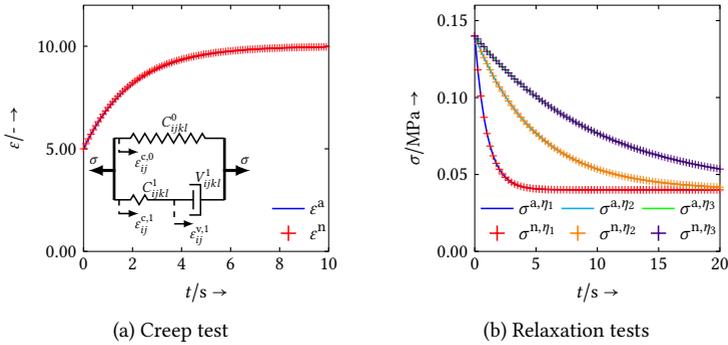
Figure 3.7: Behaviour of the visco-elastic implementation in a bulk phase: Creep and relaxation tests with a standard linear solid (General Maxwell Model with one Maxwell branch). Comparison of analytic and numeric solutions, superscripted by a and n, respectively.

the phase-inherent viscous strains from Equation (3.67) are directly used for the calculation of the phase-inherent Cauchy stresses σ^α. This approach was already thoroughly examined and evaluated for an elasto-plastic material behaviour by Herrmann *et al.* [78].
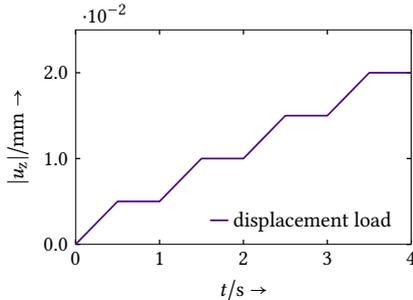
Figure 3.8: Multiphase domain: Displacement load varying with time.

To evaluate the behaviour of the visco-elastic model in a domain with multiple phases and interfaces, a rectangular bar of size $11\,\text{mm} \times 11\,\text{mm} \times 201\,\text{mm}$ is subdivided into sections of different visco-elastic and linear elastic behaviour

as depicted in Figure 3.9a. All boundaries are stress-free, except the lower and upper z-boundary, which exhibit a timely varying displacement load in the respective normal direction shown in Figure 3.8. The time step width is chosen to be $\Delta t = 0.001$ s while the spatial discretisation is $\Delta x = 1.0$ mm, and each visco-elastic material is isotropic and has one Maxwell branch. Material properties are used as listed in Table 3.5. In Figure 3.9b the evolution of the

Phase	E^0/GPa	v^0/-	E^1/GPa	v^1/-	η^1/MPa $\cdot$ s
α	5.0	0.30	20.0	0.30	$1.0 \cdot 10^4$
β	10.0	0.30	40.0	0.30	$2.0 \cdot 10^4$
γ	2.5	0.30	10.0	0.30	$0.5 \cdot 10^4$
δ	73.0	0.22	—	—	—

Table 3.5: Material properties used in the multiphase domain: Visco-elastic phases α, β, γ and linear elastic phase δ.

Cauchy stress σ_{zz} and the strain ε_{zz} is shown for the centre point of the domain in phase γ. The temporal development of the diffuse interface stress and strain resembles that of the sharp interface quantities. This indicates that linear momentum is transferred correctly throughout the interfacial regions despite the smoothed discontinuities. Examining the stress component σ_{xx}, which is tangential to the interfaces, reveals a congruent development within bulk regions, and as previously mentioned the smoothed discontinuities alter the magnitude of the discontinuity only within the interfacial regions. As in the sections about thermal and basic mechanical behaviour, the observance of turning points being at the interface centre points holds here as well.

Curing process: Degree of cure and glass transition temperature   The evaluation of the curing process involves a moderate coupling between the basic models, which happens in a staggered manner with the order *temperature*, *degree of cure* and *displacement*, but only the bulk behaviour is examined. The

(a) Domain: Size and phases

(b) Temporal evolution of σ_{zz} and ε_{zz} in γ phase centre point

(c) Plot of σ_{xx} along z centre axis at time $t = 3.3$ s
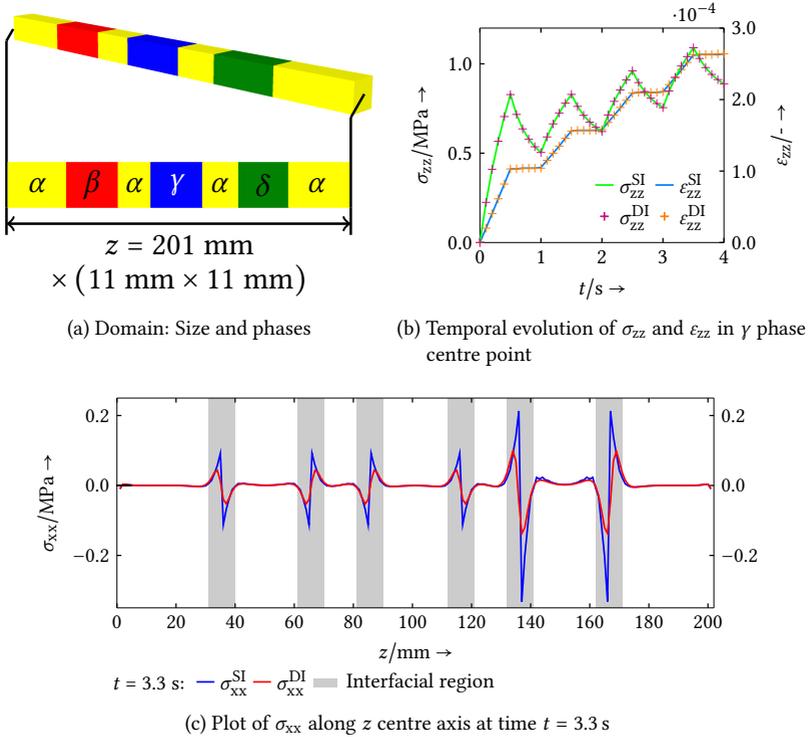
Figure 3.9: Behaviour of the visco-elastic implementation in a multiphase domain (phases α, β, γ are visco-elastic, δ only elastic): Comparison of sharp interface (SI) and diffuse interface (DI) implementation.

evolution of the absolute temperature Θ incorporates the release of reaction enthalpy as a dissipation term and the thermo-mechanical coupling (Gough-Joule effect). The temporal evolution is described by

$$\rho^\alpha c_V^\alpha \dot{\Theta} = -q_{i,i} - \mathcal{D}^{cu} - \Theta C_{ijkl}^\alpha \alpha_{kl}^\alpha \dot{\varepsilon}_{ij}^\alpha, \tag{3.82}$$

where $\mathcal{D}^{cu}$ depicts the released reaction enthalpy as noted in Equation (3.70), but simplified by just using the term incorporating h^{tot}. The phase fraction is

dropped in the formula, as no interfacial region is present in the simulation domain and hence ϕ^α = 1.0. The state equation for the degree of cure ζ^α is used as described in Equation (3.76) and also the glass transition temperature Θ^g is calculated as introduced in Equation (3.77). For the mechanical part linear elasticity is used, extended by thermal and curing strains, $\varepsilon_{ij}^{\text{th},\alpha}$ and $\varepsilon_{ij}^{\text{cu},\alpha}$,

$$\sigma_{ij}^\alpha = C_{ijkl}^{\alpha,0} \left\{ \varepsilon_{kl}^\alpha - \alpha_{kl}^\alpha \left(\Theta - \Theta^{\text{Ref}} \right) - \chi_{kl}^\alpha \zeta^\alpha \right\}, \tag{3.83}$$

and solved by the linear momentum balance (3.79). Here, ε_{kl}^α is the total strain, α_{kl}^α is the thermal expansion tensor, and χ_{kl}^α describes the maximum curing shrinkage. The simulation domain has a size $\{7.5\,\text{mm}\}^3$, and uses a spatial discretisation of Δx = 0.5 mm. The total simulation time is t = 350 s, divided into time steps of Δt = 1.0 s. The initial temperature is set to Θ^0 = 360 K, and the degree of cure starts at ζ^0 = 0. The boundary conditions are a constant temperature of $\bar{\Theta}$ = 360 K at all cube faces for the temperature evolution. To see the effect of the curing shrinkage, the lower and upper x-boundary are fixed, whereas all other boundaries are stress-free for the mechanical solver. The simulated thermoset phase α is isotropic in all material properties and none of them have dependences on other quantities. In Table 3.6 an overview is given. In Figure 3.10a domain shrinkage due to the curing process and resulting stresses are depicted qualitatively. These develop as soon as the curing process starts, as the curing strains linearly grow with the degree of cure. With the absolute system temperature Θ being reasonably high from the beginning, the curing process starts quickly which causes reaction enthalpy to be released. The released enthalpy increases the local temperature accelerating the curing reaction. In parallel the glass transition temperature rises with a progressing chemical reaction. With more and more growing degree of cure, the conversion rate begins to drop due to the construction of the underlying Kamal-Sourour model (3.76) and its description of an exothermic reaction. Less reaction enthalpy is released and the local temperature peaks and starts to decrease again. This causes the still growing Θ^g to surpass the local temperature, which

Material Parameter	Variable	Value	Unit
mechanical			
Elastic Modulus	E^α	3400	MPa
Poisson's Ratio	ν^α	0.35	—
Thermal Expansion	α^α	$6.70 \cdot 10^{-5}$	1/K
Reference Temperature	$\Theta^{\text{Ref},\alpha}$	380	K
Curing Shrinkage	χ^α	$-2.50 \cdot 10^{-2}$	—
thermal			
mass density modified Specific Heat Capacity	$\rho^\alpha c_V^\alpha$	$2.51 \cdot 10^6$	J/m³K
Thermal Conductivity	κ^α	0.34	W/mK
exothermic reaction			
mass density modified tot. Reaction Enthalpy	$\rho^\alpha h^{\text{tot},\alpha}$	-280	kJ/m³
Glass Transition	$\Theta^{\text{g},0}, \Theta^{\text{g},\infty}$	250, 430	K
Fitting Parameters	$k^{i,0}$	$1.00 \cdot 10^5, 5.13 \cdot 10^4$	1/s
	E^i	$5.50 \cdot 10^7, 4.85 \cdot 10^7$	J/mol
	m	0.79	—
	n	1.53	—
	λ	0.58	—

Table 3.6: Test of the (simplified) curing behaviour: Material properties needed to describe the thermoset phase.

marks the end of the local curing reaction. In Figure 3.10a this shows as a constant ζ^α value, and a fast drop in local temperature to the overall system temperature induced by the stopped supply of reaction enthalpy.

3.3 Phase-field fracture model from Clausius-Duhem-Inequality

The derivation of a phase-field fracture model follows the motivation and principles of the standard phase-field derivation in Section 3.1. Hence, only

(a) Shrinkage and stress due to the curing reaction in the domain

(b) Development of degree of cure, temperature and glass transition temperature and their interplay at the domain centre
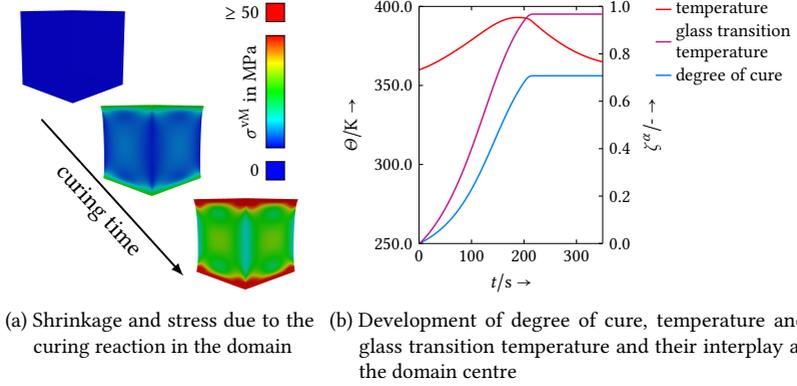
Figure 3.10: Coupled influence of temperature Θ on degree of cure ζ and the resulting rise in glass transition temperature Θ^g. When Θ drops below Θ^g, the reaction stops.

the relevant steps and main equations are pointed out. The model is directly formulated in the infinitesimal deformation regime, and the Euler notation is used. In this section, parts of the reasoning builds upon the work on multiphase-field fracture of Schneider *et al.* [155] and Nestler *et al.* [130], which especially applies to their modelling approach of balancing the crack phase against the collection of all solid phases, $\phi^c + \phi^s = \phi^c + \phi^s \sum_\alpha \phi^\alpha / \phi^s = 1$. Furthermore, solid-solid interfaces that occur are regarded as being at rest and hence are not moving. A separation between different crack resistances referencing to different crack modes is not made. The derived model behaves the same for all crack modes. Individual modifications were firstly discussed and published in Schöller [160].

3.3.1 Regularisation of a sharp interface formulation

As done previously, the Clausius-Duhem-Inequality is considered as a starting point for describing a system exposed only to mechanical effects, hence temperature or heat are neglected. Furthermore, kinetic energy density and body forces are removed. With these assumptions, the inequality simplifies to

the free energy imbalance [69]. For infinitesimal deformation in the sense of linear elastic fracture mechanics (see Section 2.2) and in Eulerian notation the integral form is

$$\int_{\partial v} v_i \sigma_{ij} n_j \mathrm{d}a - \frac{\mathrm{d}}{\mathrm{d}t} \Psi^{\text{tot}} \geq 0, \tag{3.84}$$

where in the first term v_i is the velocity, σ_{ij} is the Cauchy stress tensor and n_j is the (outer) surface normal vector. The second term is the time derivative of the total Helmholtz free energy functional Ψ^{tot}, for which

$$\int_{s^{cs}(t)} G^c \mathrm{d}a = \Psi^{\text{tot}} - \int_{v^s} \rho^s \Psi^s \mathrm{d}v - \int_{v^c} \rho^c \Psi^c \mathrm{d}v. \tag{3.85}$$

Here G^c denotes the energetic crack resistance (a surface energy density). The Helmholtz free energy Ψ^s contains the mechanical free energy of the solid region, whereas Ψ^c is the free energy of the crack region inbetween the crack surfaces. Because the crack domain is considered as non-solid, i.e. air or similar, Ψ^c is set to zero due to the absence of continuum mechanical effects and $\rho^c \approx 0$. By using Gauss' theorem (2.24) and Reynolds transport theorem (2.26), Equation (3.84) is re-written as

$$\int_v \left\{ v_i \sigma_{ij,j} + \sigma_{ij} \dot{\varepsilon}_{ij} - \rho^s \frac{\mathrm{d}\Psi^s}{\mathrm{d}t} \right\} \mathrm{d}v$$
$$- \int_{s^{cs}(t)} \rho^s \Psi^s v_i^{cs} n_i^{cs} \mathrm{d}a + \frac{\mathrm{d}}{\mathrm{d}t} \int_{s^{cs}(t)} G^c \mathrm{d}a \geq 0, \tag{3.86}$$

where jump quantities were dropped due to undefined mechanical stresses in crack regions, and therefore the only influence on the crack-solid interface $s^{cs}(t)$ comes from the solid region's Helmholtz free energy Ψ^s. The term $\sigma_{ij} \dot{\varepsilon}_{ij}$ is the stress power with $\dot{\varepsilon}_{ij}$ as the rate of the strain tensor. Next, the time derivative is evaluated and G^c is assumed to be isotropic, which gives

$$\frac{\mathrm{d}}{\mathrm{d}t} \int_{s^{cs}(t)} G^c \mathrm{d}a = \int_{s^{cs}(t)} \left\{ v_{\perp}^{cs} G^c n_{i,i}^{cs} \right\} \mathrm{d}a \tag{3.87}$$

where $v_\perp^{cs} = v_i^{cs} n_i^{cs}$ is the scalar normal velocity of the crack-solid interface and $n_{i,i}^{cs}$ is the mean curvature of the crack surface.

Letting $\Psi^s = \Psi^s\left(\varepsilon_{ij}^s\right)$ and setting the strain tensor $\varepsilon_{ij}^s = \varepsilon_{ij}$ due to a unified solid domain, the sharp interface model yields the following inequality,

$$
\int_v \left\{ v_i \sigma_{ij,j} + \left(\sigma_{ij} - \rho^s \frac{\partial \Psi^s}{\partial \varepsilon_{ij}^s} \right) \dot{\varepsilon}_{ij}^s \right\} \mathrm{d}v
$$
$$
- \int_{s^{cs}(t)} \left\{ -\rho^s \Psi^s + G^c n_{i,i}^{cs} \right\} v_\perp^{cs} \mathrm{d}a \geq 0.
$$
(3.88)

For arbitrary rates of strain $\dot{\varepsilon}_{ij}^s$, the Cauchy stress follows the thermodynamic relation $\sigma_{ij} = \rho^s \partial \Psi^s / \partial \varepsilon_{ij}^s$ and for arbitrary velocities v_i the static linear momentum balance without body forces holds, $\sigma_{ij,j} = 0$. Further, an interfacial term can be identified, where a curvature modified energetic crack resistance G^c is balanced by mechanical free energy $\rho^s \Psi^s$.

To describe the crack-solid interface numerically, the crack surface is regularised analogously to Section 3.1.2 with an order parameter - or volume fraction - ϕ^c, whose gradient $\phi_{,i}^c$ extends the normal vector field n_i^{cs} smoothly in the orthogonal direction from the hypersurface s^{cs} satisfying the *eikonal equation* (see e.g. [45, 117, 186]). This generates a set of equidistant surfaces parallel to the initial crack-solid interface, level sets, which are represented by $\phi^c\left(x_i, t\right) = \text{const}$. The order parameter is chosen to follow

$$
\phi^{cs}\left(w\right) = \begin{cases} 1, & \forall w = 0 \text{ on } s^{cs} \\ \left(1 - \frac{w}{\epsilon}\right)^2, & \forall 0 < w < \epsilon \\ 0, & \forall w \geq \epsilon \end{cases}, \quad
$$
(3.89)

which equals to a one-sided extension of thickness ϵ of the crack-solid interface from the crack region into the solid region, see Figure 3.11. The order parameter follows a quadratic profile described by positions x_i following the normal extension of the hypersurface (in Equation (3.89), for simplicity, the positions
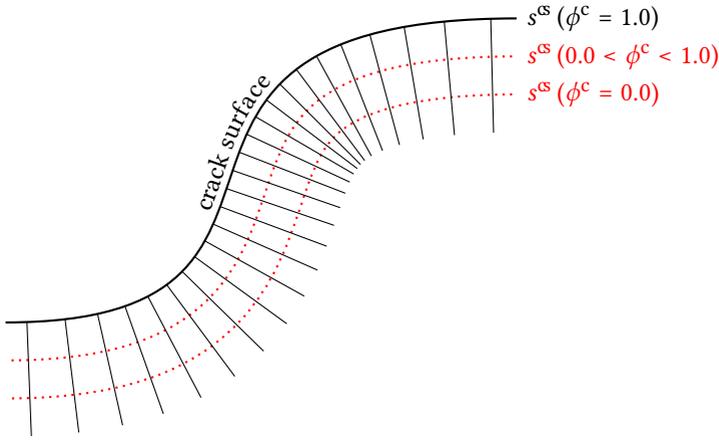
Figure 3.11: Level sets and perpendicular rays along n_i^{cs} of the sharp interface s^{cs}

along the interface normal direction are denoted by w). In the phase-field context such a profile is of an "obstacle" type as it gives a well-defined interface thickness. The profile function used is taken from the phase-field crack model described in [130, 155].

The order parameter defines the normal vector $n_i^{\mathrm{cs}} = \phi_{,i}^{\mathrm{c}}/\sqrt{\phi_{,j}^{\mathrm{c}}\phi_{,j}^{\mathrm{c}}}$, which transfers the curvature term $G^{\mathrm{c}} n_{i,i}^{\mathrm{cs}}$ into a phase-field formulation. Following [16, 179] the analogy to Equation (3.19) for the crack surface is found as

$$
\begin{aligned}
G^{\mathrm{c}} n_{i,i}^{\mathrm{cs}} &= G^{\mathrm{c}} \left(\frac{\phi_{,i}^{\mathrm{c}}}{\sqrt{\phi_{,j}^{\mathrm{c}}\phi_{,j}^{\mathrm{c}}}} \right)_{,i} \\
&= G^{\mathrm{c}} \frac{\phi_{,ii}^{\mathrm{c}}\sqrt{\phi_{,j}^{\mathrm{c}}\phi_{,j}^{\mathrm{c}}} - \phi_{,i}^{\mathrm{c}}\left(\sqrt{\phi_{,j}^{\mathrm{c}}\phi_{,j}^{\mathrm{c}}}\right)_{,i}}{\left(\sqrt{\phi_{,j}^{\mathrm{c}}\phi_{,j}^{\mathrm{c}}}\right)^2} \\
&= G^{\mathrm{c}} \frac{1}{\sqrt{\phi_{,j}^{\mathrm{c}}\phi_{,j}^{\mathrm{c}}}} \left(\phi_{,ii}^{\mathrm{c}} - \frac{\phi_{,i}^{\mathrm{c}}\left(\sqrt{\phi_{,j}^{\mathrm{c}}\phi_{,j}^{\mathrm{c}}}\right)_{,i}}{\sqrt{\phi_{,j}^{\mathrm{c}}\phi_{,j}^{\mathrm{c}}}} \right).
\end{aligned}
\tag{3.90}
$$

Further the terms

$$\sqrt{\phi_{,j}^c \phi_{,j}^c} = -\frac{2}{\epsilon}\sqrt{\phi^c},$$

(3.91)

$$\frac{\phi_{,i}^c \left(\sqrt{\phi_{,j}^c \phi_{,j}^c}\right)_{,i}}{\sqrt{\phi_{,j}^c \phi_{,j}^c}} = \frac{2}{\epsilon^2}$$

can be identified, where the former defines the shape of the distribution function shown in Figure 3.12. To extend the crack-solid interface in normal
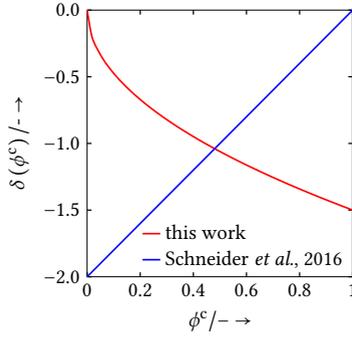

Figure 3.12: Comparision of the shape of phase-field fracture distribution functions with the one used in Schneider *et al.* [155].

direction, a regularised delta distribution $\delta^\epsilon = \sqrt{\phi_{,j}^c \phi_{,j}^c}$ is chosen, which satisfies

$$1 = \int_{-\infty}^{+\infty} \delta\left(x_i\right) \mathrm{d}w = \int_{-\epsilon}^{0} \delta^\epsilon\left(w\right) \mathrm{d}w. \tag{3.92}$$

This choice also ensures the delta distribution in the sharp interface limit

$$
\begin{aligned}
\delta\left(x_i = 0\right) &= \lim_{\epsilon \to 0^-} \left(\left.\delta^\epsilon\left(w\right)\right|_{w=0}\right) \\
&= \lim_{\epsilon \to 0^-} \left(\left.\left(-\frac{2}{\epsilon}\left(1 - \frac{w}{\epsilon}\right)\right)\right|_{w=0}\right) \\
&= \lim_{\epsilon \to 0^-} \left(-\frac{2}{\epsilon}\right) \to +\infty.
\end{aligned}
\tag{3.93}
$$

Plugging the findings into equation (3.88), and assuming for the bulk Helmholtz free energy $\rho^s \Psi^s\left(\phi^s, \varepsilon_{ij}^s\right) = \phi^s \rho^s \Psi^s\left(\varepsilon_{ij}^s\right)$, where $\phi^s = 1 - \phi^c$ in the sense of order parameters denoting volume fractions, the entropy inequality for a diffuse interface approach is

$$
\begin{aligned}
&\int_v \left\{ v_i \sigma_{ij,j} + \left(\sigma_{ij} - \phi^s \rho^s \frac{\partial \Psi^s}{\partial \varepsilon_{ij}^s}\right) \dot{\varepsilon}_{ij}^s \right\} - \rho^s \Psi^s \dot{\phi}^s \mathrm{d}v \\
&- \int_{s^{cs}(t)} \left\{ -\sqrt{\phi_{,j}^c \phi_{,j}^c} \, \rho^s \Psi^s + G^c \left(\phi_{,ii}^c - \frac{2}{\epsilon^2}\right) \right\} v_\perp^{cs} \mathrm{d}v \geq 0,
\end{aligned}
\tag{3.94}
$$

with the relation $\sigma_{ij} = \phi^s \rho^s \partial \Psi^s / \partial \varepsilon_{ij}^s$ for the Cauchy stress. The term $-\rho^s \Psi^s \dot{\phi}^s \geq 0$ ensures, that in accordance with thermodynamics, the crack phase may only be at rest or grow $\dot{\phi}^c \geq 0$ as the free energy always follows $\Psi^s \geq 0$. The driving force is weighted by the distribution function $\sqrt{\phi_{,j}^c \phi_{,j}^c}$ as previously done in [16, 179] and later applied for multiphase-field approaches in [47, 172]. A similar term is pointed out in Bourdin *et al.* [24], Tanné *et al.* [182], and Farrell and Maurini [52] as their approach follows [7, 22, 127] which also use techniques from image processing for regularisation. However, their term $c_w = \int_0^1 \sqrt{w(s)} \mathrm{d}s$ generates a constant prefactor. Furthermore, we see that due to the chosen profile, there is still a constant energetic crack resistance G^c in the absence of curvature due to the term $2/\epsilon^2$ independent of ϕ^c. This resembles the classic criterion for crack growth formulated by Griffith [65],

$$
G - G^c \leq 0,
\tag{3.95}
$$

which predicts crack propagation when the energy G surpasses the energetic crack resistance G^c and which was discussed in Section 2.2.2. The crack propagation is driven by the formation of new crack surfaces, which continues until the above inequality is fulfilled again, or the stressed region exhibits complete failure. Still, for non-planar crack surfaces, the phase-field formulation has an intrinsic curvature dependence, which is non-physical in the case of a crack description. Crack propagation should solely depend on mechanical energy and should not be curvature-driven. To suppress the curvature influence, the evolution equation for the crack phase is modified by a counter term, as introduced by Folch *et al.* [53]. A further common and wide-spread modification aims at the the Helmholtz free energy comprising the elastic energy. As a crack generally only propagates under tension, the Helmholtz free energy is re-written with the spectral decomposition of the strain tensor ε_{ij} as suggested by Miehe *et al.* [120]. Hence, the mechanical energy acting on the crack surface is modified to

$$-\sqrt{\phi^c_{,j}\phi^c_{,j}}\,\rho^s\,\Psi^s\left(\varepsilon_{ij}\right) \quad \rightarrow \quad -\sqrt{\phi^c_{,j}\phi^c_{,j}}\,\rho^s\,\Psi^s\left(\varepsilon^+_{ij}\right), \tag{3.96}$$

so that only tensile strains ε^+_{ij} induce an energetic contribution, compressive strains are neglected. A last change to the model involves factors k and k^{el}, which scale the energetic crack resistance and the elastic energy acting on the crack surface, respectively. The reasoning is the same as presented in the work of Schöller [160]. Integrating the crack surface terms in the interface normal direction defines the the factor k via

$$\int_0^L kG^c\left(\phi^c_{,ii} - \frac{2}{\epsilon^2}\right)\mathrm{d}l = \int_0^{\phi^{c,BC}} 4kG^c\sqrt{\phi^c}\,\mathrm{d}\phi^c \overset{!}{=} G^c \tag{3.97}$$

as $k = 3/8 \left(\phi^{c,BC} \right)^{-3/2}$, where the border crack value $\phi^{c,BC}$ modifies the volume fraction above which the structure exhibits local failure by setting

$$\phi^c = \begin{cases} \phi^c, & \forall \phi^c < \phi^{c,BC} \\ 1, & \forall \phi^c \geq \phi^{c,BC} \end{cases}. \qquad (3.98)$$

When the border crack value is lowered, the cut-off energy is redistributed to the remaining ϕ^c range. With the factor k^{el}, the gradient-free part of the energetic crack resistance is harmonised with the elastic energy for the equilibrium condition. Again by integrating in the interface normal direction, the factor k^{el} is found to be

$$k^{el} = \frac{2k}{N \sqrt{\phi^{c,BC} \left(1 - 0.5 \phi^{c,BC} \right)}}, \qquad (3.99)$$

where the assumption $G^c / (\Delta x \rho^s \Psi^s) = 1$ (released energy times spatial discretisation matches energetic crack resistance) is used for derivation. All modifications involving integrating over the interfacial region are for a planar interface, and therefore might not scale correctly at the crack tip. For the evolution of the crack phase an Allen-Cahn equation is used, which is noted as

$$\frac{\partial \phi^c}{\partial t} = M^{cs} \left\{ kG^c \left(\phi^c_{,ii} - \frac{2}{\epsilon^2} \right) \right.$$
$$\left. - \sqrt{\phi^c_{,j} \phi^c_{,j}} \left(k^{el} \rho^s \Psi^s - kG^c \left(\frac{\phi^c_{,i}}{\sqrt{\phi^c_{,j} \phi^c_{,j}}} \right)_{,i} \right) \right\}, \qquad (3.100)$$

where M^{cs} is a mobility parameter.

3.3.2 Modelling crack resistance in solid-solid interfaces

A common approach for material parameters inside the interfacial regions is an interpolation using the order parameters [123]. Therefore the natural treatment of the energetic crack resistance G^c in the presence of two solid

phases ϕ^α and ϕ^β has the interfacial crack resistance given as the arithmetic average using volume fractions

$$G^{\text{ari,c}}\left(\phi^{\text{s}}\right) = \bar{\phi}^\alpha G^{\text{c},\alpha} + \bar{\phi}^\beta G^{\text{c},\beta}, \tag{3.101}$$

with $\bar{\phi}^\alpha = \phi^\alpha/(\sum_{\alpha \in \text{s}} \phi^\alpha)$ being the volume fraction of phase α normalised by the sum of the locally occurring solid phases (based on Schneider *et al.* [155]). In the scope of FRTS this approach is able to cover the bulk failure mechanisms, namely matrix rupture and fibre breakage, but cannot map the third relevant mechanism of interface failure (see Section 2.2.4). The smooth transition of order parameters in interfacial regions gives a convenient tool to modify material behaviour at phase boundaries. Under the assumption that the modification has its greatest difference from the standard behaviour at the centre of the interfacial region, $\phi^\alpha = \phi^\beta = 0.5$, the volumetric averaged crack resistance in Equation (3.101) is modified to

$$\begin{aligned} G^{\text{mod,c}}\left(\phi^{\text{s}}\right) &= G^{\text{ari,c}}\left(\phi^{\text{s}}\right) - \left\{4\bar{\phi}^\alpha\bar{\phi}^\beta\left(\bar{\phi}^\alpha G^{\text{c},\alpha} + \bar{\phi}^\beta G^{\text{c},\beta} - G^{\text{c},\alpha\beta}\right)\right\} \\ &= \bar{\phi}^\alpha G^{\text{c},\alpha} + \bar{\phi}^\beta G^{\text{c},\beta} \\ &\quad - \left\{4\bar{\phi}^\alpha\bar{\phi}^\beta\left(\bar{\phi}^\alpha G^{\text{c},\alpha} + \bar{\phi}^\beta G^{\text{c},\beta} - G^{\text{c},\alpha\beta}\right)\right\}. \end{aligned} \tag{3.102}$$

Here, $G^{\text{c},\alpha\beta}$ is the interfacial crack resistance for a specific solid-solid interface α-β. In Figure 3.13 the behaviour is shown for a binary interface, where the minimum is reached at the 0.5 level set.

3.3.3 Validation and behaviour

In the following three paragraphs, the previously derived model for phase-field crack propagation is evaluated. Firstly, the model is checked for accordance with the Griffith criterion (see Section 2.2.2) at different spatial discretisations and interface widths. Additionally the influence of the border crack value $\phi^{\text{c,BC}}$ is examined. Next, the behaviour of the curvature-free formulation and
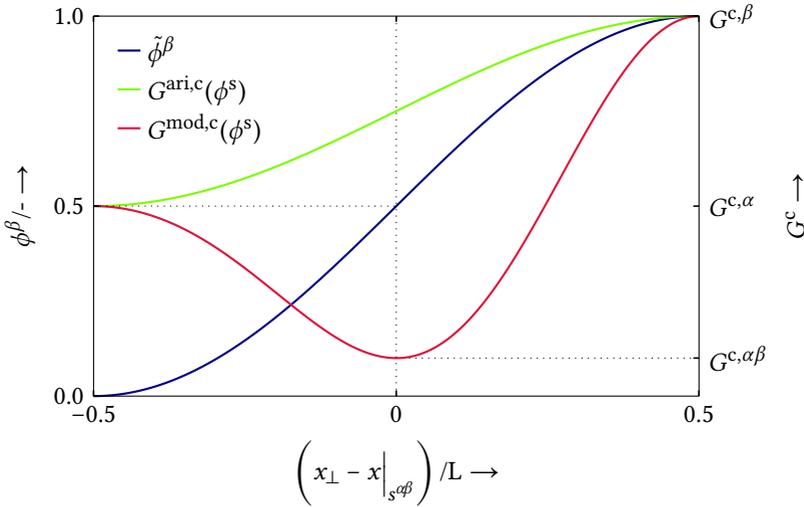
Figure 3.13: G^c (ϕ^s) development along an interface normal coordinate $x_\perp$ within an interface of thickness L. Comparison of (standard) arithmetic and modified interfacial crack resistance calculation.

the distribution function $\sqrt{\phi^c_{,j}\phi^c_{,j}}$ is qualitatively shown. Lastly, the previously introduced solid-solid interface crack resistance $G^{c,\alpha\beta}$ is used in different two phase domains which vary in geometry and material properties. The effect on crack paths is examined and discussed. Generally, for all simulations an equidistant mesh is used. The evolution of the crack phase is computed using Equation (3.100) within a finite-difference scheme, which is solved explicitly by a forward Euler integration, where the elastic energy is calculated on the basis of mechanics solved by the static linear momentum balance, $\sigma_{ij,j} = 0$, for which linear elements with full integration are used. Furthermore, the two fields are solved in a staggered manner.

Griffith criterion in bulk phases Griffith's criterion, which was discussed in Section 2.2.2, is used to evaluate the phase-field fracture model for quanti-

tativeness. The setup is taken from Schöller [160] and uses two-dimensional domains of different sizes, spatial discretisations and interface widths. For a grid spacing of $\Delta x = 2.0\,\mu$m the plane strain simulation domain has a size of $\{200\,\mu\text{m}\}^2$, for $\Delta x = \{1.0, 1/2, 1/3\}$ μm it is $\{150\,\mu\text{m}\}^2$ and the finest resolution $\Delta x = 1/4\,\mu$m uses a size of $\{100\,\mu\text{m}\}^2$. For each spatial discretisation an extra layer is added in both dimension to have an odd number of phase-field cells to be able to place the initial crack exactly in the centre between the loaded boundaries. The z-boundaries are fixed in the orthogonal direction, whereas the x-boundaries exhibit an orthogonal displacement in the normal direction of $\bar{u} = \{0.001 \cdot \text{domain length}\}$ (see Figure 3.14a). The border crack value is kept constant at $\phi^{\text{c,BC}} = 0.975$ for all simulations of this study. Each simulation

(a) Schematic initial domain for Griffith point evaluation with boundary conditions $\bar{u}$ and exemplary J-integral path.

(b) Griffith point: Energy J needed in relation to energetic crack resistance G^{c} for crack growth. Different number of interface cells and mesh resolution.
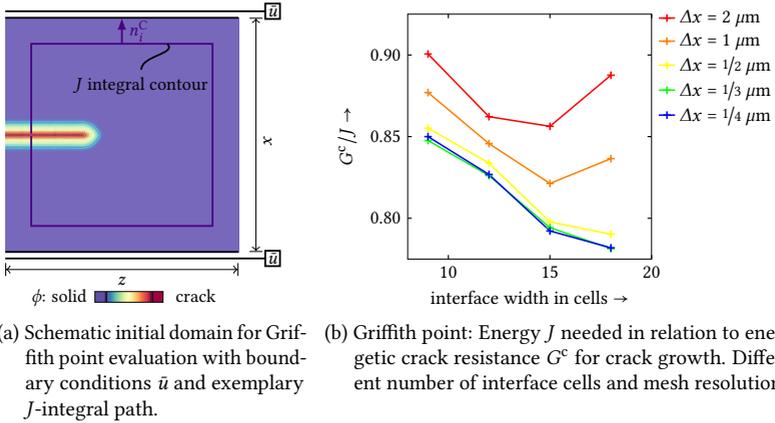
Figure 3.14: Evaluation of the Griffith point for the presented phase-field fracture model. A fraction of $G^{\text{c}}/J = 1$ perfectly fulfils the Griffith theory.

setup is tested with four interface widths of $\{9, 12, 15, 18\}$ cells. The fraction of energetic crack resistance to dissipated energy, G^{c}/J, is calculated by starting each simulation setup with a sufficient high G^{c}, which is iteratively lowered until the crack tip is just not propagating yet. For this configuration, the J-integral (see Section 2.2.3) is evaluated, as demonstrated in Figure 3.14a. The

results of this simulation study are depicted in Figure 3.14b. All configurations overestimate the energetic crack resistance G^c by at least 10 % up to approximately 20 %. By resolving the domain with a smaller spatial discretisation, the model converges in its behaviour, but also shows the highest deviation. By extrapolation towards a sharp interface solution (zero interface cells) the conclusion might be drawn that each resolution proceeds towards a fraction of $G^c/J = 1$, which indicates that in the limiting case the Griffith criterion could be met. As the phase-field method needs a certain number of interface cells to work numerically, this cannot be examined. Another trend to be observed is the flattening and partial rising of the fractions for wider crack interfaces. This is mainly due to deficiencies in the model, caused by the profile function chosen (see Equation 3.89): The more interface cells are allowed, the higher are the crack phase values ϕ^c close to the crack surface. Because the distance in crack phase value to $\phi^c = \phi^{c,BC}$, and hence local failure, becomes smaller, small increments of crack phase may easily cause to reach or surpass $\phi^{c,BC}$. To further estimate the influence of the border crack parameter, a further simulation study is shown in Figure 3.15, where the domain setup for $\Delta x = 1.0\,\mu m$ with 12 interface cells is used and $\phi^{c,BC}$ is varied. The results predict that for
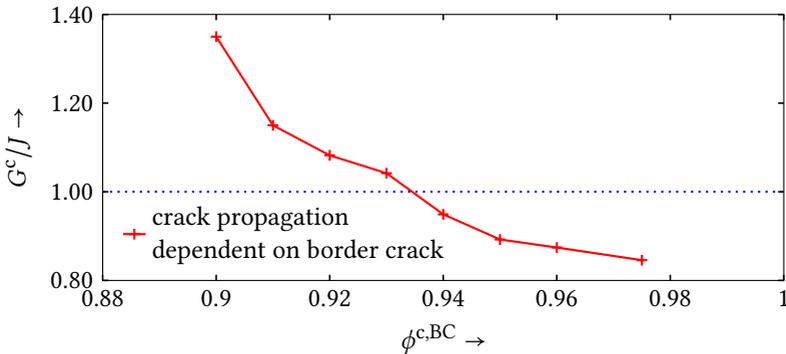
Figure 3.15: Influence of the border crack value $\phi^{c,BC}$ on the Griffith point for $\Delta x = 1.0\,\mu m$ and 12 interface cells.

$0.93 < \phi^{c,BC} < 0.94$ the Griffith criterion is fulfilled. However, this adjustment is only valid for the chosen combination of spatial discretisation and number of interface cells. Hence, a general, fixed set of model parameters to meet the Griffith criterion is not available. In the following and regarding the application in Section 4.4, the presented phase-field fracture model is not further evaluated for quantitativeness, but the general and qualitative behaviour is characterised.

Curvature influence and distribution function   The two main features of the derivation of the phase-field fracture model presented in Section 3.3.1 are the distribution function, $\sqrt{\phi^c_j \phi^c_j} = -\frac{2}{\epsilon}\sqrt{\phi^c}$, which is new in the context of crack propagation, and the modification to neglect the curvature influence by subtracting the sharp interface curvature formulation as presented by Folch *et al.* [53]. As shown in Figure 3.16 the plane strain domain has a size of $\{101\,\mathrm{mm}\}^2$ and a spatial discretisation of $\Delta x = 1.0\,\mathrm{mm}$ is used. For comparison, the behaviour of the model of Schneider *et al.* [155] is given at equal simulation steps. From the initial setup presented in Figure 3.16a the effect of the curvature counter-term is recognised. By subtracting the curvature effect the interface profile is preserved around the crack tip for the derived model, while the conventional model exhibits a distorted interface due to large curvature at the tip. This may have an impact on the representation of the energetic crack resistance $G^{c,\alpha\beta}$, which is only valid for a perfectly undistorted interface profile. In Figures 3.16b and 3.16c the same load as in the previous paragraph is applied, but amplified by a factor of 2 and 5, respectively. Here the influence of the distribution function shape (cf. Figure 3.12) becomes apparent. While the distribution function of the conventional model is unable to keep the interface profile and its width, the one derived from sharp interface regularisation barely shows any distortion, even at elevated loads. Similar to the influence of the curvature mentioned above, the progressing stretch of the interface profile may cause an alteration in the energetic crack resistance.
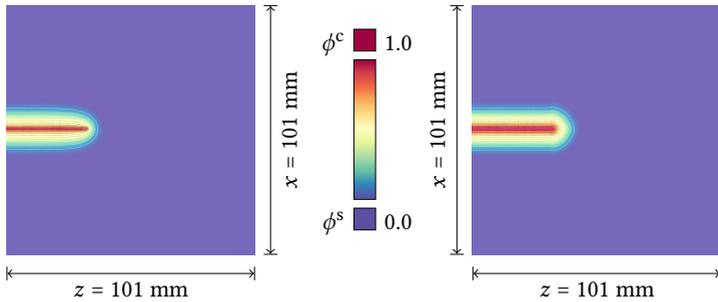
(a) Initial configuration without external load: Influence of curvature subtraction.
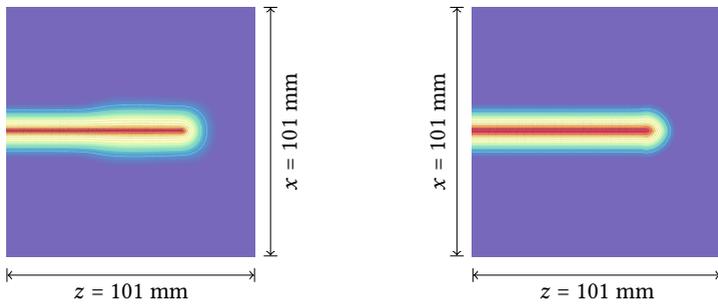
(b) Crack propagation due to distribution function, moderate external load $\tilde{u} = 2\bar{u}$
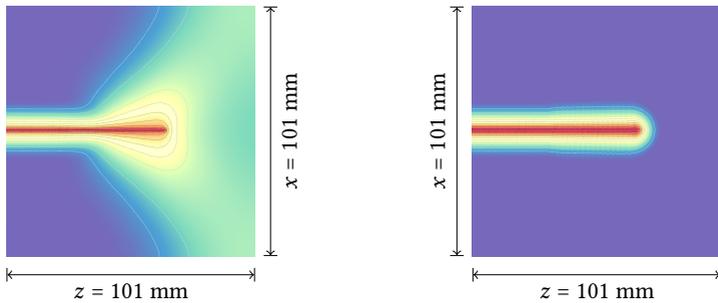
(c) Crack propagation due to distribution function, strong external load $\tilde{u} = 5\bar{u}$

Figure 3.16: Comparison of a phase-field fracture model with curvature term and conventional distribution function (left, [155]) with the phase-field fracture model presented in this work (right). Influence of curvature term and distribution function.

By using the presented square-root shaped function, this behaviour can be prevented. This is especially important as in general model validation or fitting for the Griffith point requires only loads close to equilibrium, for which no interface distortion is to be expected. Testing away from equilibrium is barely done, even if the model is used in non-equilibrium scenarios afterwards. Such implementations of the Griffith criterion, even if done thoroughly, may therefore lack validity if applied loadings leave the equilibrium range.

Crack propagation in the presence of a solid-solid interface   The influence of this modification is qualitatively investigated by means of five different simulation domains, shown in Figure 3.17, which consist of a glass fibre phase ϕ^{GF} differently embedded in a thermoset phase ϕ^{TS}. Here the interest lays in to which extent it is possible to model typical behaviour of FRPs such as debonding with the introduced G^{c} modification and to illustrate differences. A displacement load ramp is applied locally until complete separation of the
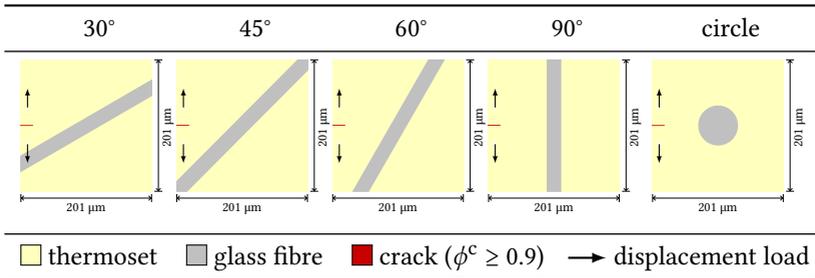
Figure 3.17: Initial domains filled with differently oriented glass fibre phase ϕ^{GF} surrounded by a thermoset matrix phase ϕ^{TS} (solid phases shown up to $\phi^{\text{GF}} = \phi^{\text{TS}} = 0.5$). The initial crack ϕ^{c} is loaded by a displacement ramp. Domain boundaries are stress-free.

domains. The plane strain domains have a size of $\{201\,\mu\text{m}\}^2$ with $\Delta x = 1.0\,\mu\text{m}$ and their boundaries are stress free. In Figure 3.18 both phases have the same material properties, but each column differs in how the energetic crack resistance G^{c} is modelled in the solid-solid interface region. The material properties
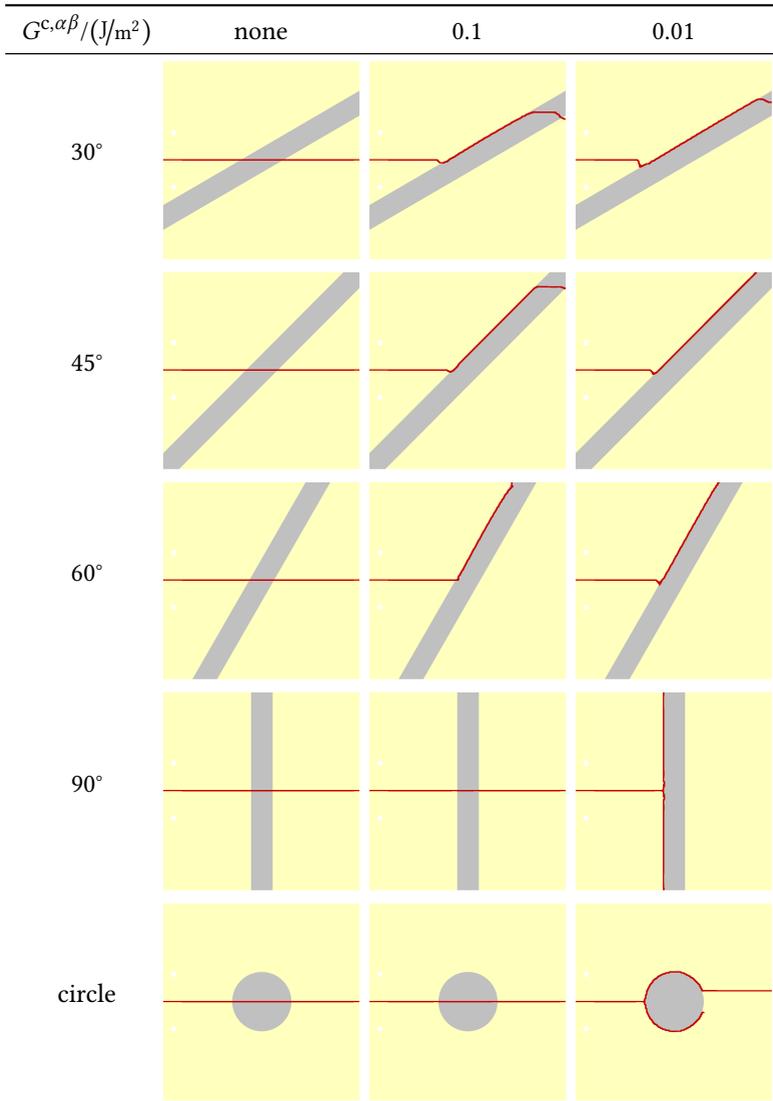
Figure 3.18: Simulation runs on domains specified in Figure 3.17. Comparison of the influence of different $G^{c,\alpha\beta}$ values on crack propagation in phases with the same elastic properties and bulk crack resistances.

are an elastic modulus of $E = 10\,\mathrm{GPa}$, Poisson's ratio of $\nu = 0.3$ and a bulk crack resistance of $G^c = 1.0\,\mathrm{J/m^2}$. For unmodified G^c, the crack propagates in all five cases straight to the right side of the simulation domain. Lowering the interfacial crack resistance with Equation (3.102) to $1/10$ of the bulk values changes the crack path significantly. As long as the crack reaches the solid-solid interface below an angle of $90°$, the fracture happens along the materials' interface with certain deviations close to the domain boundaries. In the case of the $90°$ and the circle scenario, the lower $G^{c,\alpha\beta}$ is not able to change the crack path. Lowering the interfacial crack resistance further to $1/100$ of the bulk values improves the fracture behaviour along the interface. For all cases the crack changes its direction when arriving at the interface region. Furthermore, for the $30°$, $45°$, $60°$ and $90°$ domains, the crack stays in the interface nearly until reaching the domain boundary. In the circle domain the crack follows the circumference over a long distance for more than $90°$. When not reaching the diffuse interface orthogonally, the lowered interfacial crack resistance has the effect of deflecting the crack path to directly reach the interface's 0.5 line, which shows as a kink in the growth direction before following the interface. This effect may be minimised by narrowing the diffuse interface.

When assigning different material properties to the thermoset ($E^{\mathrm{TS}} = 10\,\mathrm{GPa}$, $\nu^{\mathrm{TS}} = 0.3$, $G^{c,\mathrm{TS}} = 1.0\,\mathrm{J/m^2}$) and glass fibre ($E^{\mathrm{GF}} = 100\,\mathrm{GPa}$, $\nu^{\mathrm{GF}} = 0.3$, $G^{c,\mathrm{GF}} = 0.5\,\mathrm{J/m^2}$) phase, as is done in Figure 3.19, the bulk properties superimpose on the previously discussed fracture behaviour. By making ϕ^{GF} stiffer than ϕ^{TS}, the glass fibre phase acts as a barrier to fracture in this loading scenario - even with a lower bulk crack resistance. Therefore, even for no interfacial crack resistance, fracture paths are observed which follow the material interface to a certain extent. The most obvious difference is that the crack does not grow orthogonally to the diffuse interface centre, which can be seen in the $90°$ and circle domain. Additionally, as soon as the interface direction changes unfavourably, as in the circle domain, the crack path soon leaves the diffuse interface region. The obstacle behaviour of ϕ^{GF} also influences the simulations with lowered $G^{c,\alpha\beta}$. Generally for the $30°$, $45°$, $60°$ and $90°$ domains the crack
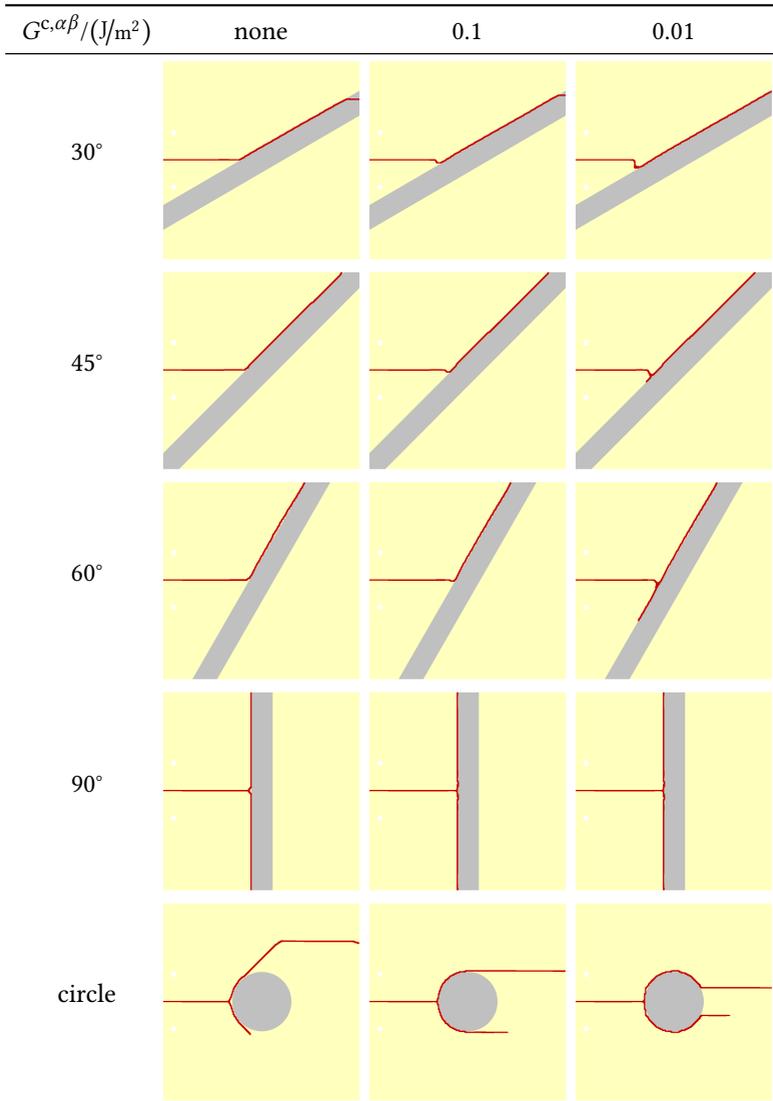
Figure 3.19: Simulation runs on domains specified in Figure 3.17. Comparison of the influence of different $G^{c,\alpha\beta}$ values on crack propagation in phases with different elastic properties and bulk crack resistances.

now stays in the interface until reaching the domain boundary - for both $G^{c,\alpha\beta}$ values. With $G^{c,\alpha\beta} = 0.01\,\text{J/m}^2$ debonding in both fibre directions may now also be observed for the 45° and 60° domains. Additionally, for $G^{c,\alpha\beta} = 0.1\,\text{J/m}^2$, crack propagation may happen along the interface for the circle domain, understandably to a lesser extent than with $G^{c,\alpha\beta} = 0.01\,\text{J/m}^2$.

The qualitative simulation results in Figures 3.18 and 3.19 emphasise the importance of introducing an interfacial crack resistance to capture certain FRP behaviour as debonding. Therefore in the following, all subsequent simulation results are achieved by using a lowered crack resistance in the diffuse interface region.

3.4   Reaction description in molecular dynamics

The molecular structure of amorphous polymers, or thermosets particularly, is highly unstructured and disordered [139]. Free chain lengths, cross-links and configurations often occur with a certain distribution, which makes the generation of artificial networks a demanding task. Hence, if a polymer networks is the subject of simulation-based research it often is generated with appropriate reaction algorithms within the simulation software itself. Different approaches exist (see, e.g. [86]), and in most cases the generation does not make use of dynamics, but statically expands the polymer network by looping bond formation criteria and a subsequent energy minimisation to adjust atom positions. Reaction algorithms mainly follow the ideas of a maximum bond formation distance (e.g. [44, 76, 200, 202], among others) and sometimes incorporate the influence of local temperature and energy barriers, e.g. via a Arrhenius-type equation (see [136, 137]). The reaction algorithm used here closely follows these ideas, but adjusts these in the context of the resin type used, whose curing reactions form urethane connections, radically propagated cross-links and peroxide group dissociations (see Section 2.3.1). In contrast to most works in molecular dynamics the reaction algorithms are applied during dynamic simulation runs to allow for a more random and natural bond forma-

tion process. The reaction algorithms presented in this section first appeared in Schwab and Denniston [164].

3.4.1 Atomistic reaction modelling

The reaction algorithm consists of three parts, which enables the simulation of the curing process of a UPPH resin (see Section 2.3.1). There exist modules for bond formation, covering urethane and the radical reaction, and for bond dissociation to simulate the initiation of the radical reaction by peroxide cleavage. A third module modifies parts of the atomic force calculation prior to time integration. The modifications include bond potential softening and disabling other intra-molecular potentials for transient bonds, which occur during the urethane reaction, and the introduction of auxiliary charges to pre-defined atoms to mimic radical atoms by introducing nucleophile and electrophile centres [114]. The basis for all presented algorithms are the *fix bond/create* and *fix bond/break* algorithms of LAMMPS and further work on this topic done by Sirk *et al.* [50, 86, 167].

Bond dissociation   Algorithm 3.20 describes the bond dissociation (B/D) procedure in a flow chart. If the module is active, the procedure is executed every N^f time steps if the absolute system temperature Θ is above a threshold temperature $\Theta^{\min}$. Within the subroutine all bonds are looped over, and their bond type is compared to bond types b^d defined to be dissociable. Each eligible bond is further processed if the calculated distance of the bond atoms is above a minimum dissociation distance d^d, which is comparable to maximal bond formation distances described in [44], among others. A last check before a bond is finally marked to be dissociated compares a randomly drawn number $P \in [0..1]$ against a bond-specific calculated threshold fraction. This fraction is
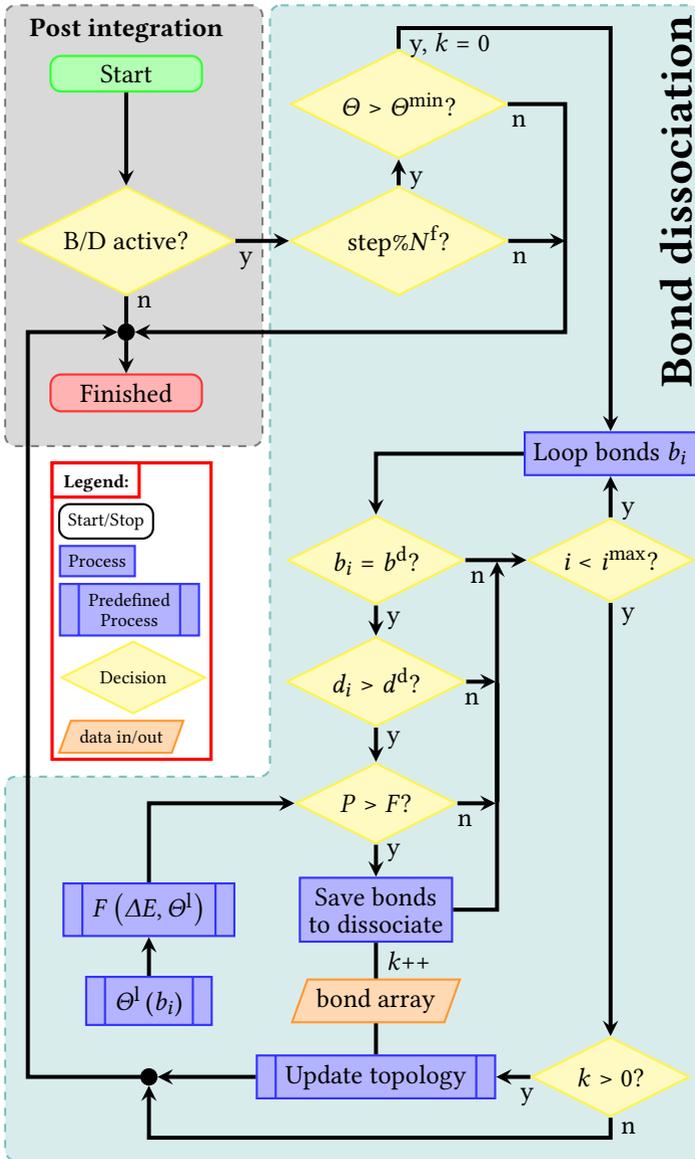
Figure 3.20: Flowchart of bond dissociation algorithm

calculated by using an Arrhenius-type equation based on reasoning done by Okabe *et al.* [136, 137],

$$F = \exp\left(-\frac{\Delta E}{k_B \Theta^{\mathrm{l}}}\right), \tag{3.103}$$

where k_B is the Boltzmann constant and Θ^{l} is the local temperature. Instead of an actual activation energy ΔE the difference between potential energy of the bond, $E^{\mathrm{b}}(b_i)$, and the dissociation energy of the bond type, E^{d}, is used (see, e.g. [17, 39, 40]). Bonds relatively close to their equilibrium length have $F \approx 1$, which results in a very small probability to dissociate the bond even at probabilities $P \gg 0$. If the local temperature Θ^{l} rises, e.g. through an elevated system temperature, the bond length tends to fluctuate and elongate more which reflects in higher $E^{\mathrm{b}}(b_i)$ and ultimately in a lower threshold fraction F. When the criterion $P > F$ is fulfilled, the bond is broken. After all bonds are looped over and at least one bond was broken, all other intra-molecular connections (see Section 2.3.2) have to be updated. All interactions which partially consisted of the dissociated bonds are removed from lists for force calculation, which completes the dissociation process. This procedure is used to initiate the radical cross-linking reaction by breaking peroxide bonds.

Bond formation   The procedure for bond formation (B/F) is summarised in Figure 3.21 as a flow chart. If active, the procedure is executed every N^{f} time steps. All atoms a_i are looped over, and for each atom a_i its neighbour atoms a_j are looped over as well. Each atom pair $\{a_i, a_j\}$ is checked to see if it consists of the bond partners for the pre-defined bond type b^{f} to be formed. Next, criteria of distance and probability are applied to determine the admissibleness of forming the new bond. Basically it is the inverted criteria already used for dissociation in the previous paragraph. Firstly, all bond partners being at distance beyond a formation distance d^{f} are sorted out. The remaining eligible atom pairs draw a random number P, which is compared to a threshold
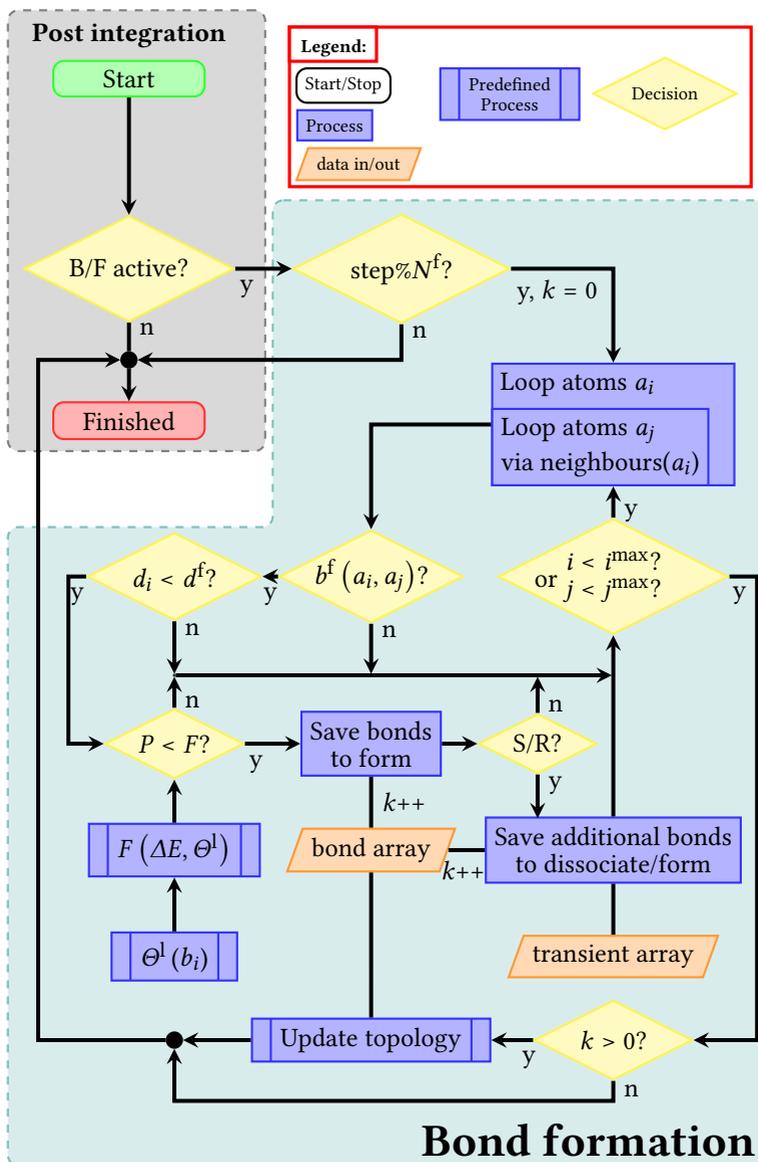
Figure 3.21: Flowchart of bond formation algorithm

fraction of the Arrhenius type equation (3.103). The new bond is established when the probability P is smaller than F, which makes bond formations more probable the closer the bond partners are to their equilibrium distance. This avoids bond formations with initially unnatural bond stretches. At elevated local temperatures Θ^l the probability for bond formation of atoms further apart becomes more likely. Bond partners satisfying these conditions are saved to update the molecular topology at the end of the procedure. Here, for every new bond the newly introduced intra-molecular connections are built and saved for force calculations. A last feature of this procedure is the possibility of allowing a side reaction (S/R), which is necessary to be able to simulate the formation of a urethane bond (see Figure 2.13). The idea is to create the new carbon-oxygen bond of the urethane connection by the standard procedure, and if such a bond is eligible to form, a side reaction is trigged to donate the hydrogen of the oxygen to the nitrogen, which completes the chemical reaction. This exchange is also saved to update the molecular topology accordingly. Furthermore the new bond partners introduced by the side reaction are saved as *transient bonds*. The purpose of this additional list is explained in the following paragraph.

Force calculation modifications   The overall bond formation procedures also install two modifications in the force calculation, which are necessary to handle the urethane and the radical reaction properly (see flow chart in Figure 3.21). As stated in the previous paragraph, the newly formed bonds, initiated by a side reaction, are saved in a separate list. These bonds are established at the time of formation of the new main carbon-oxygen bond. This makes the donation of hydrogen to nitrogen ad-hoc, which may lead to unnatural bond configurations as no prior bonding criteria are checked for the side reaction. With the list of transient bonds, the force calculation softens these bond potentials and removes other intra-molecular forces to allow for a slow and smooth transition of the hydrogen to an equilibrium configuration towards the nitrogen atom. Every time the bond formation
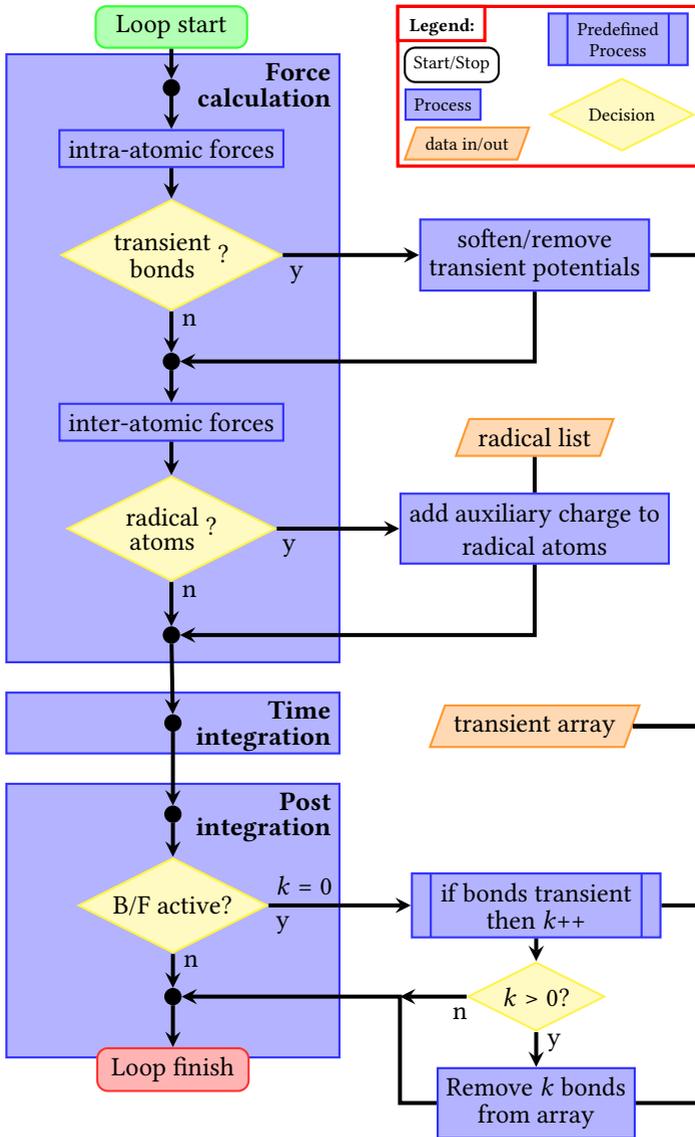
Figure 3.22: Modifications in the solver loop: treatment of transient bonds and radical centres

procedure is executed in the post integration module, all saved transient bonds are checked to see if their equilibrium is in range. The criteria for this are the same as for a standard bond formation. If the checks are positive, the respective bonds are deleted from the transient list and the full intra-molecular potentials start acting on them. The second modification introduces a radical atom list, which can be activated in case a radical polymerisation has to be simulated. The force calculation assigns pre-defined auxiliary charges to atom types saved in this list to mimic electrophile and nucleophile centres, and hence radical atoms. With these auxiliary charges the respective atoms are preferably found by each other, thus taking care to produce a proper radical propagation. Dependent on the magnitude of auxiliary charge this feature is able to increase molecule movement on the basis of the Coulombic force to speed up chemical reactions significantly, which is necessary to reduce the reaction time to fit into the molecular dynamics time scale. A discussion on effects of this speed-up is found in Section 3.4.2.

3.4.2 Reaction processes using a virtual resin system

In this section the molecular dynamics models and procedures introduced above are tried to see their general behaviour. As a test case, a virtual resin system (see Appendix B) is used, which is loosely related to the UPPH resin system described in Section 2.3.1. The simulation domain consists of 7,500 atoms with the composition described in Section 2.3.1. The simulations shown first examine the influence of auxiliary charges on reaction speed and possible influences on the polymeric networked formed. Secondly, both urethane and radical reaction procedures are tested.

Influence of auxiliary charges   In Figure 3.23a, the number of urethane connections formed over reaction time is shown. As pictured, the reaction speed increases with the magnitude of auxiliary charges added to functional groups. The increased Coulombic forces lead to bond partners locating each

other over far distances and moving faster towards each other. With increased auxiliary charges the manner of bond formation also changes: The higher the charges the closer at equilibrium distance are the bond partners at the time of bond formation as depicted in Figure 3.23b. This is strongly connected to the force field used (described in Section 2.3.2), which was not previously designed to account for reactions happening. Hence, without a modification such as the introduction of the auxiliary charges, atoms would not be able to move distances which would allow for bond formation in a reasonable time scale. Therefore, the auxiliary charges are a necessary tool to allow for bond formation at reasonable distances, which can be seen in Figure 3.23b. With lower auxiliary charges, bond formation happens at increasingly high distances, causing high initial bond stretches of the newly formed bonds, which is numerically undesirable. Furthermore, with the bond criterion based on the Arrhenius-type equation (3.103) in mind these bonds have a very low probability of being formed and their formation happens rather randomly. When disabling the auxiliary charges bond formations would not happen on the MD time scale, if not completely prohibited by the force field. While this approach is based on physical ideas, its consequences are of an artificial nature as the only purpose is to enable bonding in the chosen MD framework. It is obvious that this approach narrows the opportunities of bond formation which may occur on longer time scales, where molecule chains might re-configure. This might lead to bond partners finding each other and enabling energetically more favourable bond formations, which might be lost on the short MD time scales and in combination with the implemented models. As a result the formed polymer networks may not totally resemble their natural counterparts, and different auxiliary charges might further influence this behaviour. Figure 3.23c indicates this using the example of isotropic thermal conductivity κ^{iso}: All simulations started with the same initial configuration, but used different auxiliary charges for the urethane reaction. Analysing the resulting polymer networks, for intermediate values of the auxiliary charges a fairly isotropic material behaviour for κ^{iso} is observed. Elevated values for this artificial charge
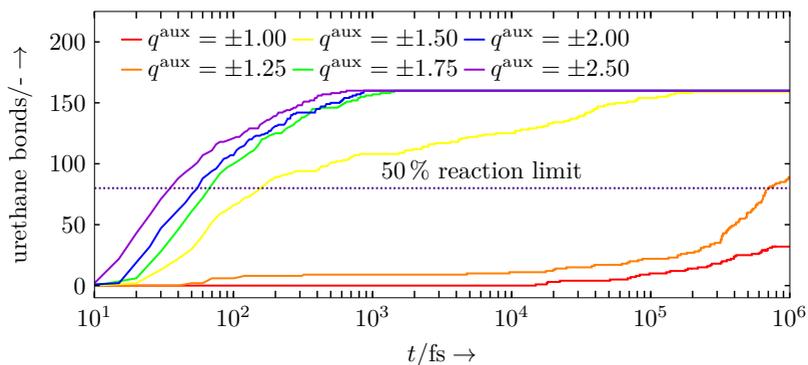
(a) Urethane reaction
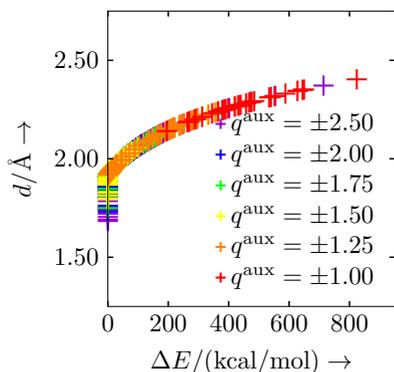
(b) Distances at bond formation
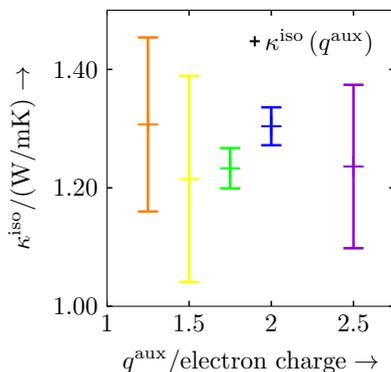
(c) Isotropic thermal conductivities κ_{iso} dependent on auxiliary charges

Figure 3.23: Virtual resin system: Acceleration of the polyurethane reaction by application of different auxiliary charges to reaction centres. Without a certain auxiliary charge reactions happen too slow for the MD timescale.

cause again stronger anisotropy, while also small auxiliary charges result in this outcome. For this scenario a possible explanation might be the lowered chance for chemical reactions as possible bond partners cannot easily move into a reasonable vicinity. This might result in chemical bonds only forming for configuration which are more easily accessed, but thus also narrowing the range of bonding configurations. As a standard thermoset generally does not exhibit noteworthy anisotropy, the magnitude of auxiliary charges is in the following chosen to be in the range of 1.5 to 2.0, dependent on the general molecule size of the resin components and numerical stability. Hence, the auxiliary charges are adjusted to a range which allows for reactions to happen within the MD time scale, but also as slow as possible to give the reactants enough time to form a more random polymer network.

Behaviour of reaction algorithms   The range of implemented reaction procedures is shown in Figure 3.24. The urethane reaction happens with auxiliary charges of $q^{\text{aux}} = \pm 1.5$ and is depicted in Figure 3.24a, which leads to nearly 100 % conversion. As the urethane reactions should result in the formation of long polymer chains, which are barely interconnected, a conversion of about 50 % is set as the final state of the reaction. This serves as an input for the radical polymerisation reaction, which is shown in Figure 3.24b. An auxiliary charge of $q^{\text{aux}} = \pm 1.0$ is assigned to radical atoms to mimic a free or available electron. Accordingly to the reaction sequence described in Section 2.3.1, the simulation starts by dissociating the peroxide bonds, which form radicals initiating the propagation of the radical reaction. The chain grows by breaking the carbon double bonds of the cross-linking molecules, which subsequentially also connect the polymer chains formed in the urethane reaction. As usual in radical reactions if radical tips of cross-linking chains meet, they terminate this particular radical propagation leading to a slower reaction progress in combination with a diminishing amount of available molecules
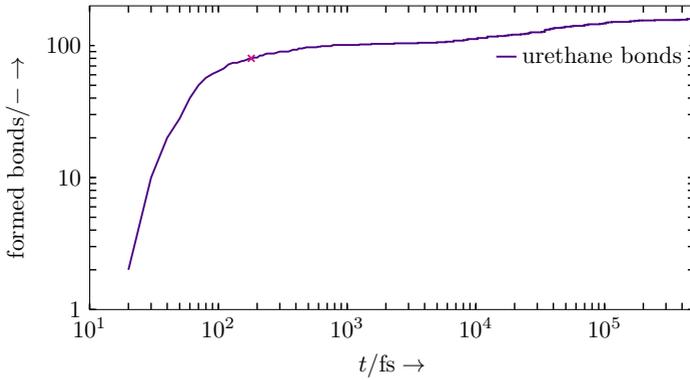
(a) Urethane reaction: violet cross marks 50 % conversion
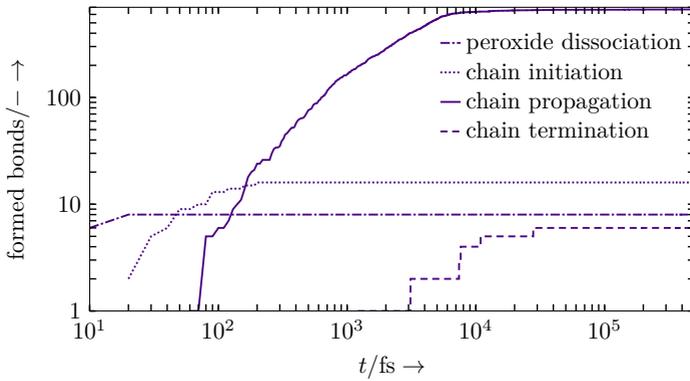
(b) Radical reaction steps, started at 50 % urethane conversion

Figure 3.24: Urethane and radical chemical reactions for the virtual resin system.

with carbon double bonds. The radical reaction ultimately stops when there are no reactants left or if they are unable to reach each other.

4

Simulations for and in the Virtual Process Chain

On the following pages, the models derived in the previous chapter are used to simulate different aspects of the curing process of fibre-reinforced thermosets (FRTS). The different aspects - thermoset (TS) characterisation simulations on a nano-scale, FRTS curing process on a micro-scale, and a follow up fracture simulation - are connected within a virtual process chain. The virtual process chain is introduced and explained in Section 4.1, where the consecutive order of the simulated aspects is given and the objectives of each field of simulations are outlined. In a first step, the curing process of the TS is simulated on the nano-scale using molecular dynamics (MD). The setup and results of these simulations are presented in Section 4.2. Selected results related to material

properties of the TS are used as input parameters for the simulation of the curing process of FRTS volume elements on a micro-scale within a phase-field (PF) framework in Section 4.3. In a last step, eigenstrain fields resulting from the curing process simulations are used to examine the micro-crack behaviour of the FRTS volume elements. This happens also on the micro-scale and within the PF framework and may be found in Section 4.4.

4.1 Virtual process chain and simulated steps

In the style of the industrial processing of FRTS, outlined in the introduction chapter 1, a virtual process chain is introduced in Figure 4.1 to illustrate the connection of simulation input, output and chronology. The general input for
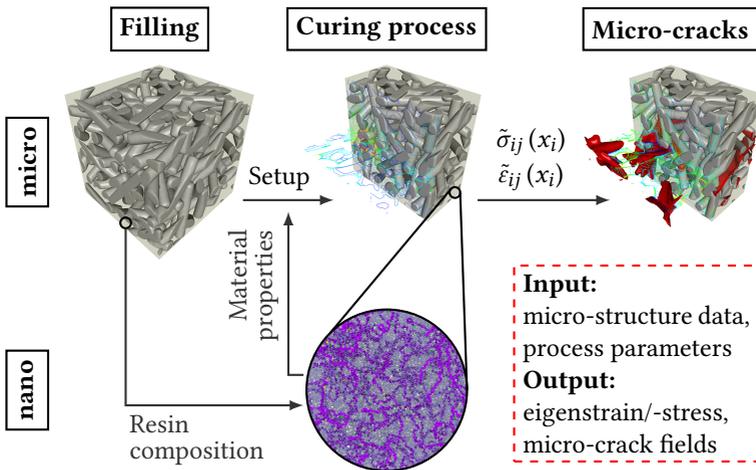
Figure 4.1: Virtual process chain: Input and output of the single simulation steps and their sequence in time.

the simulations of the virtual process chain are the materials and substances as well as their composition and arrangement on a micro- and nano-scale. Furthermore, for the process itself parameters arising from the industrial process are used as boundary and initial conditions for the simulations. From

the former, adequate and representative simulation domains may be filled or generated. In the case of the PF simulations on the micro-scale, volume elements may be created from either real data, i.e. computed tomography of details of a macroscopic structure, or artificial data, i.e. created with algorithms capable of generating images of realistic microstructures. Together with the boundary and initial conditions these volume elements are the simulation domains for the micro-scale curing process. These simulations themselves rely on a set of material properties (cf. Table 3.3) describing the substances which populate physical regions in a volume element, i.e. glass fibres and TS matrix. Commonly these material parameters are retrieved by appropriate experiments or values from literature. In this work a larger portion of the material properties describing the TS matrix is calculated from MD simulations conducted on a nano-scale.

In order to calculate material parameters of a substance by means of MD requires having molecular representations of the TS matrix. As the polymer chain network, in general, is quite irregular and of low order, these nano-scale representations are generated by simulating the curing reactions explicitly. These simulations need the composition of the TS resin, the molecular structure of each resin component and the knowledge about the involved curing reactions as an input. With the same boundary conditions as used on a micro-scale the curing process is simulated on the basis of algorithms mimicking bond formation and dissociation. The resulting polymer networks are then analysed in simulation setups measuring the change in state variables of the system domain such as volume or total energy. Either through statistical mechanical or experimental approaches thermodynamic properties may be calculated from the measured data. A convenient side-effect in using MD for retrieving material properties is that these may be calculated easily in different setups of constant temperature or constant degree of cure.

With the list of material properties being completed through MD simulations, experimental and literature data the FRTS curing process is simulated within the PF framework. These simulations allow tracking of the development of

quantities such as temperature or mechanical stresses induced by the curing process and analysis of locations where quantities adopt maxima or minima. In a next step, the mechanical eigenstress or eigenstrain fields $\tilde{\sigma}_{ij}(x_i)$, $\tilde{\varepsilon}_{ij}(x_i)$ may be used to analyse the respective volume elements for the formation and propagation of micro-cracks.

The results on the micro-scale may firstly be used to further understand behaviour and processes within the FRTS microstructure, and furthermore, they may be used as input data in the form of eigenstress or damage in macro-scale simulations of whole structures. Secondly, this virtual process chain could be cycled to study the influence of different sets of process parameters, hence boundary conditions, or material configurations on the resulting mechanical behaviour. Sets of process parameters and microstructure configurations may be identified which keep process induced eigenstresses and micro-cracks at a minimum and therefore enhance the macroscopic material behaviour. Lastly, the same procedure may be performed on a nano-scale by studying the influence of different resin components and curing parameters on the resulting polymer network behaviour, creating a possibility to find a thermoset with improved material properties.

Within this work, the virtual process chain is tested, and the connection and interplay of the single simulation steps and techniques is demonstrated. A further analysis in the form of simulation studies on process parameters or with the intent of material improvement is not the scope of this work.

4.2 Material properties through molecular dynamics simulations

Within this section MD setups are used to simulate the curing process of a TS resin on the nano-scale. As mentioned in Section 1.2, the simulations are conducted with the open source software LAMMPS [150] and use the models described in Section 3.4.1. The reaction process and progress is presented and on the basis of these results material properties of the TS are calculated. Fur-

thermore, the evaluation happens at different degrees of cure and temperatures to be able to describe the development of material properties throughout the complete curing process. The results of this sections are partially published in Schwab and Denniston [164].

4.2.1   Representation of the resin and simulation setup

Generally, if not mentioned otherwise, each MD simulation uses an NPT ensemble, thus describing a constant number of atoms, constant pressure and constant temperature. Within LAMMPS this is implemented by *fix nve* for the time integration, while temperature is controlled with a Langevin thermostat (*fix langevin*) and pressure is governed by a Berendsen barostat (*fix berendsen/press*). Furthermore all system domains use periodic boundaries and parameters use LAMMPS real units.

Based on Section 2.3.1, the TS resin's molecule types are built in the open-source software Avogadro [9]. All molecule types are placed into a simulation domain following the compound's composition listed in Table 2.3. The filling happens randomly in position and orientation as noted in the first step of Figure 4.2. For this purpose, and for adequate and unproblematic filling, the initial simulation box size is chosen to the volume occupied by the largest occurring molecule times the total amount of molecules. To complete the initial filling, the molecules' atoms and potentials have parameters assigned according to the Compass force field [176–178]. A small number of potentials whose parameters are not available in literature have parameters assigned to potentials resembling atoms of the same group of the periodic table. Potentials describing cross-terms are left blank if not parametrised in literature. After the simulation domain is filled, a randomisation run is started. At a high absolute temperature the molecules may move into random positions. In a next step the simulation box is compressed towards the expected mass density. This happens step-wise in a cycle of volume shrinkage, minimisation and equilibration runs. Lastly, the shrunk system domain is equilibrated at room temperature and standard pressure to allow the system to relax towards its natural mass density.
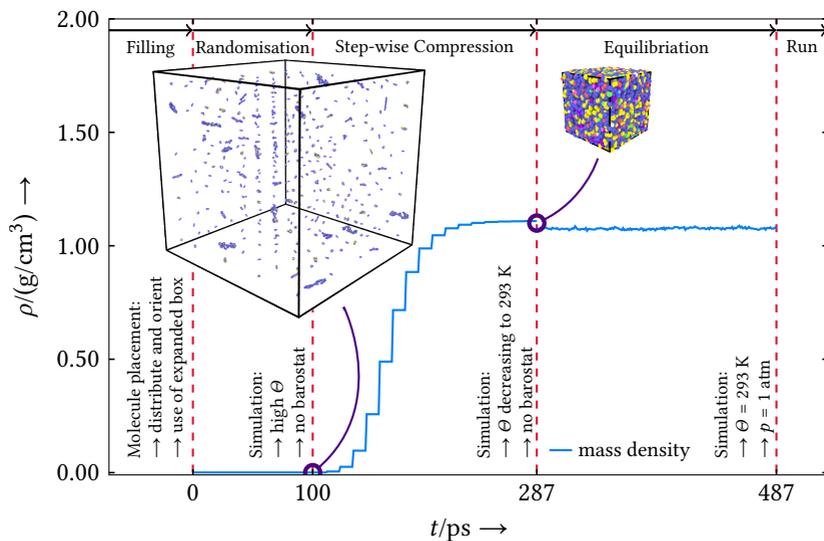
Figure 4.2: Pre-processing of the system domain: Filling, compression and equilibration.

The actual curing reaction simulations are performed according to the resin's two-step procedure, which is also applied in industrial processes (cf. Section 2.3.1). A summary of its realisation in the scope of MD is given in Table 4.1, which is based on [25]. Following this process, the polyurethane reaction is

run	time in ps	Δt in fs	ensemble	temperature in K	pressure in atm
urethane	500	0.1	NPT	313.0	1.00
radical	500	0.1	NPT	418.0	98.69

Table 4.1: Curing reaction simulations: Parameters used for the two-step reaction.

carried out first. The simulation happens at a temperature of $\Theta = 313\,\text{K}$ and standard pressure. To create the urethane connections the bond formation is allowed between hydroxyl and isocyanate groups following the algorithms described in Section 3.4.1. To accelerate the reaction, auxiliary charges of

$q^{\text{aux}} = \pm 1.5$ are applied. For the probabilistic part of the bond formation algorithm, bond dissociation energies of $E^{\text{d}} = -85.56\,\text{kcal}/\text{mol}$ (C-O) and $E^{\text{d}} = -93.45\,\text{kcal}/\text{mol}$ (N-H) are used [17, 39, 40]. The reaction is considered complete when approximately 50 % conversion is reached. This percentage is chosen arbitrarily, but accommodates the fact that this reaction yields the creation of long polymer chains with few loose interconnections. A 100 % conversion would indicate a dense polymer network, which is not desired but likely to happen in small well-mixed system domains. For the second reaction step, the radical polymerisation, the temperature is changed to $\Theta = 418\,\text{K}$ and the pressure is set to $p = 10\,\text{MPa}$ ($\approx 98.69\,\text{atm}$) to simulate the mould pressure. The dissociation of the peroxide bond is allowed for temperatures $\Theta > 333\,\text{K}$ and to guarantee breakage, the dissociation energy is kept low ($E^{\text{d}} = -0.001\,\text{kcal}/\text{mol}$). For the radical centres the auxiliary charges are set to $q^{\text{aux}} = \pm 1.0$ to resemble free electrons and electron clusters. The formation of C-O bonds uses again $E^{\text{d}} = -85.56\,\text{kcal}/\text{mol}$, while C-C bonds have $E^{\text{d}} = -82.70\,\text{kcal}/\text{mol}$ [17, 39, 40]. Both reaction steps are simulated for $t = 500\,\text{ps}$, which is sufficient to reach acceptable chemical conversions.

To verify the repeatability of the reaction simulations and for later use in material property evaluation, different configurations of the resin system are realised. Three different configurations of a *small* system domain comprising approximately 14,000 atoms are set up. A fourth, *larger* system is eight times the size of a small one and hence is filled with about 112,000 atoms.

4.2.2 Thermoset curing simulation on the nano-scale

In this section, the curing reaction simulations of the UPPH resin are presented. Firstly, the conversion with respect to the two chemical reactions is shown. From these results basic properties are evaluated, namely the change in mass density characterising the volume shrinkage due to the curing reaction and the remaining amount of styrene molecules. Styrene is a volatile organic compound (VOC), which may cause plastics to have a typical odour [201]. As a last property in this section, the change in enthalpy is documented.

The curing reaction is shown in Figure 4.3, separated into urethane polyaddition and radical polymerisation. Results are depicted for the small resin systems as well as for the large resin system. Due to the auxiliary charges, the
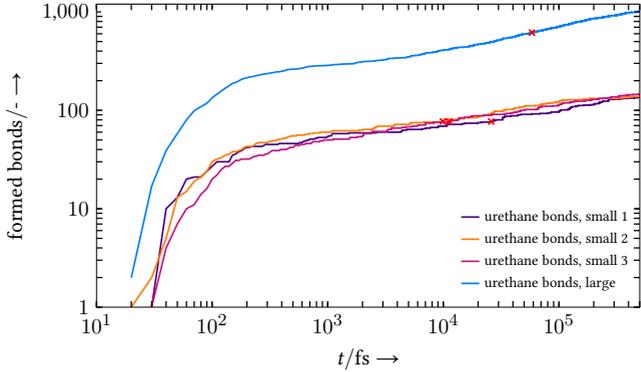
(a) Formed urethane connections: red crosses mark 50 % conversion
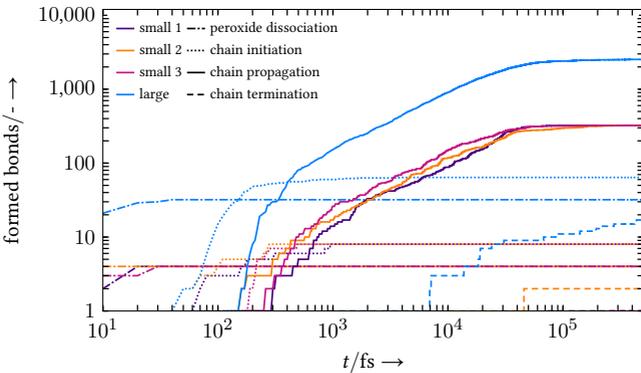
(b) Radical reaction steps, started at 50 % urethane conversion

Figure 4.3: Hybrid resin systems: Urethane and radical chemical reactions.

chemical reactions happen in a reasonable MD time scale, and after $t = 500\,\text{ps}$, the urethane reaction is far above the desired 50 % conversion limit. The radical reaction runs reach conversions of 96 % - 97 % in case of the small systems and

95 % for the large system. At this point the radical reaction is already visibly diminished for both system sizes. This is mostly due to radical centres being far apart either only able to reach each other on a much longer time scale, or completely unable to reach each other due to already being well integrated in the polymer network. The radical reaction itself follows the typical scheme of initiation, propagation and termination. At the elevated temperature the peroxide rapidly dissociates, leaving radical oxygen atoms behind. These initiate the chain propagation by forming bonds with nearby carbon double bonds, which continue the cross-link formation by successively connecting the polyurethane backbones (see Figure 4.4). At later stages, if radical centres meet, the respective chains are terminated. The remaining amount of cross-linking
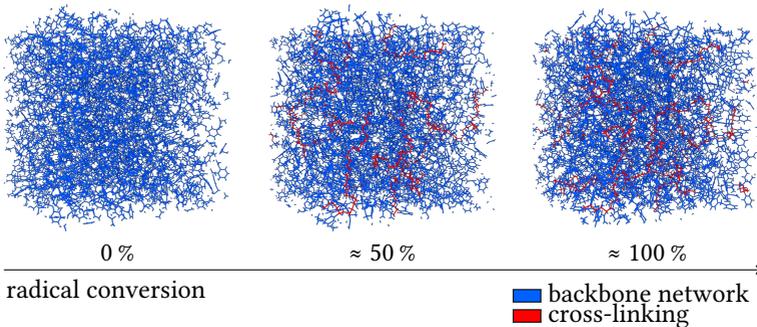
Figure 4.4: Hybrid resin system: Bonds forming cross-links are highlighted.

styrene molecules is listed in Table 4.2, which is not expected to significantly decrease further. The amount is also nearly identical for both system sizes.

	small system	large system
remaining cross-linkers	$4.01 \pm 0.57\,\%$	$4.39\,\%$

Table 4.2: Remaining styrene molecules: volatile organic compounds

The remaining styrene molecules, especially at elevated temperatures, diffuse

from the TS network and may cause a typical odour [201]. The larger the amount of remaining VOC the more persistent the odour may be, and elevated amounts may pose health risks.

To evaluate the change in mass density and enthalpy, the simulation domains are equilibrated at $\Theta = 293\,K$ and $p = 1\,atm$. The starting point for these runs are the domains after the urethane reaction and after the radical reaction. Especially the change in mass density, and hence volume, is documented and referenced at room temperature to not incorporate additional thermal expansion at higher temperatures. The change in mass density is noted in Table 4.3. Again, for both system sizes a similar result is obtained and the observed range is typical for thermosetting resins. Other hybrid resins, e.g. presented in [190], show volume shrinkages of 5.6 % and 7.5 %. Lastly, the change in enthalpy is

	small system	large system
total reaction	$-5.33^{+0.24}_{-0.20}\,\%$	$-5.42\,\%$
radical reaction	$-4.70^{+0.34}_{-0.30}\,\%$	$-4.55\,\%$

Table 4.3: Change in mass density due to chemical reactions (at $\Theta = 293\,K$ and $p = 1\,atm$)

shown in Table 4.4, where both system sizes show a similar behaviour as well. The change in enthalpy given here is the released reaction enthalpy, which is an indicator for the exothermic character of the radical polymerisation. As the chemical reaction algorithms are strongly simplified and features a partially artificial component due to the auxiliary charges, the released reaction enthalpy is not expected to match closely to experimental values. In [163], on the basis of DSC measurements of a hybrid resin, released reaction enthalpies of around 200 kJ/kg are calculated. These values are found by integration of the measured heat flux (see Section 2.3.3), and therefore may also only be in proportion to the true released reaction enthalpy.

	small system	large system
Δh in kJ/kg	-80.47 ± 1.43	-80.90

Table 4.4: Change in enthalpy due to radical reaction (at $\Theta = 293$ K and $p = 1$ atm)

4.2.3 Evaluation and material property calculation

On the following pages, the previous curing process simulations are used to determine a set of material properties necessary to describe the TS on a microscale (cf. Table 3.3). For the material parameter evaluation, the techniques described in Section 2.4, regarding equilibrium molecular dynamics (EMD) and non-equilibrium molecular dynamics (NEMD), are used. If an equilibration run is conducted prior to the evaluation run, the setup is generally an NPT ensemble at $p = 1$ atm and the desired temperature. Properties are evaluated along the complete curing process and for different temperatures around room and mould temperature. The degrees of cure are chosen to be preferably $\zeta^{\mathrm{u}} = \{0, 50\}$ % for the urethane reaction and $\zeta^{\mathrm{r}} = \{0, 20, 40, 60, 80, 100\}$ % for the radical reaction, where $\zeta^{\mathrm{u}} = 50$ % corresponds to $\zeta^{\mathrm{r}} = 0$ %. If specific degrees of cure are not met by the curing simulations, states as close by as possible are picked. For an unambiguous labelling of different degrees of cure and chemical conversions a notation of the form UxRy is adapted, where x is replaced by the amount of urethane conversion and y respectively by the amount of radical conversion. For example, the notation U50R33 would indicate a system domain, which has $\zeta^{\mathrm{u}} = 50$ % urethane conversion and $\zeta^{\mathrm{r}} = 33$ % radical conversion. The seven distinct data points along the curing reactions are accompanied by up to four temperatures located in the vicinity of the room and mould temperature, i.e. $\Theta = \{273, 313, 398, 438\}$ K. Together, the chosen degrees of cure and temperatures span the space of material property dependence. For the initial degree of cure of interest, U0R0, only the temperatures $\Theta = \{273, 313\}$ K are evaluated, because the urethane reaction happens at temperatures $\Theta < 333$ K. There will not be direct comparison of the calculated material properties to literature

values of a specific thermoset, because hybrid resins are rarely characterised and furthermore because the molecular structure and resin composition of the examined resin is not available in full detail. However, a comparison to material property ranges of common thermosets will be done.

Specific heat capacity at constant volume   All system setups were first equilibrated for $t = 1$ ns in an NPT ensemble and then restarted and simulated in an NVT ensemble for up to 5 ns. The measured fluctuations in total energy and temperature are used to calculate the mass specific heat capacity at constant volume, c_V, as denoted in Equation (2.75). The calculation happens for every data point in temperature and degree of cure in the sense of a cumulative average, which develops under consideration of all previous values of total energy and temperature. Hence, as depicted in Figure 4.5, c_V quickly converges
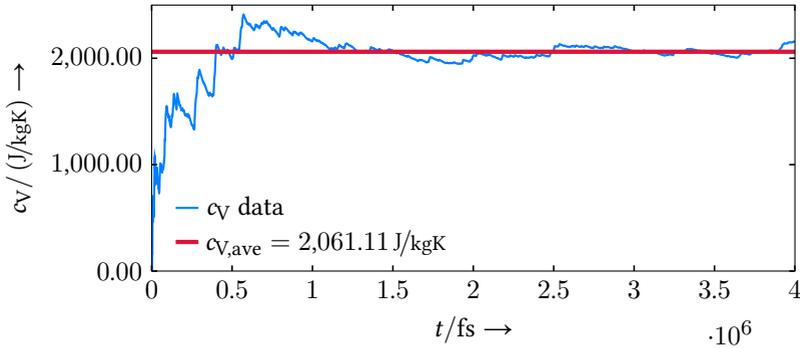
Figure 4.5: Exemplary specific heat capacity evaluation for U50R72 at 313 K

towards an average value as the occasional strong fluctuation has an decreasing influence on the cumulative average. For every calculation the initial measured data up to $t = 1$ ns is excluded from averaging to avoid effects from switching from the NPT to NVT ensemble. The results are listed in Table 4.5 and depicted in Figure 4.6, respectively. Each c_V is calculated as an weighted average of the results of all three small resin systems. As the three resins systems may not

(ζ, Θ)	273 K	313 K	398 K	438 K
U0R0$^{+0}_{-0}$	$2{,}257^{+94}_{-127}$	$2{,}034^{+116}_{-114}$	—	—
U50R0$^{+0}_{-0}$	$2{,}441^{+252}_{-144}$	$2{,}165^{+63}_{-67}$	$2{,}017^{+166}_{-208}$	$2{,}287^{+207}_{-191}$
U50R20$^{+0}_{-0}$	$2{,}362^{+149}_{-92}$	$2{,}337^{+74}_{-90}$	$2{,}273^{+134}_{-82}$	$2{,}246^{+516}_{-334}$
U50R40$^{+6}_{-5}$	$2{,}104^{+353}_{-24}$	$2{,}020^{+437}_{-63}$	$2{,}110^{+171}_{-369}$	$1{,}959^{+427}_{-34}$
U50R67$^{+5}_{-3}$	$2{,}484^{+229}_{-202}$	$2{,}299^{+116}_{-238}$	$2{,}298^{+74}_{-93}$	$2{,}497^{+286}_{-188}$
U50R82$^{+5}_{-2}$	$2{,}306^{+88}_{-253}$	$2{,}137^{+299}_{-180}$	$2{,}443^{+88}_{-26}$	$2{,}464^{+33}_{-20}$
U50R97$^{+0}_{-1}$	$2{,}124^{+308}_{-224}$	$2{,}071^{+330}_{-256}$	$2{,}298^{+127}_{-143}$	$2{,}696^{+658}_{-166}$

Table 4.5: Specific heat capacity at constant volume as a weighted average of the small hybrid resin systems, $c_V(\zeta, \Theta)$, in J/(kgK)

be evaluated at the exact same degree of cure, the calculated c_V is assigned to the respective average degree of cure. The calculated overall behaviour of the specific heat capacity at constant volume, c_V, is very diverse. Three main characteristics of the behaviour are

- a prominent ditch along temperature for a degree of cure of about U50R40,

- a crest-like structure on the left and right of the identified ditch,

- and a deviation from this topology at high curing levels and elevated temperatures, where c_V peaks.

The general trend of cured thermosets of a rising heat capacity with temperature [112] is observable, and the magnitude of c_V is in an acceptable range and agreement to polymers in general [63, 112]. The same trend is visible, but to a much lesser extent, for lower degrees of cure, often going along with an interim decrease of c_V for intermediate temperatures. This rather rough pattern of development with temperature is indeed observed for thermosetting polymers [195, 196].
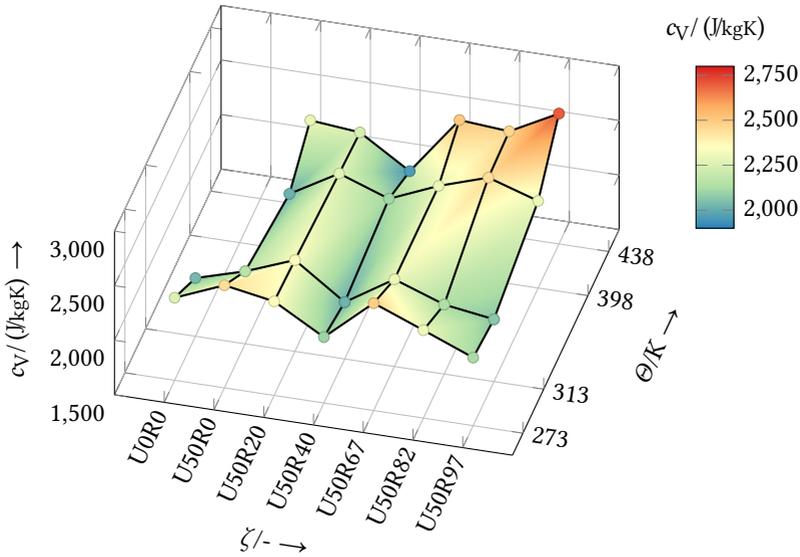
Figure 4.6: Specific heat capacity dependent on degree of cure ζ and temperature Θ

Thermal conductivity   As done previously, all system setups were first equilibrated for $t = 1\,\text{ns}$ in an NPT ensemble, and were then restarted and simulated in an NVT ensemble for up to $5\,\text{ns}$. During each NVT run the Green-Kubo formula for the thermal conductivity (2.77) is evaluated. The thermal conductivity is calculated each 8,000 time steps, which was tested to be sufficient to have no auto-correlation of the heat flux at the end of this time interval, and hence integration is able to lead to a constant value. Additionally it is pointed out that the centre-of-mass motion is subtracted during these simulations to suppress convective heat flux, which would be an undesired influence on the measured thermal conductivity [83].

Because of the unstructured polymer network of amorphous thermosets, which should not lead to a predominant direction for the heat flux for sufficient large domain sizes, the isotropy of the thermal conductivity is predisposed. As depicted in Figure 4.7, the isotropic thermal conductivity is calculated for

each combination of degree of cure and ζ temperature Θ on the basis of the time steps of the last $1\,\mathrm{ns}$ of the simulations. As described for the specific
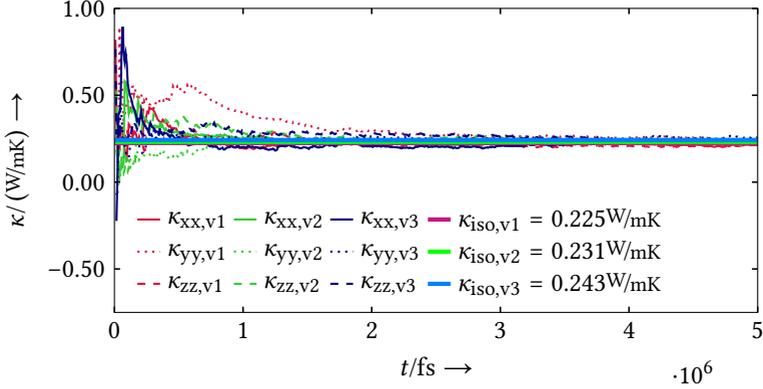
Figure 4.7: Exemplary thermal conductivity evaluation for U50R67 at 313 K

heat capacity, the values of all three systems are combined via a weighted-average for each data point in the parameter space. The results are listed in Table 4.6. In Figure 4.8 the same values are shown in a three-dimensional

(ζ, Θ)	273 K	313 K	398 K	438 K
$\mathrm{U0R0}^{+0}_{-0}$	$0.210^{+0.002}_{-0.003}$	$0.215^{+0.006}_{-0.010}$	—	—
$\mathrm{U50R0}^{+0}_{-0}$	$0.225^{+0.005}_{-0.008}$	$0.225^{+0.016}_{-0.008}$	$0.225^{+0.001}_{-0.001}$	$0.210^{+0.015}_{-0.013}$
$\mathrm{U50R20}^{+0}_{-0}$	$0.225^{+0.008}_{-0.006}$	$0.231^{+0.014}_{-0.008}$	$0.230^{+0.024}_{-0.018}$	$0.224^{+0.013}_{-0.012}$
$\mathrm{U50R40}^{+6}_{-5}$	$0.226^{+0.012}_{-0.017}$	$0.233^{+0.012}_{-0.010}$	$0.223^{+0.007}_{-0.012}$	$0.231^{+0.010}_{-0.014}$
$\mathrm{U50R67}^{+5}_{-3}$	$0.230^{+0.011}_{-0.015}$	$0.233^{+0.010}_{-0.008}$	$0.243^{+0.022}_{-0.018}$	$0.238^{+0.029}_{-0.015}$
$\mathrm{U50R82}^{+5}_{-2}$	$0.239^{+0.018}_{-0.022}$	$0.234^{+0.004}_{-0.007}$	$0.246^{+0.012}_{-0.017}$	$0.254^{+0.015}_{-0.017}$
$\mathrm{U50R97}^{+0}_{-1}$	$0.259^{+0.010}_{-0.014}$	$0.246^{+0.010}_{-0.015}$	$0.261^{+0.011}_{-0.010}$	$0.235^{+0.012}_{-0.016}$

Table 4.6: Isotropic thermal conductivity as a weighted average of the small hybrid resin systems, $\kappa\,(\zeta, \Theta)$, in $\mathrm{W/(mK)}$

plot. The magnitude and the general trend of the thermal conductivity κ
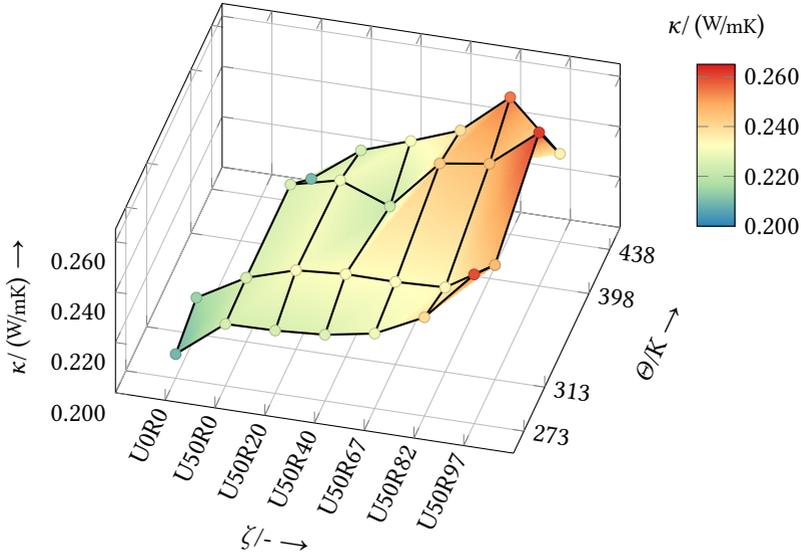
Figure 4.8: Isotropic thermal conductivity dependent on degree of cure ζ and temperature Θ

for the fully cured system is again in agreement with values for thermosets found in literature [63, 112], namely an increase in κ with temperature is found. Generally an increased thermal conductivity with degree of cure may be expected due to an increasing cross-linking density, which facilitates the transmission of temperature-dependent motions and vibrations.

Therefore, the overall picture meets the expectations, except for single data points, e.g. at $\Theta = 438\,\text{K}$ and U50R97. The deviations from the pattern might be straightened out by measuring additional realisations of the system domain and by removing single outliers.

Thermal expansion and glass transition temperature In an NPT ensemble a series of equilibration runs is conducted, each at a pressure of $p = 1\,\text{atm}$, but with different constant temperatures ranging from 233 K to 473 K, applied

in 10 K steps, and every simulation runs for 0.1 ns. The small resin system is used and for every system, temperature and degree of cure the volume is averaged over the last 50 ps. The resulting volume is referenced to the volume at a reference temperature of Θ^{Ref} = 293 K, and the same weighted averaging as in the previous two paragraphs is applied for the three different system domains. The data points found are depicted in Figure 4.9, and fitted by a continuous and piecewise linear regression allowing for one break point, where each linear part resembles the thermodynamic relation (2.78). The break points are
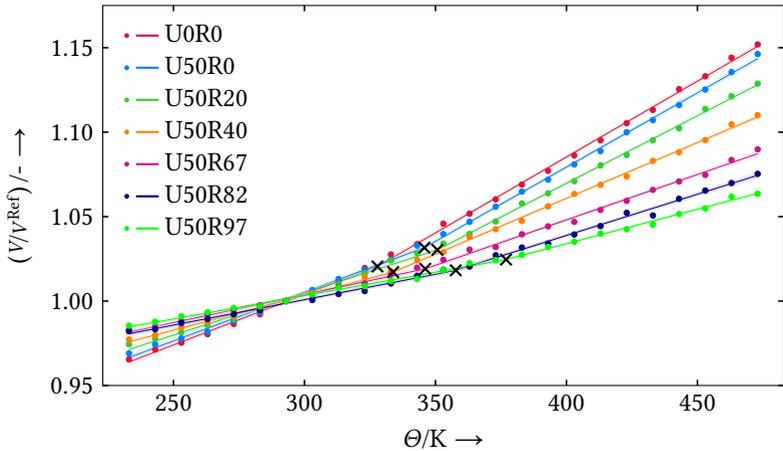
Figure 4.9: Volumetric thermal expansion for different degrees of cure ζ and with a reference temperature of Θ^{Ref} = 293 K, black crosses mark the respective glass transition temperature Θ^{g}. Each shaded area indicates the 99.75 % confidence interval of the piecewise linear fit.

associated with the glass transition temperature Θ^{g} [98], and the slope of the linear fits below and above Θ^{g} is the respective volumetric thermal expansion coefficient α^{vol}. Via the simplified relation $\alpha^{\text{lin}} = \alpha^{\text{vol}}/3$ the isotropic linear thermal expansion coefficient is calculated. The results are listed in Table 4.7. By comparison to literature values [63, 80, 112] the thermal expansion values appear to be in the range of typical thermosetting polymers. For Θ^{g} only a moderate increase is observed along the curing reaction range, which is in

ζ	Θ^g in K	α^{vol} in 10^{-5} 1/K		α^{lin} in 10^{-5} 1/K	
		$\Theta < \Theta^g$	$\Theta \geq \Theta^g$	$\Theta < \Theta^g$	$\Theta \geq \Theta^g$
U0R0	327.6	59.6	89.8	19.9	29.9
U50R0	346.3	57.7	88.0	19.2	29.3
U50R20	351.7	50.3	80.1	16.8	26.7
U50R40	334.1	41.0	66.1	13.7	22.0
U50R67	345.2	33.0	53.6	11.0	17.9
U50R82	358.4	30.2	48.9	10.1	16.3
U50R97	374.4	27.6	40.4	9.2	13.5

Table 4.7: Volumetric and linear thermal expansion coefficient below and above the glass transition temperature Θ^g, as retrieved from the piecewise linear fit in Figure 4.9.

contrast to what is to be expected for cross-linking thermosets [141, 148]. The answer to this deviation may lie in the simulatively reacted cross-links, which may not be as densely created as it is in the real process. In [148] it is pointed out, that Θ^g increases, when the length of cross-link chains is equal or smaller than the average segment size of the polymer backbone. An analysis of the simulated system domain with respect to the cross-linking structure is not part of the scope of this work, but by conclusion from the calculated material properties the cross-link density may be low or the average cross-link chain length may be too long in comparison to typical real thermosets. In such cases the cross-linked polymer network is below average in rigidity, which may allow for a less restricted movement of polymer chain segments explaining the observed increased volume expansion with temperature, among other things. From the general simulative point of view finite size effects may impact these values as well, because the longest chain segment is restricted to the system size. Analogously the range of other calculated material parameters may be classified. The development of the glass transition temperature depicted in Figure 4.9 is separately shown in Figure 4.10. Ignoring the magnitude of Θ^g and the two outliers at U50R0, U50R20, the shape of its general development is comparable to that of thermosets shown in [141, 153]. A fit to DiBenedetto's
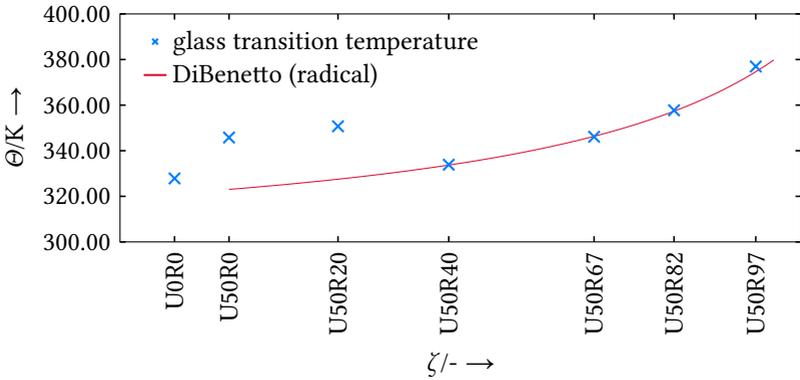
Figure 4.10: Glass transition temperature Θ^{g} for different degrees of cure ζ.

approach (2.72) for the radical part of the curing reaction supports this observation. As mentioned for the calculation of the specific heat capacity and the thermal conductivity, a larger set of variants of the same resin system and hence a broader data basis may help to achieve smoother results with respect to developing degree of cure and to identify outliers.

Bulk modulus   The bulk modulus is evaluated using the large resin system. At each combination of degree of cure and temperature the system box is firstly equilibrated in an NPT ensemble at atmospheric pressure for $t = 1\,\mathrm{ns}$. The NEMD run then is conducted for $t = 6\,\mathrm{ns}$ in an NVT ensemble and simulates one compression-expansion cycle, starting with compression. The change of the simulation box is directly controlled (*fix deform*) by uniformly and continuously shrinking the box edges by $1\,\%$ each. For fitting, the measured pressure response is referenced to the equilibrium volume at zero deformation, V^{Ref}, and averaged over intervals of ten thousand time steps as depicted in Figure 4.11. The averaged pressure values are then fit by linear regression under exclusion of the first quarter of the cycle to neglect undesired start-up effects. According to Equation (2.79) the slope of the linear fit is interpreted

as the bulk modulus at the respective degree of cure and temperature. NEMD
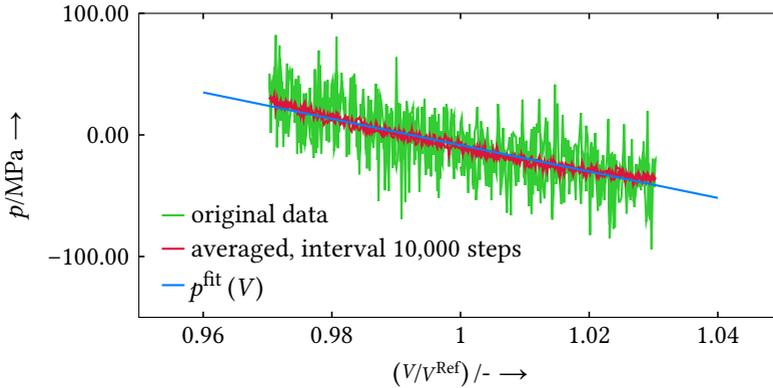
Figure 4.11: Exemplary bulk modulus evaluation for U50R0 at 398 K

runs at elevated temperatures and progressed degrees of cure caused irregular simulation failures due to quickly accelerating atoms. Attempts of solving these failures included lowering the hysteresis' amplitude or decreasing the rate of deformation. Numerically it was tried to remedy the observed behaviour by applying a multi-timescale integrator (*rRESPA*) [184], which sub-divides the time integration for different types of energy potentials. Neither of these attempts solved the problem of irregularly failing simulations. To at least predict the bulk modulus in those parameter ranges, a different time integrator was chosen. With *fix nve/limit* it is possible to limit the movement of atoms which attempt to cover a distance large than a pre-defined value in one time step, which was chosen to be 0.5 Å. While this approach is able to stop atoms from moving too far in one time step, each intervention of this algorithm violates the conservation of energy. To be able to estimate a possible error in calculation, the number of interventions was output and is exemplarily depicted in Figure 4.12 for the system with the highest temperature and degree of cure. This estimation shows, that during a simulation time of six million time steps only 55 atoms had to be limited, mostly at a few distinct time steps
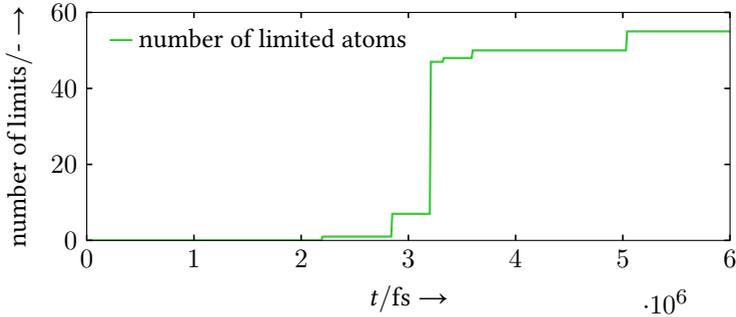
Figure 4.12: Number of interventions of the limited time integration for a system at $\Theta = 438\,\text{K}$ and a degree of cure of U50R95

in the tension regime. In relation to the run time and the large system size, this number happens to be negligibly small and is expected to not significantly alter the simulation outcome. Furthermore, analysis of the limited atoms showed, that all atoms except for one were hydrogen atoms, hence atoms not directly part of the polymer backbone and only associated with a small mass, which further lowers the energetic influence. The measured bulk moduli K are listed in Table 4.8, where values are marked by the numeral 1 if a run was conducted with *fix nve/limit*. The values are in reasonable agreement with bulk moduli of thermosets [63, 112], and in Figure 4.13 the pattern reveals a nearly linear increase in bulk modulus with degree of cure and temperature. An observation not explicitly shown in the results is the slight viscous behaviour of the pressure response. This rate-dependence, which is more obvious at lower temperatures and with higher degrees of cure, is neglected, as the simulations apply the deformation in the gigahertz range. Hence, for commonly occurring frequencies this effect should be diminished. As with to the calculations with the small resin systems, the evaluation of a larger set of independent realisations of the system domain may help to more accurately determine this material property.

(ζ, Θ)	273 K	313 K	398 K	438 K
U0R0	$2{,}012 \pm 13$	$1{,}584 \pm 10$	—	—
U50R0	$2{,}168 \pm 14$	$1{,}751 \pm 11$	$1{,}070 \pm 9$	781 ± 8
U50R20	$2{,}464 \pm 15$	$2{,}104 \pm 15$	$1{,}132 \pm 9$	$1{,}093 \pm 9^{1}$
U50R33	$2{,}679 \pm 18$	$2{,}285 \pm 16$	$1{,}546 \pm 11^{1}$	$1{,}203 \pm 10^{1}$
U50R67	$3{,}037 \pm 19^{1}$	$2{,}676 \pm 17^{1}$	$1{,}858 \pm 13^{1}$	$1{,}530 \pm 12^{1}$
U50R82	$3{,}098 \pm 21^{1}$	$2{,}762 \pm 18^{1}$	$2{,}134 \pm 15^{1}$	$1{,}750 \pm 14^{1}$
U50R95	$3{,}236 \pm 20^{1}$	$2{,}933 \pm 21^{1}$	$2{,}325 \pm 16^{1}$	$1{,}961 \pm 17^{1}$

[1] with *fix nve/limit*

Table 4.8: Bulk modulus of the large system, $K(\zeta, \Theta)$, in MPa and respective uncertainty of the linear regression
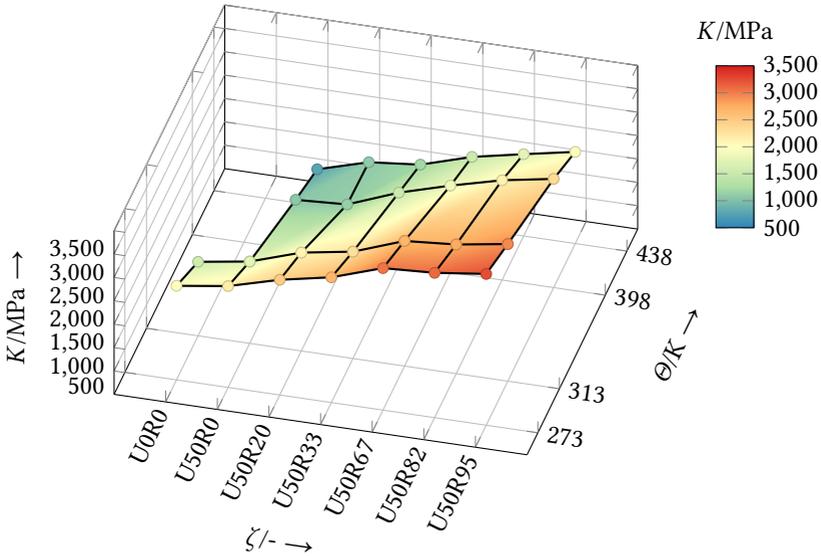
Figure 4.13: Bulk modulus dependent on degree of cure ζ and temperature Θ

Shear modulus and viscosity   Prior to the NEMD run, an equilibration is conducted in an NPT ensemble, for $t = 1$ ns, at atmospheric pressure and the desired temperature. As for the bulk modulus runs the large system domain is used. The NEMD simulation is run following the protocol in Section 2.4.2, and the shear deformation is successively applied in all three shear directions of the Cartesian coordinate system, each for $t = 10$ ns. The superposed sinusoidal shear consists of seven angular frequencies based on multiples of prime numbers, $\omega_i = \{2, 3, 5, 7, 11, 13, 17\}\, \omega^0$, where a base frequency of $\omega^0 = \pi \cdot 10^{-6}$ 1/fs is chosen. The amplitude is uniformly $a_i = 0.35$ Å.

The frequencies applied are several magnitudes higher than the usual frequencies applied in a common dynamic mechanical analysis (DMA), hence the results may be beyond the range of interest close to equilibrium deformation rates. Lower frequencies may only be achieved by longer simulation times, which is computationally expensive. Therefore, in the scope of this work, only one exemplary run is performed for a system at $\Theta = 273$ K and U50R95.

During the simulative DMA run the shear strain $\gamma(t)$ and the shear stress response $\tau(t)$ for all three shear directions are measured. The recorded quantities of the three sub-runs (see Figure 4.14) are collected in one data set as an isotropic behaviour of the material properties is assumed. These signals are Fourier transformed which allows to find the shear strain and shear stress amplitudes for the applied frequencies f, $\gamma(f_i)$ and $\tau(f_i)$, respectively. The results of the Fourier transformation are depicted in Figure 4.15. Having found the amplitudes allows the calculation of the complex shear modulus, $G^*(f_i)$, from which, under consideration of the loss factor $\delta(f_i)$, further material properties may be derived. Splitting $G^*(f_i)$ in its real and imaginary part yield the storage and the loss modulus, $G'(f_i)$ and $G''(f_i)$, respectively. The storage modulus describes the elastic response of the material, hence associated with the shear modulus G, while the loss modulus resembles the viscous response. Relating $G''(f_i)$ to its respective frequency gives the shear viscosity $\eta(f_i)$. The calculated values are shown in Figure 4.16. The values found for G' and η suggest that a plateau is reached at the applied frequencies. For the
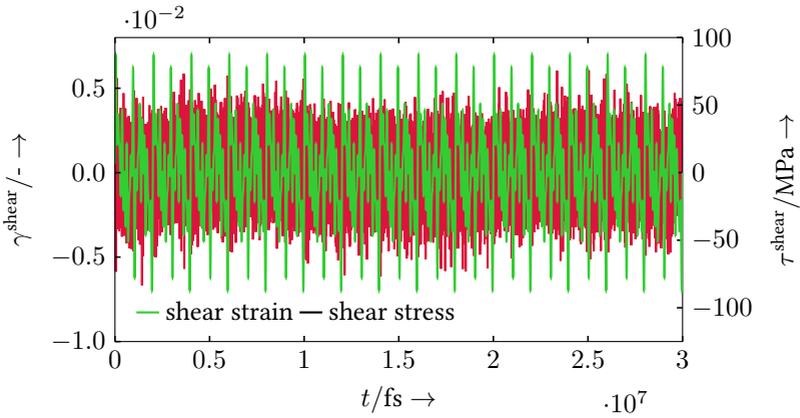
Figure 4.14: Input shear strain and shear stress response of the system domain
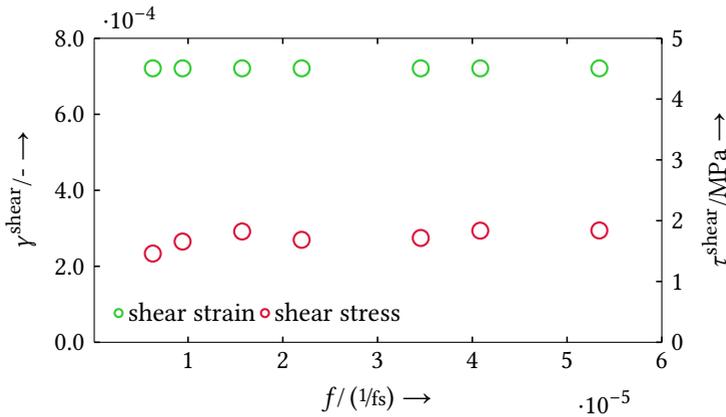
Figure 4.15: Shear strain amplitudes and associated shear stress amplitudes for the frequencies of the sinusoidal deformation
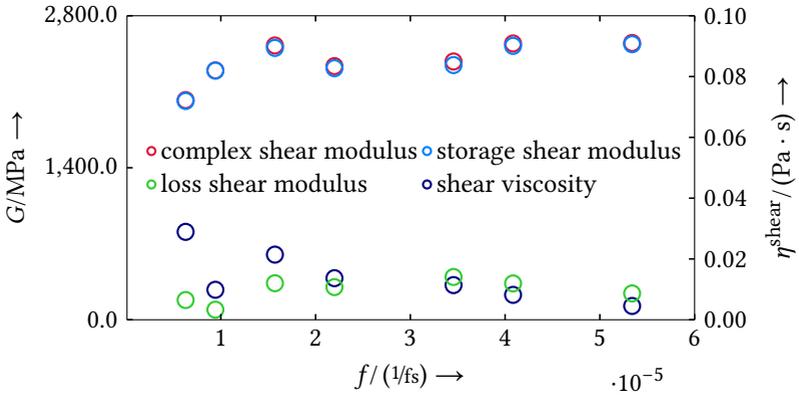
Figure 4.16: Identified material properties, shear moduli and viscosities, at their respective frequencies

lowest frequencies a decrease of the shear storage modulus and an increase in shear viscosity is observed. This indicates, that for lower frequencies the material properties may change towards an equilibrium range. The strong elastic response ($G' \approx |G^*|$) indicates that the high deformation rates do not allow for a noteworthy relaxation. At the same time, the small viscosity values are unusual for a solid at $\Theta = 273\,\mathrm{K}$ and may suggest, that due to frequencies in the gigahertz range a shear-thinning effect takes place [148]. Despite the slightly visible trend for lower frequencies, which may result in typical values of shear modulus of about $G = 1\,\mathrm{GPa}$ [63, 139], a definite statement cannot be made. With longer simulation runs, and hence possibly lower frequencies, more data points offside the plateau region may be found, which may allow for a meaningful extrapolation to common frequency ranges. Aside from this, the simulative DMA approach shows the general possibility to calculate material properties for several frequencies within one run, where the values of G' indicate the promise of reaching reasonable magnitudes of selfsame.

4.3 Curing process on the basis of the phase-field method

The application of the model for the micro-scale FRTS curing process, derived in Section 3.2, is the main objective of this section. The scope of this application is a moulding process and the simulation covers the time beginning from the mould just closing with the FRTS already being at rest, up to when the structure has cooled down to room temperature again. As noted in Section 1.2, the model is implemented and run in the software package Pace3D [82]. Material properties describing the TS behaviour are partially taken and derived from the results achieved with MD in the previous section. Simulations are performed on the basis of volume elements differing in size and filling, whose curing behaviour is presented and compared. The resulting cured volume elements are analysed for eigenstress magnitude and distribution.

4.3.1 Volume elements and simulation setup

In the following, five different microstructure volume elements are used. They are staggered by volume and come in sizes of $\{50\,\mu m\}^3$, $\{100\,\mu m\}^3$ and $\{150\,\mu m\}^3$, while the largest volume element is considered in three different configurations regarding the fibre distribution, as depicted in Table 4.9. The volume elements were generated with the software package GeoDict [113]. Due to the fibre diameter of $10\,\mu m$, a spatial discretisation of $\Delta x = 0.5\,\mu m$ is applied within an equidistant mesh of hexahedrons. This discretisation is chosen to keep a reasonable number of grid points within the volume of the single glass fibres after the diffuse interface of about eight grid points is generated. The diffuse interface region is applied by solving the phase-field equation (3.45) using only the interface terms, and happens in a pre-processing step within a finite-difference scheme [82] by using periodic boundaries for the phase-fields. Thereafter, the phase-fields are kept constant for the curing process simulation and only serve in giving a thorough and smooth representation of the fibre-matrix microstructure. The smoothing of the sharp interface may

Volume elements (variants)		Fibres		
		$l/\varnothing$ in µm	content in vol.%	distribution dev. in %
	(1x)	100/10	25.13	+10.00 +3.40 +13.40
	(1x)	100/10	21.99	−1.87 +4.57 −2.70
	(3x)	100/10	22.11	$-1.89^{+0.84}_{-0.83}$ $+1.40^{+3.97}_{-3.35}$ $+0.46^{+3.36}_{-4.81}$
Target		—	22.00	isotropy
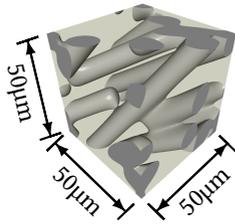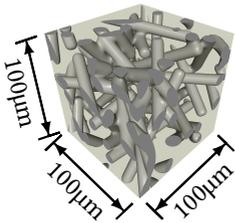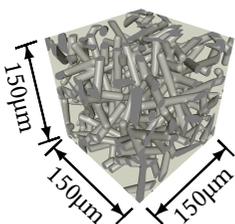
Table 4.9: Volume element sizes and their properties. Deviation in fibre distribution from isotropy is given in each Cartesian direction.

lead to a local merging of two different fibres, if they have contact points or if portions of the fibres are in very close proximity. This behaviour is inherent to the phase-field method.

The curing process itself is split into two parts as shown in Table 4.10: Firstly the actual curing process is simulated, using boundary and initial condition typical for the moulding process step in industrial processing. As described in Section 2.3.1 the urethane reaction happens prior to this and hence only the radical cross-linking reaction takes place. Secondly the microstructure is cooled down to room temperature and atmospheric pressure when the curing simulation has finished. Both simulation steps use a temporal discretisation of $\Delta t = 1.0$ s. The thermal (3.78) and mechanical (3.79) parts of the solver use lin-

run	time in s	Δt in s	temperature in K	pressure in MPa
curing process	180	1.0	418.0	$1.000 \cdot 10^{1}$
cooling	90	1.0	293.0	$1.013 \cdot 10^{-1}$

Table 4.10: Curing process simulation and follow-up cooling simulation: Parameters governing the process steps.

ear elements with full and reduced integration, respectively. The equations are solved implicitly in a backward Euler scheme, and are evaluated in a staggered manner. Hence, the equations are solved in sequence of temperature, degree of cure and displacement leading to a weak coupling. The degree of cure (3.76) is evolved implicitly as well by using a local Newton-Raphson scheme, while the evolution of the glass transition temperature (3.77) simply follows the current and local values of temperature and degree of cure. As the volume elements are periodic, selfsame boundary conditions are applied for the thermal and mechanical fields. Furthermore, the applied periodic boundary conditions control temperature and pressure accordingly to Table 4.10 by applying them in a macroscopic sense. The process parameters for the curing step are the same as in the MD simulations (cf. Table 4.1, [25]). The initial temperature is set to the

mould temperature Θ = 418 K, as the process simulation is thought to begin just at the point when the mould is closed and the filled FRTS stops moving. For the Newton-Raphson scheme evolving the degree of cure, its initial value is set to ζ^α = 0.01 for reasons of numerical stability. As aforementioned, the curing range ζ^α = $[0.0, 1.0]$ only resembles the radical curing process. The material properties used for these simulations are listed in Table 4.11 and Table 4.12 for thermoset phase α and glass fibre phase β, respectively. Due to the strong dependence of the TS properties on ζ^α and Θ, a vast amount of these were determined with MD simulations presented in Section 4.2, and hence might differ from experimentally retrieved material parameters, were they available. Furthermore, the MD calculations used a modified hybrid resin as the molecular structure of the actual UPPH resin is not fully available. Hence, simulation results may only show a qualitative behaviour. For all material properties listed, a linear development with ζ^α and Θ is assumed to keep the simulations computationally efficient. The general material property is split according to the process steps, where in the first step material properties only change with degree of cure as no large deviations in temperature are expected, and in the second step the reasoning is the other way around: In a nearly fully cured sample no significant increase in degree of cure may be expected, and hence material properties only change with temperature. A further simplification is due to a lack of data on the visco-elastic behaviour of the thermoset (cf. Section 4.2.3). Thus a purely elastic behaviour is assumed for the following simulations. The corresponding shear modulus $G^\alpha\left(\zeta^\alpha, \Theta\right)$ is calculated by using the bulk modulus K^α at room temperature and for the fully cured material. In combination with an elastic modulus of a hybrid resin found in literature, E^α = 3,100 MPa [190], the shear modulus may be calculated [116]. The value of G^α for fully cured material at mould temperature is calculated by degrading it by the same factor which is observed for the bulk modulus. The value for the uncured material is set to an arbitrarily low level to take the viscous, gum-like behaviour of the pre-cross-linked hybrid resin into account (cf. Section 2.3.1). The phenomenological models are either fitted to MD data

Material Parameter	Symbol	Unit	Values		
			U50R0, 418 K	U50R100, 418 K	U50R100, 293 K
mechanical					
Mass Density	ρ^α	kg/m³	1,004	1,110	1,147
Bulk Modulus	$K^\alpha\,(\zeta, \Theta)$	MPa	925	2,143	3,084
Shear Modulus	$G^\alpha\,(\zeta, \Theta)$	MPa	100	808	1,163
Viscosity	$\eta^\alpha\,(\zeta, \Theta)$	MPa · s	not used		
Thermal Expansion, lin.	$\alpha^\alpha\,(\zeta, \Theta)$	$10^{-5}\,1/\text{K}$	29.34	13.48	9.20
Reference Temperature	$\Theta\text{Ref},\alpha$	K	293		
Curing Shrinkage, lin.	χ^α	—	$1.567 \cdot 10^{-2}$		
thermal			U50R0, 418 K	U50R100, 418 K	U50R100, 293 K
Specific Heat Capacity	$c_V^\alpha\,(\zeta, \Theta)$	J/kgK	2,152	2,497	2,098
Heat Conductivity	$\kappa^\alpha\,(\zeta, \Theta)$	W/mK	0.218	0.249	0.254
exothermic reaction			independent		
tot. Reaction Enthalpy[1]	$h^{\text{tot},\alpha}$	J/kg	$-213,700$		
Kamal-Sourour[1]	$k^{i,0}$; E^i; m; n	1/s; J/mol; —	$1.600 \cdot 10^{-2}$; $1.667 \cdot 10^{-2}$; 32, 640; 3, 074; 0.774; 1.399		
DiBenedetto	$\Theta^{g,\infty}$; $\Theta^{g,0}$; λ	K; —	379.8; 323.0; 0.342		

[1] from experiments [131]

Table 4.11: Thermoset phase α: Material properties from MD data and experiments

(DiBenedetto's approach, cf. Figure 4.10) or are based on experiments (Kamal-Sourour model, see [163]). Due to the moderate moulding temperature and in

Material Parameter	Symbol	Unit	Value
mechanical			
Mass Density	ρ^β	kg/m³	2,575
Bulk Modulus	K^β	MPa	46,500
Shear Modulus	G^β	MPa	33,000
Thermal Expansion	α^β	10^{-6}1/K	5.0
Reference Temperature	$\Theta^{\text{Ref},\beta}$	K	293
thermal			
Specific Heat Capacity	c_V^β	J/kgK	802.4
Thermal Conductivity	κ^β	W/mK	1.275

Table 4.12: Glass fibre phase β: Material properties from literature [63], no dependence on temperature is assumed.

comparison to the TS material, the glass fibres are not expected to alter their material properties significantly in the temperature range of interest. Hence, the material parameters are set to constant values from literature [63]. As the specific heat capacity at constant volume, c_V, is difficult to measure for solids and hence is seldom listed, the specific heat capacity at constant pressure, c_p, was used to calculate it via the relation [109]

$$c_V = c_p - \frac{\alpha^2 K \Theta}{\rho},$$
(4.1)

where α is the thermal expansion coefficient, K is the bulk modulus, Θ the absolute temperature and ρ the mass density.

4.3.2 Simulation of the curing process

All five volume elements are subject to the curing process simulation and the subsequent cooling, as described in the previous section. For evaluation, the absolute temperature Θ, the degree of cure ζ^α and the von Mises stress σ^{vM} are measured throughout the domains.

In Table 4.13 four prominent time steps of the simulation for one of the $\{150\,\mu m\}^3$ domains are depicted showing the three mentioned quantities as pseudo colour plots in the TS phase. At time step $t = 0\,s$ the initial conditions apply homogeneously throughout the domain. The temperature field is at mould temperature $\Theta = 418\,K$, the degree of cure is at $\zeta^\alpha = 0.01$ everywhere in the TS phase as explained in the previous section and the von Mises stress field is zero prior to the first time step. After some further time steps, at $t = 28\,s$, the curing reaction reaches about 50 % conversion indicating the high reaction rate at the beginning of the exothermic radical reaction. A similar trend is observed in the MD simulations regarding the number of formed radical propagations (cf. Figure 4.3b). This results in a slightly elevated temperature of the system domain due to the release of reaction enthalpy. Both fields evolve homogeneously, which is reasonable as the Kamal-Sourour model (3.76) describing the local curing reaction depends on local temperature and degree of cure, which are homogeneously distributed at the beginning. The progressed state of cure also shows in values of σ^{vM}, which start to differ close to the fibres with single peaks especially at locations, where fibres touch. At the end of the curing process simulation, at $t = 180\,s$, the curing reaction has slowed down and reached nearly full conversion. Hence, a diminishing amount of reaction enthalpy is released over time allowing the temperature to cool down to the mould temperature. Nearly full chemical conversion is reached because the development of the glass transition temperature by DiBenedetto's model (3.77) stays below mould temperature at all times due to the material properties used and fitting parameters (cf. Table 4.11), and therefore the reaction is never stopped on basis of $\Theta^g > \Theta$. The von Mises stress values generally are lower
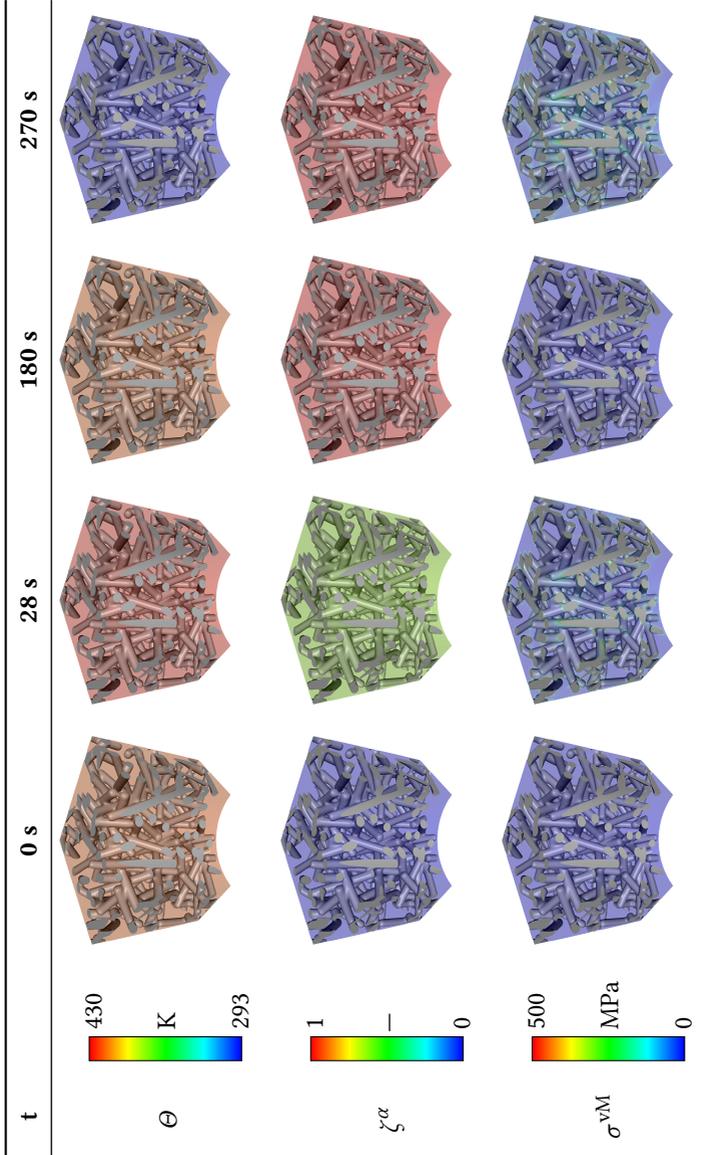
Table 4.13: Exemplary development of a $\{150\,\mu\text{m}\}^3$ volume element during the curing process, cylindrical cut

than at the beginning of the curing process, which may be due to now fully developed mechanical properties of the matrix which qualifies the TS phase to support the fibre structure taking load from fibre-fibre contact points. When the simulation domain is cooled down, at the very end of both simulation runs at $t = 270\,\mathrm{s}$, the temperature field is at room temperature $\Theta = 293\,\mathrm{K}$. During this process the temperature falls locally throughout the domain below the glass transition temperature, and therefore the curing reaction stops, leaving the local degrees of cure at about the magnitude reached at the end of the curing process simulation. By cooling down the volume element the thermal expansion in GF and TS phase lowers towards zero at room temperature. At mould temperature, the thermal expansion partially compensates the volume shrinkage of the matrix induced by the chemical reaction. With this effect gone, elevated σ^{vM} values are again observed. They mainly localise in fibre-matrix interface regions, where the difference in eigenstrains develops an increased eigenstress response. This response is intensified at points where geometrical effects (discontinuities) influence the momentum flux [62]. In fibre-reinforced polymers these are mainly the tips of the fibres, where a small radius leads to an increased curvature, and at points where fibres are in proximity to each other or touch. Here, the geometrical curvature effects of two fibres are superposed, increasing the stress response further.

4.3.3 Evaluation and trends

In the following, the previously cured and cooled FRTS structures are further analysed. Initially, the temporal development of absolute temperature Θ, the degree of cure ζ^{α} and the von Mises stress σ^{vM} is described. For this purpose, these three quantities are compared by their volume averages,

$$\bar{\Theta} = \frac{1}{v}\int_{v}\Theta\left(x_{i}\right)\mathrm{d}v, \ \ \bar{\zeta}^{\alpha} = \frac{1}{v}\int_{v}\zeta^{\alpha}\left(x_{i}\right)\mathrm{d}v, \ \ \bar{\sigma}^{\mathrm{vM}} = \frac{1}{v}\int_{v}\sigma^{\mathrm{vM}}\left(x_{i}\right)\mathrm{d}v, \ \ (4.2)$$

where v is the volume of the system domain. In Figure 4.17 the three different domain sizes are compared to each other. The general development of all quan-

tities confirm the observations made by analysing the curing process visually in the previous section. As depicted in Figure 4.17a the temperature initially adapts to the mould temperature. The high temperature triggers the exothermic curing reaction, which progresses at a high rate. This results in a steady release of reaction enthalpy which causes the system temperature to rise above the mould temperature. With higher degree of cure, the curing reaction slows down as inherent to radical reactions, which lowers the reaction enthalpy release. Hence, the system temperature slowly adjusts back to the mould temperature. At the end of the curing process simulation the conversion nearly reaches 100 %, but the reaction speed significantly diminishes. When cooling down the volume elements, the temperature quickly adapts to the applied room temperature, stopping the curing reaction completely when the local temperature falls below the glass transition temperature, which reaches $\Theta^g \approx 380\,\mathrm{K}$ when $\zeta^\alpha \approx 1.0$ in DiBenedetto's model (3.77). The development of average temperature and degree of cure happens coherently and nearly identically for all three volume element sizes (see magnification in Figure 4.17a). This may result from the identical initial conditions as discussed in the previous section. A further reason could be the small size of the systems not raising significant temperature gradients and hence differences in local temperature which would accelerate and decelerate the local evolution of degree of cure. Increasing the system size may change this as released reaction enthalpy may be balanced and dissipated slower by the boundary conditions. Similarly, the development of the average von Mises stress is following nearly the same pattern in all three volume element sizes. As aforementioned the initial peak is associated with a lack of support of the fibres from the surrounding TS matrix. With increasing degree of cure, the TS material properties develop which allows the matrix to transfer loads from the fibres. By the end of the curing process simulation, $\bar{\sigma}^{\mathrm{vM}}$ drops to a lower, nearly constant value. Releasing the mould pressure and especially the diminishing amount of thermal expansion when cooling down to room temperature increases the resulting difference in eigenstrains between fibres and matrix, which raises the average stresses again. The magnitude of
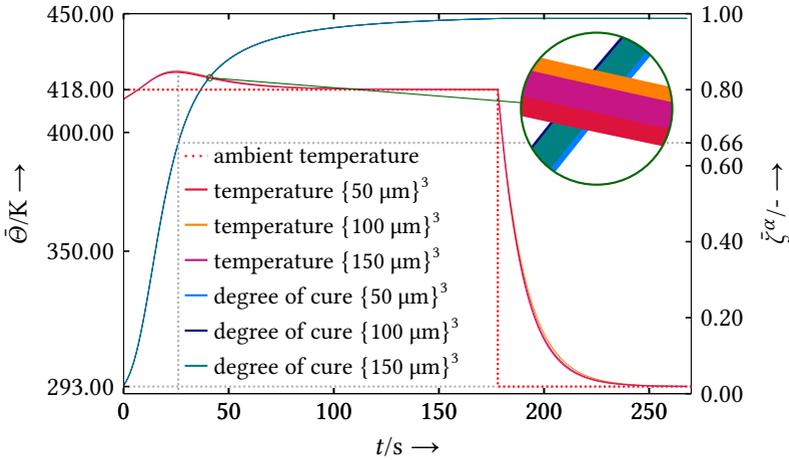
(a) Development of average temperature and average degree of cure, mould and room temperature plotted
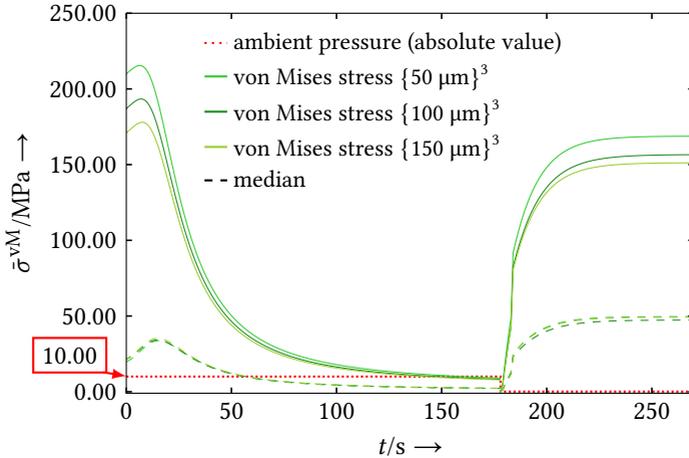
(b) Development of average and median von Mises stress, mould and atmospheric pressure plotted

Figure 4.17: Evaluation of temperature, degree of cure and von Mises stress during the moulding and cooling process step: Comparison of volume element sizes $\{50\,\mu m\}^3$, $\{100\,\mu m\}^3$ and $\{150\,\mu m\}^3$.

stress differs visibly at the beginning and at the end of the complete process: With increasing domain size, the average stress drops. This may be related to better isotropy of the fibres' distribution in larger domains and a distribution which may go along with a lesser amount of contact points and discontinuities in relation to the domain size, which together may lead to a lesser amount of extreme stress peaks. This reasoning is partially supported by the maximum von Mises values of each domain size at the end of the simulation, which do not yield a definite tendency, $\sigma^{\mathrm{vM,max}} = \{2{,}493; 3{,}055; 2{,}559\}$ MPa. Another hint in this direction is the median value of the von Mises stress, which is nearly the same for all three volume element sizes, with only the $\{100\,\mu\mathrm{m}\}^3$ domain deviating slightly from this coherency at the end. Therefore all domains posses about the same amount of volume with σ^{vM} values below the median, and due to $\sigma^{\mathrm{vM}} > 0$ the lower $\bar{\sigma}^{\mathrm{vM}}$ can only result from a lesser amount of extreme stress concentrations relative to system size. Comparing the three domains of size $\{150\,\mu\mathrm{m}\}^3$ in Figure 4.18 nearly no difference in evolution of $\bar{\Theta}$, $\bar{\zeta}^{\alpha}$ and $\bar{\sigma}^{\mathrm{vM}}$ is visible. Hence the same observations as for Figure 4.17 apply. Only in Figure 4.18b, little differences are traceable in $\bar{\sigma}^{\mathrm{vM}}$. As all three domains consist of a similar fibre distribution and fibres have the same length and diameter, the variance is related to the variance of the implementation of the isotropic fibre distribution.

Lastly, the location of eigenstress peaks is analysed. Comparing the three different volume element sizes at the very end of the simulation runs (cooled to room temperature) in Table 4.14 shows their similar outcome in terms of von Mises stress magnitude and concentration. All three sizes have the lowest σ^{vM} values in the TS phase and intermediate values at the fibre matrix interfaces. The stress peaks are always found at fibre tips or at points where two or more fibres are in close range or contact as described in the previous section. Binning the range of curvature values and weighting them by the average deviation of the von Mises stress from $\bar{\sigma}^{\mathrm{vM}}$ yields the results in Figure 4.19. Noting that the curvature of a sphere is one, the first peak may be associated to fibre-matrix interfaces, which is a lateral surface, and to the fibre tips which
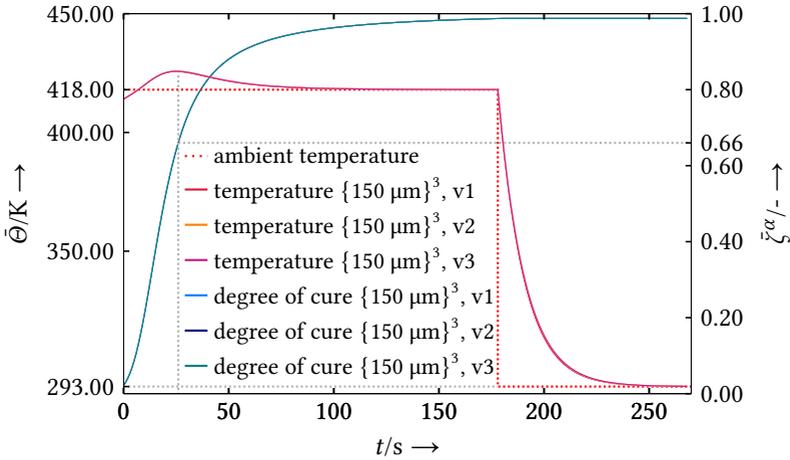
(a) Development of average temperature and average degree of cure, mould and room temperature plotted
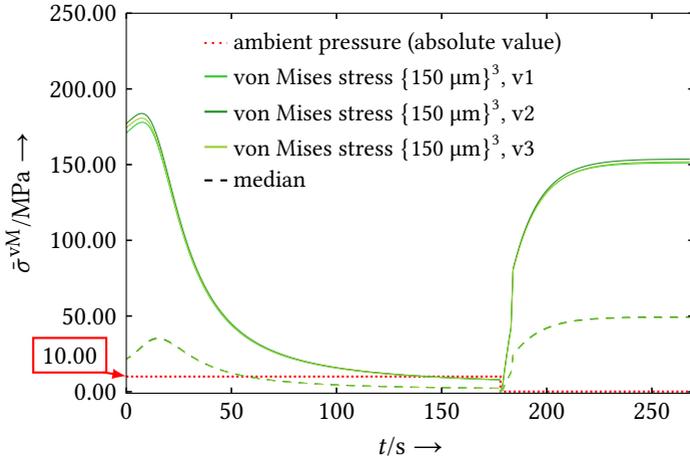
(b) Development of average and median von Mises stress, mould and atmospheric pressure plotted

Figure 4.18: Evaluation of temperature, degree of cure and von Mises stress during the moulding and cooling process step: Comparison of three different volume elements of size $\{150\,\mu\text{m}\}^3$.
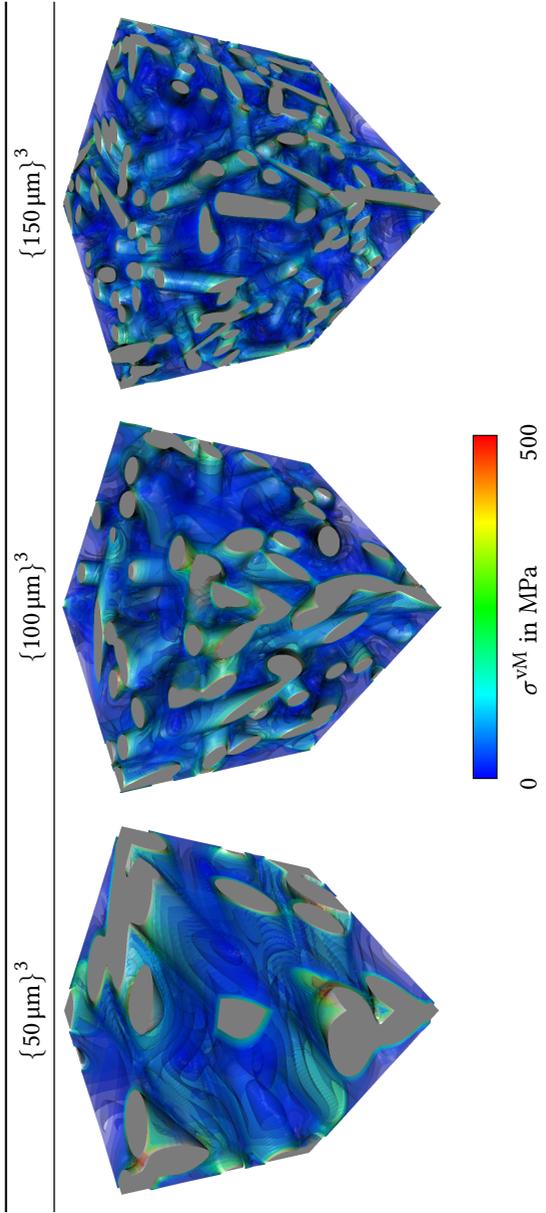
Table 4.14: Isosurfaces showing the distribution of von Mises stress in different volume elements. The isosurfaces are placed logarithmically with respect to σ^{vM} values.
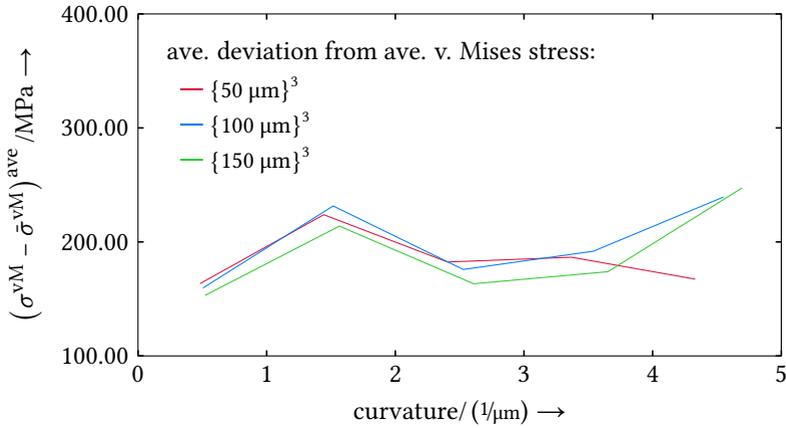
Figure 4.19: Stress distribution in the simulation domains related to local curvature

are rounded due to the initial smoothing of the interface (see Section 4.3.1) and therefore appear to be closer to a spherical shape. All curvatures which

curvature	normalised occurrence		
bin number	$\{50\,\mu m\}^3$	$\{100\,\mu m\}^3$	$\{150\,\mu m\}^3$
1	0.81165	0.86914	0.86913
2	0.13330	0.08820	0.08984
3	0.03358	0.02924	0.03079
4	0.02142	0.01340	0.01022
5	0.00006	0.00002	0.00001

Table 4.15: Occurrence of curvatures in Figure 4.19.

are larger than the ones previously identified, are mainly due to fibres being in contact, leading to additional points of curvature in the phase-field context. As depicted in Table 4.15, these make up about 5 % or less of the total amount of curvature points. The elevated stress at these points clearly is associated with the influence of the curvature on stress concentrations, which grows with the magnitude of curvature. While the stress peak at high curvature may be

due to fibres being in contact at acute angles and hence yielding the curvature value and the stress, the first stress peak is likely due to parts of fibres being in vicinity of other fibres without being in contact. Such a spatial arrangement is already sufficient to produce stress concentrations, and hence elevating the overall value of $\bar{\sigma}^{\mathrm{vM}}$ for this range of curvatures.

From the results obtained it may be concluded that the model derived in Section 3.2 is basically able to describe and simulate the curing process in a FRTS microstructure. The interplay between curing reaction, temperature and resulting mechanical stresses and the temporal development of the respective quantities follows the expectations on such a process. Especially the development of eigenstresses results in elevated values and peaks at the expected locations of fibre-matrix interfaces and fibre tips. For a realistic stress distribution, a certain volume element size seems to be necessary to have the stress peaks in a reasonable relation to the domain size (cf. Figure 4.17b), and testing larger volume elements may yield an optimal system size.

Notwithstanding the above, the highest stress peaks have values of about $\sigma^{\mathrm{vM}} = 3{,}000\,\mathrm{MPa}$, which is far above the average and median stress levels in the domains. While it may be argued that these location would not persist in the real process by initiating voids or micro-cracks, the stress level is still thought to be above realistic magnitudes as sketched in [62, 162]. The consideration of visco-elastic matrix behaviour may help to relax some of the stress peaks and lower the overall stress level. A visco-elastic material model was derived but not considered in the simulation due to a lack of appropriate material properties in literature. Furthermore, overcoming some basic modelling assumptions regarding the fibre-matrix interface may enhance the overall behaviour and further harmonise it with physical and chemical effects. Two assumptions, which may be subject to alterations, are the the kinematic compatibility condition (2.32) at fibre-matrix interfaces, which rigidly couples matrix and fibres from the beginning regardless of the local degree of cure and actually present cross-links between thermoset and fibre sizing. A second problematic assumption is the development of TS material properties,

especially mechanical properties, in the interfacial regions occurring with a progressing chemical reaction. While the former does not account for possible small rearrangements of the fibres within the thermoset matrix leading to an energetically more favourable configuration, and hence lower stresses, the latter a priori assumes that material properties develop in interfacial regions as homogeneously as in bulk regions. As it is known that the cross-linking in this region and towards the fibre sizing is not as dense as in a bulk thermoset [26, 62], only less pronounced material properties may develop in such regions giving lower values of eigenstresses.

4.4 Crack propagation on the basis of the phase-field method

In a last step, according to the sketched virtual process chain (see Section 4.1), a fully cured volume element is used to test it for the formation and possible propagation of micro-cracks in a qualitative way. The applied phase-field crack model is described in Section 3.3 and is implemented in the software package Pace3D [82].

4.4.1 Setup of the crack propagation simulation

For the phase-field crack simulation of a $\{150\,\mu\mathrm{m}\}^3$ volume element the model described in Section 3.3 is used. This model only takes into account mechanical effects, and hence no temperature or cure evolution is applied, but the system domain is set to room temperature $\Theta = 293\,\mathrm{K}$. Furthermore, as the degree of cure is observed to nearly reach $100\,\%$ conversion (see, e.g. Figure 4.18a) and there is no thermal expansion in both, GF and TS phase, because the relevant reference temperature is $\Theta^{\mathrm{Ref}} = 293\,\mathrm{K}$, the only eigenstrains are the chemical shrinkage strains, and due to their homogeneity their application happens as a constant eigenstrain value $\varepsilon^{\mathrm{c}} = 1.567 \cdot 10^{-2}$ (cf. Table 4.11) in the TS phase. As the simulation is a restarted $\{150\,\mu\mathrm{m}\}^3$ volume element, the spatial discretisation is again $\Delta x = 0.5\,\mu\mathrm{m}$ and the system domain uses periodic

boundary conditions for the phase-fields and the mechanical fields. The crack interface width is set to be about eight grid points.

In contrast to the curing process simulation, for the crack propagation simulation the phase-field is allowed to evolve to simulate crack growth. Thus, the phase-field fracture evolution equation (3.100) is active, which is solved by a forward Euler scheme on a finite-difference grid. The resulting energetic crack resistance G^c is calculated following Section 3.3.2, and the therein values used for the single phases and the interface are listed in Table 4.16. The value

region	glass fibre	thermoset	interface
G^c in J/m^2	5.0	25.0	4.0

Table 4.16: Energetic crack resistance for different regions of the domain.

for glass fibre is in the range of glass [199]. The other two values are chosen with physical reasoning: As the thermoset is not as brittle as the glass fibre, a higher energetic crack resistance is assumed. Likewise, in the interface, the cross-linking and hence connection of the thermoset to the fibre surface is weaker than in bulk thermoset. Hence, the energetic interfacial crack resistance features a lower magnitude. The time step width is set to $\Delta t = 1.0\,\mathrm{s}$, and the mobilities M^{α}, M^{β}, scaling the rate of crack growth, are set with respect to the Δt to the maximum value allowed by numerics. As the volume element is thought to be fully cured and at room temperature, the respective material properties of Table 4.11 and 4.12 apply. As previously, the mechanical fields are solved implicitly on a linear element mesh with reduced integration. The evolution of the crack phase-field ϕ^c and solving the mechanical fields happens in a staggered manner. The border crack value, re-scaling and re-distributing the energetic crack resistance, is set to $\phi^{c,BC} = 0.975$. Prior to the crack propagation simulation, the whole simulation domain receives a small amount of crack phase $\phi^c < 0.004$ applied with noise, because crack nucleation is not part of the derived model. With this, fracture is allowed to develop anywhere in the domain if Griffith's criterion is met. A downside to

this setup is that the modelling approach of subtracting the curvature (see Equation 3.100, last term) does not work with noisy crack values being present throughout the simulation domain. When the curvature is subtracted from a local crack surface, the energetic crack resistance solely arises from the profile of the crack surface, Equation (3.89). With values of ϕ^c being present everywhere, none of these positions have an energetic crack resistance yet and each position tries to construct the crack profile resulting in ϕ^c growing throughout the domain without a mechanical energy acting on them. To allow the formation of micro-cracks, the curvature subtraction is disabled for this simulation. This has the effect of an energetic crack resistance being available due to local curvature, even with no fully developed crack surface present. Hence, the result obtained in the next section may only be evaluated in terms of qualitative behaviour.

4.4.2 Micro-cracks in cured volume elements

In the following, a PF crack propagation simulation is performed on one volume element of size $\{150\,\mu m\}^3$ and is evaluated qualitatively for micro-crack formation and growth afterwards. First runs showed, that the deactivation of curvature subtraction increases the energetic crack resistance significantly. To still initiate the formation of micro-cracks, all G^c values in Table 4.16 were scaled by a factor of 0.075.

In Figure 4.20 the simulation status after t = 135 s is depicted (non-physical time). The micro-cracks grow along fibre-matrix interfaces and at points where fibres touch, the fibres debond under excessive stresses. Hence, the modelling of the energetic crack resistance in the interface yields qualitatively reasonable results in complex three-dimensional micro-structures. With progressing time, the debonding further increases, which is due to the relatively low value of G^c in this simulation.

For a further and reasonable evaluation of micro-crack formation and propagation in cured volume elements, the derived PF fracture model has to be applied in its original form. For this purpose, the underlying crack phase noise has to
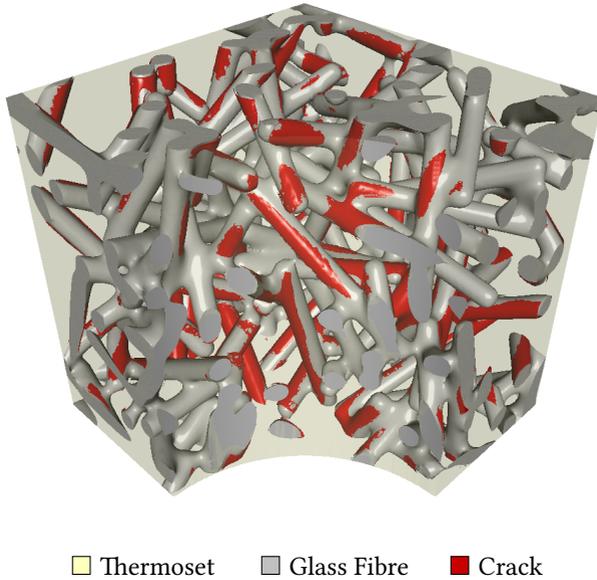
Figure 4.20: Micro-cracks within a cured $\{150\,\mu m\}^3$ volume element with cylindrical cut: Debonding of fibres.

be removed and micro-crack formation has to be triggered by an appropriate nucleation algorithm coupled to an adequate energetic criterion.

5

Conclusions and Outlook

5.1 Summary

This work deals with the simulation of the curing process of fibre-reinforced thermosets (FRTS) on the microstructure and molecular levels. The two-scale approach is adopted to examine the fibre-matrix interactions occurring on a micro-scale and their consequences in terms of eigenstresses and micro-cracks. On a nano-scale the chemical reactions within the thermoset resin are simulated and analysed with regard to material properties to characterise the micro-scale behaviour. This raises the following main topics discussed within this work:

- The derivation of a model for the curing process of a FRTS, hence describing the behaviour of fibre and thermoset in an environment of thermal, mechanical and chemical reaction effects.

- Implementation of a crack propagation model capable of handling the fracture behaviour of fibre-reinforced polymers (FRP), especially debonding of the fibre-matrix interface.

- Simulation of the curing reaction on a molecular scale, modifying and using algorithms describing bond formation and dissociation.

For the topics on a micro-scale, a phase-field (PF) approach is chosen due to the possibility of representing complex geometries, such as FRP microstructures, with ease and due to its ability to efficiently evolve free boundaries, such as crack surfaces, on the basis of implicit interface tracking through a volume fraction parametrisation [129, 172]. The nano-scale simulations use molecular dynamics (MD) as a computational model, which allows for simulation of molecules and their interaction by assigning inter- and intramolecular potentials, and hence enables interventions on atoms resembling chemical reaction processes. With these foundations, the main motivation of this work is to combine all three topics and to use the findings to implement a virtual process chain explained in Section 4.1.

In Chapter 3, the models for the PF and MD framework are derived. Initially, in Section 3.1, a PF model is regularised from sharp-interface thermodynamics, which is the basis for all other PF models used within this work. Differences to energy functional derivations are pointed out and discussed, especially the different distribution function for driving forces arising through the regularisation and the necessity of treating singular surface jump conditions in the PF context. In Section 3.2, based upon the underlying PF formulation, a curing process model with regard to FRTS is derived in accordance to thermodynamics. In the very general case this model describes a material subject to heat conduction, visco-elasticity and phenomenological curing, including

their coupling and dissipative terms. For thermal and mechanical fields their respective interfacial jump conditions are incorporated and discussed. Based on the derivation of the standard PF model, in Section 3.3 a PF model for crack propagation is derived in a similar way. Again a new distribution function is found, and furthermore the PF-inherent curvature is subtracted as crack propagation should only happen through mechanical forces. A fact, which is rarely taken into account in PF models for fracture. To account for the FRP failure mechanism of debonding, the energetic crack resistance is modified and may be altered in the interfacial region, i.e. weakening or strengthening the energetic crack resistance in such points. In Section 3.4, for the simulation of the chemical curing reactions happening in the UPPH resin described in Section 2.3.1, bond formation and dissociation algorithms are extended on the basis of available models from literature to be able to mimic urethane and radical reactions. Furthermore, auxiliary charges are introduced, an artificial attraction force to accelerate chemical reactions for the short time periods covered by the MD time scale. Each of these sections incorporates a discussion and evaluation of the models' behaviour on the basis of simulations.

Chapter 4 brings all models into a larger context by linking them into a virtual process chain for a FRTS curing process, which is described in Section 4.1. The common basis for this virtual process chain is the utilisation of the same combination of glass fibres and UPPH thermoset for all simulations. In a first step, MD runs are conducted to simulate the curing reaction of the UPPH resin on a nano-scale. The results such as volume shrinkage and enthalpy released are discussed. On the basis of the cured polymer networks, micro-scale material properties are calculated for different points in temperature and degree of cure. All results are compared and put in relation to literature values of common thermosets and are in a reasonable range. Hence, the UPPH thermoset is adequately characterised to a large extent without the need to conduct experiments, which may be complex in the context of non-constant temperature and non-constant degree of cure. The material properties are then

used to feed a micro-scale curing process simulation of artificially generated FRTS volume elements in Section 4.3. Due to a lack of available material parameters to describe the visco-elastic thermoset behaviour, linear elasticity is assumed. The progress of the curing process simulation is evaluated for different volume element sizes and realisations, showing a similar behaviour and development of all system domains. Especially for temperature and degree of cure the system sizes and realisations used have nearly no influence on their development during the curing process. The development of eigenstresses is analysed on basis of a von Mises stress field. The fields differ as they are heavily dependent on the microstructure investigated, but the values are in the same magnitude and range for all examined volume elements. A comparison of average, median and maximum stress reveals, that the values of stress peaks are at least one magnitude higher than the average or median stress, which is associated to missing relaxation effects in the simulations. Further analysis also shows, that stress concentrations develop as expected at fibre tips and when fibres touch. Generally, the von Mises stress takes elevated values in the fibre-matrix interface region. Lastly, in Section 4.4 a single fully cured volume element is taken to perform a crack propagation simulation. The result shows the basic ability of the model to simulate debonding of fibre-matrix interfaces in complex microstructures. Due to the lack of an adequate micro-crack formation algorithm the PF crack propagation model could not be applied in its contemplated form and hence no further evaluation for micro-crack propagation in FRTS is done.

5.2 Future work and outlook

In the following, some fields of research are listed, which arose while working on the different topics of this thesis, but were not within the scope of the overall work.

For the curing process simulation on FRTS microstructures, the derived model could be enhanced by making use of the diffuse interfacial region, provided

by the PF method. Similar to altering the energetic crack resistance in the PF fracture model, other material properties, e.g. the shear modulus, might be modified in tangential directions of the fibre-matrix interface. With this, the consequences of lesser pronounced cross-linking close to fibres [26, 62] may be incorporated into the overall model and its influence examined. For further simulation runs the visco-elastic material properties of the thermoset should be obtained to be able to use the whole potential of the presented model. With this, a more extensive simulation study using a larger variety in fibre length and orientation could be conducted and the influence of the process parameters could be examined.

The crack propagation model would benefit from a separate micro-crack nucleation algorithm, which would enable the model usage in its contemplated form (cf. Section 4.4.1). A further topic in this field concerns the basic model formulation: The model is not able to truly match the Griffith criterion despite the derivation by thermodynamic means (see Section 3.3.3). Apart from the difficulties in treating the crack tip - a singularity - correctly, the profile function describing the crack surface plays a key role in modelling the energetic crack resistance, and hence a more suitable profile shape may improve the model behaviour with regard to the Griffith point.

For the MD simulations, the achieved material characterisation may be refined by using additional realisations of the system domain, and the domain sizes may be analysed for finite-size effects [145]. Furthermore the characterisation may be extended by simulatively measuring the shear modulus and the shear viscosity. The micro-scale visco-elastic model would greatly benefit from such analysis. A more basic field would be an extended analysis of the reaction algorithms in terms of energy minimisation and resulting polymer network. The system behaviour, and hence the micro-scale material properties, are quite dependent on cross-link density and location [148]. A revised system behaviour may also help to improve simulation stability (cf. Section 4.2.3). In a longer run, the chemical reaction close to fibre surfaces may be simulated,

which may help to reveal weak spots in the interfacial region. Findings, which could directly be used on the micro-scale again by the aforementioned material property manipulations in diffuse interface models.

5.3 A final word

During the work on both scales, micro and nano, the relevance of having a complete view on materials was most apparent and taking a look beyond the sphere of the macro- and micro-scale should always be encouraged. Computationally, the possible achievements by combination of scales were striking - even more when considering that nearly no experiments had to be conducted regarding the material properties.

A
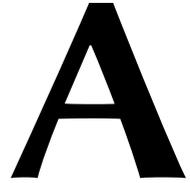
Variable Evaluation at an Interface

At an arbitrary interface $s^{\alpha\beta}$ each non-scalar quantity, e.g. ψ_i or ψ_{ij}, may be decomposed in its components normal and tangential to $s^{\alpha\beta}$, which are orthogonal to each other and which generally show different behaviour. This can be achieved through the projectors

$$\mathcal{P}_{ij}^{\mathrm{n}} = n_i n_j, \qquad \mathcal{P}_{ij}^{\mathrm{t}} = \delta_{ij} - \mathcal{P}_{ij}^{\mathrm{n}} = \delta_{ij} - n_i n_j, \qquad (A.1)$$

which map vector- or tensor-valued quantities to their normal and tangential components, respectively. This yields for vectors and tensors

$$
\begin{aligned}
\psi_i &= \mathcal{P}^n_{ij}\psi_j + \mathcal{P}^t_{ij}\psi_j \\
&= \psi^n_i + \psi^t_i \\
&\text{and} \\
\psi_{ik} &= \mathcal{P}^n_{ij}\psi_{jk} + \mathcal{P}^t_{ij}\psi_{jk} \\
&= \psi^n_{ik} + \psi^t_{ik}.
\end{aligned}
\tag{A.2}
$$

In the following this is used to specify effects of mechanical and thermal jump conditions at the interface.

Finite deformation and stress

In the way of the second law of thermodynamics and in Lagrangian description the quantities deformation gradient F_{ij} and 1$^\text{st}$ Piola-Kirchhoff stress P_{ij} are introduced via the the following terms

$$
P_{ij}\dot{F}_{ij} - \phi^\alpha \rho^{0,\alpha} \frac{\partial \Psi^\alpha}{\partial F^\alpha_{ij}}\dot{F}^\alpha_{ij} - \phi^\beta \rho^{0,\beta} \frac{\partial \Psi^\beta}{\partial F^\beta_{ij}}\dot{F}^\beta_{ij} \geq 0,
\tag{A.3}
$$

whose sum has to be greater or equal to zero, when interpreting the entropy inequality strictly. First of all the relation between P_{ij} and the Helmholtz free energies Ψ^α and Ψ^β in the bulk phases has to be determined. By adjusting the phase values to $\phi^\alpha = 1$ and hence $\phi^\beta = 0$ a purely α-region is existent and therefore the rate of the deformation gradient F_{ij} coincides with its phase-

inherent variant F_{ij}^α. For a β-region the same reasoning may be applied, and the 1st Piola-Kirchhoff stresses are identified as

$$P_{ij}\dot{F}_{ij} - \rho^{0,\alpha}\frac{\partial \Psi^\alpha}{\partial F_{ij}^\alpha}\dot{F}_{ij}^\alpha = \left(P_{ij} - \rho^{0,\alpha}\frac{\partial \Psi^\alpha}{\partial F_{ij}^\alpha}\right)\dot{F}_{ij} = 0 \rightarrow P_{ij} = \rho^{0,\alpha}\frac{\partial \Psi^\alpha}{\partial F_{ij}^\alpha} = P_{ij}^\alpha,$$

$$P_{ij}\dot{F}_{ij} - \rho^{0,\beta}\frac{\partial \Psi^\beta}{\partial F_{ij}^\beta}\dot{F}_{ij}^\beta = \left(P_{ij} - \rho^{0,\beta}\frac{\partial \Psi^\beta}{\partial F_{ij}^\beta}\right)\dot{F}_{ij} = 0 \rightarrow P_{ij} = \rho^{0,\beta}\frac{\partial \Psi^\beta}{\partial F_{ij}^\beta} = P_{ij}^\beta. \tag{A.4}$$

Using these results Equation (A.3) is evaluated by decomposing each term in its normal and tangential projection, and with the application of their orthogonality the sorted terms write as

$$P_{ij}\dot{F}_{ij} - \phi^\alpha P_{ij}^\alpha \dot{F}_{ij}^\alpha - \phi^\beta P_{ij}^\beta \dot{F}_{ij}^\beta \geq 0$$

$$\left(P_{ij}^{\text{n}} + P_{ij}^{\text{t}}\right)\left(\dot{F}_{ij}^{\text{n}} + \dot{F}_{ij}^{\text{t}}\right) - \phi^\alpha\left(P_{ij}^{\alpha,\text{n}} + P_{ij}^{\alpha,\text{t}}\right)\left(\dot{F}_{ij}^{\alpha,\text{n}} + \dot{F}_{ij}^{\alpha,\text{t}}\right)$$

$$-\phi^\beta\left(P_{ij}^{\beta,\text{n}} + P_{ij}^{\beta,\text{t}}\right)\left(\dot{F}_{ij}^{\beta,\text{n}} + \dot{F}_{ij}^{\beta,\text{t}}\right) \geq 0 \tag{A.5}$$

$$P_{ij}^{\text{n}}\dot{F}_{ij}^{\text{n}} - \phi^\alpha P_{ij}^{\alpha,\text{n}}\dot{F}_{ij}^{\alpha,\text{n}} - \phi^\beta P_{ij}^{\beta,\text{n}}\dot{F}_{ij}^{\beta,\text{n}}$$

$$+P_{ij}^{\text{t}}\dot{F}_{ij}^{\text{t}} - \phi^\alpha P_{ij}^{\alpha,\text{t}}\dot{F}_{ij}^{\alpha,\text{t}} - \phi^\beta P_{ij}^{\beta,\text{t}}\dot{F}_{ij}^{\beta,\text{t}} \geq 0.$$

A further evaluation is possible by obeying the mechanical jump conditions, which are Hadamard's compatibility condition, $[\![F_{ij}]\!]^{\alpha\beta}T_j^{\alpha\beta} = 0$, and the linear momentum balance on singular surfaces, $[\![P_{ij}]\!]^{\alpha\beta}N_j^{\alpha\beta} = 0$. Here $N_j^{\alpha\beta}$ and $T_j^{\alpha\beta}$ are the normal and tangential vector of the interface $S^{\alpha\beta}$, respectively. These imply the continuity of stresses in normal direction, $P_{ij}^{\alpha,\text{n}} = P_{ij}^{\beta,\text{n}} = P_{ij}^{\text{n}}$, and the continuity of the deformation gradient in tangential direction, $F_{ij}^{\alpha,\text{t}} = F_{ij}^{\beta,\text{t}} = F_{ij}^{\text{t}}$. Applied to Equation (A.5) the terms are rearranged to

$$P_{ij}\left(\dot{F}_{ij}^{\text{n}} - \phi^\alpha \dot{F}_{ij}^{\alpha,\text{n}} - \phi^\beta \dot{F}_{ij}^{\beta,\text{n}}\right) + \left(P_{ij}^{\text{t}} - \phi^\alpha P_{ij}^{\alpha,\text{t}} - \phi^\beta P_{ij}^{\beta,\text{t}}\right)\dot{F}_{ij}^{\text{t}} \geq 0, \tag{A.6}$$

which gives the composition of the deformation gradient and 1st Piola-Kirchhoff stress. By applying the volumetric average to all components the continuity of certain components is not violated and it follows

$$F_{ij} = \phi^\alpha F_{ij}^\alpha + \phi^\beta F_{ij}^\beta, \tag{A.7}$$

$$P_{ij} = \phi^\alpha P_{ij}^\alpha + \phi^\beta P_{ij}^\beta. \tag{A.8}$$

The result for the deformation gradient F_{ij} is implied as these terms have the phase values held constant.

Small strain and stress

In the case of infinitesimal deformation and in Eulerian description the reasoning is analogous to the previous section. Starting with the relevant terms from the entropy inequality

$$\sigma_{ij}\dot{\varepsilon}_{ij} - \phi^\alpha \rho^\alpha \frac{\partial \Psi^\alpha}{\partial \varepsilon_{ij}^\alpha} \dot{\varepsilon}_{ij}^\alpha - \phi^\beta \rho^\beta \frac{\partial \Psi^\beta}{\partial \varepsilon_{ij}^\beta} \dot{\varepsilon}_{ij}^\beta \geq 0 \tag{A.9}$$

the Cauchy stress σ_{ij}, its relation to the Helmholtz free energies Ψ^α and Ψ^β and the strain ε_{ij} in bulk phases can be identified:

$$\begin{aligned}
\phi^\alpha = 1 \text{ and } \phi^\beta = 0: &\quad \varepsilon_{ij} = \varepsilon_{ij}^\alpha, \quad \sigma_{ij} = \rho^{0,\alpha} \frac{\partial \Psi^\alpha}{\partial \varepsilon_{ij}^\alpha} = \sigma_{ij}^\alpha \\
\phi^\alpha = 0 \text{ and } \phi^\beta = 1: &\quad \varepsilon_{ij} = \varepsilon_{ij}^\beta, \quad \sigma_{ij} = \rho^{0,\beta} \frac{\partial \Psi^\beta}{\partial \varepsilon_{ij}^\beta} = \sigma_{ij}^\beta.
\end{aligned} \tag{A.10}$$

Application of the decomposition in normal and tangential direction defined by $n_j^{\alpha\beta}$ and $t_j^{\alpha\beta}$, the normal and tangential vector of the interface $s^{\alpha\beta}$, respectively, together with the respective jump conditions $[\![\sigma_{ij}]\!]^{\alpha\beta} n_j^{\alpha\beta} = 0$ (linear momen-

tum balance at an interface) and $[\![u_{i,j}]\!]^{\alpha\beta} t_j^{\alpha\beta} = 0$ (Hadamard's compatibility condition) yields

$$\varepsilon_{ij} = \phi^\alpha \varepsilon_{ij}^\alpha + \phi^\beta \varepsilon_{ij}^\beta, \tag{A.11}$$

$$\sigma_{ij} = \phi^\alpha \sigma_{ij}^\alpha + \phi^\beta \sigma_{ij}^\beta. \tag{A.12}$$

Temperature gradient and heat flux

Similar to their mechanical counterparts, the volume averaged heat flux q_i and temperature gradient $\Theta_{,i}$ can be defined. To evaluate the composition of q_i and $\Theta_{,i}$ in bulk and interfacial regions the heat conduction inequality

$$\frac{q_i \Theta_{,i}}{\Theta} \geq 0 \tag{A.13}$$

is used. As there is no relation of the heat flux to the free Helmholtz energy, the evaluation applies the decomposition of energetic quantities into its volume averaged phase-inherent parts:

$$q_i \Theta_{,i} = \phi^\alpha q_i^\alpha \Theta_{,i}^\alpha + \phi^\beta q_i^\beta \Theta_{,i}^\beta \geq 0. \tag{A.14}$$

For bulk regions it is concluded for

$$
\begin{aligned}
\phi^\alpha = 1 \text{ and } \phi^\beta = 0: \quad & \Theta_{,i} = \Theta_{,i}^\alpha, \quad q_i = q_i^\alpha, \\
\phi^\alpha = 0 \text{ and } \phi^\beta = 1: \quad & \Theta_{,i} = \Theta_{,i}^\beta, \quad q_i = q_i^\beta.
\end{aligned}
\tag{A.15}
$$

Again the decomposition in normal and tangential direction of $s^{\alpha\beta}$ is applied. The necessary jump conditions for evaluation are continuous heat flux in interface normal direction, $[\![q_i]\!]^{\alpha\beta} n_i^{\alpha\beta} = 0$, and the assumption of continuous

temperature gradient in interface tangential direction, $[\![\Theta_{,i}]\!]^{\alpha\beta} t_i^{\alpha\beta} = 0$. In interfacial region this implies

$$\Theta_{,i} = \phi^\alpha \Theta_{,i}^\alpha + \phi^\beta \Theta_{,i}^\beta, \tag{A.16}$$

$$q_i = \phi^\alpha q_i^\alpha + \phi^\beta q_i^\beta. \tag{A.17}$$

B

Virtual Resin System

For testing the molecular dynamics models a *virtual* resin system is introduced. The system described does not resemble an existing resin, but contains the same functional groups and unsaturated carbon double bonds as the UPPH resin detailed in Section 2.3.1. By assigning the same reaction sites the virtual resin system may be used as a simplified example for the chemical processes and to capture the basic behaviour.

Molecules and Composition

The schematic representations of the involved molecules (see Section 2.3.1) are replaced by molecules with a simple backbone structure. This also involves styrene, which is replaced by the even simpler ethylene. The reactive groups

are the same in functionality and number, which is to establish an adequate comparability to the commercial UPPH resin. The molecular structures are given in Table B.1. For simulations using the virtual resin system the fraction

Molecule	Schematic	Molecular structure
MDI		$\begin{array}{ccc} H & H & H \\ | & | & | \\ OCN-C\!-\!C\!-\!C\!-NCO \\ | & | & | \\ H & H & H \end{array}$
UP		$\begin{array}{ccccccccc} H & & H & H & OH & H & H & H & H & H \\ | & & | & | & | & | & | & | & | \\ C\!=\!C-C-C-C-C-C-C-C\!=\!C \\ | & | & | & | & | & | & | & | & | \\ H & H & H & H & H & H & OH & H & & H \end{array}$
Styrene		$\begin{array}{cc} H & H \\ \diagdown & \diagup \\ C\!=\!C \\ \diagup & \diagdown \\ H & H \end{array}$
Peroxide		$H-\overline{\underline{O}}-\overline{\underline{O}}-H$
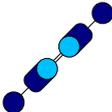
Table B.1: Composition of virtual resin system: molecules and structure

of each compound is chosen as specified for the commercial-type hybrid resin in Table 2.3.

List of Figures

List of Tables

List of Tables

List of Abbreviations and Symbols

Symbols listed twice have to be interpreted from their context.

Constants

i   imaginary number (solution of $x^2 = -1$)

π Archimedes' constant ($\pi = 3.14159\dots$)

k_B Boltzmann constant ($k_\mathrm{B} = 1.381 \cdot 10^{-23} \mathrm{J/K}$)

R universal gas constant ($R = 8.314\,\mathrm{J/molK}$)

Material and Fitting Parameters

η scalar shear viscosity

η^*, η', η'' complex, viscous and elastic shear viscosity

$\gamma^{\alpha\beta}$ surface energy density of an interface α-β

Θ^{g}	glass transition temperature
c_{V}	mass-specific heat capacity at constant volume
G	shear modulus
G^*, G', G''	complex, storage and loss shear modulus
K	bulk modulus
$M^{\alpha\beta}$	mobility parameter of an interface α-β
α_{ij}	thermal expansion tensor
χ_{ij}	chemical shrinkage tensor
κ_{ij}	thermal conductivity tensor
C_{ijkl}	stiffness tensor
V_{ijkl}	viscosity tensor
$\Theta^{\mathrm{g},\infty}$, $\Theta^{\mathrm{g},0}$, λ	fitting parameters of DiBenedetto model
k, k^{el}, $\phi^{\mathrm{c,BC}}$	fitting parameters of the phase-field fracture model
$k^{i,0}$, E^i, m, n	fitting parameters of the Kamal-Sourour model

Variables and Functions

Δt	time step width
Δx	spatial discretisation, grid spacing
ϵ	scaling parameter for the phase-field interface width

η	mass-specific entropy density
γ	scalar shear deformation
ω	angular frequency
ϕ	phase-field order parameter representing a volume fraction
Ψ	mass-specific Helmholtz free energy density
ρ	mass density
τ	scalar shear stress
Θ	absolute temperature
Y	unspecified internal variable
ζ	degree of cure
e	mass-specific internal energy density
f	frequency
G	energy release (rate)
G^{c}	energetic crack resistance
h	mass-specific enthalpy density
J	Jacobian determinant
m	mass
p	pressure

r	mass-specific heat source density
t	time
a_i, A_i	acceleration vector (Eulerian, Lagrangian)
b_i	mass-specific body force density
J_i	J-Integral vector
q_i	heat flux vector
t_i	traction vector
u_i	displacement vector
v_i, V_i	velocity vector (Eulerian, Lagrangian)
x_i, X_i	position (Eulerian, Lagrangian)
σ_{ij}	Cauchy stress tensor
ε_{ij}	infinitesimal strain tensor
C_{ij}	right Cauchy-Green tensor
E_{ij}^{G}	Green strain tensor
F_{ij}	deformation gradient
H_{ij}	displacement gradient
P_{ij}	1st Piola-Kirchhoff stress tensor
R_{ij}	rotation tensor

S_{ij}	2$^{\text{nd}}$ Piola-Kirchhoff stress tensor
U_{ij}	right stretch tensor
χ_i	motion
δ	phase-field distribution function
$\Delta^{\alpha\beta}$	driving force acting on an interface α-β
$\mathcal{D}$	dissipation term

Descriptors

Γ	contour path
$\mathbb{b}, \mathbb{B}$	material body (Eulerian, Lagrangian)
$\mathrm{d}a, \mathrm{d}A$	scalar area element (Eulerian, Lagrangian)
$\mathrm{d}s, \mathrm{d}S$	scalar surface/interface element (Eulerian, Lagrangian)
$\mathrm{d}v, \mathrm{d}V$	scalar volume element (Eulerian, Lagrangian)
$\mathrm{d}x, \mathrm{d}X$	scalar line element (Eulerian, Lagrangian)
n_i, N_i	normal vector (Eulerian, Lagrangian)
t_i, T_i	tangential vector (Eulerian, Lagrangian); traction vector
δ_{ij}	Kronecker delta
ϵ_{ijk}	Levi-Civita operator
$(\bar{\bullet})$	volume average

$(\bullet)^{\alpha\beta}$ belonging to interface α-β

$(\bullet)^{\alpha}$ belonging to phase α

$(\bullet)^{0}$ quantity with respect to Lagrangian configuration

$(\bullet)^{c}$ belonging to crack phase

$(\bullet)^{\text{Ref}}$ referential value

$(\bullet)^{s}$ belonging to solid phase

$(\bullet)^{p}$ belonging to p-th Maxwell element

$(\bullet)_{\perp}$ scalar only valid orthogonally to a surface

$(\tilde{\bullet})$ eigen-, e.g. eigenstress

Abbreviations

J-Integral   Integral to calculate the energy release rate of a fracture surface

(P-)MDI   (poly-) methylene diphenyl diisocyanate

Avogadro   molecule editor software "Avogadro"

LAMMPS   molecular dynamics framework "Large-scale Atomic/Molecular Massively Parallel Simulator"

OVITO   particle and atomistic visualisation software "Open Visualisation Tool"

Pace3D   phase-field framework "Parallel Algorithms for Crystal Evolution in 3D"

VisIt	visualisation and analysis software "VisIt"
DMA	dynamic mechanical analysis
DSC	differential scanning calorimetry
EMD	equilibrium molecular dynamics
FRP	fibre-reinforced polymer
FRTS	fibre-reinforced thermoset
GF	glass fibre
LEFM	linear elastic fracture mechanics
MD	molecular dynamics
NCO	isocyanate group
NEMD	non-equilibrium molecular dynamics
OH	hydroxyl group
PF-EF	phase-field formulation derived from energy functional
PF-SI	phase-field formulation derived from sharp interface thermo-dynamics
PF/PFM	phase-field/phase-field method/model
PU	polyurethane (resin)
TS	thermoset

UP	unsaturated polyester (resin)
UPPH	unsaturated polyester-polyurethane hybrid (resin)
VOC	volatile organic compound

Bibliography

[1] D. B. Adolf and R. S. Chambers
     "A thermodynamically consistent, nonlinear viscoelastic approach for
     modeling thermosets during cure"
     In: *Journal of Rheology* 51.1 (2007), pp. 23–50 (cit. on pp. 4, 87).

[2] S. G. Advani and E. M. Sozer
     Process Modeling in Composites Manufacturing
     2nd ed. Boca Raton, FL: CRC Press, 2010, p. 630 (cit. on p. 2).

[3] B. J. Alder and T. E. Wainwright
     "Phase Transition for a Hard Sphere System"
     In: *The Journal of Chemical Physics* 27.5 (1957), pp. 1208–1209 (cit. on
     p. 8).

[4] B. J. Alder and T. E. Wainwright
     "Studies in Molecular Dynamics. I. General Method"
     In: *The Journal of Chemical Physics* 31.2 (1959), pp. 459–466 (cit. on
     p. 8).

[5] B. J. Alder and T. E. Wainwright
"Studies in Molecular Dynamics. II. Behavior of a Small Number of Elastic Spheres"
In: *The Journal of Chemical Physics* 33.5 (1960), pp. 1439–1451 (cit. on p. 8).

[6] M. Ambati, T. Gerasimov, and L. De Lorenzis
"Phase-field modeling of ductile fracture"
In: *Computational Mechanics* 55.5 (2015), pp. 1017–1040 (cit. on pp. 5, 7).

[7] L. Ambrosio and V. M. Tortorelli
On the approximation of free discontinuity problems.
Vol. 6. 1. Nicola Zanichelli Editore, Bologna, 1992, pp. 105–123 (cit. on p. 114).

[8] AVK - Industrievereinigung Verstärkte Kunststoffe e.V., ed.
Handbuch Faserverbundkunststoffe/Composites: Grundlagen, Verarbeitung, Anwendungen
4th ed. Wiesbaden: Springer Vieweg, 2013, p. 601 (cit. on pp. 1 sq.).

[9] Avogadro Chemistry
Avogadro: an open-source molecular builder and visualization tool, Version 1.20
URL: http://avogadro.cc/ (visited on 2019-01-07) (cit. on pp. 11, 145).

[10] F. Awaja, S. Zhang, M. Tripathi, A. Nikiforov, and N. Pugno
"Cracks, microcracks and fracture in polymer structures: Formation, detection, autonomic repair"
In: *Progress in Materials Science* 83 (2016), pp. 536–573 (cit. on p. 4).

[11] E. J. Barbero
Introduction to Composite Materials Design
3rd ed. Boca Raton, FL: CRC Press, 2017, p. 534 (cit. on p. 1).

[12]   A. Bartels and J. Mosler
       "Efficient variational constitutive updates for Allen-Cahn-type phase
       field theory coupled to continuum mechanics"
       In: *Computer Methods in Applied Mechanics and Engineering* 317 (2017),
       pp. 55–83 (cit. on pp. 6, 81, 100).

[13]   J. M. Barton, G. J. Buist, A. S. Deazle, I. Hamerton, B. Howlin, and J. R.
       Jones
       "The application of molecular simulation to the rational design of new
       materials: 1. Structure and modelling studies of linear epoxy systems"
       In: *Polymer* 35 (1994), pp. 4326–4333 (cit. on p. 9).

[14]   J. M. Barton, A. S. Deazle, I. Hamerton, B. J. Howlin, and J. R. Jones
       "The application of molecular simulation to the rational design of new
       materials: 2. Prediction of the physico-mechanical properties of linear
       epoxy systems"
       In: *Polymer* 38.17 (1997), pp. 4305–4310 (cit. on p. 9).

[15]   E. Becker and W. Bürger
       *Kontinuumsmechanik: eine Einf. in d. Grundlagen u. einfache Anwend-
       ungen*
       Ed. by H. Görtler.   Leitfäden der angewandten Mathematik und
       Mechanik. Stuttgart: B.G.Teubner, 1975, p. 228 (cit. on pp. 19, 21,
       23, 25 sq., 28, 30, 34).

[16]   C. Beckermann, H. J. Diepers, I. Steinbach, A. Karma, and X. Tong
       "Modeling Melt Convection in Phase-Field Simulations of Solidification"
       In: *Journal of Computational Physics* 154.2 (1999), pp. 468–496 (cit. on
       pp. 74, 112, 114).

[17]   S. W. Benson
       "III - Bond energies"
       In: *Journal of Chemical Education* 42.9 (1965), p. 502 (cit. on pp. 130,
       147).

[18] A. Bernath, L. Kärger, and F. Henning
"Accurate cure modeling for isothermal processing of fast curing epoxy resins"
In: *Polymers* 8.11 (2016), p. 19 (cit. on pp. 52 sq.).

[19] A. Bertram
Elasticity and Plasticity of Large Deformations
Berlin, Heidelberg: Springer-Verlag, 2005, p. 326 (cit. on pp. 17, 19 sqq., 24 sq., 28 sq., 31, 36).

[20] W. Boettinger, J. Warren, C. Beckermann, and A. Karma
"Phase-field simulation of Solidification"
In: *Annual Review of Materials Research* 32.1 (2002), pp. 163–194 (cit. on p. 5).

[21] L. Boltzmann
Populäre Schriften
Leipzig: J. A. Barth, 1905, p. 440 (cit. on p. 17).

[22] B. Bourdin, G. A. Francfort, and J.-J. Marigo
"Numerical experiments in revisited brittle fracture"
In: *Journal of the Mechanics and Physics of Solids* 48.4 (2000), pp. 797–826 (cit. on pp. 7, 114).

[23] B. Bourdin, G. A. Francfort, and J. J. Marigo
"The variational approach to fracture"
In: *Journal of Elasticity* 91.1 (2008), pp. 5–148 (cit. on p. 7).

[24] B. Bourdin, J.-J. Marigo, C. Maurini, and P. Sicsic
"Morphogenesis and Propagation of Complex Cracks Induced by Thermal Shocks"
In: *Physical Review Letters* 112.1 (2014), p. 014301 (cit. on pp. 7, 114).

[25] D. Bücheler
personal communication: process parameters for moulding fibre-reinforced

thermosets
(Cit. on pp. 146, 168).

[26]   A. R. Bunsell
Handbook of Properties of Textile and Technical Fibres
2nd ed. The Textile Institute Book Series. Duxford, UK: Woodhead
Publishing, 2018, p. 1052 (cit. on pp. 1, 99, 182, 191).

[27]   J. W. Cahn
"Free energy of a nonuniform system. II. Thermodynamic basis"
In: *The Journal of Chemical Physics* 30.5 (1959), pp. 1121–1124 (cit. on
p. 63).

[28]   J. W. Cahn and J. E. Hilliard
"Free energy of a nonuniform system. I. Interfacial free energy"
In: *The Journal of Chemical Physics* 28.2 (1958), pp. 258–267 (cit. on
pp. 5, 63).

[29]   J. W. Cahn and J. E. Hilliard
"Free energy of a nonuniform system. III. Nucleation in a two compo-
nent incompressible fluid"
In: *The Journal of Chemical Physics* 31.3 (1959), pp. 688–699 (cit. on
p. 63).

[30]   C. A. Careglio, C. Canales, L. Papeleux, J.-p. Ponthot, and A. E. Mirasso
"An Implementation of the Generalized Maxwell Viscoelastic Constitu-
tive Model"
In: *Mecanica Computacional* XXXIII (2014), pp. 1179–1192 (cit. on
p. 103).

[31]   V. Carollo, T. Guillén-Hernández, J. Reinoso, and M. Paggi
"Recent advancements on the phase field approach to brittle fracture
for heterogeneous materials and structures"
In: *Advanced Modeling and Simulation in Engineering Sciences* 5.1 (2018),
pp. 1–8 (cit. on p. 7).

[32]   E. W. V. Chaves
Notes on Continuum Mechanics
1st ed. Lecture Notes on Numerical Methods in Engineering and Sciences. Dordrecht: Springer Netherlands, 2013, p. 673 (cit. on pp. 16, 25, 28, 31 sqq.).

[33]   H. Z. Chen and Y. C. Shu
"Phase-field modeling of martensitic microstructure with inhomogeneous elasticity"
In: *Journal of Applied Physics* 113.12 (2013), p. 123506 (cit. on p. 6).

[34]   L.-Q. Chen
"Phase-Field Models for Microstructure Evolution"
In: *Annual Review of Materials Research* 32.1 (2002), pp. 113–140 (cit. on p. 5).

[35]   H. Childs, E. Brugger, B. Whitlock, J. S Meredith, S. Ahern, K. Bonnell, M. Miller, G. Weber, C. Harrison, D. Pugmire, T. Fogal, C. Garth, A. Sanderson, E. W. Bethel, M. Durant, D. Camp, J. Favre, O. Rübel, P. Navratil, and F. Vivodtzev
"VisIt: An End-User Tool for Visualizing and Analyzing Very Large Data"
In: *Proceed SciDAC.* 2011, pp. 1–16 (cit. on p. 11).

[36]   B. D. Coleman and W. Noll
"The thermodynamics of elastic materials with heat conduction and viscosity"
In: *Archive for Rational Mechanics and Analysis* 13.1 (1963), pp. 167–178 (cit. on p. 34).

[37]   J. B. Collins and H. Levine
"Diffuse interface model of diffusion-limited crystal growth"
In: *Physical Review B* 31.9 (1985), pp. 6119–6122 (cit. on p. 63).

[38]   E. Cosserat and F. Cosserat
       Théorie des corps déformables
       Paris: A. Hermann et fils, 1909, p. 226 (cit. on p. 17).

[39]   T. L. Cottrell
       The Strengths of Chemical Bonds
       London: Butterworths, 1954, p. 310 (cit. on pp. 130, 147).

[40]   B. deB Darwent
       Bond dissociation energies in simple molecules
       NSRDS-NBS. Washington D.C.: U.S. National Bureau of Standards,
       1970, p. 52 (cit. on pp. 130, 147).

[41]   A. T. DiBenedetto
       "Prediction of the glass transition temperature of polymers: A model
       based on the principle of corresponding states"
       In: *Journal of Polymer Science Part B: Polymer Physics* 25.9 (1987),
       pp. 1949–1969 (cit. on pp. 53, 98).

[42]   E. H. Dill
       Continuum Mechanics: Elasticity, Plasticity, Viscoelasticity
       1st ed. Boca Raton, FL: CRC Press, 2006, p. 368 (cit. on p. 17).

[43]   R. Dimitri, P. Cornetti, V. Mantič, M. Trullo, and L. De Lorenzis
       "Mode-I debonding of a double cantilever beam: A comparison between
       cohesive crack modeling and Finite Fracture Mechanics"
       In: *International Journal of Solids and Structures* 124 (2017), pp. 57–72
       (cit. on p. 7).

[44]   D. C. Doherty
       "Polymerization molecular dynamics simulations. I. Cross-linked atom-
       istic models for poly(methacrylate) networks"
       In: *Computational and Theoretical Polymer Science* 8.1-2 (1998), pp. 169–
       178 (cit. on pp. 9, 127 sq.).

[45]   R. Duduchava, E. Shargorodsky, and G. Tephnadze
       "Extension of the unit normal vector field from a hypersurface"
       In: *Georgian Math. J.* 22.3 (2015), pp. 355–359 (cit. on pp. 71 sq., 111).

[46]   A. Durga, P. Wollants, and N. Moelans
       "Evaluation of interfacial excess contributions in different phase-field
       models for elastically inhomogeneous systems"
       In: *Modelling and Simulation in Materials Science and Engineering* 21.5
       (2013), p. 055018 (cit. on p. 6).

[47]   J. Eiken, B. Böttger, and I. Steinbach
       "Multiphase-field approach for multicomponent alloys with extrapola-
       tion scheme for numerical application"
       In: *Physical Review E - Statistical, Nonlinear, and Soft Matter Physics*
       73.6 (2006), p. 66122 (cit. on p. 114).

[48]   J. Eiken
       "The finite phase-field method - A numerical diffuse interface approach
       for microstructure simulation with minimized discretization error"
       In: *Materials Research Society Symposium Proceedings* 1369 (2011),
       mrss12–1369–xx05–05 (cit. on pp. 83 sq.).

[49]   A. Einstein
       "Die Grundlage der allgemeinen Relativitätstheorie"
       In: *Annalen der Physik* 354.7 (1916), pp. 769–822 (cit. on p. 11).

[50]   R. M. Elder, J. W. Andzelm, and T. W. Sirk
       "A molecular simulation study of the glass transition of cross-linked
       poly dicyclopentadiene networks"
       In: *Chemical Physics Letters* 637 (2015), pp. 103–109 (cit. on p. 128).

[51]   J. Ettrich, A. Choudhury, O. Tschukin, E. Schoof, A. August, and B.
       Nestler
       "Modelling of transient heat conduction with diffuse interface methods"

In: *Modelling and Simulation in Materials Science and Engineering* 22.8 (2014), p. 085006 (cit. on p. 100).

[52]   P. Farrell and C. Maurini
"Linear and nonlinear solvers for variational phase-field models of brittle fracture"
In: *International Journal for Numerical Methods in Engineering* 109.5 (2017), pp. 648–667 (cit. on p. 114).

[53]   R. Folch, J. Casademunt, A. Hernández-Machado, and L. Ramírez-Piscina
"Phase-field model for Hele-Shaw flows with arbitrary viscosity contrast. I. Theoretical approach."
In: *Physical Review. E* 60.2 Pt B (1999), pp. 1724–1733 (cit. on pp. 115, 121).

[54]   S. Fomel
"Traveltime computation with the linearized eikonal equation"
In: *SEP report* 94 (1997), pp. 123–131 (cit. on p. 72).

[55]   J. B. J. Fourier
Théorie Analytique de la Chaleur
Paris: Firmin Didot, Père et fils, 1822, p. 639 (cit. on p. 90).

[56]   G. A. Francfort and J.-J. Marigo
"Revisiting brittle fracture as an energy minimization problem"
In: *Journal of the Mechanics and Physics of Solids* 46.8 (1998), pp. 1319–1342 (cit. on p. 7).

[57]   D. Frenkel and B. Smit
Understanding Molecular Simulation: From Algorithms to Applications
San Diego: Academic Press, 2002, p. 664 (cit. on p. 54).

[58]   A. Galbis and M. Maestre
Vector Analysis Versus Vector Calculus
New York: Springer-Verlag, 2012, p. 383 (cit. on p. 25).

[59]   E. E. Gdoutos
       Fracture Mechanics: An Introduction
       2nd ed. Dordrecht: Springer Netherlands, 2005, p. 370 (cit. on pp. 40, 42 sq.).

[60]   M. Gentz, D. Armentrout, P. Rupnowski, L. Kumosa, E. Shin, J. K. Sutter, and M. Kumosa
       "In-plane shear testing of medium and high modulus woven graphite fiber reinforced/polyimide composites"
       In: *Composites Science and Technology* 64.2 (2004), pp. 203–220 (cit. on p. 3).

[61]   M. Gentz, B. Benedikt, J. K. Sutter, and M. Kumosa
       "Residual stresses in unidirectional graphite fiber/polyimide composites as a function of aging"
       In: *Composites Science and Technology* 64.10 (2004), pp. 1671–1677 (cit. on p. 3).

[62]   K. L. Goh
       Discontinuous-Fibre Reinforced Composites
       1st ed. London: Springer-Verlag, 2017, p. 190 (cit. on pp. 43, 174, 181 sq., 191).

[63]   Granta Design
       CES EduPack, version 2018
       URL: http://www.grantadesign.com/education/edupack/ (visited on 2019-01-09) (cit. on pp. 153, 156 sq., 161, 165, 171).

[64]   M. S. Green
       "Markoff random processes and the statistical mechanics of time-dependent phenomena. II. Irreversible processes in fluids"
       In: *The Journal of Chemical Physics* 22.3 (1954), pp. 398–413 (cit. on p. 56).

[65]   A. A. Griffith
       "The Phenomena of Rupture and Flow in Solids"
       In: *Philosophical Transactions of the Royal Society A: Mathematical,
       Physical and Engineering Sciences* 221.582-593 (1921), pp. 163–198 (cit.
       on pp. 7, 15, 39, 41, 114).

[66]   D. Gross and T. Seelig
       Fracture Mechanics: With an Introduction to Micromechanics
       3rd ed. Cham: Springer, 2018, p. 358 (cit. on pp. 39, 41 sqq.).

[67]   A. Gupta and D. Steigmann
       "Kinematics"
       In: *Continuum Mechanics: Encyclopedia of Life Support Systems (EOLSS)*.
       Oxford, UK: Eolss Publishers, 2012 (cit. on p. 26).

[68]   M. E. Gurtin
       Configurational Forces as Basic Concepts of Continuum Physics
       Vol. 137. New York: Springer-Verlag, 2000, p. 250 (cit. on pp. 6, 69, 71).

[69]   M. E. Gurtin, E. Fried, and L. Anand
       The Mechanics and Thermodynamics of Continua
       Cambridge: Cambridge University Press, 2013, p. 718 (cit. on pp. 63,
       110).

[70]   P. J. Halley and M. E. Mackay
       "Chemorheology of thermosets - an overview"
       In: *Polymer Engineering & Science* 36.5 (1996), pp. 593–609 (cit. on pp. 2,
       52).

[71]   B. Halphen and Q. Son Nguyen
       "Sur les matériaux standard généralisés"
       In: *Journal de Mécanique* 14 (1975), pp. 39–63 (cit. on p. 93).

[72]   I. Hamerton, C. R. Heald, and B. J. Howlin
       "Molecular modelling of the physical and mechanical properties of two

polycyanurate network polymers"
In: *J. Mater. Chem.* 6.3 (1996), pp. 311–314 (cit. on p. 9).

[73]   A. C. Hansen-Dörr, M. Gude, R. Böhm, and M. Kästner
       "Phase Field Model for Interface Failure"
       In: *Proceedings of the 7th GACM Colloquium on Computational Mechanics for Young Scientists from Academia and Industry.* Ed. by M. von Scheven, M.-A. Kep, and N. Karajan. Stuttgart: Institute for Structural Mechanics, University of Stuttgart, 2017, pp. 343–346 (cit. on p. 7).

[74]   M. D. Hanwell, D. E. Curtis, D. C. Lonie, T. Vandermeersch, E. Zurek, and G. R. Hutchison
       "Avogadro: an advanced semantic chemical editor, visualization, and analysis platform"
       In: *Journal of Cheminformatics* 4.1 (2012), p. 17 (cit. on p. 11).

[75]   P. Haupt
       Continuum Mechanics and Theory of Materials
       2nd ed. Berlin, Heidelberg: Springer-Verlag, 2002, p. 643 (cit. on pp. 35 sqq.).

[76]   D. R. Heine, G. S. Grest, C. D. Lorenz, M. Tsige, and M. J. Stevens
       "Atomistic simulations of end-linked poly (dimethylsiloxane) networks: Structure and relaxation"
       In: *Macromolecules* 37.10 (2004), pp. 3857–3864 (cit. on pp. 9, 127).

[77]   C. Herring
       "Surface Tension as a Motivation for Sintering"
       In: *The Physics of Powder Metallurgy.* Ed. by W. Kingston. New York: McGraw-Hill, 1951. Chap. 8, pp. 143–179 (cit. on p. 69).

[78]   C. Herrmann, E. Schoof, D. Schneider, F. Schwab, A. Reiter, M. Selzer, and B. Nestler
       "Multiphase-field model of small strain elasto-plasticity according to the mechanical jump conditions"

In: *Computational Mechanics* 62.6 (2018), pp. 1399–1412 (cit. on pp. 16, 82, 104).

[79]   M. Hillert
"A theory of nucleation for solid solutions"
Thesis (Sc.D.) Massachusetts Institute of Technology, 1956 (cit. on p. 63).

[80]   E. Hornbogen, G. Eggeler, and E. Werner
Werkstoffe: Aufbau und Eigenschaften von Keramik-, Metall-, Polymer- und Verbundwerkstoffen
10th ed. Springer-Lehrbuch. Berlin, Heidelberg: Springer-Verlag, 2012, p. 596 (cit. on pp. 1, 157).

[81]   M. Hossain and P. Steinmann
"Degree of cure-dependent modelling for polymer curing processes at small-strain. Part I: consistent reformulation"
In: *Computational Mechanics* 53.4 (2014), pp. 777–787 (cit. on p. 4).

[82]   J. Hötzer, A. Reiter, H. Hierl, P. Steinmetz, M. Selzer, and B. Nestler
"The parallel multi-physics phase-field framework PACE3D"
In: *Journal of Computational Science* 26 (2018), pp. 1–12 (cit. on pp. 11, 16, 82, 84, 166, 182).

[83]   P. C. Howell
"Comparison of molecular dynamics methods and interatomic potentials for calculating the thermal conductivity of silicon"
In: *Journal of Chemical Physics* 137.22 (2012), pp. 224111–1—-224111–14 (cit. on p. 154).

[84]   K. Hutter and K. Jöhnk
Continuum Methods of Physical Modeling
Berlin, Heidelberg: Springer-Verlag, 2004, p. 635 (cit. on p. 23).

[85] Y. Ichikawa and A. P. Selvadurai
Transport Phenomena in Porous Media: Aspects of Micro/Macro Behaviour
1st ed. Berlin, Heidelberg: Springer-Verlag, 2012, p. 384 (cit. on p. 26).

[86] C. Jang, T. W. Sirk, J. W. Andzelm, and C. F. Abrams
"Comparison of crosslinking algorithms in molecular dynamics simulation of thermosetting polymers"
In: *Macromolecular Theory and Simulations* 24.3 (2015), pp. 260–270
(cit. on pp. 127 sq.).

[87] M. R. Kamal, S. Sourour, and M. Ryan
"Integrated thermorheological analysis of the cure of thermosets"
In: *SPE Tech. Pap.* 19 (1973), pp. 187–191 (cit. on pp. 52, 97).

[88] A. Karma, D. A. Kessler, and H. Levine
"Phase-Field Model of Mode III Dynamic Fracture"
In: *Physical Review Letters* 87.4 (2001), p. 45501 (cit. on p. 7).

[89] A. Kelly and N. H. Macmillan
Strong solids
3rd ed. Oxford ,UK: Clarendon Press, 1986, p. 423 (cit. on p. 43).

[90] A. G. Khachaturyan
Theory of structural transformations in solids
Hoboken: John Wiley & Sons Inc, 1983, p. 574 (cit. on pp. 6, 63).

[91] B. Kiefer, T. Furlan, and J. Mosler
"A numerical convergence study regarding homogenization assumptions in phase field modeling"
In: *International Journal for Numerical Methods in Engineering* 112.9
(2017), pp. 1097–1128 (cit. on p. 6).

[92] S. Klinge, A. Bartels, and P. Steinmann
"Modeling of curing processes based on a multi-field potential . Single- and multiscale aspects"

In: *International Journal of Solids and Structures* 49.17 (2012), pp. 2320–2333 (cit. on pp. 4, 87).

[93]   R. Kobayashi
"Modeling and numerical simulations of dendritic crystal growth"
In: *Physica D: Nonlinear Phenomena* 63.3-4 (1993), pp. 410–423 (cit. on p. 63).

[94]   R. Kubo
"Statistical'Mechanical Theory of Irreversible Processes. I. General Theory and Simple Applications to Magnetic and Conduction Problems"
In: *Journal of the Physical Society of Japan* 12.6 (1957), pp. 570–586 (cit. on p. 56).

[95]   R. Kubo, M. Yokota, and S. Nakajima
"Statistical-Mechanical Theory of Irreversible Processes. Response to Thermal Disturbance"
In: *Journal of the Physical Society of Japan* 12.11 (1957), pp. 1203–1211 (cit. on p. 56).

[96]   C. Kuhn and R. Müller
"A continuum phase field model for fracture"
In: *Engineering Fracture Mechanics* 77.18 (2010), pp. 3625–3634 (cit. on p. 7).

[97]   C. Kuhn, T. Noll, and R. Müller
"On phase field modeling of ductile fracture"
In: *GAMM-Mitteilungen* 39.1 (2016), pp. 35–54 (cit. on p. 7).

[98]   J. Kulawik, Z. Szeglowski, T. Czapla, and J. P. Kulawik
"Determination of glass transition temperature, thermal expansion, and shrinkage of epoxy resins"
In: *Colloid & Polymer Science* 267.11 (1989), pp. 970–975 (cit. on pp. 57, 157).

[99]   L. D. Landau and E. M. Lifshits
       Fluid mechanics
       1st ed. Course of Theoretical Physics. Oxford, UK: Pergamon Press,
       1959, p. 558 (cit. on p. 57).

[100] L. D. Landau and E. M. Lifshits
       Theory of Elasticity
       1st ed. Course of Theoretical Physics. Oxford, UK: Pergamon Press,
       1959, p. 134 (cit. on p. 57).

[101] J. Lange, S. Toll, J.-A. E. Månson, and A. Hult
       "Residual stress build-up in thermoset films cured above their ultimate
       glass transition temperature"
       In: *Polymer* 36.16 (1995), pp. 3135–3141 (cit. on p. 3).

[102] M. M. Lavrentiev, V. G. Romanov, and V. G. Vasiliev
       Multidimensional Inverse Problems for Differential Equations
       Berlin, Heidelberg: Springer-Verlag, 1970, p. 58 (cit. on p. 72).

[103] Lawrence Livermore National Laboratory
       VisIt, Version 2.13.0
       URL: https://wci.llnl.gov/simulation/computer-codes/
       visit/ (visited on 2018-12-31) (cit. on p. 11).

[104] B. Li, C. Peco, D. Millán, I. Arias, and M. Arroyo
       "Phase-field modeling and simulation of fracture in brittle materials
       with strongly anisotropic surface energy"
       In: *International Journal for Numerical Methods in Engineering* 102.3-4
       (2015), pp. 711–727 (cit. on p. 7).

[105] C. Li, E. Coons, and A. Strachan
       "Material property prediction of thermoset polymers by molecular
       dynamics simulations"
       In: *Acta Mechanica* 225.4 (2014), pp. 1187–1196 (cit. on p. 9).

[106]   C. Li and A. Strachan
        "Molecular dynamics predictions of thermal and mechanical properties
        of thermoset polymer EPON862/DETDA"
        In: *Polymer* 52.13 (2011), pp. 2920–2928 (cit. on p. 9).

[107]   X. Li, J. Lowengrub, A. Rätz, and A. Voigt
        "Solving PDEs in complex domains - a diffuse domain approach"
        In: *Communications in Mathematical Sciences* 7.1 (2009), pp. 88–107
        (cit. on pp. 5, 87).

[108]   A. Lion and P. Höfer
        "On the phenomenological representation of curing phenomena in
        continuum mechanics"
        In: *Archives of Mechanics* 59.1 (2007), pp. 59–89 (cit. on pp. 4, 87).

[109]   I.-S. Liu
        Continuum Mechanics
        Berlin, Heidelberg: Springer-Verlag, 2002, p. 298 (cit. on pp. 21, 23, 28,
        32 sq., 65, 171).

[110]   R. Mahnken
        "Thermodynamic consistent modeling of polymer curing coupled to
        visco-elasticity at large strains"
        In: *International Journal of Solids and Structures* 50.13 (2013), pp. 2003–
        2021 (cit. on pp. 4, 87, 97).

[111]   M. Mamivand, M. A. Zaeem, and H. El Kadiri
        "A review on phase field modeling of martensitic phase transformation"
        In: *Computational Materials Science* 77 (2013), pp. 304–311 (cit. on p. 5).

[112]   J. E. Mark, ed.
        Physical Properties of Polymers Handbook
        2nd ed. New York: Springer-Verlag, 2007, p. 1076 (cit. on pp. 153,
        156 sq., 161).

[113]   Math2Market GmbH
        GeoDict
        URL: http://www.geodict.com/ (visited on 2019-01-10) (cit. on
        p. 166).

[114]   K. Matyjaszewski and T. P. Davis
        Handbook of Radical Polymerization
        Hoboken: Wiley, 2002, p. 936 (cit. on p. 128).

[115]   G. A. Maugin
        Material Inhomogeneities in Elasticity
        Applied Mathematics. Boca Raton, FL: CRC Press, 1993, p. 292 (cit. on
        p. 17).

[116]   G. Mavko, T. Mukerji, and J. Dvorkin
        The Rock Physics Handbook: Tools for Seismic Analysis of Porous Media
        2nd ed. Cambridge: Cambridge University Press, 2009, p. 524 (cit. on
        pp. 36, 169).

[117]   F. Mémoli and G. Sapiro
        "Fast computation of weighted distance functions and geodesics on
        implicit hyper-surfaces"
        In: *Journal of Computational Physics* 173.2 (2001), pp. 730–764 (cit. on
        pp. 71, 111).

[118]   M. H. H. Meuwissen, H. A. de Boer, H. L. A. H. Steijvers, P. J. G. Schreurs,
        and M. G. D. Geers
        "Residual stresses in microelectronics induced by thermoset packaging
        materials during cure"
        In: *Microelectronics Reliability* 44.12 (2004), pp. 1985–1994 (cit. on p. 52).

[119]   C. Miehe, M. Hofacker, L.-M. Schänzel, and F. Aldakheel
        "Phase field modeling of fracture in multi-physics problems. Part II.
        Coupled brittle-to-ductile failure criteria and crack propagation in
        thermo-elastic–plastic solids"

In: *Computer Methods in Applied Mechanics and Engineering* 294 (2015), pp. 486–522 (cit. on p. 7).

[120] C. Miehe, F. Welschinger, and M. Hofacker
"Thermodynamically consistent phase-field models of fracture: Variational principles and multi-field FE implementations"
In: *International Journal for Numerical Methods in Engineering* 83.10 (2010), pp. 1273–1311 (cit. on pp. 7, 115).

[121] C. Miehe, L.-M. Schänzel, and H. Ulmer
"Phase field modeling of fracture in multi-physics problems. Part I. Balance of crack surface and failure criteria for brittle crack propagation in thermo-elastic solids"
In: *Computer Methods in Applied Mechanics and Engineering* 294 (2015), pp. 449–485 (cit. on p. 7).

[122] G. P. Moeckel
"Thermodynamics of an interface"
In: *Archive for Rational Mechanics and Analysis* 57.3 (1975), pp. 255–280 (cit. on p. 26).

[123] N. Moelans
"A quantitative and thermodynamically consistent phase-field interpolation function for multi-phase systems"
In: *Acta Materialia* 59.3 (2011), pp. 1077–1086 (cit. on p. 116).

[124] N. Moelans, B. Blanpain, and P. Wollants
"An introduction to phase-field modeling of microstructure evolution"
In: *Calphad* 32.2 (2008), pp. 268–294 (cit. on p. 5).

[125] J. Mosler, O. Shchyglo, and H. Montazer Hojjat
"A novel homogenization method for phase field approaches based on partial rank-one relaxation"
In: *Journal of the Mechanics and Physics of Solids* 68 (2014), pp. 251–266 (cit. on pp. 6 sq., 81, 100).

[126]   I. Müller
        Thermodynamics
        Interaction of Mechanics and Mathematics. Boston: Pitman, 1985,
        p. 521 (cit. on p. 26).

[127]   D. Mumford and J. Shah
        "Optimal approximations by piecewise smooth functions and associated
        variational problems"
        In: *Communications on Pure and Applied Mathematics* 42.5 (1989),
        pp. 577–685 (cit. on p. 114).

[128]   B. Nestler and A. Choudhury
        "Phase-field modeling of multi-component systems"
        In: *Current Opinion in Solid State and Materials Science* 15.3 (2011),
        pp. 93–105 (cit. on p. 5).

[129]   B. Nestler, H. Garcke, and B. Stinner
        "Multicomponent alloy solidification: Phase-field modeling and simula-
        tions"
        In: *Physical Review E* 71.4 (2005) (cit. on pp. 11, 16, 82, 84, 188).

[130]   B. Nestler, D. Schneider, E. Schoof, Y. Huang, M. Selzer, and V. Nach-
        name
        "Modeling of crack propagation on a mesoscopic length scale"
        In: *GAMM Mitteilungen* 39.1 (2016), pp. 78–91 (cit. on pp. 8, 109, 112).

[131]   R. Neumann, I. Schiel, F. K. Schwab, T. Böhlke, B. Nestler, and M. Wil-
        helm
        "Thermochemomechanical Mori-Tanaka based Modeling and Simula-
        tion of the Curing Process of Glass Fiber-Reinforced Thermosets"
        In: *(in submission)* (2019) (cit. on p. 170).

[132]   T. T. Nguyen, J. Yvonnet, Q. Z. Zhu, M. Bornert, and C. Chateau
        "A phase-field method for computational modeling of interfacial dam-
        age interacting with crack propagation in realistic microstructures

obtained by microtomography"
In: *Computer Methods in Applied Mechanics and Engineering* 312 (2016), pp. 567–595 (cit. on p. 7).

[133]   T. T. Nguyen, J. Réthoré, J. Yvonnet, and M. C. Baietto
"Multi-phase-field modeling of anisotropic crack propagation for polycrystalline materials"
In: *Computational Mechanics* 60.2 (2017), pp. 289–314 (cit. on p. 7).

[134]   R. P. Nimmer
"Fiber-Matrix Interface Effects in the Presence of Thermally Induced Residual Stresses"
In: *Journal of Composites Technology & Research* 12.2 (1990), pp. 65–75 (cit. on p. 4).

[135]   C. Oberste-Brandenburg
"Ein Materialmodell zur Beschreibung der Austenit-Martensit Phasentransformation unter Berücksichtigung der transformationsinduzierten Plastizität"
Ph.D. thesis. Ruhr-Universität Bochum, 1999, p. 123 (cit. on p. 99).

[136]   T. Okabe, Y. Oya, K. Tanabe, G. Kikugawa, and K. Yoshioka
"Molecular dynamics simulation of crosslinked epoxy resins: Curing and mechanical properties"
In: *European Polymer Journal* 80 (2016), pp. 78–88 (cit. on pp. 9, 127, 130).

[137]   T. Okabe, T. Takehara, K. Inose, N. Hirano, M. Nishikawa, and T. Uehara
"Curing reaction of epoxy resin composed of mixed base resin and curing agent: Experiments and molecular simulation"
In: *Polymer* 54.17 (2013), pp. 4660–4668 (cit. on pp. 9, 127, 130).

[138]   T. A. Osswald and N. Rudolph
Polymer Rheology: Fundamentals and Applications
München: Hanser Publications, 2015, p. 237 (cit. on p. 58).

[139] T. A. Osswald and G. Menges
Materials Science of Polymers for Engineers
München: Hanser Publishers, 2012, p. 595 (cit. on pp. 2 sq., 127, 165).

[140] M. Paggi and J. Reinoso
"Revisiting the problem of a crack impinging on an interface: A modeling framework for the interaction between the phase field approach for brittle fracture and the interface cohesive zone model"
In: *Computer Methods in Applied Mechanics and Engineering* 321 (2017), pp. 145–172 (cit. on p. 7).

[141] J. P. Pascault and R. J. J. Williams
"Glass transition temperature versus conversion relationships for thermosetting polymers"
In: *Journal of Polymer Science Part B: Polymer Physics* 28.1 (1990), pp. 85–95 (cit. on pp. 53, 158).

[142] S. Plimpton
"Short-Range Molecular Dynamics"
In: *Journal of Computational Physics* 117.6 (1997), pp. 1–42 (cit. on pp. 11, 16).

[143] D. Raabe
Computational Materials Science: The Simulation of Materials, Microstructures and Properties
Weinheim: Wiley-VCH Verlag GmbH, 2004, p. 379 (cit. on p. 8).

[144] G. Raabe
Molecular Simulation Studies on Thermophysical Properties: With Application to Working Fluids
1st ed. Molecular Modeling and Simulation. Singapore: Springer-Verlag, 2017, p. 306 (cit. on pp. 55 sq.).

[145] D. C. Rapaport
The Art of Molecular Dynamics Simulation

2nd ed. New York: Cambridge University Press, 2004, p. 564 (cit. on pp. 8, 54, 191).

[146]   A. Reuss
"Berechnung der Fließgrenze von Mischkristallen auf Grund der Plastizitätsbedingung für Einkristalle"
In: *Z. Angew. Math. Mech.* 9 (1929), pp. 49–58 (cit. on p. 5).

[147]   J. R. Rice
"A Path Independent Integral and the Approximate Analysis of Strain Concentration by Notches and Cracks"
In: *Journal of Applied Mechanics* 35.2 (1968), p. 379 (cit. on p. 42).

[148]   A. Rudin and P. Choi
The Elements of Polymer Science & Engineering
3rd ed. San Diego: Academic Press, 2013, p. 584 (cit. on pp. 158, 165, 191).

[149]   E. Ruiz and F. Trochu
"Thermomechanical Properties during Cure of Glass-Polyester RTM Composites: Elastic and Viscoelastic Modeling"
In: *Journal of Composite Materials* 39.10 (2005), pp. 881–916 (cit. on p. 4).

[150]   Sandia National Laboratories
Large Atomic/Molecular Massively Parallel Simulator (LAMMPS), Version 31Mar17
URL: http://lammps.sandia.gov/ (visited on 2018-12-22) (cit. on pp. 11, 16, 144).

[151]   T. P. Sathishkumar, S. Satheeshkumar, and J. Naveen
"Glass fiber-reinforced polymer composites - a review"
In: *Journal of Reinforced Plastics and Composites* 33.13 (2014), pp. 1258–1275 (cit. on p. 1).

[152] H. Schaefer
"Das Cosserat Kontinuum"
In: *ZAMM - Journal of Applied Mathematics and Mechanics / Zeitschrift für Angewandte Mathematik und Mechanik* 47.8 (1967), pp. 485–498 (cit. on p. 17).

[153] A. Schiraldi, P. Baldini, and E. Pezzati
"Epoxy polymers: Glass transition/cure degree correlation"
In: *Journal of thermal analysis* 30.6 (1985), pp. 1343–1348 (cit. on p. 158).

[154] T. Schlick
Molecular Modeling and Simulation: An Interdisciplinary Guide
Interdisciplinary Applied Mathematics. New York: Springer, 2010, p. 723 (cit. on p. 50).

[155] D. Schneider, E. Schoof, Y. Huang, M. Selzer, and B. Nestler
"Phase-field modeling of crack propagation in multiphase systems"
In: *Computer Methods in Applied Mechanics and Engineering* 312 (2016), pp. 186–195 (cit. on pp. 5, 8, 109, 112 sq., 117, 121 sq.).

[156] D. Schneider, E. Schoof, O. Tschukin, A. Reiter, C. Herrmann, F. Schwab, M. Selzer, and B. Nestler
"Correction to: Small strain multiphase-field model accounting for configurational forces and mechanical jump conditions (Computational Mechanics, (2018), 61, 3, (277-295), 10.1007/s00466-017-1458-4)"
In: *Computational Mechanics* 61.3 (2018), p. 297 (cit. on p. 81).

[157] D. Schneider, E. Schoof, O. Tschukin, A. Reiter, C. Herrmann, F. Schwab, M. Selzer, and B. Nestler
"Small strain multiphase-field model accounting for configurational forces and mechanical jump conditions"
In: *Computational Mechanics* 61.3 (2018), pp. 277–295 (cit. on pp. 6 sq., 81, 100).

[158]   D. Schneider, F. Schwab, E. Schoof, A. Reiter, C. Herrmann, M. Selzer,
        T. Böhlke, and B. Nestler
        "On the stress calculation within phase-field approaches: a model for
        finite deformations"
        In: *Computational Mechanics* 60.2 (2017), pp. 203–217 (cit. on pp. 6 sq.,
        16, 81, 100).

[159]   D. Schneider, O. Tschukin, A. Choudhury, M. Selzer, T. Böhlke, and
        B. Nestler
        "Phase-field elasticity model based on mechanical jump conditions"
        In: *Computational Mechanics* 55.5 (2015), pp. 887–901 (cit. on pp. 6 sq.,
        16, 81, 100).

[160]   L. Schöller
        "Simulationsstudien zur Rissausbreitung in Faserverbundwerkstoffen"
        Master's thesis. Karlsruher Institut für Technologie, 2018, p. 96 (cit. on
        pp. 109, 115, 119).

[161]   E. Schoof, D. Schneider, N. Streichhan, T. Mittnacht, M. Selzer, and
        B. Nestler
        "Multiphase-field modeling of martensitic phase transformation in a
        dual-phase microstructure"
        In: *International Journal of Solids and Structures* 134 (2018), pp. 181–194
        (cit. on pp. 5, 16).

[162]   H. Schürmann
        Konstruieren mit Faser-Kunststoff-Verbunden
        Berlin, Heidelberg: Springer-Verlag, 2005, p. 574 (cit. on pp. 2, 43, 181).

[163]   F. K. Schwab
        personal communication: DSC measurements (unpublished)
        (Cit. on pp. 150, 171).

[164]   F. K. Schwab and C. Denniston
        "Reaction and characterisation of a two-stage thermoset using molecu-

lar dynamics"
In: *Polym. Chem.* (2019) (cit. on pp. 44, 128, 145).

[165] N. Sharp, C. Li, A. Strachan, D. Adams, and R. B. Pipes
"Effects of water on epoxy cure kinetics and glass transition temperature utilizing molecular dynamics simulations"
In: *Journal of Polymer Science Part B: Polymer Physics* 55.15 (2017), pp. 1150–1159 (cit. on p. 9).

[166] M. Šilhavý
The Mechanics and Thermodynamics of Continuous Media
1st ed. Berlin, Heidelberg: Springer-Verlag, 1997, p. 504 (cit. on p. 28).

[167] T. W. Sirk, K. S. Khare, M. Karim, J. L. Lenhart, J. W. Andzelm, G. B. McKenna, and R. Khare
"High strain rate mechanical properties of a cross-linked epoxy across the glass transition"
In: *Polymer* 54.26 (2013), pp. 7048–7057 (cit. on p. 128).

[168] J. C. Slattery, L. Sagis, and E. S. Oh
Interfacial transport phenomena
2nd ed. New York: Springer, 2007, p. 828 (cit. on pp. 22, 25).

[169] W. S. Slaughter
Linearized Theory of Elasticity
Basel: Birkhäuser, 2002, p. 543 (cit. on pp. 16–19, 21, 24, 28 sqq., 34, 36).

[170] C. Soutis
"Fibre reinforced composites in aircraft construction"
In: *Progress in Aerospace Sciences* 41.2 (2005), pp. 143–151 (cit. on p. 2).

[171] R. Spatschek, C. Müller-Gugenberger, E. Brener, and B. Nestler
"Phase field modeling of fracture and stress-induced phase transitions"
In: *Physical Review E* 75.6 (2007), pp. 1–14 (cit. on p. 7).

[172] I. Steinbach
"Phase-field models in materials science"
In: *Modelling and Simulation in Materials Science and Engineering* 17.7 (2009), p. 073001 (cit. on pp. 83, 114, 188).

[173] I. Steinbach
"Phase-Field Model for Microstructure Evolution at the Mesoscopic Scale"
In: *Annual Review of Materials Research* 43.1 (2013), pp. 89–107 (cit. on p. 5).

[174] A. Stukowski
"Visualization and analysis of atomistic simulation data with OVITO - the Open Visualization Tool"
In: *Modelling and Simulation in Materials Science and Engineering* 18.1 (2010), p. 015012 (cit. on p. 11).

[175] A. Stukowski
Open Visualization Tool (OVITO), Version 2.9.0
URL: https://ovito.org/ (visited on 2018-12-31) (cit. on p. 11).

[176] H. Sun
"COMPASS: An ab Initio Force-Field Optimized for Condensed-Phase ApplicationsOverview with Details on Alkane and Benzene Compounds"
In: *The Journal of Physical Chemistry B* 102.38 (1998), pp. 7338–7364 (cit. on pp. 50 sq., 145).

[177] H. Sun, P. Ren, and J. R. Fried
"The COMPASS force field: parameterization and validation for phosphazenes"
In: *Computational and Theoretical Polymer Science* 8.1 (1998), pp. 229–246 (cit. on pp. 50 sq., 145).

[178] H. Sun and D. Rigby
       "Polysiloxanes: ab initio force field and structural, conformational and
       thermophysical properties"
       In: *Spectrochimica Acta Part A: Molecular and Biomolecular Spectroscopy*
       53.8 (1997), pp. 1301–1323 (cit. on pp. 50 sq., 145).

[179] Y. Sun and C. Beckermann
       "Sharp interface tracking using the phase-field equation"
       In: *Journal of Computational Physics* 220.2 (2007), pp. 626–653 (cit. on
       pp. 74, 112, 114).

[180] A. Takezawa, S. Nishiwaki, and M. Kitamura
       "Shape and topology optimization based on the phase field method and
       sensitivity analysis"
       In: *Journal of Computational Physics* 229.7 (2010), pp. 2697–2718 (cit. on
       p. 5).

[181] R. Talreja and C. V. Singh
       Damage and Failure of Composite Materials
       Cambridge: Cambridge University Press, 2012, p. 314 (cit. on p. 43).

[182] E. Tanné, T. Li, B. Bourdin, J. J. Marigo, and C. Maurini
       "Crack nucleation in variational phase-field models of brittle fracture"
       In: *Journal of the Mechanics and Physics of Solids* 110 (2018), pp. 80–99
       (cit. on p. 114).

[183] C. A. Truesdell
       *A first course in Rational continuum Mechanics Volume 1 General Con-
       cepts*
       2nd ed. Pure and applied mathematics. London: Academic Press, 1991,
       p. 391 (cit. on p. 28).

[184] M. Tuckerman, B. J. Berne, and G. J. Martyna
       "Reversible multiple time scale molecular dynamics"

In: *The Journal of Chemical Physics* 97.3 (1992), pp. 1990–2001 (cit. on p. 160).

[185]   M. E. Tuckerman
Statistical Mechanics: Theory and Molecular Simulation
Oxford Graduate Texts. New York: Oxford University Press, 2010, p. 696 (cit. on p. 55).

[186]   A. R. Umantsev and A. L. Roitburd
"Isothermal relaxation in a nonlocal medium"
In: *Soviet Physics - Solid State* 30.4 (1988), pp. 1124–1131 (cit. on pp. 71, 111).

[187]   V. Ginzburg and L. D. Landau
"On the Theory of Superconductivity"
In: *Zh. Eksp. Teor. Fiz.* 20 (1950), pp. 1064–1082 (cit. on pp. 5, 63).

[188]   K. C. Valanis
Irreversible Thermodynamics of Continuous Media: Internal Variable Theory
Wien: Springer-Verlag, 1971, p. 172 (cit. on p. 93).

[189]   R. Verleg (Aliancys AG)
personal communication
(Cit. on p. 48).

[190]   R. Verleg and E. Hummer
"Unsaturated Polyester Urethane Hybrid Technology - Fast Track to Advanced Composites"
In: *COMPOSITES 2006 Convention and Trade Show American Composites Manufacturers Association.* 2006, pp. 1–16 (cit. on pp. 44, 150, 169).

[191]   W. Voigt
"Theoretische Studien über die Elasticitätsverhältnisse der Krystalle"
In: *Abhandlungen der königlichen Gesellschaft der Wissenschaften zu Göttingen* 34 (1887), pp. 3–100 (cit. on p. 17).

[192] W. Voigt
"Über die Beziehung zwischen den beiden Elastizitätskonstanten iso-
troper Körper"
In: *Annalen der Physik* 274.12 (1889), pp. 573–587 (cit. on p. 5).

[193] S. Vyazovkin, N. Koga, and C. Schick, eds.
*Handbook of Thermal Analysis and Calorimetry: Recent Advances, Tech-
niques and Applications*
2nd ed. Vol. 6. Handbook of Thermal Analysis and Calorimetry. Ams-
terdam: Elsevier Science B.V., 2018, p. 860 (cit. on p. 53).

[194] J. van der Waals
"Thermodynamische theorie der capillariteit in de onderstelling van
continue dichtheidsverandering"
In: *Verhandelingen - Koninklijke Nederlandse Akademie van Wetenschap-
pen, Afdeling Natuurkunde, Eerste Reeks* 1.8 (1893), p. 56 (cit. on pp. 5,
62).

[195] R. W. Warfield, M. C. Petree, and P. Donovan
The specific heat of thermosetting polymers
Tech. rep. White Oak, MD: Naval Ordnance Lab, 1959, p. 26 (cit. on
p. 153).

[196] R. W. Warfield, M. C. Petree, and P. Donovan
"The specific heat of thermosetting polymers"
In: *Journal of Applied Chemistry* 10 (1960), pp. 429–432 (cit. on p. 153).

[197] E. S. Watson, M. J. O'Neill, J. Justin, and N. Brenner
"A Differential Scanning Calorimeter for Quantitative Differential Ther-
mal Analysis"
In: *Analytical Chemistry* 36.7 (1964), pp. 1233–1238 (cit. on p. 53).

[198] A. A. Wheeler, B. T. Murray, and R. J. Schaefer
"Computation of dendrites using a phase field model"

In: *Physica D: Nonlinear Phenomena* 66.1-2 (1993), pp. 243–262 (cit. on p. 63).

[199]   S. M. Wiederhorn
"Fracture Surface Energy of Glass"
In: *Journal of the American Ceramic Society* 52.2 (1969), pp. 99–105 (cit. on p. 183).

[200]   C. Wu and W. Xu
"Atomistic molecular modelling of crosslinked epoxy resin"
In: *Polymer* 47.16 (2006), pp. 6004–6009 (cit. on pp. 9, 127).

[201]   G. Wypych
Handbook of Odors in Plastic Materials
2nd ed. Toronto, ON: ChemTec Publishing, 2017, p. 260 (cit. on pp. 147, 150).

[202]   I. Yarovsky and E. Evans
"Computer simulation of structure and properties of crosslinked polymers: application to epoxy resins"
In: *Polymer* 43.3 (2002), pp. 963–969 (cit. on pp. 9, 127).

[203]   L. G. Zhao, N. A. Warrior, and A. C. Long
"A micromechanical study of residual stress and its effect on transverse failure in polymer-matrix composites"
In: *International Journal of Solids and Structures* 43.18 (2006), pp. 5449–5467 (cit. on p. 3).